The Role of Stellar Feedback in Star Cluster Formation

Thesis by
Michael Yvan Grudić

In Partial Fulfillment of the Requirements for the
Degree of
Doctor of Philosophy

CALIFORNIA INSTITUTE OF TECHNOLOGY
Pasadena, California

2019
Defended May 22 2019

ACKNOWLEDGEMENTS

To Mom, Dad, Jenny, Jamie, and the rest of my family. I don't see you all nearly enough, but nevertheless your love and encouragement has never failed to keep me aloft these five years.

To Phil Hopkins, for being the most supportive, hard-working, inspiring, and encouraging mentor I could have asked for. You lift up everyone around you, and we are lucky to have you. You taught me how to think like a theoretician, how to convey my ideas effectively, and how to focus on the big picture instead of going down the rabbit hole of numerical nonsense. Perhaps once day I will actually put the latter lesson into practice.

To Dávid Guszejnov, the best friend I ever had at Caltech. Whether we're crawling dungeons, debugging code, or bouncing physics ideas around, I always enjoy the things we do together, and look forward to the great things we're going to achieve in our field.

To JoAnn Boyd, TAPIR's incomparable administrative assistant. You somehow keep this whole outfit running, and I have always enjoyed our chats when you stop by the office.

To the other PIs of the FIRE collaboration, including Norm Murray, Eliot Quataert, Claude-André Faucher-Giguère, Mike Boylan-Kolchin, and Dušan Kereš. Your contributions and expertise always help me turn an OK paper into a great one.

To Ernie, for making this work thermodynamically possible.

To Mark Krumholz, for providing helpful and honest feedback on my first contributions to the field, for enlightening debates and conversations, and for providing useful data compilations and software. We don't see eye-to-eye on every issue in the field, but I enjoy and learn something from every exchange we have, and admire how tirelessly you work in service of the community.

To the other members of the star formation community, especially Angela Adamo, Diederik Kruijssen, and Bruce Elmegreen. Your encouragement motivated me to push my theoretical approach to its final conclusion, turning what was a broad sketch into something that can confront observations.

To Clare Lahey, my first love, long-time partner, and now good friend. You, more than anyone else, gave me motivation and inspiration to do the best work I can do,

and to be the best person I can be. You've helped me celebrate the highs, and you were my rock during the lows. I know that wherever life takes us we can always count on each other.

ABSTRACT

A methodology for numerical magnetohydrodynamics simulations of star cluster formation, accounting for all mechanisms of stellar feedback from massive stars, is developed and used to address a range of problems regarding the formation of stars and star clusters in giant molecular clouds (GMCs). These studies culminate in a new theoretical framework that connects properties of GMCs to those of the star clusters that form in them.

The simulation methodology is established and tested, and the problem of the star formation efficiency (SFE) of molecular clouds is addressed. It is found that SFE is set by the balance of feedback and gravity, with very weak dependence upon other factors. A simple dimensional scaling law with cloud surface density emerges from the complex interplay of different feedback physics. Parameter space is found where feedback must fail, and the SFE is high, and the implications of this prediction are explored.

The star clusters formed in the simulations are found to resemble observed young, massive star clusters in the form of their surface brightness profiles, leading to the hypothesis that this structure is a result of the star formation process. It is shown that the shallow, power-law density profiles characteristic of young clusters is predicted by the hierarchical star formation scenario.

It is shown that the SFE law, when coupled to an analytic cloud collapse model, predicts that gas should be exhausted by highly-efficient star formation at a stellar surface density of $\sim 10^5 - 10^6\,\mathrm{M}_\odot\,\mathrm{pc}^{-2}$, consistent with the maximum observed.

A new suite of simulations is developed to specifically model GMCs in the Milky Way. It is found that the picture of feedback-disrupted star formation is able to account for both the normalization and the scatter in the measured SFE of GMCs in the Milky Way, the first theory to do so.

The uncertainty in the simulated SFE due to the choice of feedback prescription is quantified, by running a controlled methods study of several different prescriptions in the literature. In the cloud model simulated, the choice of prescription affects the simulated SFE at the factor of ~ 3 level, explaining discrepancies in the literature and identifying the small-scale details of massive star formation as the main uncertainty in cluster formation simulations.

Finally, the simulation suite is extended to model massive GMCs in local spiral galaxies, and to simulate 10 random realizations at each point in parameter space, mapping out the stochastic nature of star cluster formation in GMCs. A model is calibrated to the simulation results, taking the cloud bulk properties as input parameters, and predicting the detailed properties of the star clusters formed in it. A star cluster catalogue is synthesized from observed GMCs in M83, and good agreement is found with observed star cluster properties, including the fraction of stars in bound clusters, the maximum cluster mass, and the distribution of cluster sizes.

PUBLISHED CONTENT AND CONTRIBUTIONS

M. Y. Grudić, P. F. Hopkins, C.-A. Faucher-Giguère, E. Quataert, N. Murray, and D. Kereš. “When feedback fails: the scaling and saturation of star formation efficiency". MNRAS, 475:3511–3528, April 2018b. doi: 10.1093/mnras/sty035. MYG participated in the conception of the project, developed numerical code for the simulations, carried out the simulations, and analyzed the results.

M. Y. Grudić, D. Guszejnov, P. F. Hopkins, A. Lamberts, M. Boylan-Kolchin, N. Murray, and D. Schmitz. “From the top down and back up again: star cluster structure from hierarchical star formation". MNRAS, 481:688–702, November 2018a. doi: 10.1093/mnras/sty2303. MYG participated in the conception of the project, and analyzed the results of simulations from the suite in the previous paper.

M. Y. Grudić, P. F. Hopkins, E. Quataert, and N. Murray. “The maximum stellar surface density due to the failure of stellar feedback". MNRAS, 483:5548–5553, March 2019. doi: 10.1093/mnras/sty3386. MYG participated in the conception of the project, carried out the analytic calculations, and analyzed the results.

M. Y. Grudić, P. F. Hopkins, E. J. Lee, N. Murray, C.-A. Faucher-Giguère, and L. C. Johnson. “On the nature of variations in the measured star formation efficiency of molecular clouds". arXiv e-prints, arXiv:1809.08348, Sep 2018c. Submitted to MNRAS. MYG participated in the conception of the project, developed numerical code for the simulations, carried out the simulations, and analyzed the results.

M. Y. Grudić and P. F. Hopkins. “The elephant in the room: the importance of where and when massive stars form in molecular clouds". arXiv e-prints, arXiv:1809.08344, September 2018. Submitted to MNRAS. MYG participated in the conception of the project, developed numerical code for the simulations, carried out the simulations, and analyzed the results.

TABLE OF CONTENTS

LIST OF ILLUSTRATIONS

LIST OF TABLES

NOMENCLATURE

ϵ. Star formation efficiency, the fraction of initial GMC mass converted to stars at a given time.

$\epsilon_{ff,obs}$. The observational proxy for ϵ_{ff}, as inferred from available observational tracers of gas and stellar mass.

ϵ_{ff}. Per-freefall star formation efficiency, the fraction of available gas mass converted to stars per freefall time.

ϵ_{int}. Integrated star formation history, the mass of initial GMC mass converted to stars at the end of star formation.

ϵ_{obs}. Observational proxy of ϵ, ie. the current mass fraction of stellar mass as inferred from observational tracers of gas and stellar mass.

AMR. Adaptive Mesh Refinement, a technique for solving the equations of hydrodynamics in the Eulerian frame with a nested grid structure that can be refined where greater accuracy is needed..

GMC. Giant molecular clouds, the large ($\sim 10 - 100\,\mathrm{pc}$), massive ($\sim 10^4 - 10^7 M_{\odot}$) gas structures that host the majority of star formation in galaxies.

IMF. The stellar initial mass function, the empirical distribution of masses of young stars.

ISM. The interstellar medium, the gas and plasma that exists between stars within a galaxy.

MFM. Meshless Finite-Mass, a mesh-free, Lagrangian Godunov scheme for solving the equations of compressible (magneto-)hydrodynamics..

MHD. The behaviour of an electrically-conductive fluid in the presence of a magnetic field.

SFE. Star formation efficiency.

SFH. Star formation history, ie. star formation rate as it varied over time.

SFR. Star formation rate.

Star cluster. A collection 12 or more spatially- and kinematically-correlated stars that have higher local stellar density than the surrounding galactic field, and may or may not be gravitationally bound.

Stellar feedback. The various mechanisms by which stars inject mass, momentum, and energy into their surroundings.

Chapter 1

INTRODUCTION

1.1 History and Motivation

The origins of star is a problem at the heart of astrophysics. Whether one wishes to understand the galaxies that they compose, or the planets that they host, most astrophysical questions require some understanding of where stars came from, at some level. Yet for all its importance, a comprehensive theory of star formation that explains where and when stars form, in what quantity, at what rate, and with what individual stellar masses has not been achieved.

The most striking characteristic of the conversion process from gas to stars, and the most important clue about its nature, is its *inefficiency*. Gravity is the only force that could conceivably collapse objects from the density of the interstellar medium (ISM), $n_H \sim 1\,\mathrm{cm}^{-3}$, to stellar densities, $\sim 10^{23}$ times greater, and it acts on the free-fall time:

$$t_{ff} = \sqrt{\frac{3\pi}{32G\rho}} \approx 50\,\mathrm{Myr}\left(\frac{n_H}{1\,\mathrm{cm}^{-3}}\right)^{-1} \tag{1.1}$$

where ρ is the characteristic density of the system. It is then natural to presume that this is the timescale for the conversion of gas into stars, ie. the star formation rate should be simply $\dot{M}_\star = M_{gas}/t_{ff}$. In nearly all observed conditions, the time-scale of gas depletion implied by star formation rates is far longer than this, typically by a factor of ~ 100 (Kennicutt and Evans, 2012). The first hint of this inefficiency is present in the seminal work of Schmidt (1959), who found that the depletion time of gas due to star formation in the Solar neighbourhood is on the order of 1 Gyr, much longer than the galactic dynamical time $t_{dyn} \sim 30\,\mathrm{Myr}$. With the advent of radio astronomy, it was realized that HII regions in our Galaxy, associated with emission from massive (and thus young) stars, are tightly correlated with sites of bright emission of the rotational transitions of CO, now called giant molecular clouds (GMCs). These clouds were known to be cold and highly Jeans unstable, and the first efforts to model them dynamically found evidence that they were in a state of free-fall collapse (Goldreich and Kwan, 1974). However, Zuckerman and Evans (1974) pointed out that the star formation rates of GMCs, too, fall well short of the expectation of star formation on a freefall time. Specifically, if we introduce the per-freefall star formation efficiency ϵ_{ff}, such that

$$\dot{M}_\star = \epsilon_{ff} \frac{M_{gas}}{t_{ff}}, \tag{1.2}$$

observations of Milky Way GMCs were consistent with $\epsilon_{ff} \sim 1\%$. It was thus argued that GMCs are somehow supported against free-fall collapse, and thus could potentially be long-lived, quasi-equilibrium objects.

The first working theory for inefficient star formation in GMCs invoked the magnetic support of GMCs against gravity. A picture emerged in which gas in GMCs is largely supported against collapse by the magnetic field, with the star formation rate set by the rate at which mass can flow across magnetic fields lines due to the imperfect coupling of ions and neutral gas (Mestel and Spitzer, 1956). Once sufficiently decoupled from the magnetic field, the neutral gas would undergo rapid collapse as a singular isothermal sphere (Shu, 1977), but the initial decoupling process would be the rate-limiting step. The timescale for this process, ambipolar diffusion, could be reconciled with the galactic gas depletion time of ~ 1 Gyr, so this theory enjoyed the status of the “standard theory" of star formation for a time.

Eventually, toward the late 1990s, the standard theory fell into disfavour due its failure to satisfy a multitude of observational constraints (see Mac Low and Klessen (2004) for a summary of arguments against it), but also on theoretical grounds. It was argued as early as Goldreich and Kwan (1974) that the large dissipation rate of radiatively-cooled supersonic turbulence in molecular clouds would make it difficult to support GMCs against collapse over long timescales. This was demonstrated conclusively by the first 3D magnetohydrodynamics (MHD) simulations of supersonic turbulence, which found that the timescale of dissipation is on the order of the cloud crossing time (Stone et al., 1998). For most intents and purposes, “flux-freezing" does not exist in GMCs: the magnetic field is subject to intense dissipation in large-scale shocks on the cloud scale, while on the smaller scales of individual star-forming cores, the ionization fraction is very low and the effects of neutral-ion drift become important.

Supersonic turbulence, in itself, was then considered a candidate for explaining the low star formation rate. At the time, a comprehensive statistical description of supersonic, radiatively-efficient turbulence was emerging (Vazquez-Semadeni, 1994; Padoan et al., 1997; Nordlund and Padoan, 1999), and this was the basis for subsequent “gravo-turbulent" theories of star formation. The approach of these theories was suppose that the gas flow within a galaxy or a GMC is described by these statistics (which do not include the effects of gravity), and then to paint gravity on top of it by considering the statistics of the sub-regions of the ISM where turbulent support is overcome by gravity (Mac Low and Klessen, 2004; Krumholz and McKee, 2005; Padoan and Nordlund, 2011; Hennebelle and Chabrier, 2011a). This was never entirely self-consistent, as it did not incorporate gravity into the dynamics of the turbulence, and it relied on some supposed energy source to maintain the turbulence. It was presumed that this could come from some combination stellar feedback (see 1.2), accretion onto GMCs, or galactic-scale gravitational instabilities, and that some statistical equilibrium would be achieved.

Initial results were encouraging: the Krumholz and McKee (2005) theory successfully predicted many essential observational hallmarks of inefficient star formation, including the Kennicutt (1998a) relation, and the typical $\sim 1\%$ efficiency of star formation found on scales ranging from dense, $< 1\,\mathrm{pc}$ clumps to entire galaxies (Krumholz et al., 2012a). A theory invoking only gravity and supersonic turbulence is extremely appealing on this count, in that it is likely the *only* theory that could explain a truly universal star formation efficiency across such disparate scales, as their coupled equations can be cast in “scale-free" form (Guszejnov et al., 2018a), and introducing any other mechanisms would introduce characteristic scalings in ϵ_{ff}.

Once again, the most successful theory of regulated star formation came into tension with numerical simulations. A new generation of high-resolution, adaptive mesh refinement (AMR) MHD simulations was able to map out the three-dimensional parameter space of the theory, which consists of the virial parameter α_{vir} (Bertoldi and McKee, 1992), the sonic Mach number $\mathcal{M}$, and the Alfvénic Mach number $\mathcal{M}_A$. It was found that turbulence could moderate star formation to $\sim 1\%$ for sufficiently high GMC virial parameters (Padoan et al., 2012), but could not explain the low star formation rates of *bound* clouds, which account for a significant fraction of observed clouds (Heyer and Dame, 2015). Ultimately, the family of gravo-turbulent theories *could* be reconciled with simulations, but only when re-cast into their respective “multi-freefall" forms, which predict efficiencies significantly higher than is observed (Federrath and Klessen, 2012).

Meanwhile, observational evidence for a much more *dynamic* picture of star formation in GMCs emerged. Studies cross-correlating molecular clouds with HII regions in the Milky Way unanimously measured massive *scatter* in the SFE of GMCs (a result going back to Myers et al. 1986), which the turbulence-regulated theories could also not account for (Murray, 2011; Lee et al., 2016; Vutisalchavakul et al., 2016). Such observations appear more consistent with a highly *dynamic* picture of GMC evolution, in which the local SFR accelerates, to an eventual peak at which stellar feedback intervenes, and eventually disrupts the cloud, halting star formation by evacuating the gas supply (Larson, 1981; Palla and Stahler, 2000; Feldmann and Gnedin, 2011). In this picture, the timescales of gravity, turbulence, and stellar feedback are not separable, and all are equally relevant.

1.2 Feedback-regulated star formation

Thus far, little has been said about stellar feedback, a term encompassing all the mechanisms by which stars inject mass, momentum, and energy into the surrounding ISM. Feedback is a crucially important ingredient in star formation. Theoretical work unanimously finds that it is necessary for regulating and quenching star formation in galaxies formed in cold dark matter (CDM) cosmologies (Naab and Ostriker, 2017), and for setting the relation between the masses of dark matter halos and the galaxys that they host (Behroozi et al., 2013). Here we summarize the mechanisms believed to be the most important in galaxy and star formation.

- *Radiation*, most of which is emitted in the near-IR, optical, and near-UV bands from a given stellar population. Starlight dominates the overall budget of energy emitted by a stellar population by orders of magnitude. It couples to the ISM mainly through the ionization of hydrogen and helium (for sufficiently energetic UV photons), and absorption by dust. Photoionization creates HII regions in which the ISM in excess of 10^4 K, leading to the formation of rapidly ($\sim 10\,\mathrm{km\,s^{-1}}$, Spitzer 1978) expanding ionization fronts that can disrupt molecular clouds, and impart moment via the back-reaction of ionized material boiling off the surface of a cloud. The photo-electric effect on dust grains also acts as a heating mechanism. In addition to heating the ISM, radiation imparts momentum upon absorption, which may be important for the disruption of the most massive GMCs, and the driving of galactic winds (Murray et al., 2010; Hopkins et al., 2011a). [1] Over the timescales

---

[1] Note that the importance and efficiency of photon momentum as a source of feedback, either single-scattered or multiply-scattered, remains an ongoing subject of investigation: see Krumholz and Thompson (2012a); Davis et al. (2014a); Tsang and Milosavljević (2015); Raskutti et al. (2016); Grudić et al. (2018b); Zhang and Davis (2017); Kim et al. (2017a); Tsz-Ho Tsang and Milosavljevic (2017); Hopkins and Grudić (2018); Krumholz (2018).

relevant to molecular clouds ($\sim$ 10 Myr), the starlight from a stellar population is dominated by massive type OB stars, particularly in the ionizing band.

- *Stellar winds*. These are energetically dominated by the line-driven winds of OB stars (Castor et al., 1975). The momentum injection rate from line-driven winds scales with metallicity as $\propto Z^{0.8}$ (Kudritzki and Puls, 2000). From a solar metallicity population, they can contribute a feedback momentum injection rate that is comparable to that obtained from starlight and supernovae (Leitherer et al., 1999), and hence they are potentially important as a source of feedback in sufficiently metal-enriched galaxies.

- *Supernova explosions*, the violent explosions ending the lives stars of mass exceeding $8 M_\odot$ via the core-collapse mechanism, or of white dwarfs that merge or accrete beyond the Chandrasekhar mass, $1.44\,\mathrm{M_\odot}$. From a co-eval stellar population with a well-sampled initial mass function, these commence when the most massive stars start to die around 3 Myr. Type II SNe persist until $\sim 8 M_\odot$ stars die at $\sim$ 40 Myr, while type Ia SNe occur over longer timescales determined by binary evolution. Type II SNe are the dominant feedback mechanism on cosmological scales, having a dramatic influence on the structure of the ISM, the launching of galactic winds, and the structure and morphology of galaxies (Hopkins et al., 2018a). Their importance on the scale of individual GMCs is less clear: because they have a “time delay" after star formation, other feedback mechanisms are likely necessary to moderate star formation.

The other feedback mechanism deserving of mention here is protostellar outflows, the collimated jets launched from near the surfaces of accreting protostars by magnetohydrodynamic forces (Matzner and McKee, 2000; Bally, 2016). Throughout the work in this dissertation, we neglect this feedback mechanism because it is negligible in terms of the energy and momentum extracted from a well-sampled stellar population, and may only be relevant in systems with escape velocity $< 1\,\mathrm{km\,s^{-1}}$ (Matzner and Jumper, 2015). However, it may still have an important role to play in the formation of low-mass clusters: it is unique in being a source of feedback available when massive stars are absent (Krumholz et al., 2018). Numerical work has hinted that protostellar jets can be an effective feedback mechanism under the right conditions (Wang et al., 2010; Federrath, 2015a; Offner and Chaban, 2017;

Cunningham et al., 2018), but these experiments have been limited to an idealized setup simulating a small portion of a GMC.

At the time that this work was conceived, extensive work had been done to understand the roles of gravity, turbulence, and feedback in concert, acting on the scales of molecular clouds (Dale et al., 2005; Krumholz et al., 2011; Rogers and Pittard, 2013; Dale et al., 2012; Colin et al., 2013; Dale et al., 2013, 2014). The lines of simulation development stemming from these studies continue to yield enlightening results. However, these studies share some important limitations:

1. In all cases, only one or two of the potentially important feedback mechanisms were simulated. Different feedback mechanisms can potentially obey different scalings laws, such that one may be required to moderate star formation where the other cannot, so only a comprehensive approach can yield conclusive results.
2. The approach of following the formation, motion, and feedback from *individual* stars imposes a challenging constraint on resolution. As a result, mostly relatively small ($< 10^4\,\mathrm{M}_\odot$) GMCs have been simulated, which are not representative of the more massive clouds that form the majority of stars (Williams and McKee, 1997). The parameter space has thus been rather limited.
3. The feedback budget is highly sensitive to the individual predicted stellar masses, because the most massive stars source so much of the feedback. The actual physics that are necessary and sufficient to include in a simulation obtain a *numerically-converged* distribution of stellar masses in simulations are still highly debated, and indeed one of the major open problems in star formation theory (Krumholz, 2014).

In essence, these works attempting to solve an extremely challenging problem, in terms of resolution requirements, algorithmic complexity, and the multitude of the physics involved, and no one calculation has put together all of the pieces. Progress is being made, but it is hard-won.

An alternative approach is to take certain aspects of star formation and stellar evolution for granted, anchoring the simulations in phenomenology at some level. For instance, one can assume that stellar feedback is consistent with that expected from simple stellar population with a well-sampled, universal initial mass function (IMF). The well-sampled approximation is valid in the limit of massive ($> 10^3 M_\odot$)

star cluster formation, while deviations from IMF universality are tightly constrained by observations (Bastian et al., 2010a; Offner et al., 2014).

This approach rooted in the phenomenology of stellar populations has permitted the latest generation of *galaxy* formation simulations (Hopkins et al., 2011a, 2012a, 2011b; Agertz et al., 2013; Hopkins et al., 2014), which have been able to account for *all* mechanisms of stellar feedback that are potentially important on the scale of GMCs or larger. In conjunction with a realistic, explicit treatment of the multi-phase interstellar medium, including the cold phase that was previously neglected in galaxy simulations, these simulations were able to reproduce extremely realistic galaxies while taking only the stellar IMF, stellar evolution, and the ΛCDM cosmology as phenomenological inputs.

It was realized that this numerical approach, particularly at the level of development of the FIRE-2 simulations (Hopkins et al., 2018a), could be the basis for a new type of GMC simulation, that would be able to explore the effects of MHD, ISM physics, and stellar feedback acting in concert over a vast parameter space, without having to simulate the formation of individual stars. This is the key methodology of this work.

1.3 Toward a realistic picture of star cluster formation in GMCs

The goal of this body of work is to use numerical magnetohydrodynamics simulations of star cluster formation including all important stellar feedback mechanisms to develop a more complete description of the star formation process at the level of individual giant molecular clouds. Specifically, the key questions addressed are:

- What are the effects of different stellar feedback mechanisms, acting in concert with gravity, MHD, and ISM physics, in giant molecular clouds? (Ch. 2 and 5)
- What sets the efficiency of star formation at the cloud scale? (Ch. 2)
- Should the efficiency of star formation vary between galactic environments, and if so what are the implications? (Ch. 2 and 4)
- What is the assembly process of star clusters, and how does this process determine their properties? (Ch. 3)
- Can this picture of feedback-moderated star formation explain observations where previous theories have failed? (Ch. 5)

- What are the most important uncertainties in this approach to simulating star formation? (Ch. 6)
- What is the mapping from GMCs to star clusters, ie. given the properties of a self-gravitating GMC, what mass of stars should form, and how are these stars arranged spatially and dynamically? How is the mass distribution of star clusters related to that of GMCs? (Ch. 7)

In addressing these questions, we have built up a theoretical framework of feedback-moderated star formation and hierarchical cluster formation on GMC scales that has succeeded in reproducing the “big picture" observations of the process of conversion from gas to stars in galaxies: the cloud-scale star formation efficiency (predicting both the magnitude (Ch. 2) and dispersion Ch. 5), the surface density profiles of young star clusters (Ch. 3), the maximum stellar surface density (Ch. 4), and the bound fraction, masses, and sizes of star clusters in nearby spiral galaxies (Ch. 7).

1.4 Reflections and future work

These successes are encouraging, and point toward the next steps. The model for star cluster formation finalized and validated in Ch. 7 can be extended to an end-to-end analytic galactic disk model that requires only galactic bulk properties to make predictions. It can also be coupled to cosmological simulations (ie. FIRE, Hopkins et al. 2018a) to make predictions about star cluster formation across cosmic time. Important questions to address with this approach include where and how globular clusters form, what the distibution of globular clusters in age, metallicity, mass, and phase space tells us about the galactic assembly history (e.g. Forbes and Bridges, 2010), and what initial and boundary conditions ΛCDM actually predicts for detailed N-body studies.

However, while exploring our simulation technique, we have also confronted its inherent limitations. In Chapter 6 we identify the specific prescription used to *assign* feedback to star cluster particles, which varies from study to study, as the main cause for discrepancy between our and others' numerical studies. Because this prescription makes assumptions about the small-scale details of massive star formation, which are currently poorly understood, the predictive power of this approach is limited by these uncertainties, particularly in the limit of lower-mass ($< 10^4 M_\odot$) star cluster formation. This is unfortunate, because the wealth of high-quality astrometric data for young star clusters in the Milky Way (e.g. Kuhn et al.,

2019) may provide new constraints on the star formation process, if only theoretical models could confront it in a self-consistent framework.

From the above points, it follows that the next important step is to take cluster formation simulations back to their roots, and once again attempt simulate star formation self-consistently, in particular modeling star-forming conditions in the Milky Way with high fidelity. The time is now ripe for this, first because most groups are reaching a consensus upon the necessary physics needed to do this properly (Bate, 2009; Krumholz, 2011; Guszejnov et al., 2016; Federrath et al., 2017). Second, Guszejnov et al. (2018b) recently demonstrated the feasibility of a new generation of ultra-high resolution GMC simulations, following fragmentation over an unprecedented dynamic range, with mass resolution sufficient in principle to resolve the formation of stars $< 0.01\,\mathrm{M}_\odot$ in a $\sim 10^5 M_\odot$ giant molecular cloud. The new accurate, massively-scalable, Lagrangian methods for MHD (Pakmor et al., 2011; Hopkins and Raives, 2016) and radiative transfer (Kannan et al., 2019; Hopkins et al., 2018b) will trigger a renaissance of star formation simulations in the coming years. It will soon be possible to account for every star and every feedback channel as GMC evolution is followed from initial collapse to cloud dispersal.

Chapter 2

WHEN FEEDBACK FAILS: THE SCALING AND SATURATION OF STAR FORMATION EFFICIENCY

M. Y. Grudić, P. F. Hopkins, C.-A. Faucher-Giguère, E. Quataert, N. Murray, and D. Kereš. MNRAS, 475:3511–3528, April 2018b. doi: 10.1093/mnras/sty035.

Abstract

We present a suite of 3D multi-physics MHD simulations following star formation in isolated turbulent molecular gas disks ranging from 5 to 500 parsecs in radius. These simulations are designed to survey the range of surface densities between those typical of Milky Way GMCs ($\sim 10^2\,\mathrm{M_\odot pc^{-2}}$) and extreme ULIRG environments ($\sim 10^4\,\mathrm{M_\odot pc^{-2}}$) so as to map out the scaling of the cloud-scale star formation efficiency (SFE) between these two regimes. The simulations include prescriptions for supernova, stellar wind, and radiative feedback, which we find to be essential in determining both the instantaneous per-freefall (ϵ_{ff}) and integrated (ϵ_{int}) star formation efficiencies. In all simulations, the gas disks form stars until a critical stellar surface density has been reached and the remaining gas is blown out by stellar feedback. We find that surface density is a good predictor of ϵ_{int}, as suggested by analytic force balance arguments from previous works. SFE eventually saturates to ~ 1 at high surface density. We also find a proportional relationship between ϵ_{ff} and ϵ_{int}, implying that star formation is feedback-moderated even over very short time-scales in isolated clouds. These results have implications for star formation in galactic disks, the nature and fate of nuclear starbursts, and the formation of bound star clusters. The scaling of ϵ_{ff} with surface density is not consistent with the notion that ϵ_{ff} is always $\sim 1\%$ on the scale of GMCs, but our predictions recover the $\sim 1\%$ value for GMC parameters similar to those found in sprial galaxies, including our own.

2.1 Introduction

Typically, star formation in the observed Universe is inefficient in any sense of the word. Star formation is observed to occur in giant molecular clouds (GMCs) formed in galactic disks, and the per-freefall star formation efficiency of a star-forming region may be parametrized as:

$$\dot{M}_\star(t) = \epsilon_{ff}(t) \frac{M_{gas}(t)}{t_{ff}(t)}, \tag{2.1}$$

where $\dot{M}_\star$ is the star formation rate, M_{gas} is the gas mass "available" to form stars (observationally, the mass of molecular or dengas as obtained from a tracer such as CO or HCN), and $t_{ff}(t)$ is the local gravitational freefall time. ϵ_{ff} is the fraction of available gas converted to stars per t_{ff}; on galactic ($\sim$ kpc) scales, ϵ_{ff} has been estimated by fitting to the relation:

$$\Sigma_{SFR} = \epsilon_{ff}^{gal} \Sigma_{gas} t_{ff}^{-1}, \tag{2.2}$$

where Σ_{SFR} is the projected density of star formation in the disk, Σ_{gas} is the projected (cold) gas density, t_{ff} is the local freefall time evaluated from the galaxy's scale height-averaged density, and ϵ_{ff}^{gal} has been found to be ~ 0.02 (Kennicutt, 1998a). Thus, a typical galaxy converts only 2% of its potentially star-forming gas into stars each freefall time, despite the tendency of self-gravitating cold gas clouds to fragment and contract nearly all of their gas mass to high densities within only a few t_{ff}. Clearly, some physical mechanism is responsible for the moderation of star formation.

Recently, the FIRE[1] (Feedback In Realistic Environments) simulations (Hopkins et al., 2014, 2018a) have demonstrated that the inefficiency of star formation in galaxies formed within the ΛCDM cosmology can be explained by stellar feedback, obtaining good agreement with Kennicutt (1998a) independent of the numerical resolution-scale star formation model. As stars form in dense GMCs within a galaxy, some combination of of photoionization heating, radiation pressure, stellar winds, and possibly supernovae blow out the remaining gas in the cloud, terminating star formation locally. The young stars formed inject momentum, mass, and energy into the surrounding ISM, which prevents the runaway vertical collapse of the galactic disk by providing turbulent support, and the rates of turbulent dissipation and momentum injection are in equilibrium when $\epsilon_{ff}^{gal} \sim 0.02$ (see Thompson et al. (2005); Ostriker and Shetty (2011); Faucher-Giguère et al. (2013); Orr et al. (2018a)).

---

[1] `http://fire.northwestern.edu`

However, this mechanism only explains the rate of star formation on galactic scales: ϵ_{ff}^{gal} emerges from an established equilibrium over the formation and disruption of many GMCs, and is distinct from the value of ϵ_{ff} for a single GMC. Since star formation in a GMC must cease once it is disrupted, there exists another quantity of interest in characterizing the efficiency of star formation, the integrated SFE:

$$\epsilon_{int} = \frac{M_\star}{M_{tot}}, \tag{2.3}$$

where $M_\star$ is the final mass of stars formed and M_{tot} is the mass of the initial gas cloud. In Milky Way GMCs, the median value of ϵ_{int} is on the order of 1%, (Evans et al., 2009; Murray, 2011; Lee et al., 2016; Vutisalchavakul et al., 2016) with a large observed scatter of 0.8 dex (Murray, 2011; Lee et al., 2016). However, there is evidence that ϵ_{int} is much higher in denser conditions: Murray et al. (2010) points out that the masses of GMCs (Keto et al., 2005) and young star clusters (McCrady and Graham, 2007) in the M82 starburst galaxy are of a similar mass scale, suggesting that ϵ_{int} is of order unity at the greater surface densities of such regions. Indeed, the existence of young, bound star clusters *in general* may physically require high integrated SFE on at least some local scale (Tutukov, 1978; Hills, 1980; Elmegreen, 1983; Mathieu, 1983; Elmegreen and Efremov, 1997). Recent observations of young massive clusters (YMCs) have also suggested a time constraint of $< 4\,\mathrm{Myr}$ for cluster formation within the disk of M83 (Hollyhead et al., 2015), only twice the typical GMC freefall time in the central region of M83 (Freeman et al., 2017), suggesting that cluster formation may also be a dynamically-fast process. Therefore, it is necessary to explore ways in which the efficiency of star formation, both in terms of ϵ_{ff} and ϵ_{int}, can scale from Milky Way-like values of $\sim 1\%$ to greater values. Since stellar feedback is responsible for the eventual disruption of molecular clouds against gravity, it is likely that the balance of these two forces plays a major role in determining both the speed and integrated efficiency of star formation at sub-kpc scales.

In this paper, we focus on the detailed behaviour of a single star formation episode at high resolution: we present 3D MHD simulations of star-forming gas disks which use the numerical treatments of cooling, star formation and stellar feedback of Hopkins et al. (2018a) to answer certain basic questions about star formation in local galactic environments:

- Given an initial self-gravitating gas distribution, what is the resulting star formation history? In particular, what determines the observable quantities

ϵ_{ff} and ϵ_{int}, and how are they related?

- How do the initial parameters of the gas cloud map onto the properties of the formed stellar system?
- Which physical mechanisms have the greatest effect upon the answers to these questions?

The general approach of this study is to suppose some generic initial conditions for an isolated gas disk, neglecting its interaction with the surrounding galactic environment. This approximation makes sense for simulations spanning no more than a few dynamical times (which we shall show to be the case) and allows us to achieve relatively high spatial and mass resolution in the region of interest for modest computational cost.

This physics problem is most conventionally applicable to star-forming GMCs, but really any region in which the dynamical time is not significantly longer than the main sequence lifetime of massive stars ($\sim 3\,\mathrm{Myr}$) should be unstable to runaway star formation and the eventual blowout of the gas component (Torrey et al., 2017). The central regions of ultraluminous infrared galaxies (ULIRGs) may have large gas fractions and short dynamical times (Downes and Solomon, 1998; Bryant and Scoville, 1999), so for the purposes of our problem they may effectively behave as one super-GMC with particularly high ($> 10^3\,\mathrm{M_\odot\,pc^{-2}}$) surface density. Our simulations, which probe these surface densities, can therefore also serve as models of gas-rich nuclear disks, which host the most extreme star formation events in the local Universe.

This paper is structured as follows: in Section 2.2, we describe a simple model of a gas-rich, star-forming disk, and predict its general behaviour from the physical arguments. In Section 2.3, we describe the methods for our simulations, their initial conditions, and the scope of our survey of physics and simulation parameters. In Section 2.4 we present the results of the simulations concerning the global properties of the star-forming clouds: the overall behaviour of the simulated clouds, the isolated effects of various physical mechanisms, the per-freefall (ϵ_{ff}) and integrated (ϵ_{int}) star formation efficiency. Finally, in Section 7.5 we discuss some applications, implications and limitations of our results and outline future studies on the more detailed aspects of the mode of star formation we have simulated.

2.2 A Star-forming Disk Model

To guide the methodology of the numerical study, we first review some basic theory of star formation and construct a simple model that captures the essential physics of how feedback determines the SFE of a gas-rich star-forming disk over short dynamical timescales. Consider an initially-uniform disk of mass M, radius R, and scale height h that initially consists of only gas. Averaged over the diameter of the disk, the initial surface density is then:

$$\Sigma_{tot,0} = \Sigma_{gas}(t=0) = \frac{M}{\pi R^2}. \tag{2.4}$$

2.2.1 Time-scales for star formation

The longest possible time-scale for gravitational collapse within the model disk is the freefall time $t_{ff,0}$ derived from the system's physical parameters M and R:

$$t_{ff,0} = \frac{\pi}{2}\sqrt{\frac{R^3}{2GM}} = 2\,\mathrm{Myr}\left(\frac{R}{50\,\mathrm{pc}}\right)^{\frac{1}{2}}\left(\frac{\Sigma_{tot,0}}{10^3\,\mathrm{M_\odot\,pc^{-2}}}\right)^{-\frac{1}{2}}, \tag{2.5}$$

which is proportional to the outer orbital period of the disk. This is the longest relevant time-scale in the problem, since we neglect environmental interactions. $t_{ff,0}$ may overestimate the typical gravitational collapse time of a typical gas parcel, as we expect that if star formation is to occur then the dynamics are driving mass to greater-than-average densities with correspondingly shorter freefall times. Specifically, isothermal, self-gravitating turbulence has been found to produce a density PDF with a high-density power-law tail due to gravity (Kritsuk et al., 2011), and at lower densities a log-normal form, as emerges in isothermal turbulence without gravity (Vazquez-Semadeni, 1994; Padoan et al., 1997; Nordlund and Padoan, 1999). The only characteristic density is the peak of this distribution, so we define a shorter freefall time in terms of the median gas density ρ_{50} (equivalently, number density n_{50})[2]:

$$t_{ff,50} = \sqrt{\frac{3\pi}{32G\rho_{50}}} = 1.6\,\mathrm{Myr}\left(\frac{n_{50}}{10^3 cm^{-3}}\right)^{-\frac{1}{2}}, \tag{2.6}$$

where n_{50} is the median particle number density. $t_{ff,50}$ will generally be a more reasonable unit for the gas depletion time, and hence for comparing values of ϵ_{ff}.

---

[2] Note that we use the median, and not the mass-weighted mean gas density used for determining t_{ff} in Krumholz et al. (2011) and Myers et al. (2014a). The mass-weighted mean is less suitable for estimating t_{ff} in the middle of star formation because the high-density power-law tail in the density PDF biases it toward high densities. We also find that it is not robust with respect to simulation resolution, as higher resolutions will resolve more of the power-law tail. The median density generally lies near the peak of the density PDF, and is robust with respect to resolution.

In the parameter space relevant to star formation in the local Universe, the cooling time of gas that is metal-enriched or molecular is generally much less than both $t_{ff,0}$ and $t_{ff,50}$. Therefore, in absence of stars or external inputs, any thermal energy supporting against self-gravity will quickly radiate away. If the disk has some initial turbulent velocity dispersion, that energy too will be cooled away by shocks over $\sim t_{ff,50}$. Without some imposed stabilizing force the disk will be subject to gravitational instability, fragmentation, and star formation.

The process of fragmentation involves a runaway collapse to protostellar densities. If an initially-smooth disk with $\rho \sim \Sigma_{tot,0}/2h$ were to fragment hierarchically into successively denser structures, the entire conversion of gas into stars would take no longer than a time on the order of $\sim t_{ff,50}$, since the freefall time at all smaller scales is less than this. Counting the time for the initial growth of the gravitational instability, and the eventual gas evacuation due to feedback, we expect the entire period of star formation to last no longer than several freefall times (e.g. Elmegreen, 2000, 2007). This appears to be the case for Milky Way GMCs, which have a mean star-forming lifetime of 3 freefall times (Murray, 2011; Lee et al., 2016), as well as those found in simulated galaxies with low-temperature cooling and stellar feedback (Hopkins et al., 2012a), however it has also been argued that star formation should take longer (Tan et al., 2006; Krumholz and Tan, 2007).

2.2.2 Star formation efficiency

As stars form, the stellar surface density $\Sigma_\star(t)$ increases as the gas surface density $\Sigma_{gas}(t) = \Sigma_{tot,0} - \Sigma_\star(t)$ decreases. These stars will inject energy and momentum into the gas through various feedback mechanisms, however if the time-scale of star formation is so short that SNe do not occur then direct ISM heating can be neglected due to the short cooling time. Assuming that the stellar population is well-sampled from a Kroupa (2002) IMF, the rate of momentum feedback injection per unit stellar mass $\frac{\dot{P}_\star}{m_\star}$ will initially be roughly constant, dominated by radiation pressure and fast winds from the most massive stars for the first 3 Myr after the stellar population forms. For the subsequent ~ 40 Myr, the massive stars all leave the main sequence and supernovae become the dominant form of feedback. Because we are most interested in the limit of dense systems with short dynamical times, we can neglect stellar evolution and approximate $\frac{\dot{P}_\star}{m_\star}$ as being constant. Then the force of feedback upon the gas in the disk is:

$$F_{fb}(t) = \frac{\dot{P}_\star}{m_\star} M_\star = \frac{\dot{P}_\star}{m_\star} \Sigma_\star(t) \pi R^2, \tag{2.7}$$

assuming no leakage, photon trapping, or other effects arising from clumpy structure. This force will continue to increase until F_{fb} exceeds the force of gravity binding the gas to the disk. The majority of the new star formation will occur in a thin disk, so while the gas is dense enough to form stars the gravitational field binding gas to the star-forming region will be dominated by contributions from the gas itself and the newly-formed stars. Thus:

$$F_g(t) = gM_{gas}(t) = 2\pi G\Sigma_{tot,0}\Sigma_{gas}(t)\pi R^2. \tag{2.8}$$

By equating the force of feedback upon the gas (2.7) with that of gravity (2.8) we can determine the final stellar mass and hence the integrated star formation efficiency (Fall et al., 2010):

$$\epsilon_{int} = \frac{M_\star}{M} = \frac{\Sigma_{tot,0}}{\Sigma_{tot,0} + \Sigma_{crit}}, \tag{2.9}$$

where:

$$\Sigma_{crit} = \frac{1}{2\pi G}\frac{\dot{P}_\star}{m_\star} \tag{2.10}$$

is the quantity with units of surface density encoding the strength of feedback relative to gravity. The contributions to $\frac{\dot{P}_\star}{m_\star}$ from radiation pressure, stellar winds, and SNe ejecta (ignoring the work done in the energy-conserving phase) are all of order $10^3 \frac{L_\odot}{M_\odot c}$. Thus, $\Sigma_{crit} \sim 10^{3-4}\,\mathrm{M_\odot pc^{-2}}$ due to stellar feedback physics. Observationally, the average ϵ_{int} for Milky Way GMCs is $\sim 3\%$ (Murray, 2011; Lee et al., 2016), while the median GMC surface density is $\sim 100\,\mathrm{M_\odot pc^{-2}}$ (Larson, 1981; Solomon et al., 1987; Bolatto et al., 2008), so we can estimate that $\Sigma_{crit} = 3000\,\mathrm{M_\odot pc^{-2}}$ for those GMCs for which feedback from massive stars is important. See also Murray et al. (2010), Dekel and Krumholz (2013), and Thompson and Krumholz (2016) for similar derivations with various cloud and feedback models.

Equation (2.9) predicts that the efficiency of starbursts occurring over adequately short time-scales is simply dictated by the ratio of forces of feedback and gravitation. In the limit $\Sigma_{tot,0} << \Sigma_{crit}$, SFE is proportional to $\epsilon_{int} \propto \Sigma_{tot,0}$ with the constant of proportionality determined by the strength of feedback. Inversely, where $\Sigma_{tot,0} >> \Sigma_{crit}$, SFE should approach unity: gravity prevails against feedback and converts nearly all gas to stars. The importance of surface density in determining star formation efficiency in short dynamical time systems is not simply a consequence of the 'diskiness' of star-forming systems, nor of their optical depth in some band, both of which would give surface density an obvious physical relevance. It is merely a consequence of the fact that the ratio between the force of self gravity $F_g \sim \frac{GM^2}{R^2}$ and the momentum injection rate of feedback $F_{fb} \sim M_{\star}\dot{P}_{\star}/m_{\star}$ has dimensions of surface density, at least under our simplifying assumptions.

2.3 Simulations

Our simulations use GIZMO (Hopkins, 2015)[3], a mesh-free, Lagrangian finite-volume Godunov code designed to capture advantages of both grid-based and smoothed-particle hydrodynamics (SPH) methods, built on the gravity solver and domain decomposition algorithms of GADGET-3 (Springel, 2005). In Hopkins (2015) and Hopkins and Raives (2016) we consider extensive surveys of test problems in both hydrodynamics and MHD, and demonstrate accuracy and convergence in good agreement with well-studied regular-mesh finite-volume Godunov methods and moving-mesh codes (e.g. ATHENA & AREPO; Stone et al., 2008; Springel, 2010). We run GIZMO in its Meshless-Finite Mass (MFM) mode but have verified that Meshless Finite-Volume (MFV) mode produces nearly identical results (as expected from the previous studies).

2.3.1 Cooling, Star Formation, and Stellar Feedback

The simulations here use the physical models for star formation and stellar feedback developed for the Feedback In Realistic Environments (FIRE) project (Hopkins et al., 2014, 2018a), although the simulations in this paper are idealized cloud collapse experiments on small scales, at often much higher mass resolution than the FIRE simulations. In general, we expect these methods to be appropriate to the scales examined in this work because by construction the FIRE framework adopts a physics approach that requires no phenomenological tuning to different mass scales. Hydrodynamics, gravity, cooling, and stellar feedback are explicitly and approximately solved down to the resolution limit, and the physics approximations invoked have been extensively validated by more expensive and detailed simulations. We briefly summarize some key properties of the FIRE models here, but refer to Hopkins et al. (2018a) for details of the numerical implementations and extensive tests of the algorithms and physics.

When simulating gas fragmentation, it is critical to have explicit cooling physics; we therefore do *not* adopt an "effective equation of state" (Springel and Hernquist, 2003) as has been done in many works in the past, but explicitly follow a wide range of heating/cooling processes. This includes photo-ionization and photo-electric,

---

[3] A public version of this code is available at `www.tapir.caltech.edu/~phopkins/Site/GIZMO.html`.

dust collisional, Compton, metal-line, molecular, and fine-structure processes, and we self-consistently account for optically thick cooling when local regions become thick to their own cooling radiation, implementing the approximation of Rafikov (2007). We do neglect the effects of non-equilibrium chemistry in the ISM, which can be very important for predictions of observational tracer abundances (Richings et al., 2014a,b), however cooling times are generally so short in our problem that little dynamical effect can be expected.

Gas particles are converted to star particles with constant probability per unit time $t_{ff}\left(\rho\right)^{-1}$ if they satisfy all of the following star formation criteria:

- *Self-shielding and molecular:* We compute the molecular fraction f_{mol} of the gas as a function of column density and metallicity according to Krumholz and Gnedin (2011), estimating the local gas column density with a Sobolev-like estimator.
- *Contracting:* Star formation occurs only in regions of increasing density ($\nabla \cdot \vec{v} < 0$).
- *Self-gravitating:* The local Jeans mass M_{jeans} is estimated, accounting for both turbulent (Hopkins et al., 2013) and thermal contributions, with the turbulent contribution typically dominating in cold molecular gas. Star formation is allowed only in regions where the Jeans mass can no longer be resolved, as it is at this point that fragmentation should continue down to unresolved scales.

In our tests, we find that the self-gravity criterion is the most restrictive and the most physically motivated of the above. Note that these criteria are slightly different from the FIRE simulations (Hopkins et al., 2014, 2018a), as we do not enforce a threshold density for star formation, and require gas to be increasing in density to form stars. All star formation criteria are fully adaptive, with no built-in scales that could be imprinted upon the star clusters that form. To summarize, gas fragmentation is explicitly followed down to the scale where the mass resolution is insufficient to resolve fragmentation, then the gas particles quickly (within one local t_{ff}) transition into collisionless star particles.

Crucially, because the collapse time-scale of *resolved* fragments at densities much larger than the mean in our simulations is always fast compared to the global dynamical time, this is not the rate-limiting step for star formation. Rather, it is the initial formation of these fragments (Thompson et al., 2005; Faucher-Giguère et al., 2013; Ostriker and Shetty, 2011). As such, we will show that the star formation histories are insensitive to details of both our cooling and star formation prescriptions. This is consistent with a wide range of previous studies on GMC and galactic scales (Saitoh et al., 2008; Hopkins et al., 2011b, 2012a,b, 2016, 2018a; Agertz et al., 2013).

Once stars form, feedback is included in the form of radiation pressure (UV, optical, and IR), stellar winds (fast, young star winds and slow AGB winds), SNe (types Ia and II), photo-ionization and photo-electric heating. Every star particle is treated as a single stellar population with an age based on its formation time and metallicity and mass inherited from its parent gas particle. Feedback includes the relevant mass, metal (with 11 separately tracked species), momentum, and energy injection to the neighboring gas; all of the relevant quantities (stellar luminosities, spectral shapes, SNe rates, wind mechanical luminosities, yields) for the mechanisms above are tabulated as a function of time directly from the stellar population models in STARBURST99, assuming a Kroupa (2002) IMF. For SNe, if we lack the mass resolution to resolve the Sedov-Taylor phase, we estimate the work done during the energy-conserving phase and couple the appropriate momentum based on fits from high-resolution SNR simulations (Martizzi et al. (2015); Kim and Ostriker (2015), see Hopkins et al. (2014) for implementation details). This is only important for our few simulations with resolved masses greater than 10^3 $M_\odot$.

For the multi-band radiative fluxes necessary for the radiative heating and pressure terms, we use the LEBRON approximation, described in detail in Hopkins et al. (2018a). The spectrum is binned into UV, optical/near-IR, and mid/far-IR bands, and the approximate fluxes are computed explicitly at each particle. Local extinction around star particles is estimated with an effective column density computed with a Sobolev approximation; the robustness of our results to unknown order-unity factors in this prescription is demonstrated in Appendix 2.A.2. We emphasize that, unlike the model of Hopkins et al. (2012a), LEBRON does not invoke a subgrid "boost" term for the radiation pressure of multiply-scattered IR photons. Only explicitly-resolved photon absorption is accounted for in the heating and pressure terms.

We intentionally assign IMF-averaged properties to all star particles, rather than attempting to follow individual stars explicitly – our goal is to study the effects of feedback, given some IMF, *not* to solve the problem of the origins and nature of the IMF itself. The latter would require a full model for individual star formation (and much higher resolution than we are able to achieve here), and may critically depend on additional physics (e.g. heating by prostellar accretion, protostellar jets) which are negligible in an IMF-averaged feedback scenario. [4] In some of our less-massive simulated clouds, the particle mass is less than $M_{\odot}$ and the stellar IMF is nominally resolvable, so star formation tends to produce "clusters" of star particles of $100 M_{\odot}$ or less, which can be identified with the individual stars that would have formed. In this case, a sink-particle method (e.g. **?**) is certainly much more realistic and efficient, however we still adopt the standard star-particle method for consistency with the more massive clouds.

2.3.2 Initial Conditions & Problem Setup

The initial conditions of the simulations consist of a constant density gas sphere of radius R and mass M, with the parameter space of R and M tabulated in table 2.1. These values are chosen to cover a range of values of $\Sigma_{tot,0}$, which, for reasons discussed in Section 2.2, we expect to roughly parametrize the overall behaviour of the system even at disparate spatial scales, masses, and dynamical times.

The initial velocity field is a superposition of solid-body rotation about the origin and a random turbulent component. The rotational frequency is set to the gas ball's Keplerian frequency $\Omega_K = ({}^{GM}/_{R^3})^{\frac{1}{2}}$, so that the effective radius, and hence average surface density of the disk remains roughly constant [5]. The random velocity component adds a turbulent energy of 10% of the initial gravitational binding energy, with a power spectrum $E(k) \propto k^{-2}$. All velocity Fourier coefficients for which $||\vec{k}|| \geq \frac{2\pi}{R}$ are given a random phase and scaled according to this relation. The velocity components are first computed on a Cartesian grid circumscribing the gas sphere, and are then interpolated to the particle positions.

---

[4] One might worry that, by IMF-averaging, we make feedback "too smooth." In limited experiments, we have crudely modeled the effects of stochastic sampling of the IMF and concentrating feedback in individual massive stars by, for each star particle, drawing from the IMF a quantized number of massive O-stars (from a Poisson distribution with mean equal to the expectation for the total mass of the particle). All feedback effects associated with massive stars (Type-II SNe, photo-heating, fast winds, radiation pressure) are multiplied appropriately by the number of O-stars (which are lost in each Type-II SNe event). As expected, this has essentially no effect on the disk-averaged properties we consider here for disk masses $\gtrsim 1000\,M_{\odot}$, which reasonably sample massive ($\gtrsim 10\,M_{\odot}$) stars. For still smaller clouds, this (as expected) introduces additional scatter in the star formation efficiency, corresponding to the variation in the number of massive stars (hence strength of feedback). However, the mean scalings are unaffected.

[5] Note that assuming rotational support is not a realistic choice for simulating GMCs, which are generally supported by a shearing velocity gradient and turbulence. As such, the simulations are not expected to result in large-scale cloud morphologies resembling realistic galactic GMCs. However, the morphology of sub-clouds will be determined on much shorter time-scales by local turbulence and self-gravity, independently of the large-scale morphology.

Simulation parameters

$\Sigma_{tot,0}$ [M$_\odot$ pc^{-2}] (1)	R [pc] (2)	M [M$_\odot$] (3)	$t_{ff,0}$ [Myr] (4)	Modifications (5)	Mass Resolution [M$_\odot$] (6)	Minimum star softening [pc] (7)
127	5	10^4	1.85		0.03	0.001
127	50	10^6	5.86		3	0.01
127	500	10^8	18.53		300	0.1
382	5	3×10^4	1.07		0.03	0.001
382	50	3×10^6	3.38		3	0.01
382	500	3×10^8	10.70		300	0.1
1270	5	10^5	0.59		0.1	0.001
1270	50	10^7	1.85	"Standard"	10	0.01
1270	50	10^7	1.85	Random IC seeding 2	10	0.01
1270	50	10^7	1.85	Random IC seeding 3	10	0.01
1270	50	10^7	1.85	Optically-thin cooling	10	0.01
1270	50	10^7	1.85	No feedback	10	0.01
1270	50	10^7	1.85	1/2-strength feedback	10	0.01
1270	50	10^7	1.85	×2-strength feedback	10	0.01
1270	50	10^7	1.85	Radiation pressure only	10	0.01
1270	50	10^7	1.85	150^3 particle resolution	2.96	0.01
1270	50	10^7	1.85	50^3 particle resolution	80	0.01
1270	50	10^7	1.85	1% local SFR	10	0.01
1270	50	10^7	1.85	$0.01Z_\odot$ initial metallicity	10	0.01
1270	500	10^9	5.86		1000	0.1
3820	5	3×10^5	0.34		0.3	0.001
3820	50	3×10^7	1.07		30	0.01
3820	500	3×10^9	3.38		3000	0.1
12700	5	10^6	0.19		1	0.001
12700	50	10^8	0.59		100	0.01
12700	500	10^{10}	1.85		10000	0.1

Table 2.1: Initial conditions, numerical parameters and modifications of the simulations in this paper: (1): $\Sigma_{tot,0}$: the initial average gas surface density in M$_\odot$ pc^{-2}. (2): R: the radius of the initial spherical gas cloud in pc. (3): M: the initial gas mass in $M_\odot$. (4): The freefall time $t_{ff,0}$ at the initial density, defined in equation 2.5. (5): Modifications to the simulation with respect to the standard setup described in Section 2.3. (6): Particle mass resolution in $M_\odot$. (7) Minimum Plummer-equivalent force softening for star particles. No minimum softening for gas particles is imposed. The particle number is 100^3 in all simulations unless otherwise specified. All simulations start with solar metal abundances (except where stated otherwise), and an initial temperature of 10^4 K.

The seed magnetic field is constructed in a similar fashion, such that the power spectrum of magnetic energy is also proportional to k^{-2}.The only difference from the above is that the $\nabla \cdot \vec{B}$ constraint is enforced by first computing random Fourier coefficients for the magnetic potential $\vec{A}$ and then applying the curl operator in Fourier space before transforming to real space in the same fashion as the velocity. The total magnetic energy is 1% of the gravitational binding energy, which is 10% of the initial turbulent energy. This figure was chosen based upon observations suggesting that MHD turbulence in GMCs is super-Alfvénic (Troland and Crutcher, 2008), supported by high-resolution MHD simulations showing that the supersonic turbulent MHD dynamo tends to saturate the magnetic energy to 1 – 10% of the

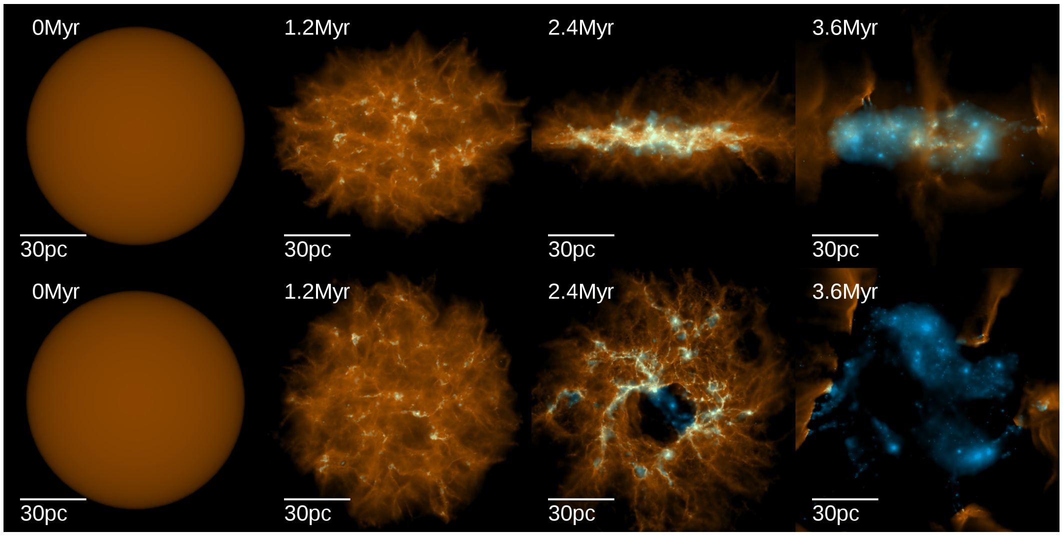

Figure 2.1: Surface density of gas (orange) and stars (blue) in our fiducial run with parameters $M = 3 \times 10^7 M_\odot$ and $R = 50\,\mathrm{pc}$, projected parallel (*top row*) and normal (*bottom row*) to the disk plane. *Far left:* The initial conditions, a uniform-density sphere. *Centre left:* After a time $\sim t_{ff,0} = 1.2\,\mathrm{Myr}$, star formation has begun. *Centre right:* After another $t_{ff,0}$ has passed, the star formation rate has peaked and large star clusters have appeared. *Far right:* The system has reached the critical stellar mass, at which point the gas is blown out of the system by feedback, evacuating the central region.

turbulent energy (Federrath et al., 2014).

The gas is initialized to a temperature of $10^4\,\mathrm{K}$, however the simulations' results are insensitive to this choice because the cooling time in all cases considered is orders of magnitude shorter than the dynamical time-scale. At the beginning of the simulation, the gas immediately cools rapidly to several tens of K, as is typical of the cold, neutral phase of the interstellar medium.

All simulations except those noted in table 2.1 have 10^6 particles, giving a fixed mass resolution of $10^{-6}M$. As discussed in Appendix 2.A.1, the star formation histories of the simulations are insensitive to our mass resolution at or above this level.

2.4 Results

Qualitatively, all simulations follow the sequence of events illustrated in Figure 2.1. The turbulent gas cloud immediately cools, with the lowest temperatures reaching $\sim 10\,\mathrm{K}$. The initial velocity and magnetic fields seed density fluctuations and the gravitational instability grows, condensing the cloud into filaments and clumps.

Global simulation results

$\Sigma_{tot,0}$ [$M_\odot pc^{-2}$] (1)	R [pc] (2)	Modifications (3)	ϵ_{int} (4)	T_{SF} [Myr] (5)	$T_{SF}/t_{ff,0}$ (6)	$T_{2\sigma}$ [Myr] (7)	$T_{2\sigma}/t_{ff,0}$ (8)	$\langle\epsilon_{ff,50}\rangle_t$ (9)	$\sigma_{\log\epsilon_{ff,50}}$ [dex] (10)
127	5		0.04	1.34	0.72	1.75	0.94	0.02	0.34
127	50		0.04	7.19	1.23	8.83	1.51	0.02	0.56
127	500		0.06	25.50	1.38	35.20	1.90	0.01	0.55
382	5		0.11	0.95	0.89	1.16	1.09	0.09	0.70
382	50		0.10	4.23	1.25	5.04	1.49	0.07	0.42
382	500		0.11	12.02	1.12	18.06	1.69	0.04	0.61
1270	5		0.31	0.77	1.31	0.81	1.38	0.11	0.77
1270	50	"Standard"	0.32	2.22	1.20	2.45	1.32	0.12	0.79
1270	50	No Magnetic Field	0.34	2.44	1.31	2.57	1.39	0.08	0.74
1270	50	Strong Magnetic Field	0.30	2.33	1.26	2.59	1.40	0.11	0.66
1270	50	No feedback	0.86+	3.25+	1.75+	3.59+	1.94+	0.52	0.62
1270	50	1/2 strength feedback	0.52	2.53	1.36	2.77	1.50	0.18	0.56
1270	50	×2 strength feedback	0.19	2.54	1.37	2.63	1.42	0.10	0.57
1270	50	Radiation pressure only	0.36	2.49	1.34	2.59	1.4	0.10	0.85
1270	50	Optically-thin cooling	0.32	2.23	1.20	2.43	1.31	0.13	0.54
1270	50	Slow subgrid SFR	0.30	1.79	0.97	1.85	1.00	0.11	1.03
1270	50	$Z = 10^{-2} Z_\odot$	0.35	2.05	1.11	2.13	1.15	0.14	0.75
1270	50	Random Seeding 2	0.30	2.06	1.11	2.32	1.25	0.11	0.56
1270	50	Random Seeding 3	0.28	2.03	1.10	2.23	1.20	0.10	0.63
1270	50	150^3 particle resolution	0.26+	1.98+	1.07+	2.12+	1.15+	0.10	0.60
1270	50	50^3 particle resolution	0.33	2.78	1.50	3.10	1.67	0.10	0.37
1270	500		0.31	7.50	1.28	7.91	1.35	0.14	0.83
3820	5		0.49	0.55	1.61	0.61	1.81	0.13	0.51
3820	50		0.51	1.58	1.48	1.73	1.62	0.14	0.48
3820	500		0.50	5.06	1.50	5.35	1.58	0.16	0.50
12700	5		0.63	0.33	1.76	0.36	1.95	0.20	0.50
12700	50		0.65	1.02	1.74	1.17	1.99	0.20	0.47
12700	500		0.64	3.14	1.69	3.37	1.82	0.20	0.73

Table 2.2: Important global quantities predicted by the simulations. Values denoted with a '+' indicate a lower bound. (1-3) As Table 2.1. (4) ϵ_{int}, the integrated star formation efficiency (equation 2.3). (5) T_{SF}, the characteristic width of the peak in the star formation history (equation 2.12), in Myr. (6) T_{SF} in units of the initial freefall time $t_{ff,0}$. (7) $T_{2\sigma}$, the interval of time containing 95% of star formation in Myr. (8) $T_{2\sigma}$in units of the initial freefall time $t_{ff,0}$. (9) $\langle\epsilon_{ff,50}\rangle_t$, the time-averaged per-freefall SFE defined in terms of the median gas density. (10) $\sigma_{\log\epsilon_{ff,50}}$, the dispersion in $\log\epsilon_{ff,50}$ in dex.

Within a freefall time, the first star clusters have formed. The star formation rate accelerates over $\sim\ t_{ff,0}$ to a peak value $\mathrm{SFR}_{max} \propto \epsilon_{ff} M/t_{ff}$, with most star formation occurring in dense molecular sub-clouds. At this point the moderating effect of feedback comes into play and the SFR starts to drop as the disk acquires significant turbulent support. Eventually, all gas is blown out of the central region by feedback and star formation ceases. The product of the starburst is invariably a population of star clusters, some of which disperse upon gas expulsion, and some of which persist to the end of the simulation and remain bound. The end result is a population of star clusters surrounded by a diffuse, expanding gas shell.

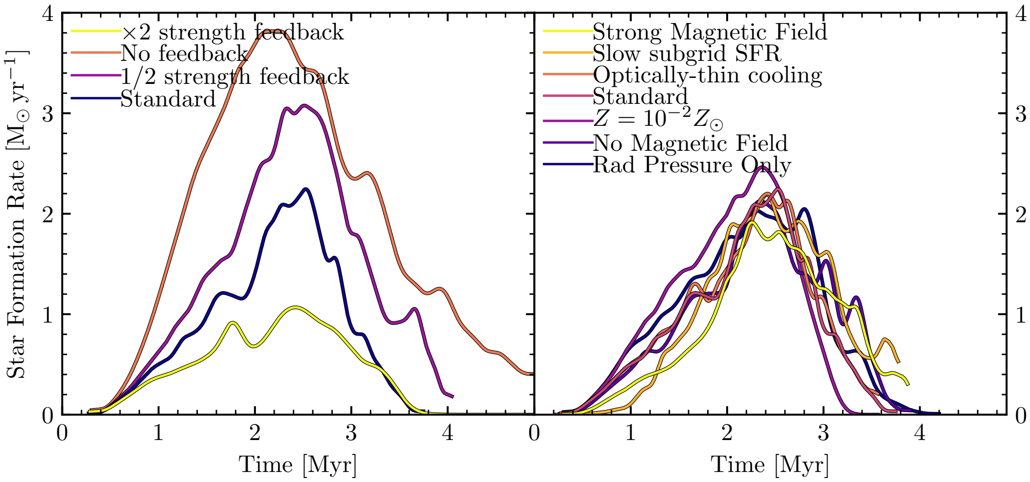

Figure 2.2: Star formation histories of the physics test runs using the standard initial parameters $M = 10^7 M_\odot$ and $R = 50\,\mathrm{pc}$. *Left:* Runs re-scaling the energy and momentum loadings of all stellar feedback mechanisms, producing large variations in the star formation history. *Right:* Our "standard" run compared to runs evolved from the same initial conditions with various physics options: (1) *Strong magnetic field*: Setting the initial magnetic energy to 10% of the binding energy, 10 times greater than standard. (2) *Slow subgrid SFR*: artificially "slowing" star formation in gas that satisfies the star formation criteria (Section 2.3.1) by multiplying the SFR by 1/100. (3) *Optically-thin cooling*: treating all radiative cooling as optically thin. (4) $Z = 10^{-2} Z_\odot$: lowering the initial metallicity from $Z_\odot$ to $0.01 Z_\odot$. (5) *No magnetic field*: turning off magnetic fields. (6) *Rad Pressure Only*: Removing all stellar feedback physics other than radiation pressure. These all produce relatively weak effects compared to simply rescaling the feedback energy and momentum fluxes, as discussed in section 2.4.1

.

2.4.1 Effects of Different Physics

In Figure 2.2, we compare the star formation histories of the simulations evolved from identical initial conditions but with different physics enabled or disabled. It can be readily seen that the effect of varying the strength of feedback dwarfs all others, analogous to the conclusions of Su et al. (2016) for galaxy-scale star formation. Here we enumerate and describe these modifications and explain why, physically, this should be the case.

Stellar feedback

In one run, we neglect feedback altogether, and in two others we scale all energy and momentum feedback rates by 1/2 and 2 respectively. We find that without

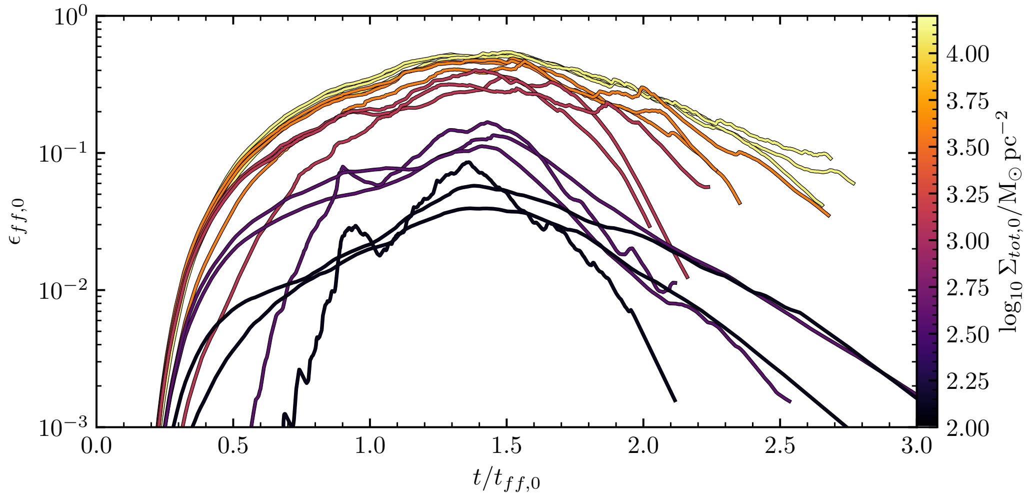

Figure 2.3: Dimensionless star formation histories of all parameter survey runs: the per-freefall SFE $\epsilon_{ff,0} = \frac{\dot{M}_\star t_{ff,0}}{M_{gas}}$ as a function of time in units of the initial freefall time $t_{ff,0}$ for the respective run. Each curve is a single run, coloured according to the value of $\Sigma_{tot,0}$. In all cases, $\epsilon_{ff,0}$ rises to a maximum dictated by the the strength of feedback relative to self-gravity, saturating to a value on the order of 1 as $\Sigma_{tot,0}$ gets large.

any feedback moderation, star formation consumes nearly all (86% by the end of the simulation) gas within $\sim 2t_{ff,0}$, with no sign of stopping. If the strength of feedback is scaled by 1/2, the star formation efficiency nearly doubles, while it is roughly halved when feedback is twice as strong, in agreement with equation 2.9. The time-scale for star formation remains unchanged, so the average per-freefall star formation efficiency ϵ_{ff} is also determined by the strength of feedback.

We also perform a run in which radiation pressure is the only feedback mechanism, and find that there is only maginally ($< 10\%$) more star formation than the standard run. Thus, radiation pressure accounts for most of the feedback budget at this point in parameter space. We expect this to be generally true in clouds where the dynamical time does not greatly exceed 3 Myr. Photoionization heating may have a significant contribution to disrupting the cloud if its escape velocity is $< 10\,\mathrm{km\,s^{-1}}$ (Dale et al., 2012), but this will be the case for only a couple points in the parameter space of this paper.

It is clear from the first panel of Figure 2.2 that the strength of feedback does not merely set the termination time of star formation: it also limits the star formation rate in an instantaneous sense - the stronger the feedback, the lesser the peak star formation rate. The specific feedback mechanism responsible for this is radiation pressure from young massive stars, as demonstrated by the radiation-pressure-only run. The radiation pressure is able to halt accretion onto cluster-forming cores, terminating star formation locally while it is still ongoing globally. Supernova feedback does not have this instantaneous effect due to its inherent time lag after initial star formation. Although we have not simulated it, a hypothetical starburst with only supernova feedback would proceed much like the zero-feedback run for the first 3 Myr, which in this case is enough time to convert nearly all gas into stars. We therefore conclude that the early feedback mechanisms from massive stars are *crucial* in setting the efficiency of rapid star formation in the high-density, short dynamical time regime studied in this work.

Optically-thin cooling

In one test run, we treating all radiative cooling as optically-thin (i.e. ignoring the optically-thick cooling suppression term from Rafikov (2007)). This increases the cooling rate at high densities substantially. However, this has no discernible effect on the simulation results, as the opacity effects on the cooling function only become important in the suppression of fragmentation at the opacity-limited mass scale $\sim 0.01\,\mathrm{M}_{\odot}$ (Rees, 1976).

Magnetic field strength

We perform a simulation with no magnetic field and a simulation with a “strong” magnetic field whose initial magnetic energy is equal to the initial turbulent energy, 10 times the standard value. A strong enough magnetic field may suppress fragmentation and the local SFR by as much as a factor of 2 on small scales (Federrath and Klessen, 2012), without considering feedback. We do see this effect in the “strong” magnetic field run: the initial star formation rate is about 1/2 that of the standard run. However, the SFR still continues to rise until it reaches the level set by feedback moderation, and the rest of the star formation history is quite similar to the other runs. Removing the magnetic field had no discernible effect upon the SFR, suggesting that the magnetic field has no large-scale dynamical relevance in the standard physics runs. However, we do note a small-scale cloud morphology in the MHD simulations that is distinctly more filamentary than the non-MHD simulation, due to the gas preferentially moving along magnetic field lines (see Collins et al., 2012).

Slow subgrid SFR

In this run, we force a small-scale star formation rate $\dot{\rho}_\star = 0.01\rho_{mol}/t_{ff}$ in gas that satisfies the star formation criteria (Section 2.3.1). This is 100 times slower than the usual choice, and comparable to the specific star formation rate on the scale of galactic disks (Kennicutt, 1998a; Krumholz et al., 2012a). This does not affect the average SFR in our simulations because the rate-limiting step of star formation is the formation of dense, unstable gas structures in the first place. Collections of gas particles that meet the star formation criteria but have not yet turned into stars will simply continue to contract to greater densities within a local freefall time, causing the local SFR to diverge until stars inevitably form. This result is notably different from simulations which enforce the same star formation law but do *not* follow low-temperature cooling below $10^4 K$ and adopt an effective equation of state for stellar feedback. In such a simulation, the local star formation law would underestimate the global star formation rate because the aforementioned gravitational contraction would be suppressed.

Note that this insensitivity to the local star formation efficiency is only obtained because the gas particle gravitational softening is fully adaptive. Otherwise, the cold gas would simply contract to inter-particle spacings comparable to the minimum softening and stop at that density, and the local SFR would stop increasing.

The most notable effect of this modification was the formation of much denser and much more plentiful bound star clusters. As gas exhaustion is slowed down locally, protoclusters spend more time radiating away energy, contracting, and damping out their internal turbulent motions before turning into star particles. This increases the compactness and boundedness of the remnants. We therefore caution that while global star formation histories are not sensitive to the local value of ϵ_{ff} (see also Hopkins et al. 2018a), the physics of star cluster formation may be.

Metallicity

In the low-metallicity test, we scale the initial gas metallicity down from $Z_\odot$ to $10^{-2} Z_\odot$. This can affect many aspects of the cooling and feedback physics. Metal line cooling is proportionally less efficient, however even at $Z \sim 10^{-2} Z_\odot$, $t_{cool} << t_{ff}$ in the most dense gas, so fragmentation should not be strongly altered. This may change at metallicities of $10^{-4} - 10^{-5} Z_\odot$ (Hopkins and Conroy, 2015). The metallicity also determines dust opacity, and thus the coupling efficiency for IR radiation pressure. Lastly, it affects the evolution of the formed stellar populations' mass, energy and momentum injection rates, which are obtained from STARBURST99. Overall, the metal-poor simulation had a star formation efficiency only marginally greater than the standard run (0.35 compared to 0.32), however it did have a faster initial growth in the SFR, suggesting that the stellar feedback at low metallicity might be less effective at halting accretion onto cluster-forming cores. The main difference in the feedback budget is due to the $\propto Z^{0.7}$ scaling of the line-driven stellar wind mass loss rate of type O stars (Vink et al., 2001). At solar metallicity, the momentum input is somewhat less than that of radiation pressure, but the same order of magnitude. At $10^{-2} Z_{\odot}$, however, the dynamical effect of the winds is negligible.

We have also performed limited experiments with our routines for cosmic ray heating, cooling, streaming and diffusion. In general, if the system is given an initial cosmic ray energy density, it will rapidly cool away into dynamical irrelevance: like the magnetic field, it is ultimately a reservoir for the energies of gravitational collapse and stellar feedback, and not a source of energy in itself. There is also the possibility of the system being immersed in a strong cosmic ray background, however such environmental interactions are beyond the scope of this work. However, Yoast-Hull et al. (2016) have found that the cosmic ray energy in nuclear starbursts tends to be considerably smaller than the magnetic field energy, suggesting that even in the full picture with a realistic galactic environment cosmic rays should not greatly influence the overall dynamics of a collapsing GMC.

2.4.2 Integrated star formation efficiency

We now arrive at our main results. In Figure 2.4 the star formation efficiencies of the parameter survey simulations are plotted against the surface density, escape velocity, 3D density, mass and radius derived from the simulation parameters M and R. Clearly, the mass, size, density, and escape velocity are *not* good general predictors of ϵ_{int}; similar ϵ_{int} values are obtained in simulations for which these quantities differ by orders of magnitude.

Of the obvious physical quantities derived from M and R, $\Sigma_{tot,0}$ is the best predictor of ϵ_{int}, with particularly good agreement between spatial scales at high $\Sigma_{tot,0}$, where the dynamical time is always short compared to main sequence lifetimes. In general, we obtain good agreement with equation 2.9: ϵ_{int} scales $\propto \Sigma_{tot,0}$ when $\Sigma_{tot,0} << \Sigma_{crit}$, and it saturates to a maximum ϵ_{int} at sufficiently high surface density. The saturation efficiency is not necessarily 1, as depends on the initial conditions and what subset

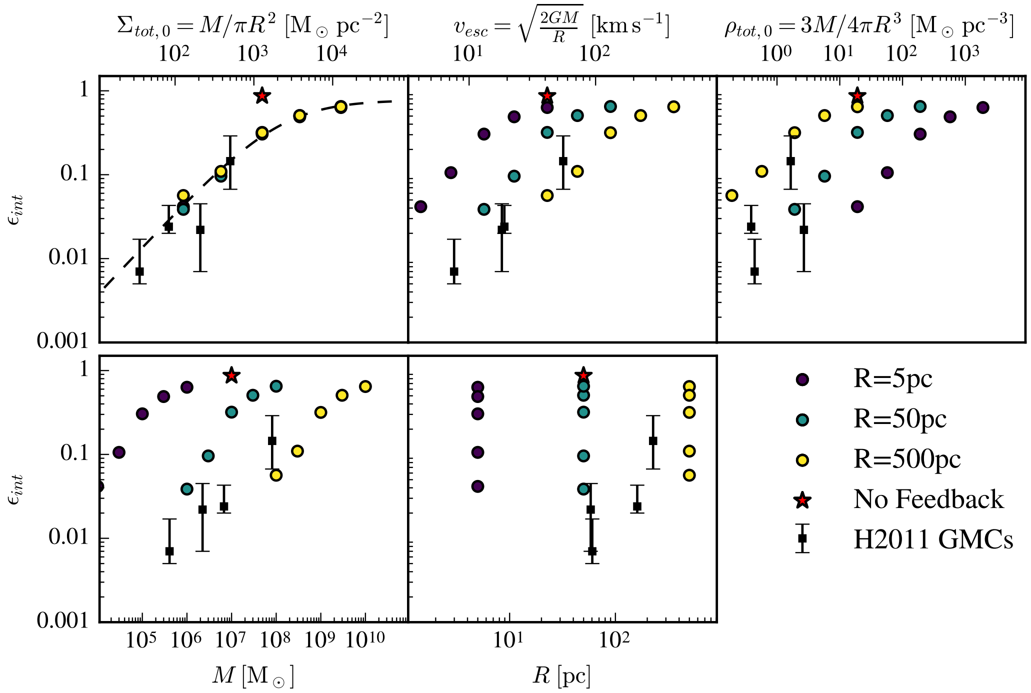

Figure 2.4: Integrated SFE ϵ_{int} of the 15 parameter survey simulations plotted against various functions of the initial simulation parameters M (mass) and R (radius). The points with error bars, "H2011 GMCs", represent the populations of giant molecular clouds extracted from previous full-scale galaxy simulations (Hopkins et al., 2011b). The points represent the population medians, and the bars represent the $\pm 1\sigma$ percentiles. The dashed line in panel 1 is the best-fit curves to equation 2.11, which gives parameters $\Sigma_{crit} = 2800 \pm 100\,\mathrm{M}_\odot\,\mathrm{pc}^{-2}$ and $\epsilon_{max} = 0.77 \pm 0.05$.

of the gas is used when defining ϵ_{int}. As an extreme example, if the initial gas density field had an extended warm diffuse background component, as it might realistically, the diffuse gas would never form stars over the time-scale of interest, but would reduce the ϵ_{int} statistic if it were included in the gas mass sum. In our simulations, it is possible that there is a similar effect for the diffuse gas at the outer edges of the disk, as well as the gas which escapes through under-dense 'chimneys' between the dense sub-clouds within the disk.

We fit ϵ_{int} to the following two-parameter model:

$$\epsilon_{int} = \left(\frac{1}{\epsilon_{max}} + \frac{\Sigma_{crit}}{\Sigma_{tot,0}} \right)^{-1}, \tag{2.11}$$

which is equivalent to the Fall et al. (2010) formula (equation 2.9) in the limit $\Sigma_{tot,0} << \Sigma_{crit}$ but approaches ϵ_{max} as $\Sigma_{tot} \rightarrow \infty$. Performing an unweighted fit on $\log \epsilon_{int}$, the best-fit parameters are $\Sigma_{crit} = 2800 \pm 100\,\mathrm{M_\odot\,pc^{-2}}$ and $\epsilon_{max} = 0.77 \pm 0.05$. The best-fit curve is plotted in panel 1 of Figure 2.4. This value of Σ_{crit} is within a factor of 2 of that found by Fall et al. (2010), and is compatible with the value of Σ_{crit} found in Section 2.2 from the average observed ϵ_{int} of Milky Way GMCs.

The residual R-dependence of ϵ_{int} is small, but is positively correlated with R. This may be explained by the built-in scales in ISM cooling and stellar feedback physics. It is expected that the thermal pressure of the warm ISM heated to 10^4 K will have a greater proportional dynamical effect in the few clouds with escape velocities that do not greatly exceed $10\,\mathrm{km\,s^{-1}}$. The time-scale of stellar evolution also introduces a scale into stellar feedback: at fixed $\Sigma_{tot,0}$, t_{ff} scales $\propto R^{\frac{1}{2}}$. Therefore, as R spans 2 dex, the time-scale of star formation spans an order of magnitude, so the timing of star formation relative to the stellar evolution within the formed stellar populations varies with R at fixed $\Sigma_{tot,0}$. Stellar evolution causes $\frac{\dot{P}_\star}{m_\star}$ to vary over time, so the effective strength of feedback that determines ϵ_{int} will be some function of the global star formation time-scale t_{ff}. The general trend is that of increasing SFE over longer dynamical times, indicating that the effective $\frac{\dot{P}_\star}{m_\star}$ decreases monotonically with time. This is *despite* the increasing relevance of supernovae in the simulations spanning longer time-scales: as massive stars die, the introduction of supernovae is not enough to make up for the loss of mechanical luminosity from radiation and stellar winds to maintain the initial $\frac{\dot{P}_\star}{m_\star}$.

In Figure 2.4, the compiled SFE statistics for GMC populations extracted from the parameter survey of full-scale galaxy simulations (Hopkins et al., 2012a) are also plotted for comparison, and happen to be largely compatible with the fit. In light of this and the agreement with the observational estimate of Σ_{crit}, we may safely generalize these results from our contrived generic gas ball setup to clouds with actual GMC morphologies as they emerge from galactic gas dynamics. While the large-scale morphology and relative importances of shear, rotation, and turbulence may be different between our simulations and GMCs that emerge in galaxy simulations, the scaling of ϵ_{int} is an inevitable result that applies to self-gravitating gas cloud that can form stars. Therefore, equation 2.11 is a general predictor of the ϵ_{int} of a star-forming gas cloud, provided that it is self-gravitating and it has some well-defined average surface density.

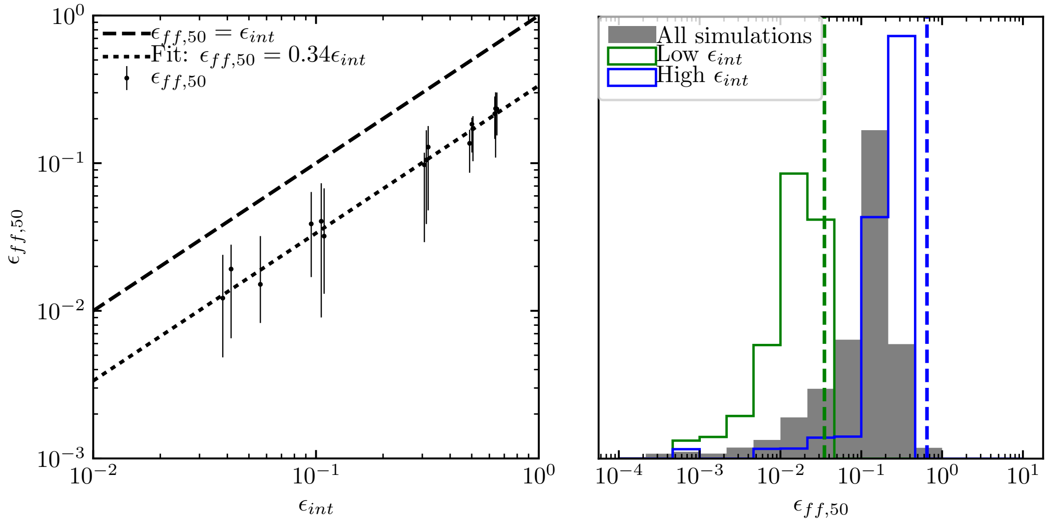

Figure 2.5: *Left:* Instantaneous per-freefall star formation efficiency $\epsilon_{ff,50} = \dot{M}_\star(t)\; t_{ff,50}(t)/M_{gas}(t)$ (see equation 2.6) as a function of integrated star formation efficiency ϵ_{int} for all parameter survey simulations. The points represent the value of $\epsilon_{ff,50}$ averaged over all times where the SFR is nonzero. Error bars represent the $\pm 1\sigma$ percentiles of $\epsilon_{ff,50}$. The dashed line marks the line of equality between ϵ_{ff} and ϵ_{int}, and the dotted line indicates the best proportional fit. *Right:* Histograms of $\epsilon_{ff,50}$ for all parameter-survey simulations (grey), a highly-efficient ($\epsilon_{int} = 0.64$) run with $\Sigma_{tot,0} = 12700\,\mathrm{M}_\odot\,\mathrm{pc}^{-2}$, $R = 50\,\mathrm{pc}$ (blue), and an inefficient ($\epsilon_{int} = 0.08$) run with $\Sigma_{tot,0} = 382\,\mathrm{M}_\odot\,\mathrm{pc}^{-2}$, $R = 50\,\mathrm{pc}$ (green). The dashed lines indicate ϵ_{int} for the respective runs. Not surprisingly, $\epsilon_{ff,50}$ scales in proportion to ϵ_{int}, but it has considerable variation ($\sim 0.4 - 0.8\,\mathrm{dex}$) throughout the star formation history of a single simulation. For Milky Way GMCs of surface density $\sim 100\,\mathrm{M}_\odot\,\mathrm{pc}^{-2}$, we expect $\epsilon_{ff,50}$ to average to 0.01, in good agreement with observations.

2.4.3 Duration of star formation and per-freefall SFE

We now discuss results concerning star formation rates and timescales. As stated in the overview, star formation in all parameter survey simulations spans no more than $\sim 3t_{ff,0}$ (see Figures 2.2 and 2.3). Here we seek to quantify this statement more precisely. As a general-purpose measure of the duration of the starburst, we define the quantity T_{SF}, the stellar mass formed divided by the mass-weighted average star formation rate:

$$T_{SF} = \frac{M_\star}{\langle \dot{M}_\star \rangle} = \frac{M_\star^2}{\int \left(\dot{M}_\star\right)^2 \,\mathrm{d}t}. \tag{2.12}$$

This is a natural measure of characteristic of the peak in the star formation history (see Figures 2.2 and 2.3). It is also a useful proxy for the lifetime of the gas disk, as star formation largely begins once the gas has settled into a disk and halts once the disk is disrupted. The values of T_{SF} are tabulated in table 2.2. T_{SF} is insensitive to the small early and late tails of the star formation history, however, so in table 2.2 we also quote $T_{2\sigma}$, the time interval containing 95% of the star formation. This is generally only slightly more than T_{SF}, as most star formation occurs in a brief burst, and feedback is able to rapidly quench star formation.

In all simulations, $T_{SF} \sim t_{ff,0}$ (see table 2.2), so most of the star formation occurs within a single initial global freefall time. This confirms our argument in Section 2.2: since $t_{ff,0}$ is longer than any other internal collapse time-scale, and turbulent support dissipates in a crossing time (e.g. Elmegreen, 2000), the disk should be able to form enough stars to reach the blowout stage within this time. This time constraint implies a tight relation between ϵ_{int} and ϵ_{ff}: if star formation is constrained to happen over N dynamical times, then $\epsilon_{ff} = \epsilon_{int}/N$ on average.

This brings us to a very important subtlety of feedback-moderated star formation: while stellar feedback determines ϵ_{int} in a simple way through the force balance described in Section 2.2, it also determines ϵ_{ff} in an “instantaneous” sense, with “instantaneous” meaning over time-scales much longer than the dynamical time of the smallest resolved units of star formation, yet still much shorter than the global timescale. Since star formation is a process of hierarchical fragmentation from the largest cloud scale down to individual stars, the total star formation history is the sum of a hierarchy of many individual smaller and shorter star formation events, each of which has its ϵ_{int} determined by the local ratio of feedback and gravity. This results in an overall star formation rate that is moderated “from the bottom up". Realistically, the “bottom” of this hierarchy would be set by the mass scale at which it is likely that the sampled IMF contains a massive star that can exert strong feedback.

It is of limited usefulness to compare star formation time-scales to $t_{ff,0}$, at least when comparing with the value of ϵ_{ff} in observed star-forming systems, as it requires knowledge of the more-diffuse initial conditions. The freefall time inferred for the gas disks as they would be observed during star formation would be something closer to $t_{ff,50}$, as derived from the mass-weighted median gas density (Equation 2.6) [6]. Average values of $\epsilon_{ff,50} \equiv \dot{M}_\star(t)\ t_{ff,50}(t)/M_{gas}(t)$ for each simulation can be found in columns 9 and 10 of table 2.2. In panel 1 of Figure 2.5 we plot $\epsilon_{ff,50}$ as a function of ϵ_{int} and confirm that there is a tight relation between two efficiencies.

---

[6] We have found that in these simulations $t_{ff,50}$ tends to be quite close to the freefall timescale derived from the volume-averaged gas density, which is closer to what is actually calculated for GMCs. We use $t_{ff,50}$ because we have found it to be more stable and robust.

The best-fit power law to the relation has an exponent within 1σ of 1, so we propose a simple proportional relation:

$$\langle \epsilon_{ff,50} \rangle_t = 0.34 \epsilon_{int}, \tag{2.13}$$

where $\langle \epsilon_{ff,50} \rangle_t$ denotes the average observed value at a random point during the star formation history. The physical implication of this relation is that star formation in the simulations is indeed constrained to occur mainly within ~ 3 dynamical times, regardless of the relative strength of feedback and gravity, as was argued in Section 2.2. This would agree with the mean GMC lifetime of 3 freefall times inferred in Murray (2011).

The shape of the distribution of ϵ_{ff}, which we show in panel 2 of Figure 2.5, is also of interest. In general, the distribution is strongly peaked near ϵ_{int}, with only brief excursions above ϵ_{int}. The distribution is negatively skewed due to the early and late tails of the star formation history, which spread the distribution over several orders of magnitude, similar to what is found in (Lee et al., 2016). The intrinsic dispersion in the value of $\epsilon_{ff,50}$ across the lifetime of the system (Table 2.2, Column 10) typically has a value between 0.4 and 0.8 dex.

2.5 Discussion

2.5.1 Star-forming clouds and clumps in the Milky Way

Many star-forming clouds, identified as associations between emission from young stars and molecular gas, have been observed in the Milky Way. These clouds can be broadly classified into two groups: GMCs proper, which have characteristic surface density $100\,\mathrm{M}_\odot\,\mathrm{pc}^{-2}$ and are typically traced in CO (Larson, 1981; Solomon et al., 1987; Bolatto et al., 2008), and dense clumps, which have a typical surface density of $10^3\,\mathrm{M}_\odot\,\mathrm{pc}^{-2}$, and are traced in higher-density tracers such as HCN (Wu et al., 2005, 2010; Heyer et al., 2016). The observational proxy of ϵ_{int} that can be obtained for these systems is:

$$\epsilon_{obs} = \frac{M_{\star,young}}{M_{\star,young} + M_{molecular}}, \tag{2.14}$$

where $M_{\star,young}$ is the mass of stars younger than 3.9 Myr, as can be traced from emission from HII regions or from direct counts of young stellar objects, and $M_{molecular}$ is the mass of molecular gas in the cloud. Note that both of these masses must vary during a star-forming cloud's lifetime, and in general $\epsilon_{obs} \neq \epsilon_{int}$. However, the trend in ϵ_{obs} with Σ_{gas} should still follow that of ϵ_{int}, so some systematic variation in the ϵ_{obs} should be evident in clouds with widely different surface densities.

In Table 2.3, we summarize the Σ_{gas} and ϵ_{obs} statistics of the GMC datasets of Lee et al. (2016) and Vutisalchavakul et al. (2016) and the dense clump datasets of Wu et al. (2010) and Heyer et al. (2016). Lee et al. provides ϵ_{obs} directly (denoted ϵ_{br} in the paper). We estimate $M_{\star,young}$ from the Vutisalchavakul et al. dataset by multiplying the provided SFR measurements from MIR flux by 3.9 Myr, the mean massive star lifetime weighted by ionizing flux (e.g. Murray, 2011) . We compute $M_{\star,young}$ in the Wu et al. clumps by converting the reported IR luminosities to the mass of a young single stellar population with a Kroupa (2002) IMF. In Table 2.3 we give values for the Heyer et al. corresponding to the value of $M_{\star,young}$ extrapolated from YSO counts assuming a Kroupa IMF (an upper bound) as well as values assuming the only mass is in stars that have been directly counted (a lower bound). As it is physically unlikely that less massive stars are not present, and the SFE from the upper bound is closer to Wu et al. (2010) and nearby star-forming regions (Lada and Lada, 2003), the true value is probably closer to the upper bound.

A ~ 1 dex scaling in the median ϵ_{obs} is evident between $\sim 1\%$ for the GMCs at $\sim 10^2\,\mathrm{M_\odot\,pc^{-2}}$ and $\sim 10\%$ for the clumps at $\sim 10^3\,\mathrm{M_\odot\,pc^{-2}}$, in agreement with the general prediction of our SFE model. However, substituting the median surface density into our model for ϵ_{int} (Equation 2.11) gives a SFE that is typically ~ 0.4 dex greater than the median ϵ_{obs}. This offset could have several possible causes, including an underestimation of the strength of feedback in the simulations, the accounting of gravitationally bound gas in the observations, or an intrinsic bias in ϵ_{obs} as an estimator of ϵ_{int}.

If the scatter in the observed ϵ_{obs} were only due to intrinsic variation from the scatter in Σ_{gas}, then we would expect the scatter in Σ_{gas} and ϵ_{obs} to be equal. This is not the case: the scatter in ϵ_{obs} is too large to be explained by the variation in Σ_{gas} alone. This is likely due to the variation in the observed ϵ_{obs} that arises from observing the clouds at random times in their star-forming lifetimes as the stellar and molecular mass content varies (e.g. Lee et al., 2016). This type of variation is present to some extent in the simulations (e.g. Figure 2.5, panel 2).

We may also compare to observational estimates of ϵ_{ff}. The Lee et al. and Vutisalchavakul et al. datasets give median ϵ_{ff} values of $\sim 2\%$ and $\sim 1\%$ respectively, which are consistent with what is found in our simulations with similar gas surface density. However, the best-fit ϵ_{ff} in dense clumps reported by Heyer et al. is also $\sim 2\%$ when the upper bound on the stellar mass is used. In Heyer et al. (2016), the SFRs are computed by dividing the inferred stellar mass by $\tau_{SF} = 0.5\,\mathrm{Myr}$,

Dataset	Class	$\log \Sigma_{gas}$ ($\mathrm{M_\odot\,pc^{-2}}$)	$\log \epsilon_{obs}$	$\log \epsilon_{int}$ predicted from median Σ_{gas}
Lee et al. 2016	GMCs	$1.88^{2.19}_{1.40}$	$-1.97^{-1.23}_{-2.76}$	-1.58
Vutisalchavakul et al. 2016	GMCs	$1.95^{2.24}_{1.68}$	$-1.93^{-1.37}_{-2.58}$	-1.51
Wu et al. 2010	Dense clumps	$3.00^{3.39}_{2.63}$	$-1.10^{-0.86}_{-1.76}$	-0.61
Heyer et al. 2016	Dense clumps	$2.79^{3.05}_{2.61}$	Upper: $-0.87^{-0.55}_{-1.29}$, Lower: $-2.14^{-1.69}_{-2.71}$	-0.76

Table 2.3: Quantiles of molecular gas surface density Σ_{gas} and the observationally-inferred SFE ϵ_{obs} (Equation 5.5) from various studies of star-forming GMCs and dense clumps in the Milky Way, in the format median$^{+1\sigma}_{-1\sigma}$. Both Σ_{gas} and ϵ_{obs} typically scale by ~ 1 dex between GMC conditions and dense clump conditions. For Heyer et al. (2016), both upper and lower bounds are provided. The final column gives the true integrated SFE ϵ_{int} predicted by substituting the median Σ_{gas} into Equation 2.11.

the evolution timescale for Class I protostars inferred from low-mass star-forming regions (Evans et al., 2009; Gutermuth et al., 2009). In general, inferred SFRs of dense clumps have relied on assumption that star formation has been steady for at least as long as τ_{SF}[7], which is questionable within the picture presented in this paper given that nearly all clumps have freefall times shorter than this. If the lifetime of HCN clumps is significantly longer than 0.5 Myr (and they are as dense as presumed) it must be due to some physics that are is not accounted for in this work. One possibility is a transition in the nature of star-forming flows at lower Mach numbers, which we have hardly surveyed in our simulations. The clumps in Heyer et al. have a characteristic velocity dispersion of $\sim 0.75\,\mathrm{km\,s^{-1}}$, corresponding to a Mach number of $2 - 3$, much less supersonic than GMCs at large, and in the range expected from monolithic isothermal collapse (Larson, 1969; Penston, 1969). Such a transition in the nature of the flow below $1\,\mathrm{km\,s^{-1}}$ is suggested by the inverse size-linewidth relation of clumps (Wu et al., 2010) compared to GMCs (Larson, 1981). However, whether this can be responsible for reducing ϵ_{ff} is unclear, as Federrath and Klessen (2012) do not find particularly low ϵ_{ff} in their $\mathcal{M} = 3$ simulations. Other alternatives would include some feedback mechanism that we have not accounted for, such as protostellar heating or outflows, or a systematic overestimation of inferred density of HCN clumps (Goldsmith and Kauffmann, 2017).

Caution is needed comparing the predicted cloud lifetimes to observationally inferred lifetimes, because this is sensitive both to the observational methods/tracers, and to the actual properties (e.g. mean densities) of the initial clouds (which we

---

[7] The SFRs of the Wu et al. (2010) HCN clumps, as determined by Heiderman et al. (2010) from infrared luminosity, have $\epsilon_{ff} \sim 1\%$, but again there is an implicit averaging window $\tau_{SF} \sim 4\,\mathrm{Myr}$ in the $L_{IR} - SFR$ conversion factor used. This figure of 1% does appear to be a general finding for dense clumps (Krumholz, 2014).

have freely varied, rather than drawing from a statistically representative sample of observed clouds). A detailed comparison will be the subject of future work (Grudić et al. 2018, in prep). However, we can make some preliminary comparisons. Lee et al. 2016 estimate a mean GMC lifetime of $\sim 24\,\mathrm{Myr}$ for a population of clouds with a median free-fall time of $6.7\,\mathrm{Myr}$ (corresponding to a mean density of 25 H_2 molecules per cm^3). Our $\Sigma = 127\,\mathrm{M}_\odot\,\mathrm{pc}^{-2}$, $R = 50\,\mathrm{pc}$ run is the closest to this in mean density ($33\,\mathrm{cm}^{-3}$) and free-fall time, and its major star formation episode lasts for $2.5\,t_{ff,0} \approx 15\,\mathrm{Myr}$ (See Figure 2.3 and Table 2.1). This is somewhat smaller than observed, although similar enough that differences in how "lifetime" is measured and observationally estimated might account for the difference. Moreover, real GMCs are not, of course, isolated, but can accrete continuously over their lifetime and may have turbulence "stirred" externally which further can slow collapse (for a review, see Fukui and Kawamura 2010). It seems likely, therefore, that clouds embedded in a realistic ISM would have somewhat longer lifetimes.

2.5.2 Slow star formation

The scaling and saturation of of ϵ_{ff} appears at first to be at odds with the notion of "slow" star formation, wherein it has been observed that $\epsilon_{ff} \sim 1\%$ universally, from Milky Way-like to ULIRG-like environments (Kennicutt, 1998a; Krumholz and McKee, 2005; Krumholz and Tan, 2007; Krumholz et al., 2012a). This slow speed of star formation has been explained theoretically in terms of the properties of the turbulent ISM alone (e.g. **?**Hennebelle and Chabrier, 2011b), so it is necessary to compare the predictions of these theories with those of feedback-moderated star formation to determine whether feedback is a necessary part of the picture. In making this comparison, we emphasize that our prediction pertains to individual unstable clouds near virial equilibrium, and not to any significant patch of a galaxy that may contain GMCs in various states of formation and disruption, as well as the other phases of the ISM. In the latter case, it has been shown in Hopkins et al. (2014) and Orr et al. (2018a) that the same physical models used in our simulations also robustly predict that $\epsilon_{ff,gal} \sim 1\%$ on galactic scales on average, despite assuming that $\epsilon_{ff} = 1$ on the smallest resolvable scales, as star formation reaches a statistical equilibrium when smoothed on $> 1\,\mathrm{kpc}$ scales.

Both the feedback-disrupted cloud picture suggested by our simulations and purely turbulence-regulated star formation theories successfully predict the median value $\epsilon_{ff} \sim 1\%$ in Milky Way GMCs, however they do so for completely different physical reasons. However, the observed *dispersion* in ϵ_{ff} for a given set of cloud conditions has not been found to be less than 0.5 dex (Heiderman et al., 2010; Evans et al., 2014; Heyer et al., 2016; Lee et al., 2016; Vutisalchavakul et al., 2016); Lee et al. found 0.91 dex from the most complete Milky Way GMC dataset that we are aware of. As they noted, the turbulence-regulated models do not predict this much scatter because they do not allow for ϵ_{ff} to vary for a given set of turbulent ISM conditions. Lee et al. showed that the scatter can arise from observing GMCs at random points in their lifetime of initial collapse, star formation, and feedback disruption. For Milky Way-like conditions, our simulations do predict intrinsic dispersions in ϵ_{ff} of the same order as what has been observed; whether the figure of 0.91 dex can be fully accounted for depends upon the relationship between ϵ_{ff} and its observational proxy, which we will address in future work.

The gas-rich nuclei in Arp 220 provide an interesting case study for the speed of star formation. The total SFR of $240\,\mathrm{M_\odot\,yr^{-1}}$, inferred from its IR luminosity (Downes and Solomon, 1998; Kennicutt, 1998b), appears to agree nicely with the theory of slow star formation, yet our simulations at comparable gas surface density $\sim 10^4\,\mathrm{M_\odot\,pc^{-2}}$ predict $\epsilon_{ff} \sim 20\%$. Considering several $10^9\,\mathrm{M_\odot}$ of gas localized within two disks, each with radius smaller than 100 pc (Scoville et al., 2017), the resulting SFR should be well in excess of $10^3\,\mathrm{M_\odot\,yr^{-1}}$, an order of magnitude greater than the L_{IR}-inferred value. Our simulations do not consider the stabilization of the gas disk due to the presence of the central SMBH, but this can probably only reduce the predicted SFR by a factor of a few (Utreras et al., 2016). The apparent discrepancy may lie in the use of L_{IR} to determine the SFR, as it only provides an average value over the lifetime of OB stars, 4 Myr. Because the dynamical time in the nuclear disks is of order 10^5 yr (Scoville et al., 2017), it is unlikely that the SFR has been steady over this comparatively long averaging window. Estimates of the SFR from supernova rates have the same limitation. Therefore, the possibility that the SFR in Arp 220 has recently been in excess of $10^3\,\mathrm{M_\odot\,yr^{-1}}$ cannot be excluded on this basis (Anantharamaiah et al., 2000; Parra et al., 2007).

2.5.3 Comparison with other GMC star formation studies

Many numerical studies have been performed that are conceptually similar to the ones in this paper, following the collapse of an idealized turbulent cloud and the resulting star formation and feedback processes. It is useful to compare and contrast our predictions with these studies, in particular in cases where specific feedback mechanisms have been considered in greater detail.

Our run without stellar feedback is most comparable with previous simulations of isothermal supersonic MHD turbulence with gravity (Kritsuk et al., 2011; Collins et al., 2012; Padoan et al., 2012; Lee et al., 2015). In these simulations, the SFR tends to grow until ϵ_{ff} is of order unity, with its particular value depending somewhat upon the regular and Alfvénic Mach numbers, the virial parameter, and the details of the turbulent driving, and the final $\epsilon_{int} \sim 1$ due to the lack of feedback. The value $\epsilon_{ff} = 0.52$ we obtain in feedback-free cloud collapse without feedback is most consistent with the Federrath and Klessen (2012) models with mixed or solenoidal driving.

Dale et al. (2012) ran a parameter study of feedback-disrupted clouds, considering only photoionization heating. We have found in tests that photoionization heating only is insufficient to disrupt a cloud with an escape velocity that is large compared to the sound speed $c_s \sim 10\,\mathrm{km\,s^{-1}}$ of photoionized gas. This agrees with the trend of Dale et al. (2012), which found order-unity ϵ_{int} in clouds with high escape velocity (Runs 'X' and 'F'). Also, our $M = 10^4\,\mathrm{M_\odot\,pc^{-2}}$, $R = 5\,\mathrm{pc}$ has the same physical parameters as Run 'J' in Dale et al. (2012). This had $\epsilon_{int} = 0.04$, while the final stellar mass in Run 'J' was 35% and rising at 3.5 Myr. We re-simulated this run with photoionization heating only and radiation pressure only, and the one with photoionization heating had a very similar star formation history and cloud morphology to Run 'J'. The one with radiation pressure only had $\epsilon_{int} = 0.05$, very close to the full physics run. Radiation pressure is thus the primary feedback mechanism even in this region of parameter space where photoionization heating alone could still theoretically disrupt the cloud.

The radiation hydrodynamics star formation simulations of Raskutti et al. (2016) focus upon the effects of stellar feedback from the single-scattered monochromatic photons at a high opacity corresponding to UV photons. They use the radiation hydrodynamics code Hyperion, evolving the radiation field on a fixed grid according to the M1 closure (Skinner and Ostriker, 2013). They overpredict the efficiency of their fiducial Milky Way-like GMC run by an order of magnitude, obtaining $\epsilon_{int} = 0.43$ for a cloud with $M = 5 \times 10^4\,\mathrm{M_\odot}$ and $R = 15\,\mathrm{pc}$, which has average surface density $70\,\mathrm{M_\odot\,pc^{-2}}$. Extrapolating our simulation results using equation 2.11 gives $\epsilon_{int} = 0.02$ for a cloud with these parameters, in much better agreement with observations (Section 2.5.1 and references therein). We have found that $\epsilon_{int} \sim 0.04$ in a test run with otherwise similar initial conditions to Raskutti et al. and radiation pressure as the only feedback (Appendix 2.A.2).

This order of magnitude discrepancy may be due to the behaviour of the M1 closure in such an optically-thick, multi-source radiative transfer problem. Experiments in developing GIZMO's own M1 RHD scheme have shown that the momentum imparted to the gas by the radiation field around an embedded source can be underestimated by an order of magnitude if the attenuation length $\lambda = \rho^{-1}\kappa_{UV}^{-1}$ is not well-resolved, which it certainly is not at the densities, opacities, and spatial resolution typical in the Raskutti et al. simulations [8]. Secondly, photons propagated via the M1 scheme behave collisionally: colliding streams will form a shock rather than passing through each other. As stars form in a tightly-clustered configuration in isothermal fragmentation (Guszejnov et al., 2017, 2018c), neighbouring stars particles can cancel each other's fluxes. In summary, it is reasonable to suspect that ability of radiation pressure to disrupt the GMC was underestimated.

Tsz-Ho Tsang and Milosavljevic (2017) simulated super star cluster formation in cloud with mass $10^7\,\mathrm{M}_\odot$ and diameter 25 pc, for a mean surface density of $1.6 \times 10^4\,\mathrm{M}_\odot\,\mathrm{pc}^{-2}$, comparable to the densest runs in our parameter study. They accounted for feedback via infrared radiation pressure, which is expected to dominate, with an accelerated Monte Carlo scheme that is more realistic than our more approximate treatment. They found that radiation pressure reduced ϵ_{int} by $\sim 30\%$ compared to the run with no feedback. Our simulations at this surface density had $\epsilon_{int} \sim 0.64$, compared to 0.86+ with no feedback, so despite our different treatments of radiation pressure the agreement is quite good.

It should be noted that most star formation in all simulations mentioned in this subsection occurs within some small ($\sim 2-3$) number of global freefall times, regardless of the final ϵ_{int} if the cloud is disrupted. This naturally leads to the linear relation between ϵ_{int} and ϵ_{ff} shown in Section 2.4.3, suggesting that this is a very general feature of the star formation-cloud disruption process, insensitive to the details of stellar feedback. The role of feedback on cloud scales is to make star formation less efficient in a given amount of time, not to prolong the star-forming lifetime as it does on galactic scales.

2.5.4 Bound star cluster formation

ϵ_{int} should be an important quantity for the formation of bound star clusters. If all other factors are equal, the fraction of a star cluster remaining gravitationally bound after gas expulsion should increase with ϵ_{int} (Tutukov, 1978; Hills, 1980;

---

[8] This problem is averted by the shell-driving test problem presented by Raskutti et al., because the radiation first propagates through an optically-thin medium where the field is well-resolved.

Mathieu, 1983; Lada et al., 1984; Elmegreen and Clemens, 1985)[9]. It can thus be argued that the bound cluster formation efficiency Γ, the fraction of stars found in bound clusters, is a function of ϵ_{int}, and hence of $\Sigma_{tot,0}$ by equation 2.9. If equation 2.9 holds, then cluster formation should be generic to regions of high Σ_{gas}. And indeed, rich populations of young bound clusters are ubiquitous in dense nuclear starbursts, including notable examples Arp 220 (Wilson et al., 2006), M82 (McCrady and Graham, 2007), and M83 (Bastian et al., 2012; Ryon et al., 2015). However, whether there actually is a general scaling in Γ that depends on a single environmental parameter associated with surface density is currently an open problem: Adamo et al. (2015) and Johnson et al. (2016) appear to support this hypothesis, while Chandar et al. (2015) does not; correlations between Σ_{gas} [10] and Γ are apparent, but whether they are universal has not been established conclusively (Adamo et al., 2017).

GMCs in the Milky Way and other nearby galaxies typically have $\Sigma_{gas} \sim 100\,\mathrm{M_{\odot}pc^{-2}}$ (Larson, 1981; Solomon et al., 1987), giving $\epsilon_{int} \sim 3\%$ at best, yet young bound star clusters are still observed to have formed within the galaxy (Portegies Zwart et al., 2010a). Rather than simply turning off below a certain surface density threshold, Γ is theoretically expected to scale smoothly as a function of Σ_{gas}, saturating to a value of $\sim 70\%$ (Kruijssen, 2012). Star cluster formation may be possible in environments that are less dense on average because star-forming clouds are hierarchically structured, with a broad surface density PDF. If ϵ_{int} is determined in a scale-free fashion according to equation 2.9, it will apply just as well on the scale of denser-than-average subclumps once they decouple from their environment, allowing them to have high ϵ_{int} locally even if ϵ_{int} is small on larger scales (e.g. Kruijssen et al. (2012a)). If this argument is valid, we expect to see some amount of bound cluster formation in any star-forming environment.

The production of bound star clusters is generally associated with high-pressure environments, where the pressure associated with the midplane of a galactic disk can be estimated as $P \sim G\Sigma_{gas}\Sigma_{tot}$ (Elmegreen and Efremov, 1997). Elmegreen and Efremov proposed a picture wherein GMCs are confined by this pressure $P \sim \rho v_t^2$, rather than their self-gravity, and the gas mass loss rate in a protocluster was assumed to be $\dot{M} \propto L/v_t^2$, where L is the protocluster luminosity. Thus the fraction of the

---

[9] Other factors influencing the bound fraction of a cluster include the virial state of the stars at gas expulsion Goodwin (2009) and the degree of initial degree of clumpy substructure (Smith et al., 2011, 2013)

[10] Or equivalently Σ_{SFR} (e.g. Kennicutt, 1998a)

gas mass converted to stars with fixed ϵ_{ff} is greater when P is greater. The picture suggested by the simulations in this paper is presents an alternative to this; ϵ_{ff} is not fixed, and the timescale of mass loss is always on the order of the freefall time. Clouds are confined by self-gravity, rather than external pressure, and their SFE is greater at greater $P \sim G\Sigma_{gas}^2$ because of the relative scaling of the strength of feedback and self-gravity.

In future work we will use these simulations to study the mapping between galactic environments and the populations of bound star clusters they produce, providing the stepping stone between lower-resolution cosmological simulations and single-cluster dynamical studies. This development is necessary, in particular, for the theory of cosmological SMBH seed formation from runaway stellar mergers in dense clusters (see Portegies Zwart and McMillan (2002); Mouri and Taniguchi (2002); Gürkan et al. (2004); Devecchi and Volonteri (2009)). It would also allow a more self-consistent model of pairing and evolution of the population of massive ($\sim 60 M_\odot$) black hole binaries like the progenitor of GW150914 (Abbott et al., 2016); a significant fraction of these are expected to be found in bound star clusters (Rodriguez et al., 2015, 2016).

2.5.5 The nature of nuclear star formation

Our results here illustrate the claim of Torrey et al. (2017): *no equilibrium exists* for gas-rich nuclear disks with short dynamical times, and their dynamics have an inherently transient nature: they undergo rapid fragmentation followed by rapid gas expulsion. Star-forming nuclear disk calculations *must* account for stellar feedback in a way that is appropriate to their short time-scales, or else risk obtaining unphysical solutions. This caveat may very well limit the validity of isolated nuclear disk simulations that use a Springel and Hernquist (2003)-like effective-EOS ISM model and a slow sub-grid star formation law, both of which have been widely used in the field of galaxy simulations. For example, Hopkins and Quataert (2010) simulated circumnuclear disks of similar mass and radius to the ones in this paper, but in absence of the appropriate feedback physics the SFR of the disks was quite likely underestimated by at least an order of magnitude.

A robust result of our simulations is that both ϵ_{int} and ϵ_{ff} must saturate to ~ 1 at surface densities in excess of $10^4\,\mathrm{M_\odot pc^{-2}}$. Barring other unaccounted-for feedback physics (see Section 2.5.7), and neglecting environmental interactions, we conclude that a gas-dominated cloud with $\Sigma_{gas} >> 10^3\,\mathrm{M_\odot\,pc^{-2}}$ will convert nearly all of its gas to stars in a few crossing times. In this limit, we expect a result similar to our simulations: a population of massive star clusters will form, and will eventually merge into a single cluster because the high global SFE will allow the system to remain bound. If a relatively low-mass SMBH is present, it may sink to the centre of this cluster under dynamical friction. However, it is also possible that before the final nuclear cluster has formed, the SMBH and clusters effectively behave as a few-N-body system, which has chaotic behaviour and often results in the ejection of one or more members. Such ejections will prolong the time necessary for SMBH to form binary pairs in galaxy mergers, and may lower the resulting low-frequency gravitational wave background.

If star formation occurs near an SMBH, the gravity of the SMBH also contributes to the binding force on the gas. If we re-derive 2.9 and consider only the force of gravity of the SMBH on the gas, we obtain a lower bound for the integrated SFE of a gas disk of radius R around a black hole of mass M_{BH}:

$$\epsilon_{int} \geq \left(1 + \frac{\pi R^2 \Sigma_{crit}}{M_{BH}}\right)^{-1}. \tag{2.15}$$

This assumes that the gas is not somehow being prevented from forming stars by AGN feedback and that the dynamical effect of the black hole upon the gas flow does not slow star formation enough to make the gas consumption time longer than $\sim 10\,\mathrm{Myr}$. The characteristic radius at which ϵ_{int} saturates to ~ 1 is then:

$$R_{SF} \sim \sqrt{M_{BH}/2\pi\Sigma_{crit}} = 6\,\mathrm{pc}\left(\frac{M_{BH}}{10^6 M_{\odot}}\right)^{\frac{1}{2}}, \tag{2.16}$$

using $\Sigma_{crit} = 2800\,\mathrm{M_{\odot}\,pc^{-2}}$.

Under these assumptions, the in-situ formation of a nuclear star cluster could proceed as follows: if enough low-angular momentum gas falls within R_{SF} of an SMBH to become gravitationally unstable, it will be rapidly consumed by star formation, leaving behind a nuclear star cluster and little remaining gas. The fiducial value 6 pc derived here does lie in the range of effective radii of nuclear star clusters found in several different types of galaxies (see Hopkins et al. (2010) and references therein).

Such efficient star formation near black holes may have drastic implications for the ability of gas from the galactic disk to be accreted onto a central SMBH, as the gas may fragment into stars before reaching the hole within a few dynamical times, at which point it can no longer lose angular momentum efficiently. This contrasts greatly with models which assume star formation must be slow ($\epsilon_{ff} \sim 1\%$) all the way down to the black hole; in this case, a steady supply of gas can reach the black hole even with modest torques, as gas has ~ 100 dynamical times to lose its angular momentum before being converted to stars. As such, it is important that studies of AGN accretion on $\sim$ pc and smaller scales consider the physics of the multiphase ISM and star formation in some detail.

2.5.6 Absence of metal-enriched supermassive direct-collapse objects

These simulations were originally conceived as an attempt to reproduce the mechanism for direct-collapse supermassive black hole formation simulated in Mayer et al. (2010) and Mayer et al. (2015) with a more realistic approach to cooling and star formation. To summarize, these works propose that in the gas-rich nuclear disk resulting from a galaxy merger, fragmentation can be suppressed by some combination of turbulence and suppression of cooling due to optical thickness, enabling accretion onto a supermassive quasi-star even for ISM with solar metal abundances. To avoid over-cooling in optically thick regions, we implemented the optically-thick cooling approximation of Rafikov (2007) so as to interpolate between the optically-thin and -thick cooling regimes where appropriate. In previous tests we also chose a rather high ($10^7 cm^{-3}$) density threshold for star formation and allowed star formation only when the local Jeans mass is $< 10^3 M_{\odot}$, so as to prevent premature conversion of gas particles into star particles where they may otherwise form a supermassive object. Our simulations reach comparable optical depths and turbulent velocity dispersions to the nuclear disks in the Mayer simulations, however we report no formation of direct-collapse objects. In numerical experiments, we have only been able to produce anything resembling a supermassive quasi-star if we implement a temperature floor of 10^4 K and slow the local star formation rate $\dot{\rho}_{\star}$ to 1 % of the usual value. As these are similar to the choices made for Mayer et al. (2010) and Mayer et al. (2015), it seems that metal-enriched direct-collapse object formation is a numerical artifact of slow subgrid star formation and a lack of low-temperature cooling. Our conclusions agree with those obtained by Ferrara et al. (2013) using a one-dimensional disk model: if realistic low-temperature cooling is accounted for, the cooling time in the metal-enriched ISM is invariably too short to suppress fragmentation down to the scales required to directly form a supermassive object.

2.5.7 Feedback physics uncertainties

Most of what is known about the effects of stellar feedback on GMC scales has been learned from observations of star-forming complexes within the Milky Way, and even then the true efficiencies of many feedback mechanisms acting in Milky Way-like environments are still loosely constrained, to say nothing of generalizing these mechanisms to ULIRG-like environments. Here we list uncertainties in the strength of feedback which could conceivably affect our results:

The Initial Mass Function

Throughout this work, we have assumed that the initial stellar mass function, and hence $\dot{P}_\star/m_\star$, is independent of the environment of star formation. If the IMF were to become more top-heavy in environments of high surface density, $\dot{p}_\star/m_\star$ would increase, and as our simulations have shown, this is the quantity to which our results are most sensitive. Supposing that $\frac{\dot{P}_\star}{m_\star}$ did scale at least linearly with Σ_{gas} due to enhanced type O star production, this would limit the maximum star formation efficiency. There is some observational evidence of a dearth of low-mass stars in dense nuclear environments (Smith and Gallagher, 2001; Bartko et al., 2010), however such observations can be subject to significant sampling bias because the time-scale for mass segregation is short in dense systems. For this reason and others, Bastian et al. (2010b) concluded that current observations were still largely consistent with a universal IMF.

Infrared radiation pressure

Radiation pressure plays an important role in the feedback budget in many of our simulations; even in cases where the final gas blowout is ultimately due to SNe, radiation helps prevent an initial runaway of the SFE before SNe start to occur. We have found that ϵ_{int} saturates to a value close to 1 as surface density becomes large, however Murray et al. (2010) argued that the IR opacity of dust grains should limit the saturation point of ϵ_{int} for gas with solar abundances, as radiation pressure in the optically thick regime is the only force of feedback which can conceivably scale as fast as the gas self-gravity. By this argument, the saturation SFE ϵ_{int}^{max} is expected to scale $\sim (\kappa_{IR}\Sigma_{crit})^{-1}$, which takes a value of $\sim \frac{1}{2}$ for gas with solar metal abundances. However, in a realistic, 3-dimensional scenario where hydrodynamics is coupled to the radiation field in an inhomogeneous ISM, it is actually unlikely that radiation pressure can achieve the whole "τ_{IR} boost", either because photons will have a tendency to leak out of the most optically-thin lines of sight, or because the radiative Rayleigh-Taylor instability is able to efficiently dissipate kinetic energy (Krumholz and Thompson, 2012b). Radiation hydrodynamics studies on this problem are ongoing (see also Krumholz and Thompson (2013); Rosdahl and Teyssier (2015); Tsang and Milosavljević (2015); Davis et al. (2014b); Skinner and Ostriker (2015); Zhang and Davis (2017)), and although results have varied with the radiative transfer scheme used, they do generally agree that the scaling of the momentum deposited to the gas with the mean τ_{IR} is sublinear for sufficiently large τ_{IR}, forcing the integrated SFE to ultimately saturate to ~ 1.

2.6 Summary

We have performed a parameter study of 3D multi-physics MHD simulations of star-forming gas disks with initial parameters spanning two orders of magnitude in surface density and in spatial scale, including the physics of supernovae, stellar winds, radiation pressure, and photoionization heating. Due to the generality of the simulation setup, we have been able to study the nature of star formation in gas-rich environments in general, including nuclear starbursts and GMCs. Our main findings are as follows:

- In any bound, gas-rich star-forming cloud with short ($\sim$ 10Myr or less) dynamical time, star formation proceeds until it causes an inevitable gas blowout, with the final SFE determined mainly by the balance of feedback and gravitation, with other physical mechanisms having secondary importance.

- The integrated SFE ϵ_{int} of such a system scales strongly with the initial gas surface density $\Sigma_{tot,0}$ with weak dependence upon other parameters, and saturates to a value ~ 1 at adequately high surface density, despite the effects of strong feedback. We find good agreement with analytic derivations of ϵ_{int} which take the form of equation 2.9 (Fall et al., 2010; Murray et al., 2010; Dekel and Krumholz, 2013; Thompson and Krumholz, 2016), fitting a value $\Sigma_{crit} = 2800\,\mathrm{M}_\odot\,\mathrm{pc}^{-2}$ from the simulations. The agreement across different spatial scales is non-trivial and somewhat surprising, as our parameter space bridges distinct time-scale regions where radiation pressure (< 3 Myr) and SN explosions (> 3 Myr) dominate the feedback energy and momentum budget. The prediction of this SFE model is that ϵ_{int} in self-gravitating clouds should scale from $\sim 1\%$ at $10^2\,\mathrm{M}_\odot\,\mathrm{pc}^{-2}$ and $\sim 10\%$ at $10^3\,\mathrm{M}_\odot\,\mathrm{pc}^{-2}$, as is found in local GMCs and dense clumps (Section 2.5.1 and references therein). The model also predicts that SFE ultimately saturates to $\sim 100\%$ in the limit of very high surface density.

- We find a proportional relation between the integrated SFE ϵ_{int} and the per-freefall SFE ϵ_{ff} (equation 2.13) for self-gravitating clouds, essentially because the clouds always produce enough stars to self-destruct within $\sim 2-3$ dynamical times. ϵ_{ff} is determined only initially by such details as cooling and magnetic fields, and will inevitably grow until moderated by stellar feedback. The observed ϵ_{ff} distribution for Milky Way GMCs can be accounted for by combining the spread from this relation and a modest intrinsic spread due to the time-varying SFE of a single cloud. The variation in ϵ_{ff} is at odds with a universal slow star formation ($\epsilon_{ff} \sim 1\%$) law when applied to individual clouds, but the same physics used in this study recover the $\epsilon_{ff,gal} \sim 1\%$ relation in cosmological simulations (Hopkins et al., 2014, 2018a).

Thus we have determined the basic properties of feedback-moderated star formation for self-gravitating, unstable gas complexes. In a subsequent paper, we have used these simulations to study the process of star cluster assembly (Grudić et al., 2018a). Future work will elucidate the relation between theoretical predictions of cloud SFE and its observational proxies, the mapping between galactic environmental properties and populations of star clusters, and the detailed dynamical history of star cluster formation as determined by feedback.

ACKNOWLEDGMENTS

We thank Neal J. Evans II, Eve Ostriker, Dávid Guszejnov, Chris Hayward, Matthew Orr and Andrew Wetzel for helpful comments and critique. We also thank the anonymous referees for highly comprehensive and helpful feedback that motivated a more thorough understanding of our results. Support for PFH and MG was provided by an Alfred P. Sloan Research Fellowship, NASA ATP Grant NNX14AH35G and NSF Collaborative Research Grant #1411920 and CAREER grant #1455342. Numerical calculations were run on the Caltech computer cluster 'Zwicky' (NSF MRI award #PHY-0960291) and allocation TG-AST130039 granted by the Extreme Science and Engineering Discovery Environment (XSEDE) supported by the NSF.

APPENDIX

2.A Code Tests

2.A.1 Convergence and consistency

The methods for cooling, star formation and feedback used in this paper have been tested in previous studies of galactic-scale simulations resolving spatial scales of $\sim 1\,\mathrm{pc}$ and masses $> 10^3\,\mathrm{M}_\odot$. However, their behaviour at the higher resolutions of these simulations has been much less well-studied. It is therefore necessary to determine how the simulation behaviour depends (1) upon mass and spatial resolution, (2) upon the particular random seeding in the initial conditions and (3) upon the particular physics included and parameters chosen. Because the star formation histories (SFH) are the main data of interest, we shall focus on the effects of these choices on the SFH as a proxy for the behaviour of the simulation as a whole.

We choose the parameters $R = 50\,\mathrm{pc}$, $M = 10^7\,\mathrm{M}_\odot$ as the point in parameter space at which to investigate these questions. Because all runs are qualitatively identical with only differences in numerical scalings, the conclusions drawn for these parameters should apply across our parameter space, obviating the need to perform the tests at all points. We vary the particle number from 50^3 to 150^3 to isolate resolution effects. Because we use adaptive softening, the effective gravitational force resolution naturally follows mass resolution with no need for manual tuning. To assess the effect of the random velocity seeding, we compare runs from 3 random realizations at the standard resolution and with standard physics.

From the first panel of Figure 2.A.1 it is evident that mass resolution does have certain systematic effects upon the computed SFH: in particular, low-resolution runs have a SFR which is greater at early times. This is an artifact the cutoff in the turbulent length scale that can be followed before the turbulent Jeans mass is no longer resolved. A gas structure that is well-resolved and supported against its self-gravity by internal motions at high resolution may not be considered so if down-sampled to low resolution where it consists only of a few particles. Thus, in the absence of any feedback moderation, as is the case at early times, the SFR will rise sooner at low resolution. While this resolution effect is conspicuous, it apparently does not have a strong effect upon the integrated SFE.

The variation in SFE due to resolution is in fact comparable to the variation arising

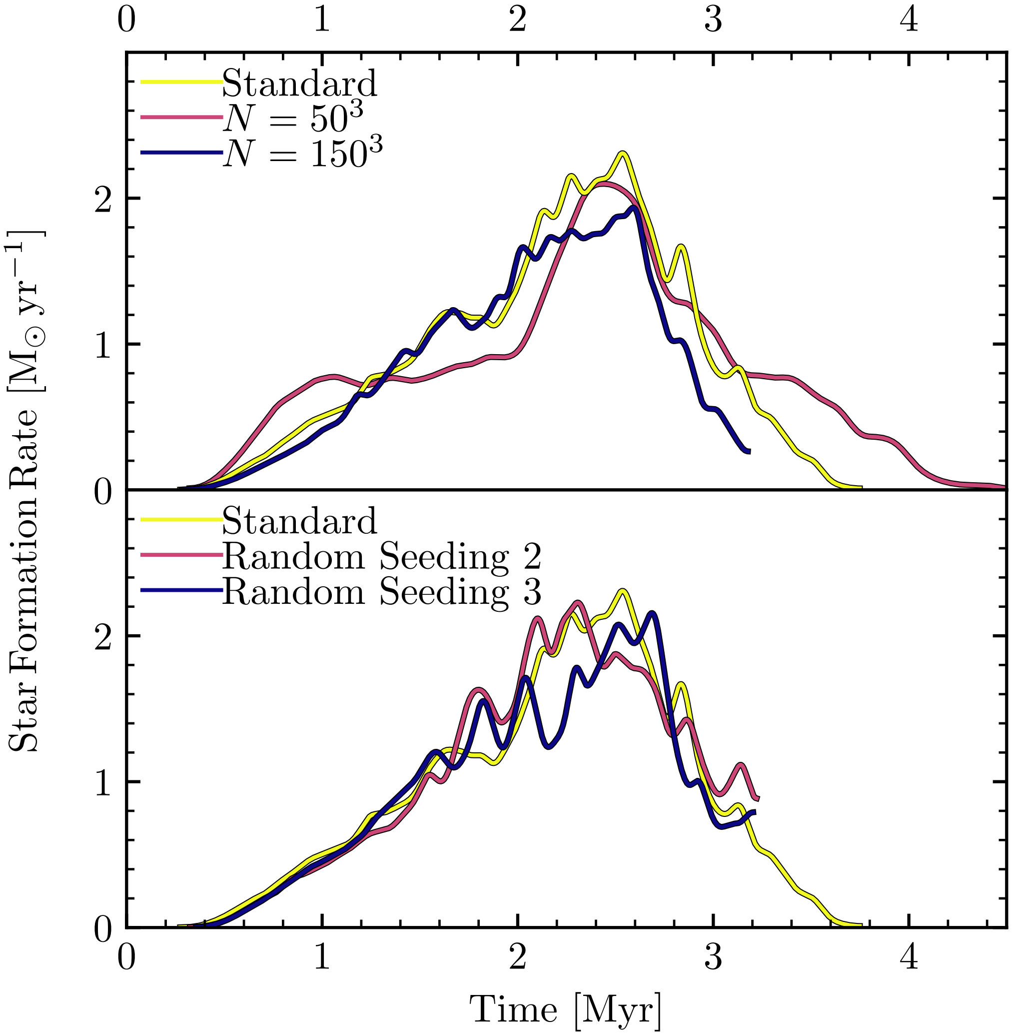

Figure 2.A.1: Star formation histories of test runs with parameters $M = 10^7\,\mathrm{M}_\odot$ and $R = 50\,\mathrm{pc}$. *Top:* Convergence tests with particle number varied from 50^3 to 200^3. *Bottom:* Consistency tests using 3 different random seeds for the initial perturbations.

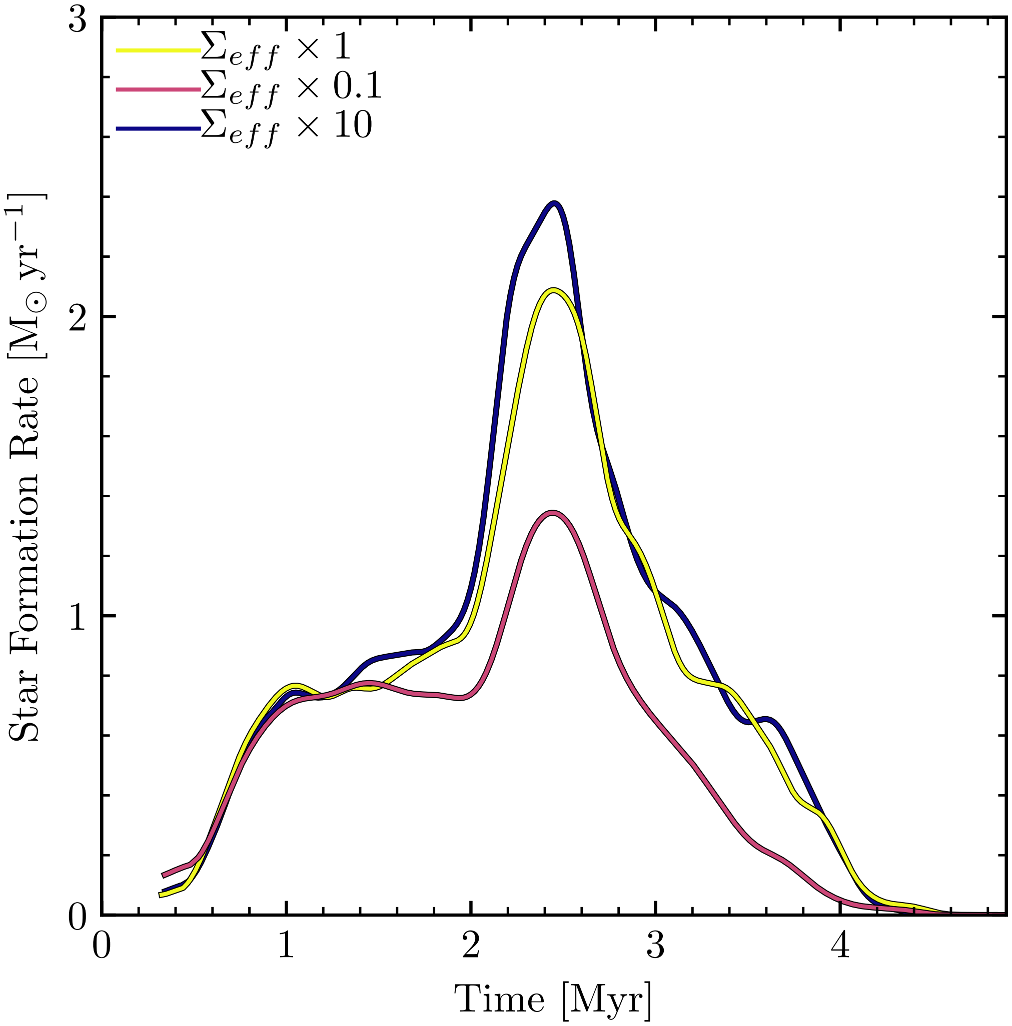

Figure 2.A.2: Effect of varying the local extinction column density estimator Σ_{eff} by factors of 0.1 and 10 in our treatment of radiation pressure.

from different random seedings at fixed resolution, visible in panel 2 of Figure 2.2. In both cases, the mass of gas converted to stars varies only by$\sim 1\%$ between runs. We therefore conclude that the star formation efficiencies computed as the central result of this study are consistent between runs with the same physical parameters. As discussed in the main text, our results concerning star formation efficiency can be understood in terms of simple force balance considerations. As such, it is not surprising that the SFE should converge rapidly and be robust with respect to perturbations.

2.A.2 Radiation pressure

In our survey of the effects of different physics (Section 2.4.1), it was found that radiation pressure was most responsible for the moderation of star formation. Therefore, it is particularly important to test the robustness of the radiative transfer prescription we have used. Radiation pressure is treated with a combination of short-ranged, local coupling within the kernel encompassing a star particle's nearest neighbouring gas particles (most importantly handing single-scattered UV photons), and a long-ranged component treated in the optically-thin approximation (mainly handling reprocessed IR photons). The estimated local extinction around a particle relies upon an estimate of the local column density Σ_{eff} obtained by a Sobolev approximation; for details see Hopkins et al. (2018a).

To test the sensitivity of our results to this local extinction approximation, we both increased and decreased the estimated Σ_{eff} by a factor of 10 in our fiducial $10^7 M_{\odot}$, 50pc run at 50^3 resolution. The resulting star formation histories are shown in Figure 2.A.2. Increasing Σ_{eff} by a factor of 10 had very little effect on the the star formation history. This is because the local extinction fraction $1 - \exp\left(\Sigma_{eff}\kappa_{UV}\right)$ is typically already quite close to 1 in the default run. Decreasing Σ_{eff} by a factor of 10 reduced the peak SFR by roughly a factor of 2, and decreased the final SFE from 0.32 to 0.23, as leakage of UV photons from the local kernel is increased. We conclude that the SFE results of this paper do have some amount of sensitivity to the assumed geometric factor in the prescription for Σ_{eff}, but this sensitivity is quite sublinear: variations of a factor of 10 lead to SFE variations within a factor of 2.

Finally, we also performed a series of radiation pressure-only tests with a cloud of mass $5 \times 10^4\,\mathrm{M}_{\odot}$ and radius 15 pc, with a statistically-isotropic solenoidal initial turbulent velocity field scaled to give an initial virial parameter of 2, emulating the setup in Raskutti et al. (2016). At mass resolutions at which the formation of dense protostellar envelopes starts to be resolved ($<< 1\,\mathrm{M}_{\odot}$), one might worry that some qualitative change in the nature of the density field would affect the local column density estimates in such a way that the net photon momentum budget at large is affected, and hence the SFE. We ran this test with particle numbers of 12^3, 25^3, 50^3, and 100^3, and obtained ϵ_{int} of 0.082, 0.052, 0.042, and 0.040 respectively, suggesting convergence. As with our convergence test with all physics enabled (2.A.1), the SFE tends to converge from above; the star formation criterion is in some sense stricter at higher resolution, as local velocity gradients supporting against gravitational collapse are better-resolved.

Chapter 3

STAR CLUSTER STRUCTURE FROM HIERARCHICAL STAR FORMATION

M. Y. Grudić, D. Guszejnov, P. F. Hopkins, A. Lamberts, M. Boylan-Kolchin, N. Murray, and D. Schmitz. MNRAS, 481:688–702, November 2018a. doi: 10.1093/mnras/sty2303.

Abstract

Young massive star clusters spanning $\sim 10^4 - 10^8 M_{\odot}$ in mass have been observed to have similar surface brightness profiles. We show that recent hydrodynamical simulations of star cluster formation have also produced star clusters with this structure. We argue analytically that this type of mass distribution arises naturally in the relaxation from a hierarchically-clustered distribution of stars into a monolithic star cluster through hierarchical merging. We show that initial profiles of finite maximum density will tend to produce successively shallower power-law profiles under hierarchical merging, owing to certain conservation constraints on the phase-space distribution. We perform N-body simulations of a pairwise merger of model star clusters and find that mergers readily produce the shallow surface brightness profiles observed in young massive clusters. Finally, we simulate the relaxation of a hierarchically-clustered mass distribution constructed from an idealized fragmentation model. Assuming only power-law spatial and kinematic scaling relations, these numerical experiments are able to reproduce the surface density profiles of observed young massive star clusters. Thus we bolster the physical motivation for the structure of young massive clusters within the paradigm of hierarchical star formation. This could have important implications for the structure and dynamics of nascent globular clusters.

3.1 Introduction

Most stars in the Universe are field stars, gravitationally bound only to their host galaxies and not to any discernible smaller element of structure. However, when the locations of initial star formation are considered, there is strong evidence that most stars are born in a statistically clustered, correlated configuration (Lada and Lada, 2003; McKee and Ostriker, 2007; Bressert et al., 2010; Gouliermis et al.,

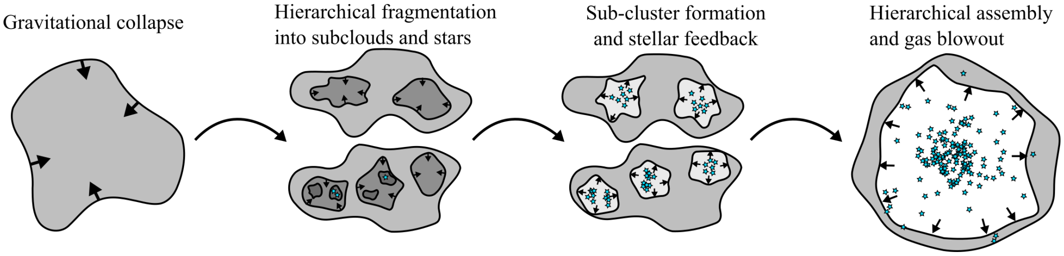

Figure 3.1: Proposed model of cluster formation from hierarchical star formation. *Far left:* An unstable molecular cloud undergoes gravitational collapse. *Centre left*: The gravitational instability causes hierarchical fragmentation, producing a hierarchy of sub-clouds that eventually fragment into individual stars. *Centre right:* Stars that fragmented out of the same sub-clouds form in sub-clusters. Feedback from massive stars starts to evacuate gas locally. *Far right:* The sub-clusters merge hierarchically into a single cluster as stellar feedback blows out any remaining gas.

2015; Grasha et al., 2017; Gouliermis, 2018). The star formation efficiency $\frac{M_\star}{M_{gas}}$ of typical giant molecular clouds is only of order $1-10\%$ (Myers et al., 1986; Mooney and Solomon, 1988; Williams and McKee, 1997; Evans et al., 2009; Lada et al., 2010; Heiderman et al., 2010; Murray, 2011; Kennicutt and Evans, 2012; Lee et al., 2016), possibly due to stellar feedback disrupting the molecular cloud once a certain stellar mass has formed (Murray et al., 2010; Hopkins et al., 2012a, 2014; Grudić et al., 2018b). The loss of binding energy from the blowout of the remaining gas can unbind the initial stellar distribution (Tutukov, 1978; Hills, 1980; Mathieu, 1983; Lada et al., 1984; Elmegreen and Clemens, 1985; Baumgardt and Kroupa, 2007; Parmentier et al., 2008), allowing most or all stars to disperse into the surrounding galaxy. However, the existence of young, apparently well-relaxed star clusters within the Milky Way (Portegies Zwart et al., 2010a) suggests that a certain fraction of star formation does lead to bound cluster formation, even in Milky Way-like conditions. In many cases, young star clusters have not had time to evolve under the effects of evaporation, dynamical relaxation, and stellar evolution, so their structures should contain some information about their initial formation. A successful model of star cluster formation will be able to clarify this relationship.

In this paper, we discuss the formation of young massive star clusters (YMCs): star clusters that are younger than $\sim 100\,\mathrm{Myr}$ and more massive than $10^4\,\mathrm{M}_\odot$ (Portegies Zwart et al., 2010a)[1]. Unlike mature globular clusters, which are generally well-fit

---

[1] The definition of Portegies Zwart et al. (2010a) also implcitly includes gravitational boundedness, however we emphasize that the observed YMCs we refer to in this text are not necessarily bound.

by tidally-truncated models such the King (1966) profile, YMCs have been found to have extended power-law profiles with no discernible truncation, and hence are better fit by the Elson et al. (1987) surface brightness model (hereafter Elson et al. (1987)). This model consists of a core of finite surface brightness μ_0 with an outer surface brightness profile that decays as $\mu \propto R^{-\gamma}$, where γ is the parameter determining the logarithmic slope of the surface brightness profile, hereafter referred to as the "profile slope". If $\gamma \leq 2$, the integrated stellar mass is divergent, so Elson et al. (1987) profiles with $\gamma \sim 2$ are referred to as "shallow", and have a greater proportion of their light in the power-law portion of the surface brightness profile compared to steeper profiles.

YMCs quite often do have shallow profile slopes with γ typically ranging from 2.2 to 3.2 (Elson et al., 1987; Mackey and Gilmore, 2003a,b; Portegies Zwart et al., 2010a; Ryon et al., 2015), which correspond to 3D density profiles $\rho \propto r^{-3.2} - r^{-4.2}$ in the outer regions. The super star clusters (SSCs) of NGC 7252, despite being three to four orders of magnitude more massive than YMCs of the Local Group, also have profile slopes in this range (Bastian et al., 2013). This agreement across mass scales suggests some scale-free physical mechanism of bound star cluster formation, such that a shallow Elson et al. (1987)-like surface brightness profile is generally produced.

One might suppose that the shallow power-law profile of young clusters somehow reflects the initial stellar configuration at the time of star formation, and a smooth cloud of gas turns into a structureless star cluster (e.g. Goodwin 1998). However, observations and simulations (Mac Low and Klessen, 2004; McKee and Ostriker, 2007; Kruijssen, 2013; Krumholz et al., 2014) of star-forming clouds agree that the initial distribution of stellar positions in a star cluster is clumpy and hierarchical, not smooth and monolithic. Thus, presently-observed smoothly-distributed star clusters are likely to have assembled from a hierarchy of sub-clusters that fragmented out of the parent molecular cloud. If so, the present-day structure of young star clusters is the direct result of top-down fragmentation into stars followed by bottom-up assembly into a single star cluster (see Figure 4.1). In this work we investigate this physical process, arriving at an explanation for the observed structure of YMCs.

This paper is structured as follows: in Section 3.2 we review observations of the structure of YMCs and compare them to the catalogue of star clusters formed in the Grudić et al. (2018b) (hereafter Grudić et al. (2018b)) suite of star cluster formation simulations. We argue that the profile slopes of YMCs are established early in a cluster's lifetime, and hence must emerge from their hierarchical formation events. In 3.3 we discuss how this happens, arguing analytically that the hierarchical merging of sub-clusters generally creates clusters with shallower power-law slopes through phase-space mixing. In Section 3.4, we test our analytic predictions against N-body simulations of collisionless pairwise star cluster mergers and the collisionless relaxation of a hierarchically-clustered mass distibution. In Section 7.5 we discuss various possible implications and generalizations of our results, and in Section 7.6 we summarize our main results. Appendix 3.A describes our algorithm for identifying bound star cluster membership from N-body particle data in the simulations of Grudić et al. (2018b). In Appendix 3.B we derive, plot, and provide approximations for various functions that are useful in the analysis of a Elson et al. (1987) star cluster model in collisionless equilibrium with arbitrary γ.

3.2 Profile Slopes of YMC Populations

The Elson et al. (1987) surface brightness model commonly used to fit YMCs has the form

$$\mu(R) = \mu_{max} \left(1 + \frac{R^2}{a^2}\right)^{-\gamma/2}, \tag{3.1}$$

where μ_{max} is the central surface brightness, R is the projected distance from the centre, a is a scale radius, and γ gives power law index of the outer brightness profile, hereafter referred to as the "profile slope". The corresponding 3D density profile assuming a constant mass-to-light ratio is

$$\rho\left(r\right) = \rho_0 \left(1 + \frac{r^2}{a^2}\right)^{-\frac{\gamma+1}{2}}, \tag{3.2}$$

where

$$\rho_0 = \frac{M}{a^3} \frac{\Gamma\left(\frac{\gamma+1}{2}\right)}{\pi^{3/2}\Gamma\left(\frac{\gamma-2}{2}\right)} \tag{3.3}$$

is the central density, M the total mass, a the scale radius, and γ the profile slope. This density profile can be recognized as a generalization of the Plummer (1911) model (corresponding to $\gamma = 4$) to arbitrary profile slope.

Several observed YMC populations are rich enough to be able to discern an underlying distribution of profile slopes. In Figure 3.1 we plot the distribution of γ as measured by Ryon et al. (2015) for YMCs in M83, (Ryon et al., 2017) for NGC 628 and NGC 131, and Mackey and Gilmore (2003a,b) for the Magellanic Clouds. These clusters range from $\sim 10^6 - 10^8$ yr in age and $\sim 10^4 - 10^6\,\mathrm{M}_\odot$ in mass. In

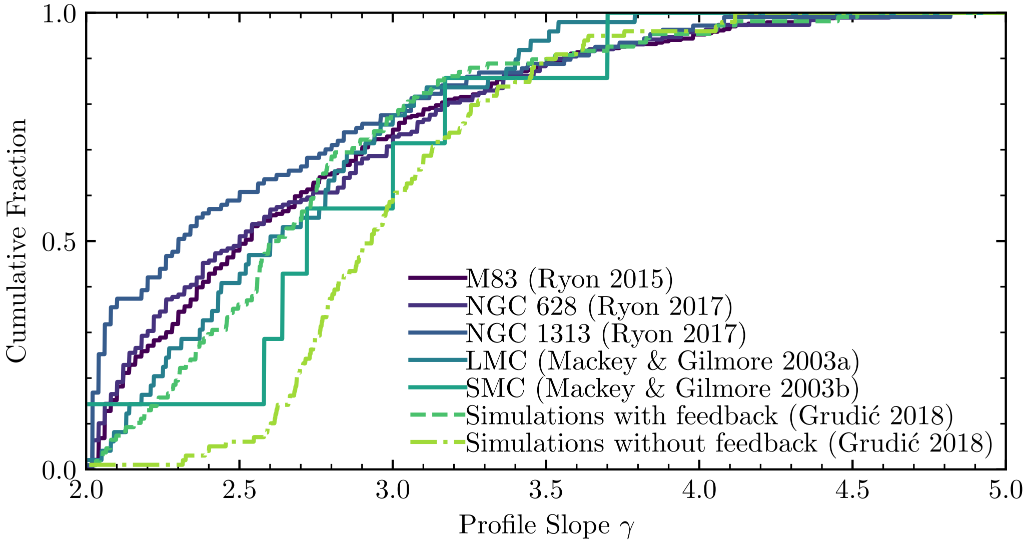

Figure 3.1: *Solid:* Cumulative distribution of star cluster profile slope in the YMC populations of M83 (Ryon et al., 2015), NGC 628, NGC 1313 (Ryon et al., 2017), and the Small and Large Magellanic Clouds (Mackey and Gilmore, 2003b,a). *Dashed:* CDF for the star cluster population extracted from the simulations of Grudić et al. (2018b), with and without stellar feedback. For both real and simulated cluster populations, we include only those clusters that have $\gamma > 2$, as in Ryon et al. (2015). Agreement between the observed populations is quite good, however the simulations without feedback appear to have a deficit of shallow clusters. This may be due to the greater compactness of star clusters produced in absence of feedback, which decreases the cross section for the dynamical interactions that lead to shallower profiles.

all three populations, the median γ is around 2.5. In general, agreement between the observed distributions is quite good, suggesting that a population of Elson et al. (1987)-like clusters with this γ distribution arises from some common underlying physical process.

Power-law density profiles have been proposed to emerge in star clusters in various ways. A power law density profile is the hallmark of gravothermal core collapse, but an inner density profile of $\rho \propto r^{-2.2}$ should generally result (Lynden-Bell and Eggleton, 1980; Cohn, 1980), which is unlike the outer power-law profile $\rho \propto r^{-3.5}$ typically observed in YMCs. von Hoerner (1957) and Hénon (1964) found that a $\rho(r) \propto r^{-4}$ (hence $\gamma = 3$) density profile results when a uniform collisionless sphere with a Maxwellian velocity distribution undergoes violent relaxation toward collisionless equilibrium. More generally, it results from a discontinuity in the distribution of stellar mass in energy space across the boundary between bound and free orbits, as is caused by the escape of stars with positive energy after a violent relaxation event (Aguilar and White, 1986; Jaffe, 1987; Merritt et al., 1989). As such, this may be a good model of the initial relaxation of the smallest bound substructures, or at the resolution limit in star cluster formation simulations that do not resolve individual stars (e.g. Grudić et al., 2018b). However, it does not explain the fact that the majority of star clusters have $\gamma < 3$.

Elson et al. (1987) suggested that the typically observed value $\gamma \sim 2.5$ corresponds to the $\rho \propto r^{-3.5}$ profile found in Spitzer and Shapiro (1972) as a steady-state solution for the outer halo of a star cluster with an inner core, but they proceeded to point out that this structure would have to be established on the two-body relaxation timescale (Spitzer, 1987; Portegies Zwart et al., 2010a):

$$t_{rh} = 4 \times 10^7\,\mathrm{yr} \left(\frac{M}{10^4 M_\odot}\right)^{1/2} \left(\frac{R_{eff}}{1\,\mathrm{pc}}\right)^{3/2}, \tag{3.4}$$

where R_{eff} is the half-mass radius (we have also assumed here that the mean mass of a star is $0.5\,\mathrm{M}_\odot$). Many YMCs are much younger than their respective two-body relaxation timescale, so this picture is not satisfactory.

In general, scenarios requiring more than a few Myr can be ruled out, as good Elson et al. (1987) fits appear to have been achieved for quite young star clusters. Indeed, Ryon et al. (2015) found no correlation of γ with cluster age in M83, suggesting that any secular evolutionary processes occurring within these YMCs typically takes longer than $\sim 100\,\mathrm{Myr}$ to have an appreciable systematic effect on the outer structure. Such young cluster have not existed long enough to experience any significant number of dynamical relaxation times or orbits around the host galaxy during which they may be tidally stripped. Thus, we will explore explanations in which γ is established over a relatively short cluster formation timescale and then evolves only slowly. The most promising of these is the other physical explanation proposed by Elson et al. (1987): dissipationless relaxation following a rapid star formation event. It was noted that simulations of the collisionless relaxation of galaxies from a clumpy, non-equlibrium state (van Albada, 1982; McGlynn, 1984a) could reproduce the range of profile slopes observed in star clusters. We will revisit this scenario in the context of modern star formation theory.

3.2.1 Simulated cluster populations

To guide our analytic exploration, we consider simulations of star cluster formation. The multi-physics N-body MHD simulations of Grudić et al. (2018b) followed the collapse of a parameter survey of unstable gas clouds with a wide range of initial conditions, e.g., $10 - 1000\,\mathrm{pc}$ in diameter and $10^2 - 10^4\,\mathrm{M_\odot\,pc^{-2}}$ in mean surface density. We found that the clouds form stars until a certain critical stellar surface density has been reached, sufficient to disrupt the cloud via stellar feedback, which included the combination of photoionization heating, radiation pressure, shocked stellar winds and supernova explosions, approximated numerically according to the methods developed for the FIRE project in Hopkins et al. (2014, 2018a). In general, we have found that the simulations with greater star formation efficiency place end with a significant fraction of the total stellar mass in gravitationally-bound, virialized star clusters.

These star clusters form via hierarchical assembly[2], as has been found in previous simulations following the collapse and turbulent fragmentation of molecular clouds (Klessen and Burkert, 2000; Bonnell et al., 2003). Many small subclusters first fragment out of the molecular cloud, which them go on to merge with their neighbours, eventually building up a massive star cluster. Unlike N-body simulations of star cluster assembly that have relied upon certain assumptions about the mass-loss history of the system (e.g. Scally and Clarke, 2002; Fellhauer and Kroupa, 2005), the process of star cluster assembly in concert with feedback-induced mass loss is followed self-consistently by including stellar feedback physics [3].

We identify and catalogue those star clusters that are both well-resolved (greater than 10^3 particles) and gravitationally bound via the algorithm described in Appendix 3.A. We have found that the surface density profiles of star clusters formed in the simulations are generally well-fit by the Elson et al. (1987) profile, covering a range of slope parameters. In Figure 3.1 we plot the distribution of slopes extracted from the star cluster populations formed in the simulations of Grudić et al. (2018b), both with and without stellar feedback. We find that the agreement with the observed populations is within the observational scatter for the simulations that include stellar feedback, suggesting that at least the most important physics necessary for realistic star cluster structure are accounted for in the simulations. We find no strong correlation between γ and cluster mass, age[4], or radius, in agreement with Ryon et al. (2015).

---

[2] A visualization of the star cluster formation process can be found at `http://www.tapir.caltech.edu/~mgrudich/gmc.mp4`

[3] Unlike these works, our simulations do not resolve the motions of individual stars, however.

[4] Note however that these simulations follow the isolated formation of star clusters, and do not follow a cluster's subsequent evolution in a galactic environment.

The simulations without stellar feedback also have a significant population of shallow clusters, but there is a deficit of very shallow clusters having $\gamma < 2.5$. Without stellar feedback, the population of bound star clusters tends to be richer: more stars form overall due to the absence of a force that moderates star formation. Also, the clusters are generally denser on average due to the lack of energy input from feedback; they do not undergo dynamical expansion due to mass loss. These dense, compact clusters are much less likely per orbit to merge with their neighbours, whereas mergers are more common in simulations with feedback because the clusters undergo some amount of dynamical expansion, increasing the cross section for merging. This suggests that the formation of shallow clusters has something to do with the dynamics of the cluster assembly process.

The above simulations and observations lead us to several hypotheses about the origin of YMC mass profiles:

1. The distribution of profile slopes does not differ greatly between different observed or simulated cluster-forming environments, if one accounts for stellar feedback in the simulations.
2. Interactions with the galactic environment are not necessary to reproduce the observed γ distribution, as the simulations do not include these physics.
3. Few-body interactions must play a secondary role in determining the bulk structure of the cluster, as even if the simulations were capable of resolving these effects (which they are not) they do not run for any significant fraction of a half-mass relaxation time. Structural details on the scale of individual stars, such as the stellar mass function, can be neglected in favour of a mean-field, IMF-averaged approximation over timescales much less than the two-body relaxation timescale.

It is therefore plausible that star clusters generally form with Elson et al. (1987)-like surface brightness profiles, directly from their initial relaxation from their hierarchically-clustered state.

3.3 Shallow Clusters Through Merging Substructure

We will now develop physical intuition for how hierarchical star formation leads to the formation of star clusters with shallow power-law profiles. Consider first the initial conditions of the problem: a gas cloud collapses and undergoes star formation.

Observations of the M83 YMC population suggest that the majority of the YMCs evacuate their natal gas as soon as $2-3\,\mathrm{Myr}$ (Hollyhead et al., 2015), at most a few orbital times. This is also the case in the Grudić et al. (2018b) simulations. This process of rapid star formation still has some finite duration, but we may consider an idealized model wherein the stars are formed in place instantaneously, and the system then relaxes as a dissipationless N-body system.

This initial arrangement of stars resulting from the fragmentation of the cloud will be hierarchically clustered (e.g. Bonnell et al. 2003; Gouliermis et al. 2015; Guszejnov et al. 2017; Grasha et al. 2017). This is because fragmentation will leave behind substructures of all scales from the size of the parent cloud to the scale of protostellar disks (Hopkins, 2013). The proportion of the original gas cloud that is actually converted into stars will be limited by the dynamical ejection of gas and the eventual blowout due to stellar feedback (e.g. Murray et al. 2010; Grudić et al. 2018b), but let us assume that the cloud has high ($> 50\%$) star formation efficiency, which generally leads to the formation of a bound star cluster (Hills, 1980; Elmegreen and Efremov, 1997). Subclusters that fragmented from the same self-gravitating parent will then be gravitationally bound to each other on average, so once they have turned into stars they will eventually merge together under dynamical friction. The result will be a sequence of hierarchical merging: subclusters will merge with their immediate neighbours that fragmented from the same parent, then the more massive cluster will merge with its neighbour, etc (see Figure 4.1). The smallest and densest structures will merge first because their respective dynamical times are the shortest, as their orbital time will be essentially the freefall time at the mean density of their parent structure, $t_{ff} \propto \rho^{\frac{-1}{2}}$.

This process is certainly complex, but the success of the Grudić et al. (2018b) simulations in producing star clusters with the correct structure out of softened, equal-mass star particles encourages us to consider a collisionless kinetic treatment of the problem. We approximate the dynamics as those of an ensemble of stars with phase-space distribution function $f\left(\boldsymbol{x}, \boldsymbol{v}, t\right)$, which evolves according to the collisionless Boltzmann equation:

$$\frac{\mathrm{D}f}{\mathrm{D}t} = 0, \tag{3.5}$$

where $\frac{\mathrm{D}}{\mathrm{D}t}$ denotes the Lagrangian time derivative along the flow of the system determined by the Hamiltonian with the usual kinetic and gravitational terms. In other words, the phase-space density f is conserved along trajectories of the system.

Formally, this does link the initial state of a hierarchical stellar distribution to the final state of a monolithic star cluster. However, it cannot be applied directly: while the fine-grained distribution function f is indeed conserved in a dissipationless relaxation process, the measurable quantity in any observation or N-body simulation is the coarse-grained distribution $\bar{f}$:

$$\bar{f}\left(\boldsymbol{x}, \boldsymbol{v}, t\right) = f\left(\boldsymbol{x}, \boldsymbol{v}, t\right) * K\left(\frac{\boldsymbol{x}}{\sigma_x}, \frac{\boldsymbol{v}}{\sigma_v}\right), \tag{3.6}$$

where K is some 6-dimensional smoothing kernel, σ_x and σ_v are the practical resolution limits of position and velocity measurements, and $*$ represents phase-space convolution. In observations and N-body simulations, the finite masses of the bodies impose a mass scale that ultimately determines the practical limit of phase-space resolution: the support of the smoothing kernel must contain a certain number of bodies to be able to convert between the full discrete description and the continuum approximation in any meaningful way.

The collisionless Boltzmann equation does not require that $\bar{f}$ be conserved along phase-space trajectories. To the contrary, in a system relaxing violently toward equilibrium, phase-space elements of varying f tend to be stretched out and tangled together until eventually it is impossible to recover the original value of f at any resolution at which the continuum limit actually applies (Lynden-Bell, 1967; Dehnen, 2005). The result is a "dilution" of mass in phase-space, wherein $\bar{f}$ will generally decrease. This process is clearly essential in the relaxation of a hierarchically-clustered mass distribution into a monolithic cluster, as the the initial clumpy state contains more information than the smooth final state, so this information must be effectively lost as mixing entropy. We expect that in collisionless hierarchical cluster assembly dominated by typically equal-mass mergers, violent relaxation should be efficient at driving this phase-space dilution.

The phase-space mixing theorem derived in Dehnen (2005) makes it possible to constrain the evolution of the phase-space distribution in hierarchical merging. Dehnen found that when two collisionless self-gravitating systems merge, the following function of the coarse-grained phase-space density must strictly decrease for all f:

$$D\left(f\right) = \int_{\bar{f}(\mathbf{x},\mathbf{v})>f} \left(\bar{f}\left(\mathbf{x}, \mathbf{v}\right) - f\right) \,\mathrm{d}^3\mathrm{x}\,\mathrm{d}^3\mathrm{v}, \tag{3.7}$$

which is known as the *excess mass function*. This mixing theorem was used to explain why the inner density profile of a collisionless merger product must have the same slope as the steeper of the progenitors (e.g. Boylan-Kolchin et al., 2005;

Kazantzidis et al., 2006). It thus immediately follows that two EFF-like systems must merge into a system with a flat inner density profile [5].

We can also use the mixing theorem to constrain the outer density profile of the merger. For this purpose, it is more convenient to consider the *reciprocal* excess mass function $M - D(f)$, where M is the total mass of the system; this quantity must strictly increase during mixing. Dehnen showed that for a system with an 3D outer density profile $\rho \propto r^{-\gamma-1}$,

$$M - D(f) \propto f^{\frac{2\gamma-4}{2\gamma-1}}. \tag{3.8}$$

For values of γ giving finite mass ($\gamma > 2$), the exponent $f^{\frac{2\gamma-4}{2\gamma-1}}$ increases monotonically from 0 at $\gamma = 2$ to 1 as $\gamma \rightarrow \infty$. Hence $M - D(f)$ is a steeper function of f for star clusters with steeper outer profiles. Therefore, when two collisionless systems merge, the requirement that the reciprocal mass function for the whole system must increase for all f implies that the function must be at least as shallow as the shallower of the two systems in isolation. Consequently, *the outer density profile of merger product of two collisionless systems can be no steeper than the shallower of the two progenitors*. We are thus able explain why hierarchical merging does not produce steeper density profiles than existed originally, however it remains to explain why it might drive the system toward shallower slopes.

3.3.1 Similarity solution

A shallow outer density profile profile can be associated with mass being spread over many orders of magnitude in phase space density. In particular, $\mathrm{d}M/\mathrm{d}\log\bar{f} \sim \epsilon$, where ϵ is some small fraction of the total mass of the system. More generally, if we consider any parameter describing a “scale" that approaches 0 far away from the system, be it spatial scale, density, phase-space density, or velocity dispersion, it also holds that

$$\frac{\mathrm{d}M}{\log x} \sim const. \tag{3.9}$$

for shallow clusters, where x is the chosen scale parameter. In Guszejnov et al. (2018a), we argue that such a broad distribution of mass across different scales is a general feature of systems formed under the action of gravity and supersonic turbulence, whose equations can be cast in a scale-free form under the physical conditions relevant to star formation. Therefore, $\gamma \sim 2$ is the expected result of

---

[5] In fact, this follows intuitively from the requirement that the maximum phase-space density cannot increase. Systems in virial equilibrium with flat inner profiles have a maximum phase-space density, while systems with power-law inner profiles do not.

hierarchical cluster formation in the limit where the hierarchy of substructures covers a large range of scales. In both the fragmentation that produces the hierarchical structure, and the merging that effaces it, the physics can prefer no particular scale, and hence leave a small fraction of the total mass behind at each scale, hence the flat distribution of mass in $\log f$.

This argument predicts $\gamma = 2$ in the limit of cluster formation from a deep hierarchical merger tree; in effect, this is the fixed point for the outer density profile in hierarchical merging. However, clusters with $\gamma > 2$ remain to be explained. Furthermore, we know that some of the simulated star clusters plotted in Figure 3.1 do not have particularly extended merger histories; inspection of their merger histories of the least well-resolved clusters considered generally reveals no more than $2 - 3$ major mergers. There is clearly some mechanism that allows clusters to reach shallow slopes with only limited merger histories, which must arise from some change in γ in the pairwise merging of star clusters.

3.3.2 Shallower density profiles through pairwise merging

Let us idealize hierarchical cluster formation as a sequence of pairwise cluster mergers. By symmetry, such a merger would most typically involve two clusters of similar size, mass and shape, so we will determine the outcome of a merger of identical star clusters described by EFF profiles with $M = a = 1$ and a particular value of γ. Since the two clusters fragmented out of the same parent under gravitational instability, the two clusters can be expected to be gravitationally bound to each other; for simplicity we will consider the case in which they collide on a marginally-bound parabolic orbit with pericentre smaller enough for the clusters to disrupt each other in one or two passes. In a marginally-bound, collisionless merger, mass and energy are approximately conserved (White, 1979), so we assume mass and energy are conserved for simplicity. Furthermore, we assume that the merger product is another star cluster with an Elson et al. (1987) profile with parameters $M' = 2M$, a' and γ'

If the merger is homologous ($\gamma' = \gamma$), mass and energy conservation imply that $M' = 2$ and $a' = 2$. Then the coarse-grained phase-space density $\bar{f} \propto G^{-3/2} M^{-1/2} a^{-3/2}$ in the neighbourhood of an average star is rescaled by $\frac{1}{4}$, which satisfies the constraint that $\bar{f}$ must decrease in the evolution of the system. This "uniform mixing" approximation has proven to be quite predictive in the case of dissipationless elliptical galaxy mergers (Shen et al., 2003; Cole et al., 2000; Boylan-Kolchin et al.,

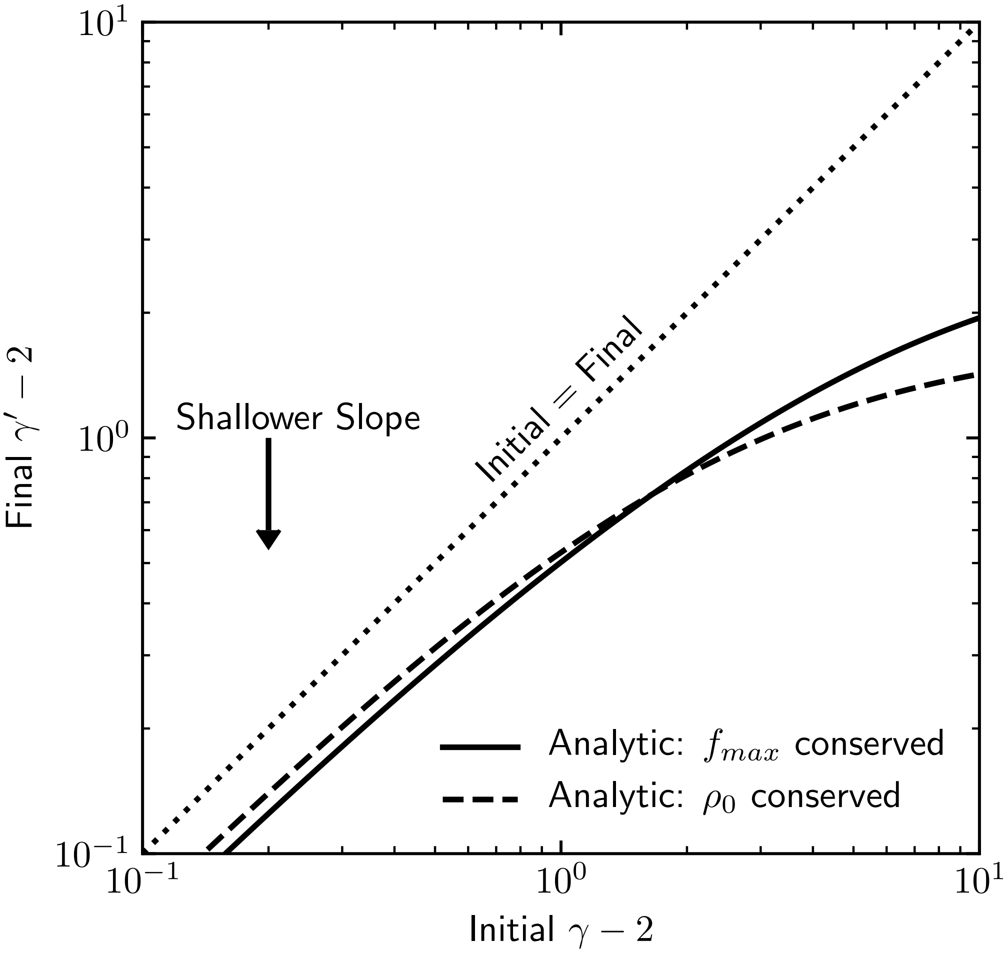

Figure 3.1: Final surface brightness slope γ' of the star cluster produced in a merger as a function of the initial γ of two merging clusters with equal γ, mass, and size, assuming that the relaxed merger has an Elson et al. (1987) profile. We plot the analytic predictions assuming that the maximum phase-space density f_{max} (solid) and the maximum density ρ_0 (dashed) are conserved; the two models predict similar results: merging of clusters of equal size and mass always produces a shallower profile than existed before, driving star clusters toward $\gamma = 2$ regardless of their initial structure. We also plot the results of the simulated mergers described Section 3.4.1, which do not agree exactly with either model but predict the same overall trend of the formation of shallower profiles.

2005; Hopkins et al., 2009). However, the physical nature of phase-space mixing and violent relaxation in elliptical galaxy mergers may well be qualitatively different from star cluster mergers: the cusps of elliptical galaxies are scale-free, so the phase-space dilution factor tends to be roughly constant throughout the system, leading to uniform mixing. Meanwhile star clusters with flat inner profiles do have a characteristic scale imprinted by the maximum density or maximum phase-space density; some memory of the maximum density should persist in the merger.

We make the ansatz, to be justified in §3.4.1, that the maximum phase-space density persists throughout the merger, as phase mixing becomes less efficient as $f \longrightarrow f_{max}$, where f_{max} is the maximum phase-space density found in either cluster. If so, then γ cannot remain the same while preserving mass and energy, as if it did then f_{max} would take $1/4$ its original value. Assuming that the merger product is an Elson et al. (1987) cluster, and conservation of mass, energy and f_{max}, we arrive at the following equation for the final cluster's slope γ':

$$\mathcal{F}(\gamma') = 2^{5/2}\frac{\mathcal{F}(\gamma)}{\mathcal{W}(\gamma)}, \tag{3.10}$$

where $\mathcal{W}(\gamma)$ and $\mathcal{F}(\gamma)$ are the dimensionless functions that contain the γ dependence of a cluster's energy and maximum phase-space density (see Equations 3.24 and 3.27 for approximate forms and Figures 3.B.2 and 3.B.4 for plots of these functions). This equation can be solved for γ' numerically. In the case of merging equal mass and size Plummer (1911) models ($\gamma = 4$), the solution is $\gamma' = 2.83$: the final cluster is shallower than its progenitors.

We also consider the ansatz that the central density ρ_0 is conserved. In practice, the predictions of the two ansätze are similar (see Figure 3.1). In general, the models predict that $2 < \gamma' < \gamma$, so a sequence of mergers will drive γ toward a fixed point of 2. Intuitively, mass and energy conservation require the final mass and effective radius to roughly double. This must be achieved without changing the central (phase-space) density significantly, so a shallower slope is required, because a shallower cluster has greater central (phase-space) density for a given half-mass radius.

By the arguments above, even very steep ($\gamma \sim 10$) clusters of similar size and mass will merge into a cluster with $\gamma \sim 4$, so only $1 - 2$ major mergers are needed to get a cluster into the interval between 2 and 3 in which most YMCs lie (Figure 3.1). As we have established that γ must be established quite early in a cluster's lifetime, this merger history comes from the star cluster's hierarchical assembly process.

Run	M	R_{eff}	γ	M'	R'_{eff}	γ'	Predicted γ'	Ellipticity	$\hat{\chi}^2_{fit}$
Merger 1	1.00	1.30	4.00	1.90	2.24	2.69 ± 0.06	2.83	0.25	78.04
Merger 2	1.90	2.24	2.69	3.57	4.22	2.48 ± 0.03	2.37	0.14	212.24
Merger 3	3.57	4.22	2.48	6.53	7.65	2.21 ± 0.01	2.27	0.13	142.20

Table 3.1: Parameters and results of the sequence of simulated mergers of identical EFF-like star clusters: Initial cluster masses M, initial half-mass radii R_{eff}, initial profile slope γ, final cluster mass M', final half-mass radius R'_{eff}, final fitted profile slope γ', analytically-predicted γ' according to Equation 3.10, cluster ellipticity, and the reduced χ^2 for the fit of the final surface density profile to the EFF model. We give $\hat{\chi}^2_{fit}$ for the worst of three fits of the final cluster's surface density profile as projected in three orthogonal planes. The quoted uncertainty in γ' includes the variation between the three different fit results.

3.4 N-body experiments

In the previous section, two claims were made that require verification: that the maximum phase-space density is conserved in a collisionless star cluster merger, and that the sequence of mergers necessary to produce an Elson et al. (1987)-like cluster with $\gamma \sim 2 - 3$ can arise from the relaxation of a hierarchically-clustered stellar distribution. Now we shall verify these claims with N-body numerical experiments, first of a sequence of pairwise mergers and then of a hierarchically-clustered configuration. We use the multi-physics code GIZMO (Hopkins, 2015) in a pure N-body configuration. Gravity is solved with a hierarchical BH-tree algorithm derivative of GADGET-3 (Springel, 2005). We do not simulate the motion of individual stars, but rather approximate the solution of the collisionless Vlasov-Poisson equation with a Monte Carlo sampling of the distribution function with equal-mass, softened particles. Throughout, we adopt units such that $G = 1$.

3.4.1 Pairwise cluster mergers

We first simulate the merger of two Plummer model clusters ($\gamma = 4$) to test the ansätze that their maximum phase-space density should be conserved and that the end product should be well-fit by an Elson et al. (1987) profile with γ given by the solution of Equation 3.10. Once these clusters have merged and the cluster has relaxed to a steady state, we extract this cluster, copy it, and set it up to merge with its copy. To avoid building up a spurious anisotropy along the axis of approach, the orientations of the clusters are randomized between mergers. We repeat this for a total of three simulated mergers. The Plummer-equivalent gravitational softening length is fixed at 0.1 in all runs.

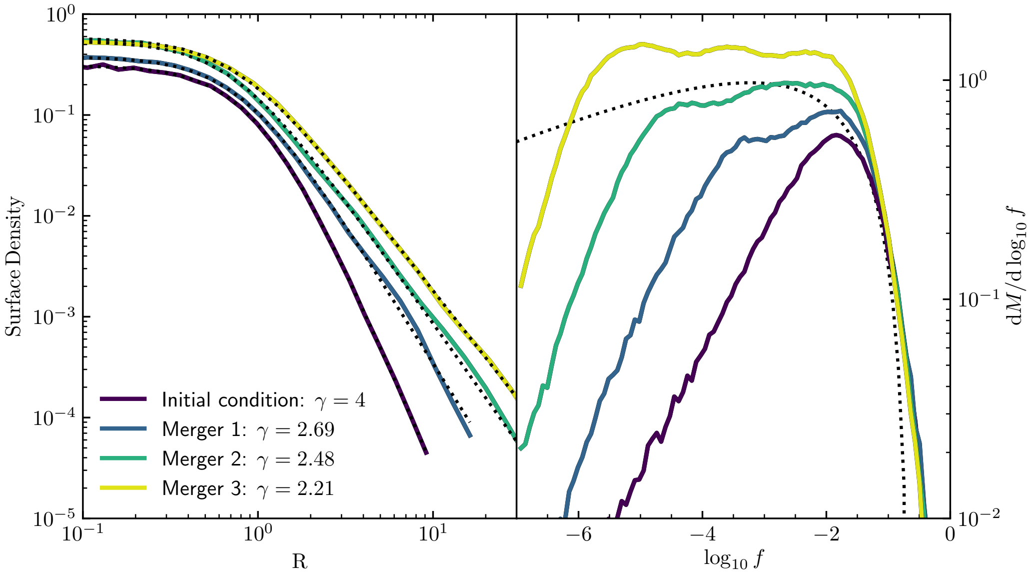

Figure 3.1: Results of the successive pairwise merging of star clusters, starting with a pair of identical Plummer models. *Left*: Cluster surface density profiles for the initial Plummer model and the three successive merger products. The mergers generally do shallow the surface density profile toward $\gamma = 2$. Fits to the EFF model are shown as dotted lines. *Right*: Distribution of mass in log phase-space density, $\frac{\mathrm{d}M}{\mathrm{d}\log_{10} f}$, for the simulated clusters. The mergers generally conserve the maximum phase-space density and distribute the mass across more orders of magnitude in f, gradually building up the flat distribution associated with shallower surface density profiles ($\gamma \sim 2$). The dotted line shows what $\frac{\mathrm{d}M}{\mathrm{d}\log_{10} f}$ would be for Merger 3 if the phase-space distribution function were that of an isotropic Elson et al. (1987) model with fitted parameters fitted from the surface density profile.

Initial conditions

We construct two Plummer cluster models in collisionless equilibrium, randomly sampling the positions of 125000 particles per cluster according to the 3D EFF distribution (Equation 3.2) with $M = a = 1$ and $\gamma = 4$. The velocity distribution is assumed to be isotropic and is randomly sampled according to the phase-space distribution function of Equation 3.26, which is exact for the Plummer model. We find that a single such cluster evolved in isolation for 10^4 half-mass dynamical times has no significant evolution from the Plummer model, so we expect that the particle number is sufficient so that collisional effects play no major role in the merger, which happens after ~ 300 dynamical times. We place the cluster centres 100 length units from each other, with the relative velocity adjusted for a parabolic encounter with a pericentric radius of 1.6, which is just close enough that the clusters merge in a single pass. We set up the two subsequent mergers in the same way, but we scale the pericentric radius to the half-mass radius of the cluster.

Results

In all simulations, the clusters approach and merge in a single pass after $O(10^2)$ time units, and by the end of the simulation at $t = 1000$ the new cluster has approached a new collisionless equilibrium. A fraction of the particles are ejected from the system, so the assumption that the final cluster will contain all initial mass and energy does not hold exactly, but the fraction is always $< 10\%$. Free particles are deleted from subsequent merger simulations.

Data on the formed clusters are presented in Table 3.1. We perform Elson et al. (1987) fits on the final surface density profiles as projected in three orthogonal different planes. The particle positions are binned into annuli around the centre of the cluster, and we fit the masses within each bin to the EFF model via χ^2 minimization. Since we interpret the particle states as a Monte Carlo sampling of the phase-space distribution, the uncertainty of the mass m in each bin is taken to be the Poisson sampling error $\frac{m}{\sqrt{N}}$, where N is the number of particles in the bin (valid for sufficiently large N). We find that the EFF model always fits the surface density profiles reasonably well (Figure 3.1, panel 1), but not exactly; the reduced χ^2 of the fits are on the order of 100. The clusters are only weakly triaxial, with ellipticity 0.25 at most, so the fit results from different projection planes do not vary greatly. Mergers 2 and 3 both reduce the ellipticity initially created by Merger 1.

We find that the successive mergers do shallow the surface density profiles (Figure 3.1 clusters with $\gamma = 4$ merge into $\gamma = 2.69$, then 2.69 into 2.48, and then 2.48 into 2.21. This is not in exact agreement with the analytic predictions of Section 3.3.2 assuming either conservation of density or phase-space density, however the analytic and numerical predictions of γ agree to within 0.1, and agree upon the general trend of a decrease toward $\gamma = 2$. Perfect agreement with the model is not expected because of the many approximations we have invoked. In particular, it is likely that the obtained slope of 2.69 is shallower than the predicted 2.8 due to the fact that the merger orbit had non-zero angular momentum, which must be redistributed in the final configuration. This would give a mass distribution that is more extended (ie. with a shallower slope) than a cluster of equal energy with no net angular momentum.

The last assumption of Section 3.3.2 to be verified is conservation of the maximum phase-space density. We estimate the coarse-grained phase-space density in the neighbourhood of particle i in the most straightforward way, generally known as the pseudo-phase-space density (Taylor and Navarro, 2001):

$$\bar{f}_i \propto \frac{\rho_i}{\sigma_i^3}, \tag{3.11}$$

where $\rho_i = \frac{m_i}{V_i}$ is the density of the particle estimated from its effective volume (Hopkins, 2015), and σ_i is the local velocity dispersion computed from the velocities of the particle's 32 nearest neighbours. [6] In Figure 3.1, panel 2 we plot the distribution $\frac{\mathrm{d}M}{\mathrm{d}\log f}$ and find that indeed, the maximum phase space density (corresponding to the upper cutoff of the distribution) is conserved from the initial Plummer model to the final merger. Thus, the deviation of γ from analytic predictions is due to the deviation of the phase-space distribution of the cluster from from that of an isotropic EFF model. This is evident in Figure 3.1: despite the good apparent fits of the surface density of Merger 3 to the EFF model, its distribution of phase space densities looks quite different from that of an isotropic EFF model in collisionless equilibrium (shown as the dotted line). Rather than having the predicted asymptotic $\propto f^{\frac{2\gamma-4}{2\gamma-1}}$ dependence for small f, the distribution is flat over a finite interval, then falls off steeply above and below that interval. The phase-space density at the lower cutoff corresponds to the mean phase-space density of particles near 100 distance units from the cluster centre, which is the initial separation between the clusters in the merger setup and hence where we expect any scale-free behaviour to break down.

From these results we may conclude that the assumptions of Section 3.3.2 were largely valid: the collisionless merger of two Elson et al. (1987) clusters fits reasonably well to another Elson et al. (1987) cluster, at least in its surface density profile. The profile slope γ is close to that analytically determined by conservation of mass, energy and f_{max}; conservation of mass and energy hold approximately, while conservation of f_{max} holds exactly, to the extent that can be tested by our noisy estimate of the phase-space density.

3.4.2 Relaxation of a Hierarchically-Clustered Mass Distribution

Now we wish to examine whether a hierarchically-clustered distribution of stars with realistic spatial and kinematic scaling relations can form an Elson et al. (1987)-like star cluster as it relaxes toward collisionless equilibrium. We arrange particles in

---

[6] Much more accurate estimates of $\bar{f}$ from N-body data exist (Arad et al., 2004; Ascasibar and Binney, 2005), but the pseudo-phase-space density is suitable for the purposes of this limited analysis.

such a configuration and simulate their dynamical evolution from the hierarchically-clustered state.

Initial Conditions

We initialize 64^3 particles in a hierarchically-fragmented configuration by recursively bifurcating a population of subclusters, starting with a single cluster of unit mass centred at the origin. In each bifurcation, the mass ratio q of the two child fragments is sampled from the log-normal distribution [7] with $\langle q \rangle = 1$ and $\sigma_{\log q} = 1$. The masses of the fragments are then

$$\begin{aligned} m_1 &= \frac{q}{1+q} m_{parent}, \\ m_2 &= \frac{1}{1+q} m_{parent}. \end{aligned} \tag{3.12}$$

The relative separation of the fragments $\Delta \boldsymbol{x}$ is sampled from a 3D normal distribution with variance σ_x^2. We scale σ_x^2 to achieve the desired two-point spatial correlation function $\xi(r) \propto r^{-2}$, where

$$1 + \xi(r) = \frac{\langle n(r) \rangle}{\langle n \rangle}, \tag{3.13}$$

is the ratio between the average number density of particles in a spherical shell of radius r around a star to the mean stellar number density of the system. $\xi(r)$ quantifies the tightness of the hierarchical clustering at a given scale r. The form $\xi(r) \propto r^{-2}$ matches observations of young star clusters on scales greater than 0.01 pc, and is predicted by numerical simulations and general considerations of the scale-free interplay of gravity and supersonic turbulence (Guszejnov et al., 2017, 2018a). This scaling is achieved by the "isothermal" scaling $\sigma_x \propto m_{parent}$, so σ_x is thus determined down to a constant scale factor.

With the separation $\Delta \boldsymbol{x}$ thus sampled, the child clusters are displaced so as to preserve the centre of mass:

$$\begin{aligned} \boldsymbol{x}_1 &= \boldsymbol{x}_{parent} + \frac{1}{1+q} \Delta \boldsymbol{x}, \\ \boldsymbol{x}_2 &= \boldsymbol{x}_{parent} - \frac{q}{1+q} \Delta \boldsymbol{x}. \end{aligned} \tag{3.14}$$

Lastly, the relative velocity $\Delta \boldsymbol{v}$ of the child clusters is sampled from a 3D normal distribution scaled to emulate the $v^2 \propto R$ kinematic relation of that is generally

---

[7] The choice of a lognormal mass ratio distribution was arbitrary; we have also run simulations where q is always 1, and have found no major difference in our results.

observed in GMCs (Larson, 1981; Solomon et al., 1987; Bolatto et al., 2008) and is robustly reproduced in simulations of isothermal, self-gravitating turbulent clouds (Kritsuk et al., 2013), the idea being that protostars will inherit the kinematics of the ISM from which they formed. This scaling relation is achieved by setting $\sigma_v^2 \propto M^{4/3}$. Then, to conserve momentum,

$$\begin{aligned} \boldsymbol{v}_1 &= \boldsymbol{v}_{parent} + \frac{1}{1+q}\Delta\boldsymbol{v}, \\ \boldsymbol{v}_2 &= \boldsymbol{v}_{parent} - \frac{q}{1+q}\Delta\boldsymbol{v}. \end{aligned} \tag{3.15}$$

The bifurcation iteration described by equations 3.12 to 3.15 is applied recursively until the mass of a single particle is reached, so structures exist on all mass scales down to the mass of individual particles. However, recall that these N-body simulations of equal-mass, softened particles are to be interpreted as a Monte Carlo approximation of the solution of the collisionless Boltzmann equation. For this to be valid, any resolved structures should be sampled by a certain number of particles, as biases in the dynamics due to the discreteness of the particles are not part of the desired solution. For this reason, once the clustered configuration has been generated, we smooth the initial conditions by displacing each particle by a random normally-distributed offset with $\sigma = 10^{-3}$; this ensures that structures in the initial conditions are sampled by at least ~ 100 particles. We also set the Plummer-equivalent gravitational softening length to 10^{-3} for consistency (e.g. Barnes, 2012).

This procedure generates a clustered particle distribution with the desired spatial and velocity correlations, as shown in Figure 3.2. The gravitational binding energy W for this distribution is computed with $G = 1$ and the system is rescaled by a scale factor $\frac{1}{W}$ so that it has unit binding energy. The velocities are scaled to have a total kinetic energy of 0.5, so that the system as a whole has a virial parameter $\alpha = \frac{T}{W} = 0.5$.

Results

We generate three different sets of initial conditions and evolve each system for 35 time units; the unit of time is on the order of the dynamical timescale of the system[8]. Within the first few time units, sub-clusters undergo hierarchical assembly into a population of clusters that fly apart from each other and relax into a steady state.

---

[8] A visualization of of Run 2 can be found at `http://www.tapir.caltech.edu/~mgrudich/hierarchical.mp4`

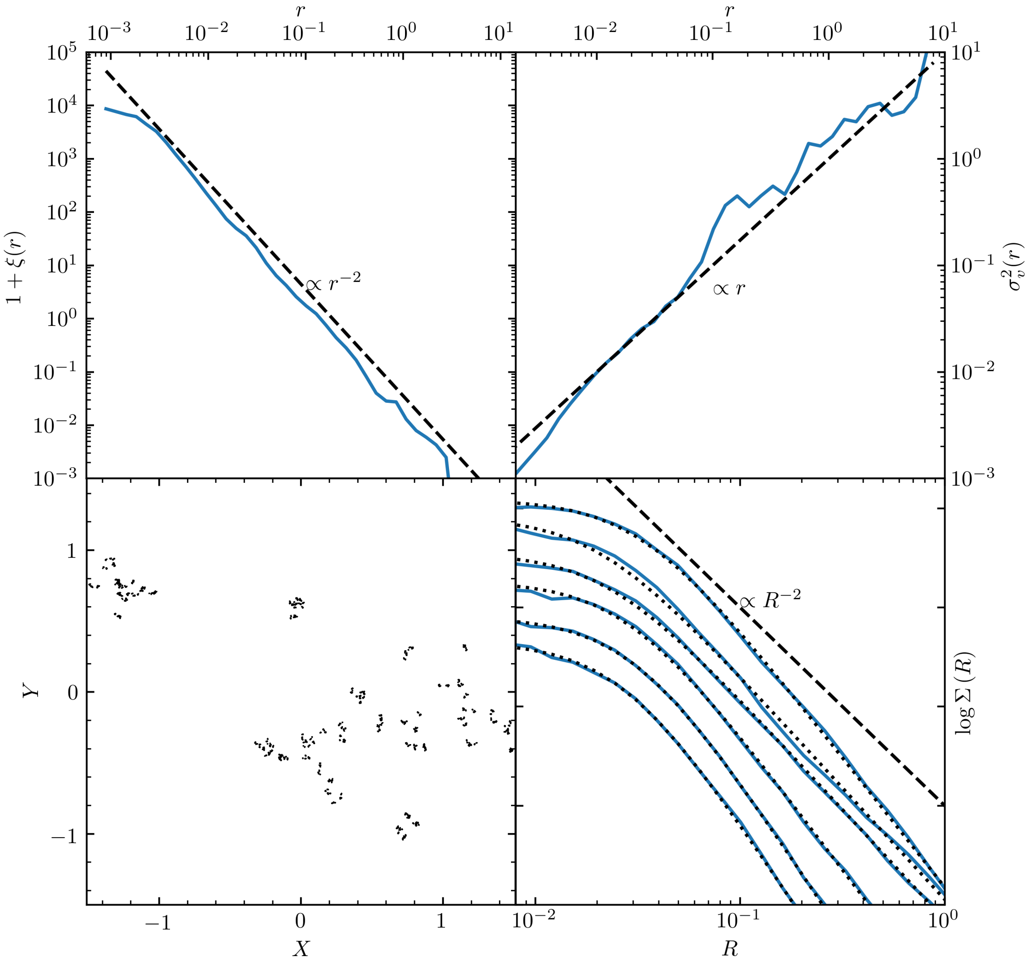

Figure 3.2: Initial conditions and final results of a simulation of hierarchical cluster formation, as described in Section 3.4.2. *Top left:* Initial 3D correlation function of particle positions, which is $\propto r^{-2}$ above the resolution limit . *Top right:* Initial size-velocity dispersion relation. $\sigma_v^2(r)$ is the average velocity dispersion of particles within distance r of any given point, and is constructed to be $\propto r$ to agree the observed relation of GMC kinematics (Bolatto et al., 2008). *Lower left:* Initial hierarchically-clustered distribution of 64^3 equal-mass particles, constructed by the stochastic fragmentation iteration described in Section 3.4.2. *Lower right:* Surface density profiles of the best-resolved clusters formed by the end of the simulation. The profiles are offset from each other on the plot for visibility. They are well-described by the Elson et al. (1987) model (Equation 3.1).

Run	Mass	R_{eff}	γ	Ellipticity	$\hat{\chi}^2_{fit}$
1	0.204	0.108	2.62 ± 0.02	0.13	8.44
1	0.202	0.166	2.26 ± 0.03	0.17	39.87
1	0.195	0.192	2.23 ± 0.02	0.12	13.80
1	0.115	0.074	2.75 ± 0.03	0.15	4.46
1	0.110	0.068	3.16 ± 0.02	0.22	1.12
1	0.054	0.052	3.11 ± 0.04	0.16	1.71
1	0.022	0.038	3.15 ± 0.05	0.12	1.29
1	0.019	0.035	3.19 ± 0.06	0.15	1.31
2	0.382	0.249	2.28 ± 0.03	0.12	104.24
2	0.364	0.171	2.35 ± 0.04	0.17	105.77
2	0.174	0.089	2.89 ± 0.03	0.10	1.78
3	0.147	0.099	2.58 ± 0.02	0.13	4.36
3	0.139	0.083	2.75 ± 0.03	0.21	2.49
3	0.114	0.078	2.62 ± 0.03	0.20	9.19
3	0.106	0.068	2.78 ± 0.03	0.15	6.39
3	0.092	0.067	2.86 ± 0.03	0.26	2.96
3	0.092	0.062	3.22 ± 0.07	0.12	1.54
3	0.053	0.050	3.22 ± 0.04	0.33	1.33
3	0.048	0.051	3.17 ± 0.07	0.25	2.05
3	0.045	0.046	3.48 ± 0.05	0.20	1.28
3	0.043	0.056	2.76 ± 0.03	0.20	2.60
3	0.031	0.040	3.40 ± 0.06	0.13	1.63
3	0.025	0.038	3.32 ± 0.05	0.22	1.10

Table 3.2: Parameters of the clusters produced in the hierarchical relaxation simulations of Section 3.4.2: Masse, half-mass radius R_{eff}, fitted profile slope γ, ellipticity, and the reduced χ^2 of the surface density fit to obtain γ. Uncertainties in γ include the variation in the parameters from fitting the surface density profiles as projected in three different orthogonal planes.

The rate-limiting step for the formation of a given cluster is merging timescale of its last two remaining sub-clusters, which is on the order of their mutual orbital period, at most on the order of several time units.

We identify bound clusters at the end of the simulation via the algorithm described in Appendix 3.A. In general, roughly 80% of particles are found to be gravitationally bound to a cluster, the rest having been dynamically ejected from their original hosts in the violent merging process. The surface density profiles of the clusters are generally well-fit by the Elson et al. (1987) model, and we present the fitted γ values in Table 3.2. The uncertainties quoted in Table 3.2 include the variation in the γ obtained when projecting the surface density profile in three different orthogonal planes. This variation is generally small compared to the magnitude of γ, as the clusters are only weakly triaxial: their histories of statistically-isotropic mergers tend to average away preferred orientations. This is also reflected in the clusters' modest ellipticities, which we also tabulate in Table 3.2. The ellipticities lie in a similar range to those observed in the LMC cluster population (Frenk and Fall, 1982; Kontizas et al., 1989).

It is readily seen from Table 3.2 that the most massive clusters tend to have γ closer to 2. The initial conditions were smoothed over an effective fixed mass scale M_0, so a hierarchically-assembled cluster of mass M would have to have experienced an effective number of mergers $N = \log_2 \frac{M}{M_0}$, so in these simulations the more massive clusters have experienced more mergers, each of which creates a shallower profile. This anticorrelation between mass and γ should not be interpreted as a prediction of the statistics of actual YMC populations, because observed YMCs are the product of many statistically-independent star formation events involving physics with only weak dependence on the mass scale (e.g. Fall et al. 2010; Guszejnov et al. 2018a). In contrast, we have simulated only three different events, all at a single mass scale.

In summary, these numerical experiments demonstrate that an EFF profile can emerge from the relaxation of a generic, hierarchically-clustered mass distribution with power-law spatial and kinematic scaling relations consistent with observations of GMCs and young star clusters.

3.5 Discussion

3.5.1 Smooth vs. clumpy initial conditions for globular cluster formation

Goodwin (1998) concluded that the assembly of a YMC from an initially clumpy and asymmetric configuration was unlikely, for two main reasons. First, it was found that if the level of initial clumpiness is too great, some subclusters can survive for many orbits around the primary assembled cluster. However, Goodwin (1998) simulated the evolution of a collection of clumps with comparable mass and uncorrelated initial positions, not accounting for correlations between subcluster positions imprinted by the structure formation process. This problem is averted by a hierarchical configuration, as neighbouring subclusters are all but guaranteed to merge. In the numerical experiments of Section 3.4.2, no persistent satellite clumps were found; the clusters that form tend to do so within a few dynamical times and disperse from each other, and within those clusters substructure is erased efficiently.

The other problem with clumpy initial conditions noted by Goodwin (1998) was that the ellipticity of the final cluster is sensitive to the flattening of the initial conditions, and essentially any amount of initial flattening produced clusters with ellipticities much larger than have been observed,in the range $[0, 0.28]$ (Kontizas et al., 1989). This problem is averted by the specific hierarchical picture we have considered in this work, wherein mergers at different levels in the hierarchy are uncorrelated in orientation due to an assumed statistical isotropy. From these experiments we find no cluster with ellipticity greatly exceeding the maximum observed. However, it should be noted that the assumption of statistical isotropy would not necessarily hold if, for example, the initial subclusters consisted of "beads" along a filament or a galactic spur. Indeed, it is quite possible that hierarchical star formation does impose large-scale statistical anisotropies. As such, an interesting direction for future work on this problem would be to investigate the effect of physically- or observationally-motivated anisotropy on hierarchical star cluster assembly. One avenue would be a straightforward modification to our fragmentation model (§3.4.2) wherein the directions of the separations Δx and relative velocities Δv from one level to another are given a non-zero correlation.

Overall, we find the structure of YMCs to be largely compatible with the paradigm of hierarchical cluster formation that we have considered here. The constraints of Goodwin (1998) upon clumpy initial substructure apply to the specific scenario that they simulated, with initial clumps of comparable masses and uncorrelated positions. The nature of the relaxation process appears to be qualitatively different when the initial stellar density and velocity field are initialized in a hierarchical fashion in the manner we have investigated, which takes into account the underlying spatial and kinematic correlation functions observed in star-forming regions.

3.5.2 Applicability of the collisionless approximation

Throughout this paper we have approximated the dynamics of the ensemble of stars by assuming that the evolution is collisionless and that stars of different masses are well-mixed. Working in this approximation, our N-body simulations represented the stellar distribution as an ensemble of equal-mass, gravitationally-softened particles. This picture is clearly not entirely realistic for star clusters, which are generally are dense enough for stellar close encounters to be common enough to affect their long-term dynamical evolution. Bonnell et al. (2003) found that an order-unity fraction of stars have close encounters during hierarchical star cluster formation, so the the granularity of stellar mass should clearly have some effect. We expect the collisionless approximation to break down for clusters in which the the 2-body relaxation time is less than the orbital time, which Equation 3.4 predicts is the case for clusters less massive than $\sim 250 M_\odot$. Therefore, we expect the physics considered in this work to be most applicable to the regime of massive star clusters that assembled from sub-clusters more massive than this.

The success of the collisionless approximation in producing star clusters with realistic coarse-grained structure in both multi-physics star cluster formation simulations (Grudić et al., 2018b) and the numerical experiments of this paper suggests that it is be sufficient for these purposes. The orbital evolution in the hierarchical merging scenario is dominated by rapid changes in the gravitational potential driving violent relaxation, which affects stellar trajectories independently of their mass (Lynden-Bell, 1967).

3.5.3 Star cluster initial conditions

It has become possible in recent years to simulate the direct N-body evolution, and other processes governing the post-formation dynamical evolution, of a globular cluster consisting of as many as $\sim 10^6$ stars (Wang et al., 2016). Such simulations are important for understanding the rich variety of physical mechanisms that caused young star clusters to evolve into present-day mature globulars, but they must assume some initial cluster properties ad-hoc. Typically, either the Plummer (1911) or King (1966) model is used as the initial model (Portegies Zwart et al., 2010a).

However, since YMCs are well-described by the Elson et al. (1987) model, and we have given this observation further physical motivation in this paper, we propose that a shallower Elson et al. (1987) model is a more realistic initial condition for globular cluster simulations, rather than something that resembles a mature globular cluster. According to the distribution of profile slopes (Figure 3.1), a typical model would have $\gamma \sim 2.5$. Compared to a Plummer model of equal mass and half-mass radius, the central density of a $\gamma = 2.5$ profile is more than ten times greater, so collisional effects such as mass segregation and core collapse would likely have much earlier onset [9]. This could easily mark the difference between runaway core collapse happening before or after the mass loss and death of massive stars ~ 3 Myr after star formation. This is a critical factor determining whether it is possible for runaway stellar mergers to form a very massive star or an IMBH in the centre of the cluster (Portegies Zwart and McMillan, 2002; Gürkan et al., 2004; Freitag et al., 2006). It should also influence the pairing and hardening of massive stellar binaries centre of

---

[9] Although they would still take longer than the initial formation of the cluster.

dense clusters, which would alter the rate of massive (e.g. $\sim 60\,\mathrm{M}_\odot$) binary black hole mergers like GW150914 (Abbott et al., 2016; Rodriguez et al., 2015, 2016). Clearly the detailed early dynamical evolution of realistic YMC models warrants further study with more realistic initial conditions.

3.5.4 The outer NFW profile

We have established that the phase-space dilution caused by violent relaxation and phase mixing in the hierarchical merging of star clusters generally drives clusters toward shallower mass profiles approaching $\rho \propto r^{-3}$. Cold dark matter halos also merge hierarchically, and are generally well-described by the Navarro et al. (1996) (NFW) profile in cosmological simulations, which also has an r^{-3} dependence. Indeed, it has long been established that such a profile has some relationship with hierarchical merging (White, 1979; Villumsen, 1982; Duncan et al., 1983; McGlynn, 1984b; Pearce et al., 1993). To explain this, we cannot invoke exactly the same argument as the one we have made for star clusters in §3.3, because the NFW model has no maximum phase-space density to conserve. Nevertheless, the Dehnen (2005) mixing theorem still implies that the hierarchical merging of dark matter halos cannot create steeper density profiles. Furthermore, the outer density profile should behave in a manner that is insensitive to the details of whether the inner profile is a core or a cusp, so shallower density profiles should generally result in mergers. We therefore argue that the $\propto r^{-3}$ outer NFW profile can be understood as the endpoint of the same process of phase-space dilution that we have argued drives star clusters to shallow density profiles.

3.6 Conclusions

We arrive at the following conclusions about the formation of young massive clusters:

- We compile observational data of young massive cluster populations (Ryon et al., 2015, 2017; Mackey and Gilmore, 2003a,b) and find that the distribution of surface brightness profile slopes (Figure 3.1) is similar between different cluster populations, suggesting that it is universal due to common star formation physics.

- MHD star cluster formation simulations with resolved cooling, fragmentation, and stellar feedback (Grudić et al., 2018b) have produced a population of star clusters with profile slopes that agree with observations (Figure 3.1), despite the fact that the simulations do not resolve the formation of individual stars.

To capture the essential physics that determine the shapes of nascent massive star clusters, it suffices to resolve some fraction of the dynamic range of fragmentation.

- Stellar feedback clearly has an important role in shaping star clusters, as simulations without feedback are different from observed YMCs in many ways. The role of stellar feedback in setting star cluster structure should be elucidated in detailed cluster formation simulations.
- Based on the the observational and simulation data mentioned above, evidence is strong that a YMC's profile slope is established when it is dynamically young, so must be established in the cluster formation process.
- We develop an analytic model for the evolution of a cluster's profile slope γ in a sequence of collisionless pairwise mergers between star clusters modelled by the Elson et al. (1987) model. Phase-space mixing requires that the final slope is no shallower than that of either progenitor. Furthermore, assuming conservation of mass, energy, and maximum phase-space density, we find that mergers must always shallow the slope toward 2 by some amount. Thus a sufficiently large number of hierarchical mergers will result in $\gamma \sim 2$, as argued in Guszejnov et al. (2018a) from more general considerations.
- We perform collisionless N-body simulations of three iterated star cluster mergers, starting with a pair of identical Plummer (1911) models and then merging the result with a copy of itself twice. The results of these simulations are in good agreement with our analytic model: at most $\sim 10\%$ of mass and energy are ejected in each merger, the maximum phase-space density is conserved, and the mergers drive γ from 4 initially to a value close to 2 (Table 1). The collisionless merger of two Elson et al. (1987) clusters produces another cluster whose surface density profile is also well-described by the Elson et al. (1987) model, however deviations from the model are more apparent in the phase-space structure (Figure 3.1).
- We have performed N-body experiments following the collisionless relaxation of a hierarchically-clustered mass distribution with spatial and kinematic scaling relations corresponding to those observed in GMCs and young star clusters. We find that sub-clusters rapidly merge hierarchically into steady-state star clusters with Elson et al. (1987)-like surface density profiles, despite no initial surface density model being assumed. Thus the Elson et al. (1987)

model is physically motivated within the paradigm of hierarchical star cluster formation, and indeed Elson et al. (1987)'s explanation in terms of dissipationless relaxation following rapid star formation is venerated.

- Because clusters resembling YMCs emerge so readily from plausible star formation physics, a shallow EFF profile is a more plausible model of a nascent star cluster than the commonly-simulated Plummer (1911) or King (1966) models. This may have interesting implications for the detailed dynamical evolution of dense star clusters.

Acknowledgements

We thank Michael S. Fall, Bruce Elmegreen, Scott Tremaine, and the anonymous referee for helpful feedback. Support for MG and TAPIR co-authors was provided by an Alfred P. Sloan Research Fellowship, NASA ATP Grant NNX14AH35G, and NSF Collaborative Research Grant #1411920 and CAREER grant #1455342. MB-K acknowledges support from NSF grant AST-1517226 and from NASA grants NNX17AG29G and HST-AR-13888, HST-AR-13896, and HST-AR-14282 from the Space Telescope Science Institute, which is operated by AURA, Inc., under NASA contract NAS5-26555. Numerical calculations were run on the Caltech compute clusters 'Zwicky' (NSF MRI award # PHY-0960291) and 'Wheeler' and allocation TG-AST130039 granted by the Extreme Science and Engineering Discovery Environment (XSEDE) supported by the NSF.

APPENDIX

3.A Cluster finding algorithm

To identify bound star clusters from the star particle mass, velocity and position data of the Grudić et al. (2018b) simulations, we use an algorithm based on identifying potential wells. This is generally more robust than methods based on identifying density maxima because the gravitational potential contains all necessary information for cluster finding, while being inherently smoother and hence less susceptible to noise. The algorithm is as follows:

1. Determine some fixed number N_{ngb} of each star particle's nearest neighbors in position space.
2. From each particle, move to the neighbour particle with the lowest gravitational potential. Repeat until a local minimum in the potential is found. This is the bottom of the potential well, to which the initial particle is now "associated".
3. Compute the gravitational potential as sourced only by the particles associated with this potential well in isolation.
4. Associated particles that are bound to the potential well are considered bound members of the cluster.

In practice, we take $N_{ngb} = 32$, which is the number of neighbour elements used for constructing the hydrodynamic mesh and force softening in the simulations, so it is on the order the size of the least massive self-gravitating structure that can exist in the simulation. A larger value could potentially lump together distinct bound star clusters, while smaller values generally increase the population of spurious clusters. We find this algorithm to have satisfactory accuracy for this problem; it has been tested on control datasets for which the cluster associations are known a priori, and stably identifies the same cluster between different simulation snapshots.

3.B (Semi-) Analytic Properties of the EFF model

Here we derive useful quantities for calculations involving star clusters modeled by the Elson et al. (1987) density profile (Equation 3.2) with arbitrary profile slope γ:

$$\rho\left(r\right) = \rho_0 \left(1 + \frac{r^2}{a^2}\right)^{-\frac{\gamma+1}{2}}. \tag{3.16}$$

The quantities needed to construct a dynamical model with this density profile are only generally expressible in closed form in the special case $\gamma = 4$, which is the Plummer (1911) model. This has ensured its popularity as an initial condition for N-body simulations that is easy to construct. However, as discussed in Section 3.2, a much more typical initial condition for a star cluster would be $\gamma \sim 2-3$. For those quantities that lack closed-form expressions, we provide approximate expressions or upper and lower bounds for use with numerical root solvers. The reader is also directed to (Lupton et al., 1989) for the derivation of the collisionless Jeans model.

3.B.1 Cumulative mass distribution

The cumulative mass distribution for arbitrary γ is:

$$\begin{aligned} M\left(<r\right) &= \int_0^r 4\pi r'^2 \rho\left(r'\right) \mathrm{d}r' \\ &= \frac{4\pi\rho_0}{3} r^3 \, {}_2F_1\left(\frac{3}{2}, \frac{\gamma+1}{2}; \frac{5}{2}; -\frac{r^2}{a^2}\right), \end{aligned} \tag{3.17}$$

where ${}_2F_1\left(a, b; c; z\right)$ is the Gauss hypergeometric function (Abramowitz and Stegun, 1965, chap. 15).

3.B.2 Half-mass radius

The three-dimensional half-mass radius R_{eff} may be obtained by solving $M\left(<r\right)/M = \frac{1}{2}$. For the Plummer model ($\gamma = 4$), the solution is $\frac{1+\sqrt[3]{2}}{\sqrt{3}} a \approx 1.3$. For general γ, there is no closed form solution. We may derive upper and lower bounds from the constant and power-law parts of the density profile respectively from the expansions of $M\left(r\right)$ about 0 and ∞:

$$\left(\frac{3M}{4\pi\rho_0}\right)^{\frac{1}{3}} \leq R_{eff} \leq \left(\frac{4\Gamma\left(\frac{\gamma+1}{2}\right)}{\sqrt{\pi}\Gamma\left(\frac{\gamma}{2}\right)}\right)^{\frac{1}{\gamma-2}} a. \tag{3.18}$$

Equipped with these bounds, R_{eff} can be computed efficiently with a bounded root-finding algorithm such as Brent's method. In the limit $\gamma \to 2$, the solution will approach the upper bound, as most of the mass will be in the power-law portion. Similarly $R_{eff} \to \left(\frac{3M}{4\pi\rho_0}\right)^{\frac{1}{3}}$ as $\gamma \to \infty$ because most of the mass will be in the core.

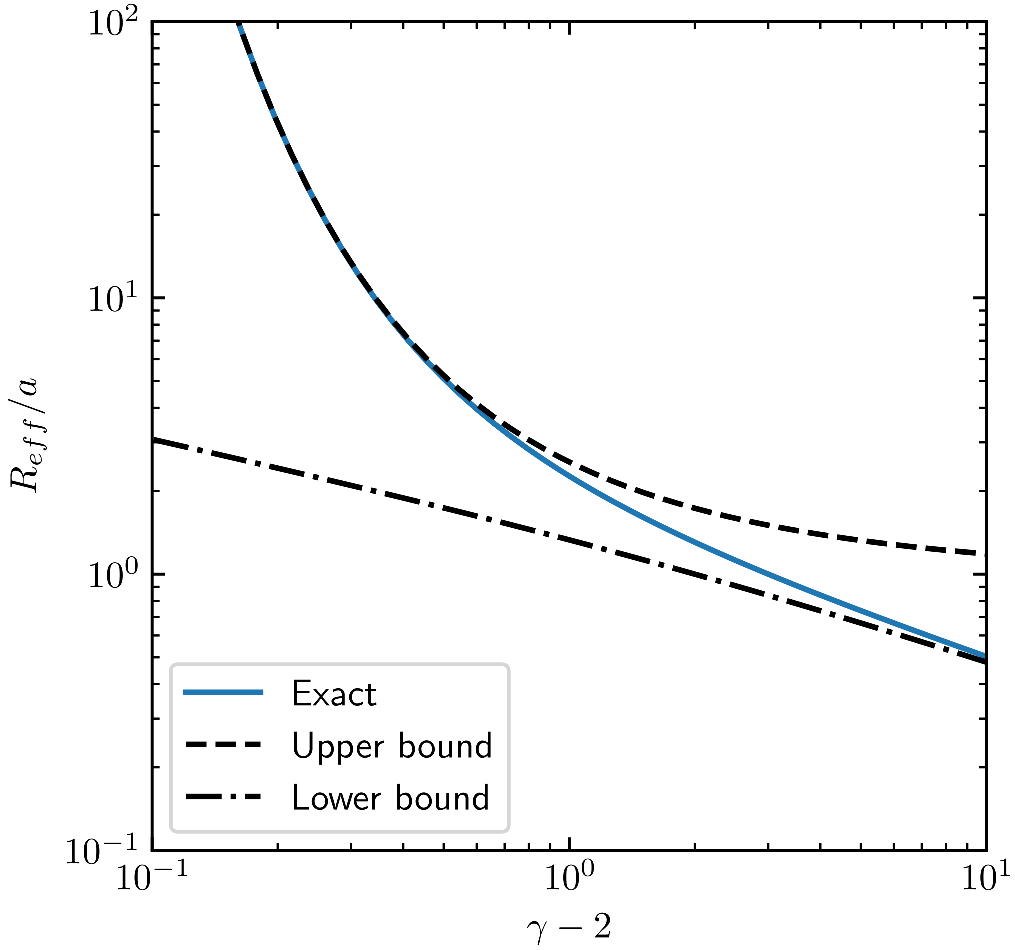

Figure 3.B.1: Three-dimensional half-mass radius R_{eff} as a function of γ in units of the scale radius a. The numerical solution is shown in blue, between the bounds given in Equation 3.18.

3.B.3 Potential

The gravitational potential is given by the integral

$$\begin{aligned}\Phi(r) &= \int_{\infty}^{r} \frac{GM(r')}{r'^2}\mathrm{d}r' \\ &= -\frac{4\pi G a^2 \rho_0 \, {}_2F_1\left(\frac{1}{2}, \frac{\gamma-1}{2}; \frac{3}{2}; -\frac{r^2}{a^2}\right)}{\gamma - 1}. \end{aligned} \tag{3.19}$$

The expansion of $\Phi(r)$ about the center is:

$$\Phi(r) = 4\pi G \rho_0 \left(\frac{r^2}{6} - \frac{a^2}{\gamma - 1}\right) + O\left(r^4\right). \tag{3.20}$$

The shortest possible orbital frequency in the cluster is that associated with simple harmonic motion in the central potential well, which depends only on the central density:

$$\Omega_{max} = \sqrt{\frac{4\pi G\rho_0}{3}}. \tag{3.21}$$

Expanding about $r = \infty$, we see that the leading order correction to the monopole term $-\frac{GM}{r}$ is:

$$\Phi(r) + \frac{GM}{r} \approx \frac{GM}{a} \frac{\Gamma\left(\frac{\gamma-1}{2}\right)}{\sqrt{\pi}\Gamma\left(\frac{\gamma}{2}\right)} \left(\frac{r}{a}\right)^{1-\gamma}. \tag{3.22}$$

Thus, for larger values of γ, the leading correction to the point mass potential is $\propto r^{1-\gamma}$, which will be very small, so the potential is well-approximated by a Keplerian potential. This approximation will be less valid for $\gamma \longrightarrow 2$, as most of the mass will be in the power law portion of the profile.

3.B.4 Energy

A star cluster in dynamical equilibrium will satisfy the virial theorem: $E = -W/2$, where W is the magnitude of the gravitational potential energy. The potential energy associated with the mass distribution may be computed as the integral:

$$W = \int_0^\infty \frac{GM(r)}{r} 4\pi r^2 \rho(r)\, \mathrm{d}r = \mathcal{W}(\gamma) \frac{GM^2}{a}, \tag{3.23}$$

where $\mathcal{W}(\gamma)$ is a dimensionless function of γ, plotted in Figure 3.B.2. For the Plummer model, $\mathcal{W}(\gamma) = \frac{3\pi}{32}$. The expression in terms of the hypergeometric function is cumbersome, however it is asymptotically $\propto (\gamma-2)^2$ as $\gamma \longrightarrow 2$ and $\propto (\gamma-2)^{\frac{1}{2}}$ as $\gamma \longrightarrow \infty$. It can be very well approximated by the following expression:

$$\mathcal{W}(\gamma) = \left(\left(c_1(\gamma-2)^2\right)^\alpha + \left(c_2(\gamma-2)^{\frac{1}{2}}\right)^\alpha\right)^{\frac{1}{\alpha}}, \tag{3.24}$$

with $c_1 = 0.780$, $c_2 = 0.284$, and $\alpha = -0.692$. This expression interpolates between the two asymptotic behaviours, and is indistinguishable from $\mathcal{W}(\gamma)$ as plotted in Figure 3.B.2.

3.B.5 Phase-Space Distribution Function

With the potential given by Equation 3.19, and assuming an isotropic velocity distribution, the phase-space density $f(\boldsymbol{x}, \boldsymbol{v})$ is a function of specific orbital energy alone. We may determine the phase-space density $f(\mathcal{E})$ with the usual integral formula (Binney and Tremaine, 1987):

$$f(\mathcal{E}) = \frac{1}{\sqrt{8}\pi^2} \frac{\mathrm{d}}{\mathrm{d}\mathcal{E}} \int_{\psi=0}^{\psi=\mathcal{E}} \frac{\mathrm{d}\rho}{\sqrt{\mathcal{E}-\psi}}, \tag{3.25}$$

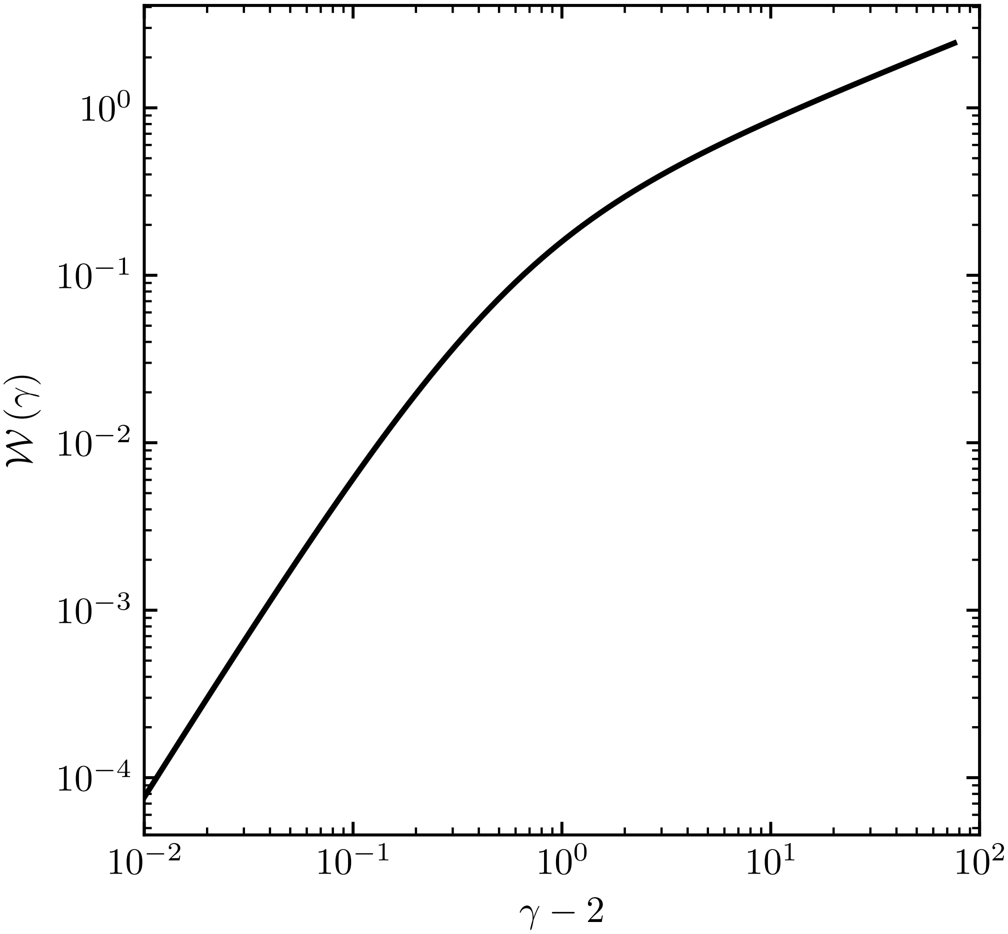

Figure 3.B.2: $\mathcal{W}(\gamma)$ as a function of γ, where the gravitational binding energy is given by $W = \mathcal{W}(\gamma)\frac{GM^2}{a}$. The function is very well approximated by Equation 3.24. It is $\propto (\gamma - 2)^2$ in the limit $\gamma \to 2$ and $\propto (\gamma - 2)^{\frac{1}{2}}$ in the limit $\gamma \to \infty$.

where $\psi = -\Phi$ and $\mathcal{E} = \left(-\Phi - \frac{1}{2}v^2\right)$. In the limit $r >> R_{eff}$, we may approximate $f(\mathcal{E})$ by substituting the Keplerian potential and the approximation $\rho \sim \rho_0 r^{-\gamma-1}$. In this limit:

$$f(\mathcal{E}) \approx \frac{\Gamma(\gamma+1)\Gamma\left(\frac{\gamma+3}{2}\right)}{\sqrt{2}\pi^3\Gamma\left(\frac{\gamma-2}{2}\right)\Gamma\left(\gamma+\frac{1}{2}\right)}\mathcal{E}^{\gamma-\frac{1}{2}} \tag{3.26}$$

Remarkably, for the Plummer model ($\gamma = 4$), this power law approximation holds exactly. For all other values this is not so, and the integral and derivative in Equation 3.25 must be taken numerically. The derivative in Equation 3.25 may be taken with a high-order finite difference stencil, as the integral is smooth everywhere except at

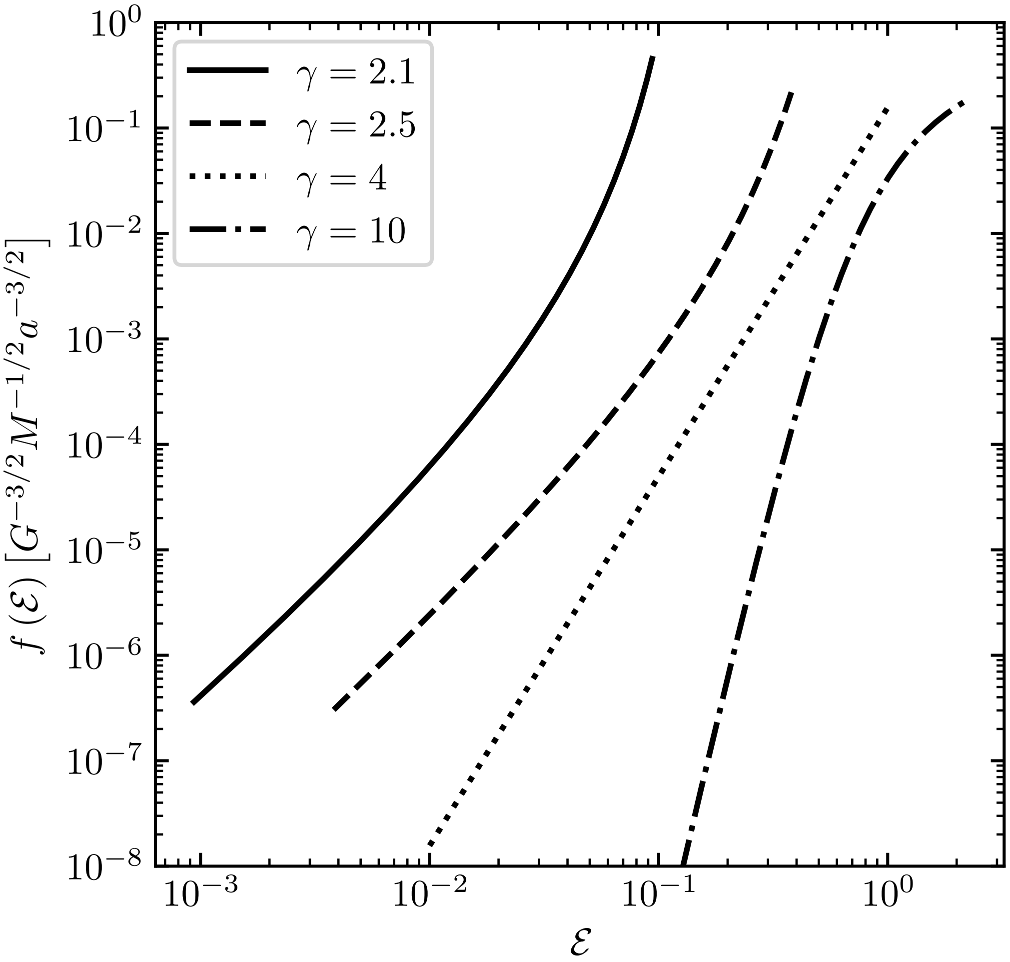

Figure 3.B.3: Phase-space density $f(\mathcal{E})$ in units of $G^{-3/2}M^{-1/2}a^{-3/2}$ for isotropic cluster models with different γ. The Plummer model ($\gamma = 4$) is the only one that is a true power law $\propto \mathcal{E}^{7/2}$, hence its popularity as an analytic model for N-body initial conditions.

$\mathcal{E} = \psi(0)$. Figure 3.B.3 plots the numerically-computed $f(\mathcal{E})$ for various values of γ. It is clear that for the non-Plummer models, the phase-space distribution for the lowest energy (largest $\mathcal{E}$) orbits deviates significantly from a power law. Figure 3.B.4 shows the dependence of the maximum phase-space density upon γ. In the usual units in terms of G, M and a, the Plummer model has the lowest maximum phase-space density, and with M and a held constant f_{max} increases without bound as $\gamma \to 2$ and $\gamma \to \infty$. We may roll the γ dependence into a dimensionless function $\mathcal{F}(\gamma)$, such that $f_{max} = \mathcal{F}(\gamma)\, G^{-3/2}M^{-1/2}a^{-3/2}$. An approximation of $\mathcal{F}$

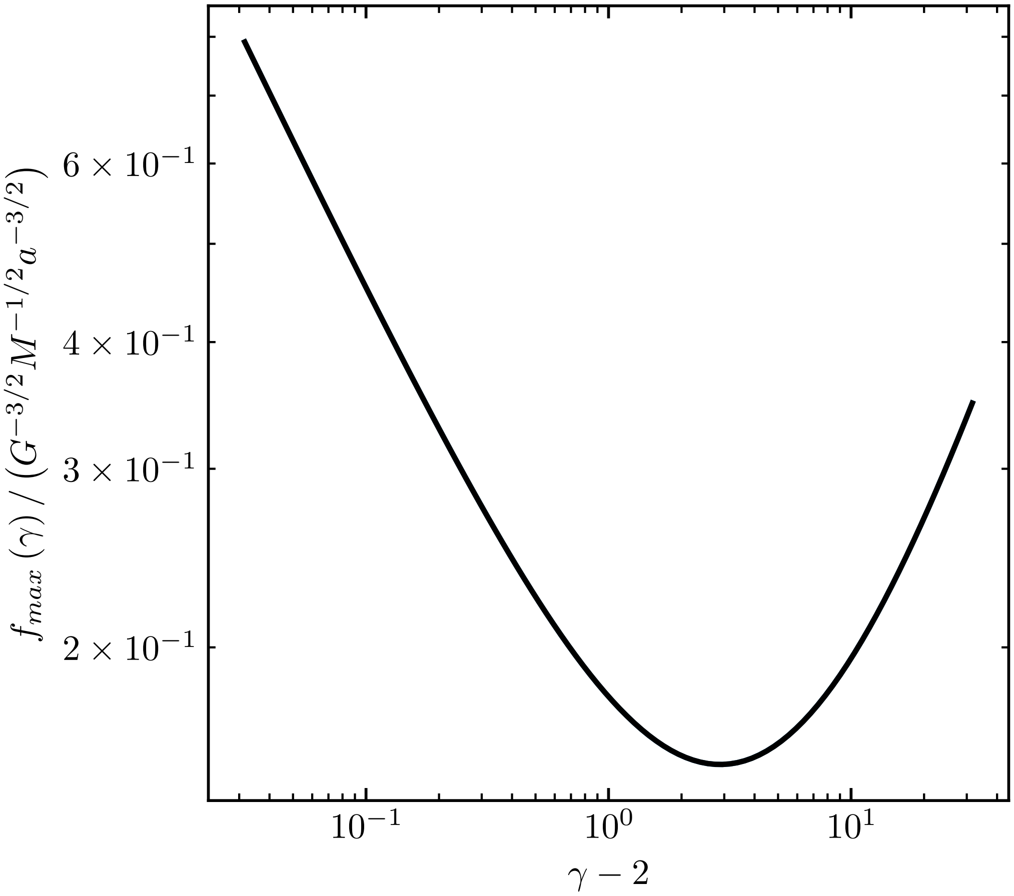

Figure 3.B.4: Maximum phase-space density f_{max} as a function of γ, in units of $G^{-3/2}M^{-1/2}a^{-3/2}$. The function is $\propto (\gamma-2)^{-1/2}$ in the limit $\gamma \to 2$, $\propto (\gamma-2)^{3/4}$ in the limit $\gamma \to \infty$, and minimized for the Plummer model ($\gamma = 4$). It is well approximated by Equation 3.27.

with maximum error $\sim 10^{-4}$ over $\gamma \in [2.01, 10]$ is:

$$\mathcal{F}(\gamma) \approx \left(\left(c_1(\gamma-2)^{\frac{3}{4}}\right)^{\alpha} + \left(c_2\,(\gamma-2)^{-\frac{1}{2}}\right)^{\alpha}\right)^{\frac{1}{\alpha}}, \tag{3.27}$$

where $c_1 = 0.0228$, $c_2 = 0.139$, and $\alpha = 0.816$.

3.B.6 Cumulative Phase-Space-Density Distribution $M(<f)$

$M(<f)$, the amount of mass at phase-space density less than f, is a useful diagnostic quantity in N-body simulations because it is robust to noisy estimates of f from Monte Carlo particle data. It is also useful for placing analytic constraints on merger products because it strictly increases in collisionless evolution as phase mixing occurs.

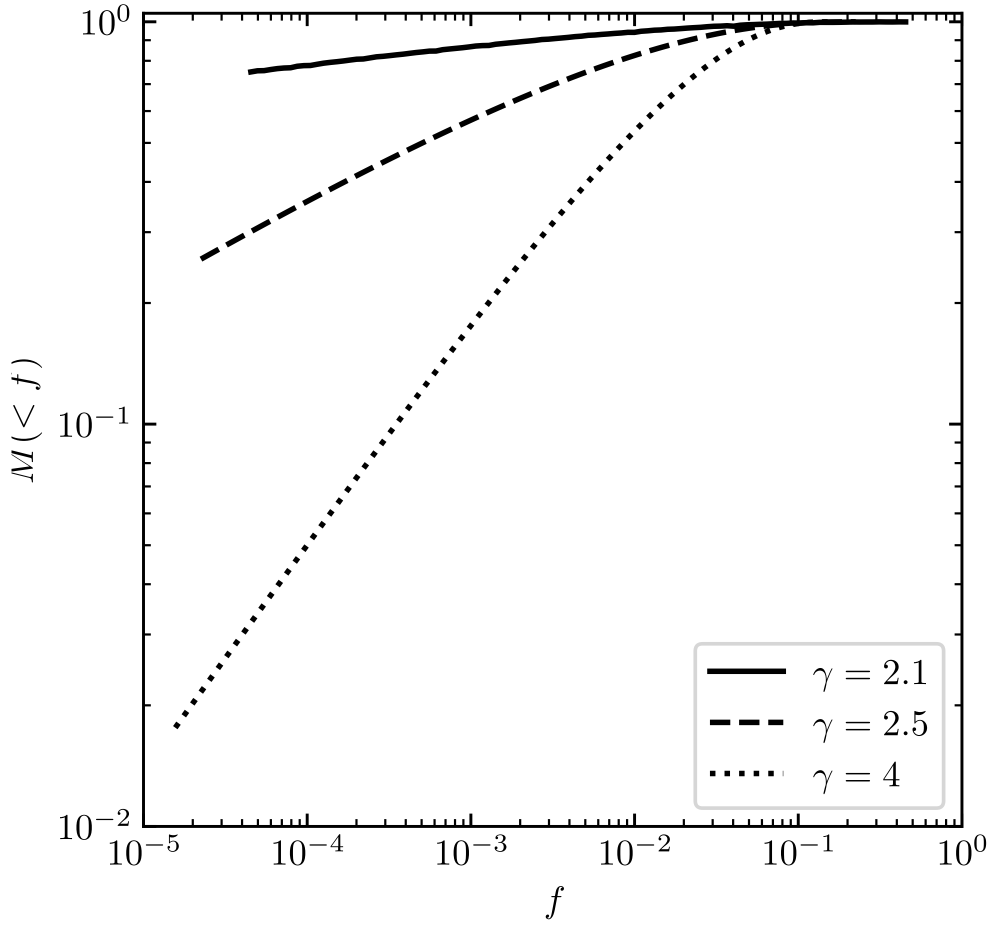

Figure 3.B.5: Cumulative phase-space density distribution $M\,(<f)$ for a series of clusters varying γ while keeping mass and energy fixed. At equal mass and energy, the distribution is more spread-out for γ values closer to 2, and is asymptotically $\propto f^{\frac{2\gamma-4}{2\gamma-1}}$.

For a spherically-symmetric, isotropic cluster model, f is a monotonic function of $\mathcal{E}$, so it is convenient to compute $M\left(<f\right)$ as the integral

$$M\left(<f\right)=\int_0^{\mathcal{E}(f)} f\left(\mathcal{E}\right)g\left(\mathcal{E}\right)\mathrm{d}\mathcal{E}, \tag{3.28}$$

where $\mathcal{E}(f)$ is the inverse function of $f(\mathcal{E})$ and $g\left(\mathcal{E}\right)\mathrm{d}\mathcal{E}$ is the phase-space volume within the interval $[\mathcal{E},\mathcal{E}+\mathrm{d}\mathcal{E}]$, computable as

$$g\left(\mathcal{E}\right)=\sqrt{2}\left(4\pi\right)^2\int_0^{r(\mathcal{E})} r^2\sqrt{\psi\left(r\right)-\mathcal{E}}\,\mathrm{d}r, \tag{3.29}$$

where again $r\left(\mathcal{E}\right)$ is the radius at which $\psi\left(r\right)=\mathcal{E}$. In the Keplerian approximation, this gives

$$g\left(\mathcal{E}\right)\approx\sqrt{2Ma^5}\pi^3\mathcal{E}^{-5/2}. \tag{3.30}$$

Combining this with 3.26, the asymptotic form of $M\left(<f\right)$ is

$$M\left(<f\right)\approx\frac{2^{\frac{\gamma-2}{2\gamma-1}}\pi^{\frac{9}{1-2\gamma}+3}\hat{f}\left(\frac{\hat{f}\Gamma\left(\frac{\gamma}{2}-1\right)\Gamma\left(\gamma+\frac{1}{2}\right)}{\Gamma(\gamma+1)\Gamma\left(\frac{\gamma+3}{2}\right)}\right)^{\frac{3}{1-2\gamma}}}{\gamma-2}\propto f^{\frac{2\gamma-4}{2\gamma-1}}, \tag{3.31}$$

where $\hat{f}=f/\left(G^{-3/2}M^{-1/2}a^{-3/2}\right)$. In general, the integral 3.28 must be performed numerically. In Figure 3.B.5, we plot $M\left(<f\right)$ for a sequence of Elson et al. (1987) clusters with varying γ but equal mass and energy. Note how smaller values of γ have a flatter distribution, so their mass is effectively spread over more orders of magnitude in f.

Chapter 4

THE MAXIMUM STELLAR SURFACE DENSITY DUE TO THE FAILURE OF STELLAR FEEDBACK

M. Y. Grudić, P. F. Hopkins, E. Quataert, and N. Murray. MNRAS, 483:5548–5553, March 2019. doi: 10.1093/mnras/sty3386.

Abstract

A maximum stellar surface density $\Sigma_{\rm max} \sim 3 \times 10^5\,{\rm M_\odot\,pc^{-2}}$ is observed across all classes of dense stellar systems (e.g. star clusters, galactic nuclei, etc.), spanning ~ 8 orders of magnitude in mass. It has been proposed that this characteristic scale is set by some dynamical feedback mechanism preventing collapse beyond a certain surface density. However, simple analytic models and detailed simulations of star formation moderated by feedback from massive stars argue that feedback becomes *less* efficient at higher surface densities (with the star formation efficiency increasing as $\sim \Sigma/\Sigma_{\rm crit}$). We therefore propose an alternative model wherein stellar feedback becomes ineffective at moderating star formation above some $\Sigma_{\rm crit}$, so the supply of star-forming gas is rapidly converted to stars before the system can contract to higher surface density. We show that such a model – with $\Sigma_{\rm crit}$ taken directly from the theory – naturally predicts the observed $\Sigma_{\rm max}$. We find $\Sigma_{\rm max} \sim 100\Sigma_{\rm crit}$ because the gas consumption time is longer than the global freefall time even when feedback is ineffective. Moreover the predicted $\Sigma_{\rm max}$ is robust to spatial scale and metallicity, and is preserved even if multiple episodes of star formation/gas inflow occur. In this context, the observed $\Sigma_{\rm max}$ directly tells us where feedback fails.

4.1 Introduction

Hopkins et al. (2010) (hereafter Hopkins et al. (2010)) showed that the central surface densities of essentially all dense stellar systems exhibit the same apparent upper limit $\Sigma_{\rm max} \sim 3 \times 10^5\,{\rm M_\odot\,pc^{-2}}$. This includes globular clusters (GCs), super star clusters (SSCs), dwarf and late-type galaxy nuclear star clusters (NSCs), young massive clusters (YMCs), ultra-compact dwarfs (UCDs), compact ellipticals (cEs), galactic bulges, nearby and high-redshift early-type/elliptical galaxies, even nuclear stellar disks around Sgr A* and the Andromeda nuclear black hole. These span mass scales of $10^4 - 10^{12}\,M_\odot$, spatial sizes $0.1 - 10^4$ pc, *three-dimensional* densities

$1 - 10^5\,M_\odot\,\mathrm{pc}^{-3}$ (free-fall times $\sim 10^4 - 10^7$ yr), N-body relaxation times $\sim 10^6 - 10^{17}$ yr, escape velocities $\sim 20 - 600\,\mathrm{km\,s^{-1}}$, metallicities $Z \sim 0.01 - 5\,Z_\odot$, and formation redshifts $z \sim 0 - 6$, yet agree in Σ_{max}.

In Figure 4.1 we compile more recent observations of dense stellar systems of all classes, and find that this still holds largely true, although some nuclear star clusters exceeding the fiducial value of Σ_{max} by a factor of a few have since been found. Figure 4.2 is adapted from the original compilation of mass profiles of individual objects in Hopkins et al. (2010) – it shows that even many systems with "effective" surface densities (measured at R_{eff}) have *central* surface densities which approach (but do not appear to exceed) Σ_{max}, at least where resolved.

Hopkins et al. (2010) speculated that the universality of Σ_{max} might owe to stellar feedback processes.[1] After all, it is widely-recognized that feedback plays an important role regulating star formation (SF) in cold, dense molecular clouds (see Kennicutt and Evans, 2012, for a review). As gas collapses and forms stars, those stars inject energy and momentum into the ISM via protostellar heating and outflows, photoionization and photoelectric heating from UV photons, stellar winds, radiation pressure and supernova explosions. All of these mechanisms may moderate SF, either by contributing to the disruption of molecular clouds (Larson, 1981; Murray et al., 2010; Hopkins et al., 2012a; Krumholz et al., 2014; Grudić et al., 2018b) or the large-scale support of galaxies against vertical collapse (Thompson et al., 2005; Ostriker and Shetty, 2011; Faucher-Giguère et al., 2013; Hopkins et al., 2014; Orr et al., 2018a). These mechanisms have various roles on different scales, but stellar feedback is generally the only force strong enough to oppose gravity in dense, star-forming regions, so the characteristic scale of a newly-formed stellar system should be determined by the balance point of feedback and gravity.

The specific possibility discussed in Hopkins et al. (2010) was that multiple-scattering of IR photons might build up radiation pressure to exceed the Eddington limit for dusty gas. However, the value of Σ_{max} predicted according to this argument is inversely proportional to metallicity, so does not explain why Σ_{max} is apparently the same in SSCs in metal-rich starbursts (Keto et al., 2005; McCrady and Graham, 2007) (or super-solar massive elliptical centers) and in metal-poor

---

[1] They also discussed some possible explanations related to e.g. mergers, angular momentum transport processes, or dynamical relaxation, which they showed could *not* explain Σ_{max} across the wide range of systems observed (e.g. dynamical relaxation cannot dominate the systems with relaxation times much longer than a Hubble time, and global processes unique to galaxy mergers cannot explain star cluster interiors).

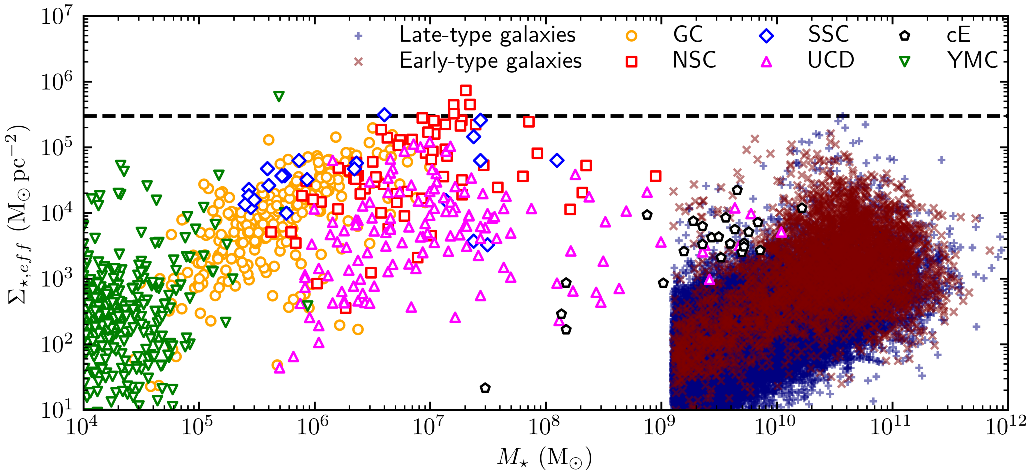

Figure 4.1: "Effective" stellar surface density ($\Sigma_{*,\,\mathrm{eff}} \equiv M_*/(2\pi\, R^2_{\mathrm{eff}})$) as a function of stellar mass for various types of stellar systems. Late- and early-type galaxies range from redshifts $z = 0 - 3$ and are taken from van der Wel et al. (2014). Globular clusters (GC), nuclear star clusters (NSC), ultra-compact dwarfs (UCD), and compact ellipticals (cE) are from the compilation of Norris et al. (2014). Super star clusters (SSC) are from the populations in M82 (McCrady and Graham, 2007), NGC 7252 (Bastian et al., 2013), NGC 34 (Schweizer and Seitzer, 2007), and NGC 1316 (Bastian et al., 2006). Young massive clusters (YMC) are from the Milky Way (Portegies Zwart et al., 2010b) and M83 (Ryon et al., 2015) populations. *Dashed:* Fiducial maximum effective surface density $\Sigma_{\mathrm{max}} = 3 \times 10^5\,\mathrm{M_\odot\,pc^{-2}}$.

GCs (or metal-poor high-z, low-mass compact galaxies). The argument therein also relied on scalings between IR luminosity and star formation rate (SFR) valid only for continuous-star forming populations with duration longer than $\sim 10 - 30\,\mathrm{Myr}$, which exceeds the dynamical times of many of these systems. Finally, Norris et al. (2014) noted that this effect cannot prevent the system from exceeding Σ_{max} if SF occurs in multiple episodes.

Since then, various theoretical works have noted the importance of surface density in setting the ratio between the momentum-injection rate from massive stars and the force of self-gravity in a star forming cloud (Fall et al., 2010; Murray et al., 2010; Dekel and Krumholz, 2013; Thompson and Krumholz, 2016; Raskutti et al., 2016; Grudić et al., 2018b). For a cloud with total mass M and stellar mass $M_\star = \epsilon_{\mathrm{int}} M$,

$$\frac{F_{\mathrm{gravity}}}{F_{\mathrm{feedback}}} \sim \frac{\frac{GM^2}{R^2}}{\epsilon_{\mathrm{int}} M \langle \frac{\dot{P}_\star}{M_\star} \rangle} \sim \frac{\Sigma}{\Sigma_{\mathrm{crit}}}, \tag{4.1}$$

where $\langle \frac{\dot{P}_\star}{M_\star} \rangle$ is the specific momentum injection rate from stellar feedback assuming a simple stellar population with a well-sampled IMF, which is $\sim 10^3\,\frac{\mathrm{L_\odot}}{\mathrm{M_\odot c}}$ for the first

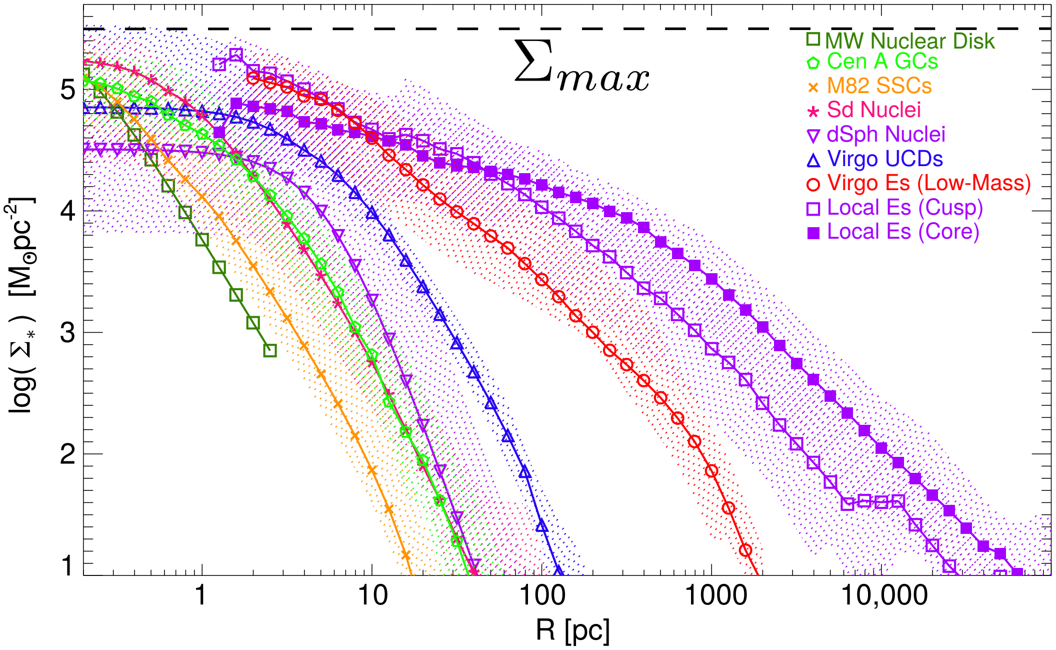

Figure 4.2: Observed stellar surface density *profiles* $\Sigma_*(r)$ as a function of projected radius, within individual stellar systems – reproduced from Fig. 2 of Hopkins et al. (2010). Lines show the median $\Sigma_*(r)$ from each sample, and the shaded range shows the $\pm 1\,\sigma$ range in $\Sigma_*(r)$ from all profiles in the sample. Samples are: Milky Way nuclear stellar disk (Lu et al., 2009), Cen A GCs (Rejkuba et al., 2007), M82 SSCs (McCrady and Graham, 2007), NSCs in late-type (Sd) galaxy nuclei (Böker et al., 2004), NSCs in dwarf-Spheroidal galaxy nuclei (Geha et al., 2002), UCDs in Virgo (Evstigneeva et al., 2007), early-type galaxies in Virgo (separated into low-mass "dwarf ellipticals" from Kormendy et al. 2009, and massive "cusp"/steep profile or "core"/shallow-profile systems from Lauer et al. 2007). Although many of these (e.g. the massive early-type galaxies) have $\Sigma_{*,\,\rm eff}$ (defined at large radii $\gtrsim$ kpc) well below $\Sigma_{\rm max}$, all systems appear to approach (and where resolved, saturate around) the fiducial maximum surface density $\Sigma_{\rm max} = 3\times10^5\,{\rm M}_\odot\,{\rm pc}^{-2}$.

3 Myr after SF, and $\Sigma_{\rm crit} \sim \langle \frac{\dot{P}_\star}{M_\star} \rangle / G \approx 3000\,M_\odot\,{\rm pc}^{-2}$ is the characteristic surface density that parametrizes the strength of feedback. If the final SF efficiency (SFE) $\epsilon_{\rm int}$ is ultimately set by the balance of feedback and gravity, one expects that $\epsilon_{\rm int} \rightarrow 1$ for $\Sigma \gg \Sigma_{\rm crit}$ (Fall et al., 2010). The detailed simulations of Grudić et al. (2018b) (Grudić et al., 2018b) showed that this argument is valid across a wide range of metallicities, surface densities and spatial scales, and the final SFE of a molecular cloud is a function mainly of Σ, with weak dependence upon other factors. Grudić et al. (2018b) also found that the final ratio of stellar mass to initial gas mass, $\epsilon_{\rm int}$, is proportional to the fraction of gas converted to stars within a freefall time, $\epsilon_{\rm ff}$, because a GMC always tends to form enough stars to destroy itself within a few

freefall times. Thus, Σ should parametrize the per-freefall efficiency of SF in a manner insensitive to spatial scale and metallicity.

In this paper, we show that if gas contracts globally (for any reason), as it becomes denser (Σ increases), and gravity becomes stronger relative to stellar feedback, gas is converted more and more rapidly into stars (above a characteristic surface density $\Sigma_{\rm crit}$). This exhausts the gas supply, preventing any significant fraction of the inflow from reaching surface densities $> \Sigma_{\rm max}$. We calculate $\Sigma_{\rm max}$ in terms of $\Sigma_{\rm crit}$ and show that the observed $\Sigma_{\rm max} \sim 3 \times 10^5\,{\rm M_\odot\,pc^{-2}}$ is naturally predicted by the value $\Sigma_{\rm crit} = 3000\,{\rm M_\odot\,pc^{-2}}$ set by feedback from massive stars (Fall et al., 2010; Grudić et al., 2018b).

4.2 Derivation

4.2.1 Setup and Assumptions

Consider a discrete SF episode involving a finite collapsing gas mass M, as illustrated in Figure 4.1. At a give time, the mass is localized within a radius R, so that its *mean* surface density is:

$$\Sigma = \frac{M}{\pi R^2}. \tag{4.2}$$

It is forming stars at some SFR, which we can parameterize with the SFE:

$$\mathrm{SFR} \equiv \frac{\mathrm{d}M_*}{\mathrm{d}t} = \frac{\epsilon_{\rm ff} M_{\rm gas}}{t_{\rm ff}}, \tag{4.3}$$

where $\epsilon_{\rm ff}$ is the (possibly variable) per-freefall SFE and $t_{\rm ff} = \frac{\pi}{2}\sqrt{\frac{R^3}{2GM}}$ is the freefall time.

Now, since we are only interested in the *maximum* stellar surface density such a system might reach, we will assume the "best-case" scenario for forming a dense stellar system. Specifically, assume:

1. The gas cloud is collapsing at a speed on the order of the escape velocity:

   $$\frac{\mathrm{d}R}{\mathrm{d}t} = -x_{ff}\sqrt{\frac{2GM}{R}}, \tag{4.4}$$

   where x_{ff} is a constant of order unity.

2. There is no support against collapse from large-scale turbulent motions,[2] tidal forces, rotation, shear, magnetic fields, cosmic rays, or the dynamical effects

---

[2] Note that some amount of turbulence must be assumed if stars are forming. We assume that such turbulent eddies are small compared to R, and thus are advected with the large-scale collapse without strongly opposing it.

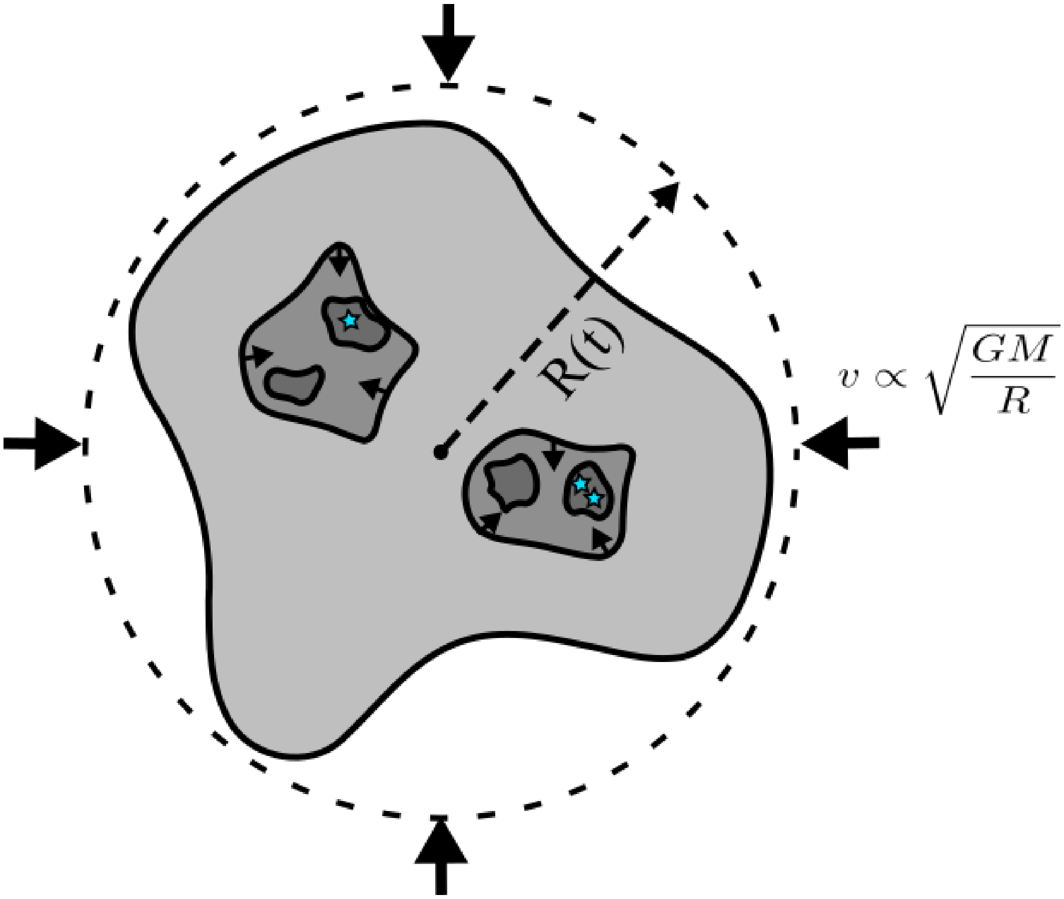

Figure 4.1: Schematic of our proposed “best-case” scenario for the formation of a dense stellar system (§ 4.2.1). A star-forming gas cloud of initial gas mass M is localized within a sphere of radius R. It collapses coherently at the freefall velocity $v_{\mathrm{ff}} = \sqrt{\frac{2GM}{R}}$, while fragmenting locally and forming stars in dense sub-regions. In this “best case”, no dynamical mechanism slows the collapse significantly.

> of stellar feedback. We neglect all of these because we are interested in the best-case scenario for producing a dense stellar system according to a give SFE law – any of these may be present, but they will only *slow* collapse, making a lower-density system in the end.

This is an idealization, but Kim et al. (2017b) did find that bound star clusters do form in a coherent collapse with velocity on the order of the freefall velocity in cosmological simulations, and stellar feedback does not greatly affect the dynamics until a significant fraction of the gas mass has been converted to stars.

4.2.2 Star Formation Efficiency Law

We shall assume that $\epsilon_{\rm ff}$ has some explicit dependence upon Σ, as is motivated by previous work. Accounting for radiation pressure, stellar winds, photoionization heating, and SN explosions, Grudić et al. (2018b) found

$$\epsilon_{\rm ff} = \epsilon_{\rm ff}(\Sigma) = \left(\frac{1}{\epsilon_{\rm ff}^{\rm max}} + \frac{\Sigma_{\rm crit}}{\Sigma}\right)^{-1}, \tag{4.5}$$

where $\Sigma_{\rm crit} = 3000\,\mathrm{M}_\odot\,\mathrm{pc}^{-2}$ is set by the strength of these feedback mechanisms. The dimensionless quantity $\epsilon_{\rm ff}^{\rm max}$ is the maximum per-freefall SFE attained as $\Sigma \rightarrow \infty$. In star-forming clouds supported at a fixed mean surface density, Grudić et al. (2018b) (see their Eq. 13 and Fig. 5) found that $\epsilon_{\rm ff} \approx 0.34\,\epsilon_{\rm int}$ (where $\epsilon_{\rm int}$ is the fraction of gas turned into stars over the entire integrated SF history, which of course just saturates at $\epsilon_{\rm int}^{\rm max} = 1$ as $\Sigma \rightarrow \infty$). However, this was the median over the entire SF history including initial collapse and eventual blowout. Therefore – in our "best-case" coherent collapse scenario, we are only interested in the "peak SFR" event, so $\epsilon_{\rm ff}^{\rm max}$ should be somewhat greater, ~ 0.5 (see Grudić et al. (2018b), Figure 3), and subject to further order-unity corrections due to the different collapse geometry from these simulations. In general, $\epsilon_{\rm ff}^{\rm max}$ should be similar that predicted by turbulent molecular cloud simulations that do not include stellar feedback, which have generally found $\epsilon_{ff} \sim 0.5 - 1$ in the limit of large turbulent Mach number and realistic turbulent forcing (Federrath and Klessen, 2012).

Adding turbulence and magnetic fields in succession, but without feedback initially, Federrath (2015a) found average values of $\epsilon_{ff} \sim 0.1$ and ~ 0.25 respectively, somewhat lower values than discussed above. These simulations were stopped at an arbitrary integrated SFE of 20% as ϵ_{ff}, just as ϵ_{ff} peaked, which may have reduced the measured average efficiency. These simulations were also at a much lower Mach number, $\mathcal{M} \sim 5$, than the high-efficiency clouds in Grudić et al. (2018b), $\mathcal{M} \sim 30 - 300$, and both analytic theory and simulation results find lower values of ϵ_{ff} in this $\mathcal{M}$ range when feedback is not present (e.g. Hopkins (2012), Fig. 11). Notwithstanding, Federrath (2015a) also showed that feedback from protostellar jets could maintain a small ϵ_{ff} over several freefall times. However, we again do not expect this moderation to scale up for clouds of greater $\mathcal{M}$, due to the dimensional scaling of the feedback mechanism. Assuming that outflows coupled a momentum $\langle P_\star / M_\star \rangle$ per stellar mass formed, the value of ϵ_{ff} required to support the cloud scales $\propto \sqrt{\frac{GM}{R}} / \langle P_\star / M_\star \rangle \propto \mathcal{M}$, so it is unlikely that protostellar feedback can maintain a low ϵ_{ff} in the progenitor clouds of the dense, massive stellar systems considered here (generally with velocity dispersions corresponding to $\mathcal{M} > 30$).

Overall, for the progenitor clouds of the types of system plotted in Figure 4.1, we favour values in the range $\epsilon_{ff,max} \sim 0.3 - 0.5$. We acknowledge some amount of uncertainty when generalizing to various geometries and turbulence properties such as solenoidal vs. compressive driving.

4.2.3 Solution

The SFR of the cloud is

$$\frac{\mathrm{d}M_*}{\mathrm{d}t} = \epsilon_{\mathrm{ff}} \frac{M_{\mathrm{gas}}}{t_{\mathrm{ff}}} = \frac{M_{\mathrm{gas}}}{\left(\epsilon_{\mathrm{ff}}^{\mathrm{max}}\right)^{-1} + \frac{\Sigma_{\mathrm{crit}}}{\Sigma}} \sqrt{\frac{8GM}{\pi^2 R^3}}, \tag{4.6}$$

where M_{gas} is the gas mass that has not been converted to stars at time t. The differential equation for the gas mass converted to stars when the cloud has radius R follows:

$$\frac{\mathrm{d}M_{\mathrm{gas}}}{\mathrm{d}R} = -\frac{\mathrm{d}M_*}{\mathrm{d}t}\frac{\mathrm{d}t}{\mathrm{d}R} = -\frac{2}{\pi x_{ff} R} \frac{M_{\mathrm{gas}}}{\left(\epsilon_{\mathrm{ff}}^{\mathrm{max}}\right)^{-1} + \frac{\pi R^2 \Sigma_{\mathrm{crit}}}{M}}. \tag{4.7}$$

The solution for the fraction of the gas mass surviving to radii $< R$ is

$$\frac{M_{\mathrm{gas}}\left(< R\right)}{M} = \left(1 - \frac{M}{M + \epsilon_{\mathrm{ff}}^{\mathrm{max}} \pi R^2 \Sigma_{crit}}\right)^{\epsilon_{\mathrm{ff}}^{\mathrm{max}}/\pi x_{ff}}. \tag{4.8}$$

Thus, as $R \rightarrow 0$ we see that $M_{\mathrm{gas}} \rightarrow 0$, ie. the gas is exhausted as the system contracts to surface densities $\Sigma \gg \Sigma_{\mathrm{crit}}$. The stellar system formed will subsequently undergo a period of relaxation, but energy conservation requires that the stars remain on orbits with apocentres on the order of the radius R at which they formed [3]. We may thus construct a radial stellar density profile as the superposition of the top-hat mass distributions formed at each radius. The corresponding projected stellar surface density profile is

$$\Sigma_*\left(R\right) = 2\int_R^\infty \sqrt{R'^2 - R^2} \frac{\mathrm{d}M_{gas}\left(< R'\right)}{\mathrm{d}R'} \Big/ \left(\frac{4\pi}{3} R'^3\right) \mathrm{d}R', \tag{4.9}$$

which we plot for various values of $\epsilon_{\mathrm{ff}}^{\mathrm{max}}$ and x_{ff} in Figure 4.2. In general, we find that the characteristic stellar surface densities for plausible values of $\epsilon_{\mathrm{ff}}^{\mathrm{max}}$ and x_{ff}

---

[3] We have verified with collisionless Monte Carlo simulations that the functional form of Equation 4.8 does closely match the final stellar mass distribution after violent relaxation to virial equilibrium, provided that the initial virial parameter $2E_{kin}/|E_{grav}| \sim 1$.

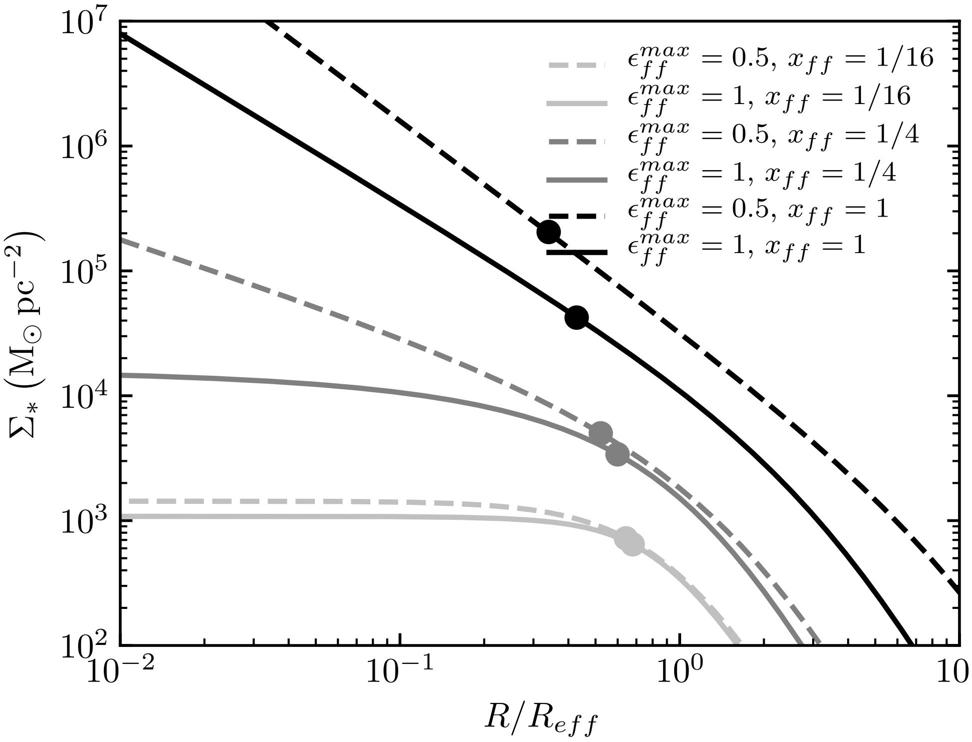

Figure 4.2: Radial stellar surface density profiles computed from the cloud collapse model described in § 4.2.1 for various values of the maximum per-freefall SFE $\epsilon_{\rm ff}^{\rm max}$ and the rate of collapse relative to freefall x_{ff}, with radius in units of the half-mass radius R_{eff}. The point on each curve gives the effective stellar surface density $\Sigma_{*,eff} = M_* / \left(2\pi R_{eff}^2\right)$ of the model. The characteristic surface densities obtained over the parameter ranges $\epsilon_{\rm ff}^{\rm max} \sim 0.5 - 1$ and $x_{ff} \sim 0.1 - 1$ span the range $10^3 - 10^6\, M_\odot\,\mathrm{pc}^{-2}$ in which most dense stellar systems lie (see Fig. 4.1). To form a system with $\Sigma_{*,eff} >> 3 \times 10^5\, M_\odot\,\mathrm{pc}^{-2}$ would require $\epsilon_{\rm ff}^{\rm max} << 0.5$ or $x_{ff} >> 1$, both of which are unphysical.

span the range of surface densities found in dense stellar systems (Figs. 4.1 and 4.2). Furthermore, if $x_{\mathrm{ff}} = 1$ then effective surface densities $\sim 10^5 \mathrm{M}_\odot\,\mathrm{pc}^{-2}$ are obtained, corresponding to the maximum observed.

It should be noted that the inner surface density profile plotting in Figure 4.2 is $\Sigma \propto R^{-2+\frac{2\epsilon_{\mathrm{ff}}^{\mathrm{max}}}{\pi x_{\mathrm{ff}}}}$, which is nearly as steep as R^{-2} for the physically-plausible parameters $\epsilon_{\mathrm{ff}}^{\mathrm{max}} = 0.5$ and $x_{\mathrm{ff}} = 1$, ie. the profile has nearly constant mass per interval in $\log R$. In such a case a non-negligible fraction of the mass can be concentrated on scales < 0.1pc. Such a high degree of central concentration is not generally found in any type of stellar system, so the inner profiles in this model are an unphysical artifact of the imposed condition of unopposed, spherically-symmetric collapse. This is never realized in nature because even an initially-monolithic supersonic collapse is unstable to fragmentation (Guszejnov et al. 2018, in prep.), and the subsequent violent relaxation of stars produces a much shallower (typically flat) inner density profile (Klessen and Burkert, 2001; Bonnell et al., 2003; Grudić et al., 2018a). Thus, our free-collapse model lacks the physics necessary to establish a hard limit upon the central stellar surface density [4], although it should scale in a similar way to the effective surface density when combined with the action of the scale-free physics of gravity and turbulence during star formation.

In Figure 4.3, we consdier the maximally-freefalling case $x_{\mathrm{ff}} = 1$ to plot the depedence of Σ_{max} on $\epsilon_{\mathrm{ff}}^{\mathrm{max}}$. We find that if $\Sigma_{\mathrm{crit}} = 3000\,\mathrm{M}_\odot\,\mathrm{pc}^{-2}$ and the plausible range for $\epsilon_{\mathrm{ff}}^{\mathrm{max}}$ is $0.5 - 1$, the predicted Σ_{max} lies within an order of magnitude of the observed $\Sigma_{\mathrm{max}} \sim 3 \times 10^5\,\mathrm{M}_\odot\,\mathrm{pc}^{-2}$ (Figure 4.1). We also present results for two alternate models for $\epsilon_{\mathrm{ff}}(\Sigma)$: a constant value, and a step-function equal to 0.01 (e.g. Kennicutt, 1998a; Krumholz et al., 2012a) below Σ_{crit} and $\epsilon_{\mathrm{ff}}^{\mathrm{max}}$ above Σ_{crit}. First, we note that while our preferred model gives Σ_{max} independently of initial cloud surface density, these do not – we therefore take the initial density to be $100\,\mathrm{M}_\odot\,\mathrm{pc}^{-2}$, typical of local GMCs (Bolatto et al., 2008). Second, we see the "$\epsilon_{\mathrm{ff}} =$constant" model predicts a Σ_{max} that is more sensitive to the chosen ϵ_{ff} (and the "preferred" value, ~ 0.2, is small). The step-function model, however, gives very similar results to our default model, so we see that the conclusions are not specific to the *details* of how ϵ_{ff} scales, so long as ϵ_{ff} is small when $\Sigma < \Sigma_{\mathrm{crit}}$ and grows to a value of order unity above $\Sigma \sim \Sigma_{\mathrm{crit}}$. Ultimately, the 2 dex separation between Σ_{crit} and Σ_{max} can be understood as follows: the system forms stars slowly until reaching $\Sigma \sim \Sigma_{crit}$,

---

[4] Indeed, there is at least one YMC in M83 with central surface density in excess of $10^6 M_\odot\,\mathrm{pc}^{-2}$ in the catalogue of (Ryon et al., 2015), suggesting that the same bound for *central* surface density might not strictly hold.

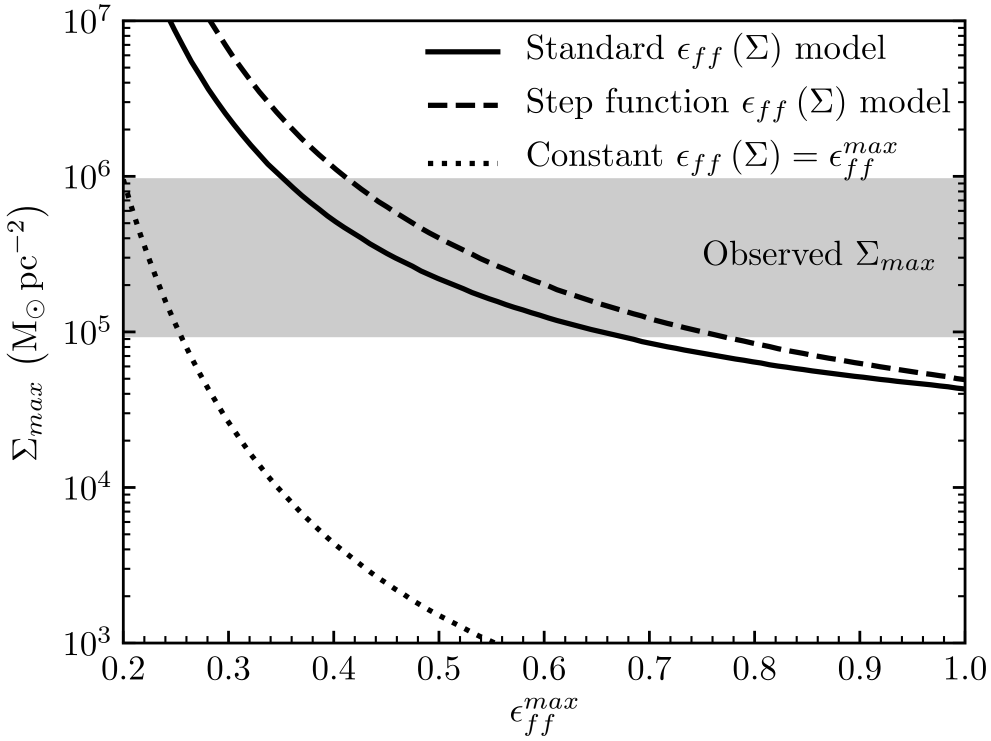

Figure 4.3: Maximum effective surface density $\Sigma_{\rm max}$ predicted by the model in § 4.2.1 as a function of the parameter $\epsilon_{\rm ff}^{\rm max}$ (maximum SFE per free-fall time, as $\Sigma \rightarrow \infty$), assuming $\Sigma_{\rm crit} \approx 3000\,M_{\odot}\,{\rm pc}^{-2}$. Simulations and analytic theory give $\epsilon_{\rm ff}^{\rm max} \approx 0.5 - 1$ (Hopkins, 2012; Federrath and Klessen, 2012). Different lines compare different models for how the efficiency $\epsilon_{\rm ff}$ scales at finite Σ. *Solid*: Our fiducial model (Eq. 5.4), where $\epsilon_{\rm ff}$ scales with $\Sigma/\Sigma_{\rm crit}$ as expected from simple analytic comparison of feedback and gravity (Eq. 4.1) or detailed SF simulations (Grudić et al. (2018b)). *Dashed*: A model where $\epsilon_{\rm ff}$ scales as a step function, with $\epsilon_{\rm ff} = 0.01$ when $\Sigma < \Sigma_{\rm crit}$, and $\epsilon = \epsilon_{\rm max}$ when $\Sigma > \Sigma_{\rm crit}$. This gives similar results to the fiducial case, demonstrating that the details of *how* $\epsilon_{\rm ff}$ scales do not matter here, so long as it rises efficiently above $\sim \Sigma_{\rm crit}$. *Dotted*: A model with constant $\epsilon_{\rm ff} = \epsilon_{\rm ff}^{\rm max}$, *independent* of surface density Σ. This gives a very steep dependence and can only be reconciled with the observed $\Sigma_{\rm max}$ if we fine-tune $\epsilon_{\rm ff}^{\rm max}$ to a value outside the range predicted by analytic theory and numerical simulations (assuming other mechanisms not considered here cannot reduce it, see Federrath (2015a) and discussion in §4.2.2).

and only then does significant star formation happen, during which global collapse still proceeds. Thus this system is significantly denser than Σ_{crit} at the median star formation time.

4.3 Discussion

We have shown that the observed, apparently universal maximum stellar surface density of dense stellar systems is a natural consequence of feedback-regulated SF physics. Specifically, assuming standard stellar evolution and feedback physics (from e.g. the combination of stellar winds, radiation pressure, SNe, etc.), then as surface densities (Σ) increase, the strength of gravity relative to feedback (assuming some fixed fraction of gas has turned into stars) increases in direct proportion to Σ (Eq. 4.1; see references in § 4.1). Essentially, the strength of gravity scales $\propto G\,M^2/R^2 \propto M\,\Sigma$, while the strength of feedback is proportional to the number of massive stars $\propto M$. So SF becomes more efficient, until the gas depletion timescale becomes comparable to the free-fall time, and the gas is exhausted before it can collapse to yet higher densities (even if it is getting denser as rapidly as possible, by collapsing at the escape velocity). Adopting standard scalings for the efficiency of feedback from simulations of star-forming clouds that span the relevant range of densities (Grudić et al. (2018b)), we show this predicts a $\Sigma_{\rm max}$ in good agreement with that observed.

This explanation has several advantages over the previously-proposed explanations of the maximum surface density from Hopkins et al. (2010). As Grudić et al. (2018b) found that the parameters $\epsilon_{\rm ff}^{\rm max}$ and $\Sigma_{\rm crit}$ were insensitive to spatial scale below $\sim 1\,$kpc, our explanation applies equally well across the *entire* range of sizes of observed stellar systems in Figure 4.1. Grudić et al. (2018b) also found SFE to be relatively insensitive to metallicity, so the $\Sigma_{\rm max}$ we calculate is not specific to a particular metallicity. The main effect of metallicity is the aforementioned opacity to reprocessed FIR emission, but radiation hydrodynamics simulations of SF in the IR-thick limit (Skinner and Ostriker, 2015; Tsz-Ho Tsang and Milosavljevic, 2017) have shown that this can only reduce $\epsilon_{\rm ff}$ by $\sim 30\%$, down to levels consistent with Grudić et al. (2018b). At fixed Σ, this explanation is also insensitive to the three-dimensional density, N-body relaxation time, formation redshift, and escape velocity of the stellar systems (see e.g. Fig. 4 in Grudić et al. (2018b)).

This model also explains why SF in a pre-existing dense stellar system does not generally drive Σ_* beyond $\Sigma_{\rm max}$ – in other words, if one continuously or repeatedly "trickled" gas into e.g. a galaxy center, why could one not continuously add new stars to the central cusp, eventually exceeding $\Sigma_{\rm max}$? The key here is that the pre-existing stellar mass still contributes to the binding force of gravity: recall, Σ in our model is the *total* mass, of gas+stars. This drives up the SFE whenever the *total* surface density exceeds $\Sigma_{\rm crit}$. Thus, for example, if fresh gas falls coherently into the centre of a bulge or dwarf nucleus with $\Sigma \sim \Sigma_{\rm max}$, then the total surface density will exceed $\Sigma_{\rm crit}$ out at larger radii, driving the SFE to high values and exhausting the gas. Multiple SF episodes would therefore be expected to build up the stellar mass by *increasing the radius inside of which* $\Sigma \sim \Sigma_{\rm max}$, *not* by increasing $\Sigma_{\rm max}$.

We also stress, of course, that $\Sigma_{\rm max}$ is not a “hard” limit, either in observations (Figs. 1-2), or in our model (Fig. 4). *Some* gas can survive to reach higher densities (and must, to fuel super-massive black holes, for example), and some gas may be re-injected by stellar mass loss in these dense nuclei. And the key parameters of our model (the efficiency of feedback, which appears in $\Sigma_{\rm crit}$, and $\epsilon_{\rm ff}^{\rm max}$) are not expected to be *precisely* universal, as e.g. variations in IMF sampling (since massive stars dominate the feedback) will alter $\Sigma_{\rm crit}$ and the exact geometry of collapse will alter $\epsilon_{\rm ff}^{\rm max}$ (at the tens of percent level).

Acknowledgements

We thank Arjen van der Wel for providing the galaxy size and mass data from van der Wel et al. (2014). Support for MG and PFH was provided by an Alfred P. Sloan Research Fellowship, NASA ATP Grant NNX14AH35G, and NSF Collaborative Research Grant #1411920 and CAREER grant #1455342. Numerical calculations were run on the Caltech compute clusters ‘Zwicky’ (NSF MRI award # PHY-0960291) and ‘Wheeler’.

Chapter 5

ON THE NATURE OF VARIATIONS IN THE MEASURED STAR FORMATION EFFICIENCY OF GIANT MOLECULAR CLOUDS

M. Y. Grudić, P. F. Hopkins, E. J. Lee, N. Murray, C.-A. Faucher-Giguère, and L. C. Johnson. arXiv e-prints, arXiv:1809.08348, Sep 2018c. Submitted to MNRAS.

Abstract

Measurements of the star formation efficiency (SFE) of giant molecular clouds (GMCs) in the Milky Way generally show a large scatter, which could be intrinsic or observational. We use magnetohydrodynamic simulations of GMCs (including feedback) to forward-model the relationship between the true GMC SFE and observational proxies. We show that individual GMCs trace broad ranges of observed SFE throughout collapse, star formation, and disruption. Low measured SFEs ($\ll 1\%$) are "real" but correspond to early stages; the true "per-freefall" SFE where most stars actually form can be much larger. Very high ($\gg 10\%$) values are often artificially enhanced by rapid gas dispersal. Simulations including stellar feedback reproduce observed GMC-scale SFEs, but simulations without feedback produce 20× larger SFEs. Radiative feedback dominates among mechanisms simulated. An anticorrelation of SFE with cloud mass is shown to be an observational artifact. We also explore individual dense "clumps" within GMCs and show that (with feedback) their bulk properties agree well with observations. Predicted SFEs within the dense clumps are $\sim 2\times$ larger than observed, possibly indicating physics other than feedback from massive (main sequence) stars is needed to regulate their collapse.

5.1 Introduction

Giant molecular clouds (GMCs) are the sites of star formation within the Galaxy (Myers et al., 1986; Shu et al., 1987; Scoville and Good, 1989). They are regions of elevated ($> 100\,\mathrm{cm}^{-3}$) molecular gas density with typical masses $M \sim 4 \times 10^4 - 4 \times 10^6\,\mathrm{M}_\odot$ and radii $R \sim 10 - 100\,\mathrm{pc}$, with a characteristic surface density on the order of $\Sigma \sim 100\,\mathrm{M}_\odot\,\mathrm{pc}^{-2}$ in local galaxies (Solomon et al., 1987; Bolatto et al., 2008). Star-forming GMCs tend to host massive stars and HII regions, have supersonically-turbulent internal gas motions (Larson, 1981), and may be self-gravitating (McKee and Tan, 2003). It is thus believed that the evolution of star-forming clouds is the result of a complex interplay of stellar and protostellar feedback, supersonic magnetohydrodynamic (MHD) turbulence, and gravity in concert (McKee and Ostriker, 2007; Krumholz et al., 2014).

Possibly the most powerful diagnostic of the effects of these physical mechanisms is the *star formation efficiency* (SFE) of a molecular cloud: the fraction of the molecular gas mass converted to stars. The question of what fraction of a molecular cloud's mass is converted to stars, and how quickly, is a fundamental one in star formation theory. Turbulence, magnetic fields, and feedback can all oppose the gravitational collapse that leads to star formation, and in doing so they can reduce the SFE to varying degrees.

The SFE of star-forming clouds has been measured with many different methodologies and tracers of both stellar mass and molecular gas mass[1], but virtually all studies of Local Group clouds have found that typical (i.e. median) values are on the order of 1% (Myers et al., 1986; Mooney and Solomon, 1988; Williams and McKee, 1997; Evans et al., 2009; Lada et al., 2010; Heiderman et al., 2010; Murray, 2011; Lee et al., 2016; Vutisalchavakul et al., 2016; Ochsendorf et al., 2017). However, the cited studies have also generally found considerable *scatter* in the SFE – typically at least 0.5 dex.

If this scatter reflects an actual diversity in the intrinsic scale of the SFE of molecular clouds with otherwise similar properties, then it presents a serious challenge to theories that attempt to explain the SFE of molecular clouds in terms of their large-scale turbulent properties such as the virial parameter or Mach number (e.g. Krumholz and McKee, 2005; Padoan and Nordlund, 2011; Hennebelle and Chabrier, 2011a; Federrath and Klessen, 2012), as the variations in these properties were found to account for less than ~ 0.24 dex of the observed scatter (Lee et al. (2016)). It would also challenge theories that attempt to explain the SFE of molecular clouds in terms of the balance of feedback from massive stars and gravity in a collapse-blowout scenario (Fall et al., 2010; Murray et al., 2010; Dale et al., 2012, 2014; Hopkins et al., 2012a; Myers et al., 2014a; Raskutti et al., 2016; Kim et al., 2017a; Grudić et al., 2018b): stochastic variations in the SFE for a fixed set of cloud parameters tend to be rather small in numerical simulations, and the SFE spread predicted from the variations in the cloud properties that determine the SFE (e.g. surface density for momentum-conserving feedback, escape velocity for expanding HII bubbles)

---

[1] See §5.2 for the various definitions of SFE and how they are measured; our discussion thus far is not specific to any in particular.

are also much smaller than observed. However, a more likely explanation for the scatter comes from the fact that these observationally-inferred efficiencies have intrinsic variation over the lifetime of a GMC that does not necessarily reflect the true SFE. Although one theoretical picture of star-forming clouds is one of quasi-equilibrium (Zuckerman and Evans, 1974; Shu et al., 1987; Krumholz et al., 2006) with a relatively steady star formation rate (SFR), the age distributions of nearby star-forming regions suggest an accelerating SFR (Palla and Stahler, 2000). This can produce large variations in the stellar mass tracer over the lifetime of a single cloud. Such acceleration has a theoretical basis in the behaviour of self-gravitating isothermal supersonic turbulence, wherein it is expected that $\dot{M}_\star \propto t$ from both analytic considerations (Murray and Chang, 2015) and hydrodynamics simulations (Lee et al., 2015; Vazquez-Semadeni, 2015; Murray et al., 2017).

The inferred gas mass will also vary over the lifetime of the cloud: while the effect of gas consumption might be negligible if overall efficiencies are small, molecular gas will also be destroyed and ejected by stellar feedback, so toward the end of a cloud's star-forming lifetime the inferred efficiency might be biased upward. Semi-analytic models of cloud evolution that model both the effects of time-varying SFR and mass loss due to feedback have been found to produce SFE scatter similar to that observed (Feldmann and Gnedin, 2011; Lee et al., 2016). Meanwhile, many simulations of star-forming clouds have been done that consider at least some subset of the important stellar feedback channels (Murray et al. 2010; Vazquez-Semadeni et al. 2010; Dale et al. 2012, 2013; Colin et al. 2013; Dale et al. 2014; Skinner and Ostriker 2015; Raskutti et al. 2016; Howard et al. 2016, 2017; Vazquez-Semadeni et al. 2017; Dale 2017; Kim et al. 2017a; Gavagnin et al. 2017; Grudić et al. 2018b; Kim et al. 2018a, for review see Krumholz et al. 2014; Dale 2015), however of these only Geen et al. (2017) has addressed the specific problem of the interpretation of predicted molecular cloud SFEs vis-a-vis observations. They performed MHD simulations of the evolution of a low-mass molecular cloud with ionizing radiation feedback, and compared simulation results with SFE measurements in nearby star-forming regions derived from YSO counts (e.g. Lada et al., 2010). Notably, they found that errors and biases in the inferred SFE can be quite large depending upon the time of observation during the cloud lifetime. The also found that the stellar feedback was necessary to reproduce observations, finding that observations were most consistent with simulated clouds of mean surface density $\Sigma_{gas} \sim 40\, M_\odot \mathrm{pc}^{-2}$.

In this paper we use a suite of MHD cloud collapse simulations modeling Milky

Symbol	Name	Definition
ϵ_{int}	Integrated SFE	Eq. 5.1
ϵ	Instantaneous SFE	Eq. 5.2
ϵ_{ff}	Per-freefall SFE	Eq. 5.4
ϵ_{obs}	Tracer-inferred instantaneous SFE	Eq. 5.5
$\epsilon_{ff,obs}$	Tracer-inferred per-freefall SFE	Eq. 5.6

Table 5.1: Summary of the various concepts of star formation efficiency discussed in this paper, with defining equations in Section 5.2.

Study	Class	M_{gas} Tracer	$M_\star$ Tracer	$\log \frac{n_{\mathrm{H}_2}}{\mathrm{cm}^{-3}}$	$\log \frac{\Sigma_{gas}}{M_\odot\,\mathrm{pc}^{-2}}$	$\log \epsilon_{obs}$	$\log \epsilon_{ff,obs}$
Wu et al. (2010)	Dense clumps	HCN $1 \rightarrow 0$	FIR	$4.08^{4.68}_{3.38}$	$3.00^{3.38}_{2.63}$	$-1.10^{-0.86}_{-1.76}$	$-1.44^{-0.82}_{-2.03}$
Evans et al. (2014)	GMCs	Dust Extinction	YSO counts	$2.62^{2.99}_{2.33}$	$1.86^{1.97}_{1.76}$	$-1.72^{-1.37}_{-2.19}$	$-1.79^{-1.48}_{-2.38}$
Heyer et al. (2016)	Dense clumps	Dust Emission	YSO counts	$4.11^{4.62}_{3.64}$	$2.78^{3.04}_{2.56}$	$-1.11^{-0.62}_{-1.66}$	$-1.32^{-0.84}_{-1.87}$
Vutisalchavakul et al. (2016)	GMCs	^{13}CO $1 \rightarrow 0$	Free-free, MIR	$2.20^{2.72}_{1.69}$	$1.94^{2.23}_{1.67}$	$-2.26^{-1.82}_{-2.94}$	$-2.40^{-1.99}_{-2.89}$
Lee et al. (2016)	GMCs	^{12}CO $1 \rightarrow 0$	Free-free	$1.36^{1.82}_{0.78}$	$1.88^{2.19}_{1.40}$	$-1.97^{-1.20}_{-2.76}$	$-1.73^{-0.96}_{-2.66}$

Table 5.2: Methodologies, parameter space, and summarized SFE results of several recent studies of star-forming clouds or clumps in the Milky Way. All quantities are given in the format median$^{+\sigma}_{-\sigma}$. *Class*: class of star-forming cloud studied: GMC or dense clump. M_{mol} *Tracer*: method used to obtain the properties of the molecular gas distribution. $M_\star$ *Tracer*: Emission type or object count used to estimate the SFR or stellar mass present. n_{H_2}: number density of molecular hydrogen at the volume-averaged cloud density $3M/\left(4\pi R^3\right)$, in cm^{-3}. Σ_{gas}: of the mean gas surface density $M/\pi R^2$. ϵ_{obs}: observed instantaneous SFE (Eq. 5.5). $\epsilon_{ff,obs}$: Observed per-freefall SFE (Eq. 5.6).

Way GMCs to make a self-consistent prediction for the evolution of the SFE-related observables of a star-forming cloud. By including the effects of feedback from massive stars (in the form of stellar winds, radiation, and supernova explosions), we are able to follow the entire cloud lifetime from initial collapse to eventual disruption by stellar feedback. We will show the SFE observations are reasonably consistent with the hypothesis that GMCs with a given set of bulk properties do not have widely different star formation histories – rather, the observed spread in SFE is comparable to that observed over the lifetime of a single cloud. The model of feedback-moderated star formation can thus explain the observed SFEs of molecular clouds.

5.2 Star Formation Efficiency in Theory and Observation

There are several flavours of star formation efficiency, some of which are motivated by observational convenience and others which are motivated by theory. First, we emphasize that we are interested in SFE as on the scale of individual gas clouds, rather than the SFE integrated over a larger region or an entire galaxy. In principle, these two SFEs can be completely decoupled from one another, and in feedback-regulated models for the Kennicutt (1998a) relation, they generally are to some extent (Thompson et al., 2005; Ostriker and Shetty, 2011; Faucher-Giguère et al., 2013; Orr et al., 2018b).

Among the possible cloud-scale SFEs, the most conceptually straightforward is the “integrated” star formation efficiency, the fraction of the gas mass that is converted to stars across the entire lifetime of a cloud:

$$\epsilon_{int} = \frac{M_\star \left(t = \infty\right)}{M_{gas} \left(t = 0\right)}, \tag{5.1}$$

where $M_\star$ is the total mass in stars formed and M_{gas} is the total gas mass. ϵ_{int} is of particular interest because it is sensitive to the details of stellar feedback physics, as eventually a sufficient number of massive stars will form to expel the gas. ϵ_{int} ultimately determines the mapping between the GMC and star cluster mass functions in a galaxy, and dictates the fraction of stars remaining in a gravitationally-bound clusters after gas expulsion (Tutukov, 1978; Hills, 1980; Mathieu, 1983; Lada et al., 1984; Elmegreen and Clemens, 1985; Baumgardt and Kroupa, 2007). Although this quantity is ubiquitously reported in numerical simulations of star-forming clouds, it is not readily observable. It is difficult to define an unambiguous “initial” gas mass because the evolution of the mass of GMCs is often highly dynamic, subject to ongoing processes of accretion, merging and splitting (Dobbs and Pringle, 2013). However, even supposing that a completely isolated, self-gravitating initial gas mass can be identified, the desired gas and stellar masses must be measured at the beginning and the end of the star-forming lifetime respectively. Thus, although ϵ_{int} is a quantity of great theoretical interest, we must resort to measuring it by proxy.

Instead, one might measure the “instantaneous" star formation efficiency, which is simply the mass fraction of stars associated with the star-forming cloud at a given time (Myers et al., 1986):

$$\epsilon = \frac{M_\star \left(t\right)}{M_\star \left(t\right) + M_{gas} \left(t\right)}. \tag{5.2}$$

ϵ will evolve from 0 to some finite value during the star-forming lifetime of a cloud, so a certain amount of scatter in this quantity is expected even for a population of clouds with identical properties. As $t \longrightarrow \infty$, $\epsilon \longrightarrow \epsilon_{int}$.

The natural timescale for the evolution of self-gravitating objects is the gravitational free-fall time,

$$t_{ff} = \sqrt{\frac{3\pi}{32G\bar{\rho}}} = 13.2\,\mathrm{Myr}\left(\frac{\Sigma}{50\,\mathrm{M_\odot\,pc^{-2}}}\right)^{-\frac{1}{2}}\left(\frac{R}{100\,\mathrm{pc}}\right)^{\frac{1}{2}}, \tag{5.3}$$

where $\bar{\rho}$ is the volume-averaged density of the cloud, $\Sigma = M/\pi R^2$ is the average surface density, and R the effective radius. This fact has motivated the development of theoretical models that predict the *per-freefall* SFE ϵ_{ff}, the fraction of gas converted to stars per freefall time (Krumholz and McKee, 2005; Padoan and Nordlund, 2011; Hennebelle and Chabrier, 2011a; Federrath and Klessen, 2012):

$$\epsilon_{ff} = \frac{\dot{M}_\star(t)\, t_{ff}(t)}{M_{gas}(t)}, \tag{5.4}$$

where $\dot{M}_\star$ is the star formation rate (SFR). These theories typically predict $\epsilon_{ff} \sim 1\%$ for molecular clouds with properties similar to those observed in local spiral galaxies (e.g. Bolatto et al., 2008), solely from the properties of isothermal supersonic turbulence plus a gravitational collapse criterion. Because these physics are scale-free, this could potentially explain the observation that $\epsilon_{ff} \sim 1\%$ on a wide range of scales from galaxies to dense star-forming clumps (Krumholz et al., 2012a).

However, such a steady and universal SFE has not been found in hydrodynamics simulations of self-gravitating isothermal turbulence, with or without a source of turbulent stirring to maintain a constant virial parameter (Kritsuk et al., 2011; Padoan et al., 2012; Lee et al., 2015; Murray et al., 2017). Rather, simulations with virial parameters ~ 1 have found that ϵ_{ff} tends to increase roughly linearly to a saturation point on the order of several tens of percent. This saturation point has a residual dependence upon the magnetic field strength at the factor of 2 level (Federrath and Klessen, 2012). The reason for this discrepancy is that in the presence of self-gravity, the density PDF deviates from the log-normal form assumed by the analytic theories, forming a high-density power-law tail. Such power-law tails have been observed in the extinction maps of star-forming clouds (Kainulainen et al., 2009; Lombardi et al., 2014; Schneider et al., 2015a,b). When this power-law tail is incorporated into analytic theory, the effect upon the SFE is captured more accurately (Burkhart, 2018).

Grudić et al. (2018b) (hereafter Grudić et al. (2018b)) argued that $\epsilon_{ff} \sim 1\%$ is the typical value observed for molecular clouds because feedback from massive stars is able to prevent runaway star formation, and that the ubiquity of the observed 1%

value is a consequence of the lack of variation of cloud surface density Σ, which they found determined both ϵ_{int} and ϵ_{ff}. However, this cannot explain slow star formation in regions where massive stars are absent. Federrath (2015b) found that protostellar outflow feedback can bring ϵ_{ff} down to values on the order of 1% in the regime of low-mass cluster formation, but this mechanism is unlikely to scale up to more massive systems. It is thus possible that the protostellar and massive stellar feedback complement each other in limiting the per-freefall SFE of molecular clouds on different scales.

Measuring ϵ and ϵ_{ff} requires some estimate of the stellar mass formed and the currently-present gas mass. We distinguish between the true instantaneous SFE ϵ and its observational tracer-inferred value:

$$\epsilon_{obs} = \frac{M_{\star,tr}\left(t\right)}{M_{\star,tr}\left(t\right) + M_{mol,tr}\left(t\right)}, \tag{5.5}$$

where $M_{mol,tr}$ and $M_{\star,tr}$ are the tracer-inferred molecular gas and stellar masses, respectively. Similarly, we define the tracer-inferred proxy for ϵ_{ff}:

$$\epsilon_{ff,obs} = \frac{M_{\star,tr}\left(t\right)\, t_{ff}\left(t\right)}{M_{mol,tr}\left(t\right)\, \tau_{tr}}, \tag{5.6}$$

where we introduce the characteristic lifetime τ_{tr} of the species being traced, so that the SFR $\dot{M}_{\star}$, which is not directly observable, may be estimated as $M_{\star,tr}/\tau_{tr}$.

5.2.1 Stellar Mass Tracers

There are several methods for estimating $M_{\star}$. The most readily-measured tracer of stellar mass is the emission associated with HII regions, such as far IR (Myers et al., 1986), mid IR (Vutisalchavakul et al., 2016), or free-free emission (Murray and Rahman, 2010; Lee et al., 2012; Vutisalchavakul et al., 2016). This flux is dominated by the contribution from the reprocessed radiation from young, massive stars, and effectively traces the mass in stars younger than the ionizing flux-weighted mean stellar lifetime of a stellar population, $\tau_{MS} = 3.9\,\mathrm{Myr}$ (McKee and Williams, 1997; Murray, 2011). We refer to this stellar mass as the "live" stellar mass, $M_{\star,live}$. $M_{\star,live}$ can underestimate the total stellar mass formed in a cloud if its star formation history spans longer than τ_{MS}, which appears to be the case for a majority of local GMCs (Kawamura et al., 2009; Fukui and Kawamura, 2010; Murray, 2011; Lee et al., 2016).

Another tracer of the formed stellar mass is the mass of young stellar objects (YSOs), M_{young}, which can be measured in sufficiently well-resolved star-forming clouds or clumps (Evans et al., 2009; Heiderman et al., 2010; Evans et al., 2014; Heyer et al., 2016). In this case the measured mass traces the stars formed over the characteristic evolutionary timescale τ_{SF} for the class of YSO that is being counted, typically taken to be 0.5 Myr and 2 Myr for Class I and II YSOs respectively (Evans et al., 2009).

Whatever the stellar mass tracer, the characteristic lifetime τ_{tr} introduces certain biases in the inferred stellar mass. If the star-forming lifetime of a cloud scales with the freefall time, then $M_{\star,tr}/M_\star \sim \tau_{tr} t_{ff}$, so $M_{\star,tr}$ would typically underestimate $M_\star$ in less-dense clouds that have longer freefall times. On the other hand, assuming $\dot{M}_\star = M_{\star,tr}/\tau_{tr}$ provides a reasonably accurate estimate of the SFR of clouds with lifetimes longer than τ_{tr}, averaged over τ_{tr}, but if the star formation has only been occurring for a shorter time $\Delta t \ll \tau_{tr}$, this method will under-estimate the true SFR by a factor $\sim \Delta t/\tau_{\rm tr}$.

When comparing simulations to observations, we will model stellar mass tracers from simulation data in a straightforward manner, simply taking $M_{\star,tr}$ to be the mass of the star particles that formed more recently than τ_{tr}.

5.2.2 Gas Mass Tracers

The ro-vibrational lines of molecular hydrogen are not excited in cold molecular clouds, so it is also necessary to use a tracer to measure M_{mol}. Most commonly, this tracer is CO, the second most common molecule in the cold ISM and its primary coolant. M_{mol} can be estimated by measuring the total luminosity L_{CO} of a CO rotational transition and convert this to a gas mass via the CO-to-H_2 conversion factor X_{CO} (Bolatto et al., 2013). Most studies of molecular clouds measure the brightest line, the ^{12}CO $J = 1 \rightarrow 0$ transition, which traces the gas mass of molecular number density $n_{\rm H_2} > 100\,{\rm cm}^{-3}$. Higher transitions, or emission from the less-abundant ^{13}CO species, trace higher densities, $> 10^3\,{\rm cm}^{-3}$.

In addition to CO observations, we shall consider observations of dense clumps within GMCs. Dense clumps are typically traced by the HCN $J = 1 \rightarrow 0$ transition, which generally have been understood to trace the gas mass of density $10^4\,{\rm cm}^{-3}$ or greater (Gao and Solomon, 2004), however recent work has brought into question whether HCN emission really originates from such high density gas (Kauffmann et al., 2017; Goldsmith and Kauffmann, 2017). Gas at this density is believed to have a more direct relationship with star formation, as there is a proportional relationship between FIR luminosity and HCN luminosity on the scale of galaxies (Gao and Solomon, 2004; Wu et al., 2005) and dense clumps within the Milky Way (Wu et al., 2010). This is also roughly the threshold above which Lada et al. (2010) proposed a linear relationship between gas mass (derived from dust extinction mapping) and the SFR derived from YSO counts. However, the correspondance between the gas mass actually measured by Lada et al. (2010) and the gas mass denser than $10^4\mathrm{cm}^{-3}$ is questionable (Clark and Glover, 2014). We will be able to examine this relationship in our simulations (§5.5).

All of these methods of tracing the gas distribution of a cloud have their own uncertainties, biases, and limitations. A fully rigorous comparison between theory and observations would use a calculation that models the relevant dust and molecular abundances self-consistently. One would then model the species' observed emission or extinction self-consistently via a radiative transfer calculation to produce mock observations to which the same analysis can be applied as the actual observation. We consider this to be beyond the scope of this work, and throughout we shall simply compare the simulated gas mass directly with observationally-reported gas masses. We will model M_{mol} from the simulation data in a straightforward manner, using the Krumholz and Gnedin (2011) prescription to derive the abundance of H_2, and assuming that a faithful tracer of H_2 is available.

5.2.3 Data Compilation

We will compare simulations with measurements from several recent studies that have measured ϵ and ϵ_{ff} in both GMCs and dense clumps in the Milky Way with various methodologies. These studies, their tracers, and their results are summarized in Table 5.2. We consider star-forming GMC data from Evans et al. (2014), Vutisalchavakul et al. (2016), and Lee et al. (2016). We also consider data from star-forming dense clumps from Wu et al. (2010) and Heyer et al. (2016).

All of the studies in Table 5.2 report values for $\epsilon_{ff,obs}$, but only Lee et al. (2016) reported ϵ_{obs} (their ϵ_{br}). Where stellar masses are not reported, the measured stellar mass $M_{\star,tr}$ is obtained by simply multiplying reported SFRs by the tracer lifetime τ_{tr}. For Vutisalchavakul et al. (2016), we compute it by multiplying the SFRs inferred from the clouds' 24 μm luminosities by the ionization-weighted mean stellar lifetime $\tau_{MS} = 3.9\,\mathrm{Myr}$. We compute the stellar mass in the Wu et al. (2010) clumps by assuming that their IR luminosities are due to reprocessed radiation from a stellar population with a Kroupa (2002) IMF, and hence:

$$M_{\star,tr} = 8 \times 10^{-4} \left(\frac{L_{IR}}{L_{\odot}}\right) M_{\odot} \tag{5.7}$$

M ($M_\odot$)	R (pc)	Random Seed	Modifications	t_{ff} (Myr)	$t_{2\sigma}$ (Myr)	$\log \frac{n_{H_2}}{\mathrm{cm^{-3}}}$	$\log \epsilon_{int}$	$\log \epsilon_{obs}$	$\log \epsilon_{ff,obs}$
2×10^4	10	1		3.79	2.48	1.83	-1.39	$-0.79^{-0.68}_{-1.08}$	$-0.86^{-0.52}_{-1.45}$
2×10^4	10	1	No Feedback	3.79	7.27	1.83	-0.23	$-0.18^{-0.07}_{-1.08}$	$-0.40^{0.12}_{-1.49}$
2×10^4	10	2		3.79	3.08	1.83	-1.37	$-1.28^{-0.96}_{-1.69}$	$-1.44^{-0.70}_{-2.10}$
2×10^4	10	3		3.79	3.19	1.83	-1.36	$-1.06^{-0.02}_{-1.40}$	$-1.06^{0.20}_{-1.86}$
2×10^5	30	1		6.22	5.12	1.39	-1.43	$-1.45^{-0.91}_{-2.44}$	$-1.58^{-0.64}_{-2.67}$
2×10^5	30	1	No Feedback	6.22	14.19	1.39	-0.16	$-0.12^{-0.04}_{-1.20}$	$0.16^{0.43}_{-1.39}$
2×10^5	30	2		6.22	6.64	1.39	-1.45	$-1.48^{-0.99}_{-2.10}$	$-1.57^{-0.63}_{-2.32}$
2×10^5	30	3		6.22	5.06	1.39	-1.42	$-1.35^{-0.99}_{-2.28}$	$-1.47^{-0.67}_{-2.53}$
2×10^6	100	1		11.98	15.83	0.825	-1.45	$-1.55^{-0.99}_{-2.64}$	$-1.38^{-0.28}_{-2.60}$
2×10^6	100	1	No Feedback	11.98	28.61	0.825	-0.14	$-0.44^{-0.09}_{-1.62}$	$-0.21^{0.42}_{-1.54}$
2×10^6	100	1	No Radiative Feedback	11.98	13.72	0.825	-1.10	$-1.33^{-0.54}_{-2.21}$	$-1.17^{0.01}_{-2.16}$
2×10^6	100	1	No SNe	11.98	14.19	0.825	-1.46	$-1.57^{-1.03}_{-2.43}$	$-1.41^{-0.46}_{-2.39}$
2×10^6	100	1	No OB Winds	11.98	12.66	0.825	-1.59	$-1.52^{-1.27}_{-2.36}$	$-1.36^{-0.75}_{-2.31}$
2×10^6	100	1	Radiative Feedback Only	11.98	14.89	0.825	-1.59	$-1.39^{-1.00}_{-2.26}$	$-1.20^{-0.37}_{-2.22}$
2×10^6	100	1	SN Feedback Only	11.98	12.43	0.825	-0.96	$-1.03^{-0.65}_{-2.22}$	$-0.90^{-0.15}_{-2.18}$
2×10^6	100	2		11.98	15.83	0.825	-1.53	$-1.65^{-1.22}_{-2.77}$	$-1.51^{-0.63}_{-2.71}$
2×10^6	100	3		11.98	10.79	0.825	-1.57	$-1.70^{-1.09}_{-3.00}$	$-1.62^{-0.60}_{-2.97}$

Table 5.3: Parameters and basic results of the simulations. (1) M: the initial total gass mass. (2) R: the initial cloud radius. (3) Random seed: the random realization of isothermal MHD turbulence used for the initial conditions. (4) Modifications: variations of subset of feedback mechanisms included. (5) t_{ff}: the initial freefall time computed from the mean density $3M/4\pi R^3$. (6) $t_{2\sigma}$: the length of time between the $\pm 2\sigma$ star formation times. (7) n_{H_2}: volume-averaged initial number density of H_2. (8) ϵ_{int}: fraction of M converted to stars by the end of the simulation. (9-11) Star formation efficiencies, see Table 5.1. $\log \epsilon_{obs}$ and $\log \epsilon_{ff,obs}$ are given in the format median$^{+\sigma}_{-\sigma}$, with the quantiles computed over "observable" lifetime of the cloud, during which massive stars are present and the cloud is above the assumed molecular gas surface density sensitivity threshold of $10\,M_\odot\,\mathrm{pc}^{-2}$ (see §5.4.2).

and we consider only those clumps with $L_{IR} > 10^{4.5}\,L_\odot$ so that the IMF is well-sampled (Heiderman et al., 2010). The stellar mass obtained directly from YSO counting by Heyer et al. (2016) is a lower bound on M_{young}, while an upper bound is obtained by correcting the total stellar mass assuming a Kroupa IMF. Throughout, we will take the IMF-corrected SFEs computed in this way, but emphasize that these are in fact upper bounds. For consistency with Heyer et al. (2016), we estimate SFRs in the Wu et al. (2010) clumps via Equation 5.6 assuming the same $\tau_{tr} = 0.5$Myr as for Heyer et al. (2016). Under the above assumptions, SFEs for both catalogues of dense clumps are in good agreement.

5.3 Simulations

We perform a suite of 3D MHD simulations of GMC collapse, star formation, and cloud disruption with the GIZMO[2] code (Hopkins, 2015; Hopkins and Raives, 2016), with the prescriptions for star formation, cooling and stellar feedback developed for the Feedback In Realistic Environments (FIRE) simulations (Hopkins et al., 2014)[3]. The simulations are similar in methodology to the Grudić et al. (2018b) simulations, using the Meshless Finite Mass (MFM) Lagrangian MHD method (Hopkins and Raives, 2016) and feedback prescriptions as in FIRE-2 (Hopkins et al., 2018a). However, the simulations differ in the following ways that we shall describe in turn: the initial conditions (ICs), the star formation prescription, and a modification of the feedback routines that accounts for the effects of under-sampling the IMF when the total stellar mass is small. The reader is referred to Grudić et al. (2018b) paper for a description of the general results and behaviour of this type of simulation, and to Hopkins et al. (2018a) for the details of the numerical implementations of feedback and ISM physics.

5.3.1 Initial Conditions

To model Milky Way GMCs more closely than Grudić et al. (2018b), we simulate three points in mass-radius parameter space, with masses $M = 2 \times 10^4\,\mathrm{M}_\odot$, $2 \times 10^5\,\mathrm{M}_\odot$, and $2 \times 10^6\,\mathrm{M}_\odot$, and radii $R = 10\,\mathrm{pc}$, $30\,\mathrm{pc}$, and $100\,\mathrm{pc}$ respectively, for a mean surface density of $64\,M_\odot \mathrm{pc}^{-2}$. This parameter space falls within the range of parameters in which most star-forming GMCs in the MWG lie (e.g. Miville-Deschenes et al., 2017). However, we emphasize that selecting a single surface density is not fully representative of a real GMC population, and since we expect the SFE to be dependent on the surface density, we expect there to be residual variations in SFE that this parameter study does not account for.

Unlike Grudić et al. (2018b), the initial velocity field has no bulk rotation component to support it at constant mean surface density – it is dominated by turbulent motions, which is more consistent with the properties of GMCs in the Local Group, which have quite weak rotation (Braine et al., 2018). Krumholz et al. (2012b) found that the initial rise of the SFR was artificially fast when an initial tophat-density distribution was used, as in Grudić et al. (2018b). As this can potentially affect the SFE observables of interest, we follow Krumholz et al. (2012b) by using ICs extracted

---

[2] A public version of this code is available at `http://www.tapir.caltech.edu/~phopkins/Site/GIZMO.html`.

[3] `http://fire.northwestern.edu`

from a simulation of driven isothermal supersonic MHD turbulence without self-gravity. The turbulent forcing is realized as a Orstein-Uhlenbeck process as in Bauer and Springel (2012), with purely solenoidal forcing, normalized so that the RMS Mach number saturates to ~ 10 and the turbulent plasma β to ~ 20 (e.g. Federrath et al., 2014). For each set of cloud parameters, we effectively sample three independent statistical realizations of the turbulent ICs by extracting snapshots separated by 10 crossing times each. From each of these snapshots, we excise a sphere centred upon the density-weighted centre of mass and rescale the particle masses, positions, and velocities to achieve the desired mass and radius and virial parameter $\alpha_{vir} = \frac{2E_{turb}}{|E_{grav}|} = 2$. The magnetic field is rescaled to preserve the turbulent plasma β from the original turbulent box simulation. In all simulations, the gas mass is initially resolved in 10^6 particles.

5.3.2 Star Formation

We handle star formation with an accreting sink particle prescription, derived from Federrath et al. (2010) and described fully in Guszejnov et al. (2018b). To summarize, gas cells are converted to sink particles when they are self-gravitating at the resolution scale (including thermal, turbulent, and magnetic energy contributions), or equivalently, the effective Jeans mass is no longer resolvable. They must also be a local density maximum within their hydrodynamic stencil of nearest neighbor cells, and be a site of converging flow ($\nabla \cdot \mathbf{v} < 0$). Gas cells are accreted by an existing sink particle if they are gravitationally bound to it and fall within an accretion radius of 0.01pc. This is a more appropriate method for this problem than the discretization of stellar mass into equal-mass star particles used in Grudić et al. (2018b), as the mass resolution of the simulations is always $\ll 100 M_{\odot}$, sufficient to resolve the formation of some stellar-mass objects.

5.3.3 Stellar Feedback

A fully self-consistent determination of the stellar feedback budget would require a self-consistent treatment of massive star formation, which is currently an open physics problem that is sensitive to radiative transfer physics on scales of 1000 AU or less (Zinnecker and Yorke, 2007; Krumholz et al., 2009; Tan et al., 2014; Rosen et al., 2016), which we do not resolve in our simulations. Therefore, in the spirit of Grudić et al. (2018b), we choose not to attempt to model the IMF self-consistently, and assume that the mass, energy, and momentum fluxes from stellar feedback are consistent with that from a single stellar population with a well-sampled Kroupa

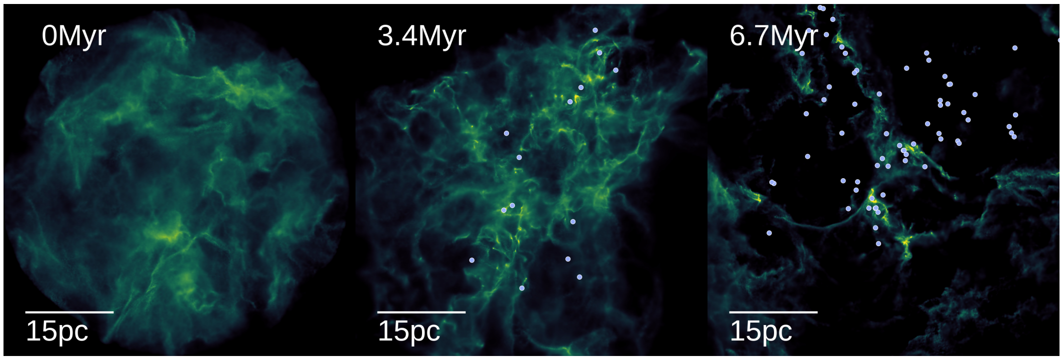

Figure 5.1: Gas surface density map showing the evolution of a simulated GMC with mass $2 \times 10^5 M_\odot$ and radius 30pc, with a dynamic range of $10 - 1000 M_\odot\,\mathrm{pc}^{-2}$. The cloud undergoes a turbulent, disordered collapse into stars until the combined feedback of massive stars (shown as dots) destroys the cloud. A movie of this sequence can be found at `http://www.tapir.caltech.edu/~mgrudich/M2e5_R30.mp4`.

(2002) IMF. We discretize this feedback budget among sink particles as in Sormani et al. (2017) and Su et al. (2018), giving each particle a discrete number of 'O-stars' sampled from a Poisson distribution with mean $\lambda = \frac{\Delta m}{100 M_\odot}$, where Δm is the mass of the particle. The O-star number is incremented by a Poisson-sampled value whenever a sink particle is spawned or accretes. This captures some of the effect of under-sampling the IMF in low-mass clusters. Fluxes due to stellar feedback are scaled in proportion to the number of O stars a particle has, and in the limit where the total stellar mass is $\gg 100 M_\odot$, the IMF-averaged stellar feedback budget is recovered.

5.4 GMC Star Formation Histories

5.4.1 True SFE Values

In all simulations, the cloud initially collapses in a disordered manner, with multiple centres of collapse and little initial global contraction (see Figure 5.1). Stars eventually form in dense, gravitationally-bound subregions until stellar feedback is sufficient to halt collapse and accretion locally. Eventually, a sufficient stellar mass forms that the entire cloud is disrupted by stellar feedback and star formation ceases. At this point, a fraction ϵ_{int} of the initial gas mass has been converted to stars. As has generally been found in similar simulations, an order-unity fraction of the gas mass is rapidly converted to stars on the freefall timescale when stellar feedback is neglected. When stellar feedback is included, ϵ_{int} is always a few per cent and does not vary greatly across our parameter space. This is because all of the cloud models have

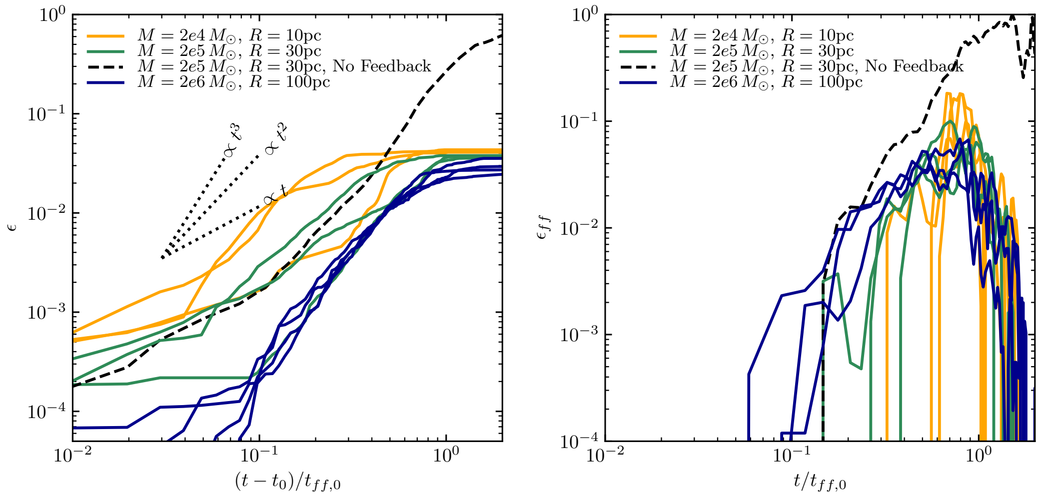

Figure 5.2: Star formation histories of the simulations. *Left*: the fraction of the initial gas mass converted to stars $M_\star/M_{tot}$ as a function of time since the formation of the first sink particle at t_0, in units of the global cloud freefall time t_{ff}. In most cases, the stellar mass is $\propto (t-t_0)^2$ as the SFR ramps up, so there is intrinsic variation in the SFR that would translate into a range of observed ϵ_{ff}. Eventually, sufficient stellar mass forms to disrupt the cloud via stellar feedback, and $M_\star/M \rightarrow \epsilon_{int}$, which is on the order of a few per cent when stellar feedback is included, but approaches 100% in absence of feedback.

the same mean initial surface density, which determines ϵ_{int} for feedback-disrupted self-gravitating molecular clouds (Fall et al., 2010; Grudić et al., 2018b). This is in good agreement with the median value of ϵ_{obs} found in Milky Way GMCs (see Table 5.2), however much greater and smaller values are also observed, which we will address in §5.4.2. The variation in ϵ_{int} for different random realizations of a given point in parameter space is also quite small (< 0.1 dex). Therefore, even when fully-turbulent initial conditions are considered, the instrinsic SFE variations due to variations in specific microstates of the initial conditions clearly cannot explain the observed range of SFE values.

In Table 5.3, we report $T_{2\sigma}$, the length of time containing 95% of star formation, as well as ϵ_{int} and the average value of ϵ_{ff} over entire the star formation history. Here the freefall time used to compute ϵ_{ff} is that computed from the initial volume-averaged density, $t_{ff,0} = \frac{\pi}{2\sqrt{2}}\sqrt{\frac{R^3}{GM}}$, however in §5.4.2 we will consider the effects of a dynamic mean cloud density upon the observed ϵ_{ff}. The volume-averaged density tends to increase slightly due to turbulent dissipation in the initial stages of cloud collapse, but it then decreases rapidly as stellar feedback launches outflows.

In general $t_{2\sigma} \sim t_{ff,0}$, so most star formation is found to take place within a single initial freefall time (although this can be several *local* free-fall times in the denser gas that forms as fragmentation proceeds), as found in Grudić et al. (2018b) and similar works. In all instances, the SFR, and hence ϵ_{ff}, is found to vary significantly throughout the GMC lifetime. The SFR tends to continue to increase until star formation is quenched abruptly when the molecular cloud is disrupted by feedback. In Figure 5.2 we present the detailed star formation histories of all simulations, plotting ϵ and ϵ_{ff} as functions of time in panels 1 and 2 respectively. We find that the initial growth of ϵ from the beginning of star formation is superlinear, with the exception of the $M = 2 \times 10^4\,\mathrm{M}_{\odot}$ runs, and is typically initially well-described by a power-law with index close to 2, as has been predicted analytically and found in hydrodynamic simulations without stellar feedback (Murray and Chang, 2015; Lee et al., 2015; Murray et al., 2017) and with a more limited subset of feedback channels (Raskutti et al., 2016; Vazquez-Semadeni, 2015; Geen et al., 2017). However, this state of affairs does not continue indefinitely, and stellar feedback eventually causes the SFR to level off and eventually fall to 0.

The lowest-mass cloud models, with $M = 2{\times}10^4 M_{\odot}$, have the noisiest star formation histories (e.g. Fig 5.2 panel 2). These clouds only ever only form 4 – 8 massive stars before being disrupted, so the proportional effect of an individual massive star on the overall cloud evolution is much greater than in the more massive clouds, which form tens to hundreds of massive stars, making the onset of feedback effectively "smoother". The more pronounced effect of the discreteness of massive stars also explains the shallower, nearly linear initial growth of the SFR in the low-mass clouds compared to the more massive ones. We have confirmed that when feedback is disabled, the growth in stellar mass is superlinear as in the more massive cloud models.

Because $t_{2\sigma} \sim t_{ff,0}$, ϵ_{ff} is on average of the same order as ϵ_{int}, which is $\sim 100\%$ without stellar feedback and several per cent with stellar feedback. To summarize, we find the key results of the simulations of Grudić et al. (2018b) concerning the true star formation efficiencies of molecular clouds still hold for the more realistic GMC and stellar feedback models we have considered here. Most star formation occurs within a single $t_{ff,0}$, and during this time only several per cent of the initial gas mass is converted to stars, because this fraction is sufficient to disrupt the cloud via stellar feedback. This fraction ϵ_{int} is approximately the same for clouds of the same surface density, and depends upon spatial scale only weakly. We also find

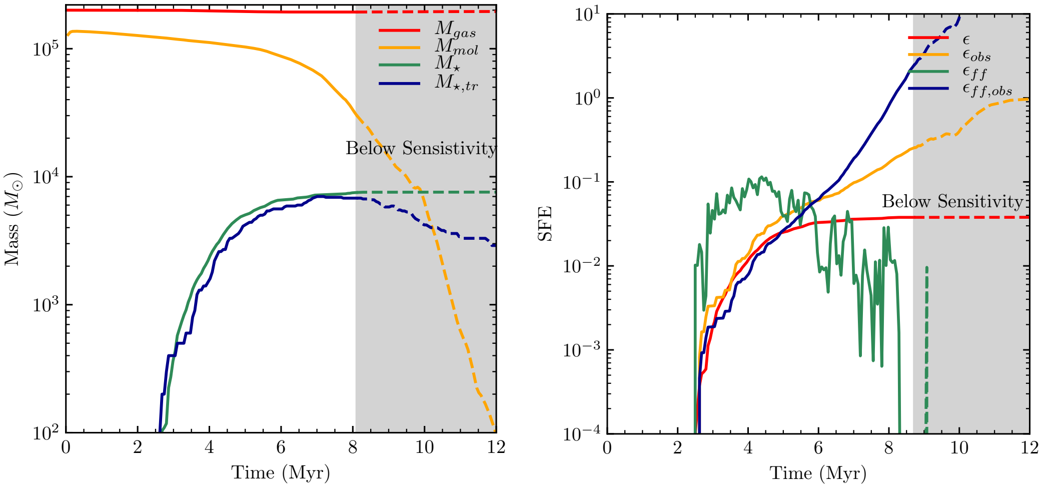

Figure 5.3: Comparison of the true and observable masses and SFEs in the simulation with $M = 2 \times 10^5 M_\odot$, $R = 30$pc and random seed 1. Solid lines denote the portion of the lifetime during which the cloud would plausibly be identified in a star-forming GMC catalogue according to the criteria given in §5.4.2. *Left:* total gas mass, molecular gas mass, total stellar mass, and traced stellar mass (with $\tau_{tr} = 3.9$Myr) as a function of time. Both the observed molecular gas and stellar mass underestimate the true gas and stellar masses present at all times. The observed molecular gas mass decreases rapidly once cloud disruption begins. The observed stellar mass also decays to 0 at late times, but not necessarily as rapidly as the observed gas mass, possibly leading to large observed SFE. *Right:* various measures of SFE (see §5.2 and Table 5.1)

a time-varying ϵ_{ff} that initially grows in a manner similar to what was found in previous calculations that did not include stellar feedback (Murray and Chang, 2015; Lee et al., 2015; Murray et al., 2017), however stellar feedback eventually halts the growth. We will now consider how these highly dynamic star formation histories would imprint upon the observed distributions of star formation efficiencies.

5.4.2 Tracer-Inferred Values

Modeling of observables

To forward-model ϵ_{obs} and $\epsilon_{ff,obs}$ from the simulations, we must estimate the observationally-inferred $M_\star$ and M_{mol}. One possibility is to perform ISM chemistry and radiative transfer calculations to directly model the observed emission maps, and apply the same procedure for identifying clouds and correlating them with young stars as was used in a particular study. This would be necessary to compare with observations in detail. This approach is possible in principle, but here we merely

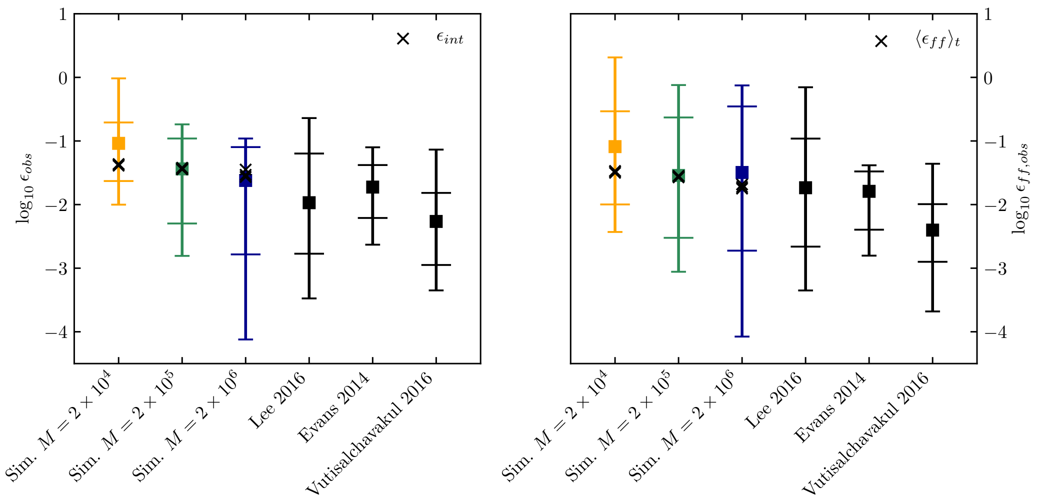

Figure 5.4: Quantiles of the distributions of ϵ_{obs} (left) and $\epsilon_{ff,obs}$ (right) arising from "observing" simulated molecular clouds at random points in their observable star formation history, compared with observed cloud SFEs in the Milky Way. Points plot median values, inner whiskers plot $\pm\sigma$ quantiles, and outer whiskers plot $\pm2\sigma$ quantiles. Both ϵ_{obs} and $\epsilon_{ff,obs}$ can both be measured to be considerably higher or lower than the true typical efficiencies (overlaid as black markers), depending on when they are measured. The spread in ϵ_{obs} is as great as 0.8dex and the spread in $\epsilon_{ff,obs}/\langle\epsilon_{ff}\rangle$ is $0.8-1.1$dex. The median observed ϵ_{obs} is anticorrelated with cloud mass, as has been observed (Murray, 2011; Lee et al., 2016). Details of how ϵ_{obs} and $\epsilon_{ff,obs}$ are modeled are described in §5.4.2.

aim to explain various general features and trends from many studies of widely varying methodology, so in this initial investigation we use simple approximations, leaving a more detailed treatment to future work.

We estimate the observed $M_{\star,tr}$ in the simulation data by taking $M_{\star,live}$, approximately the mass in stars younger than the ionization-weighted mean stellar lifetime 3.9 Myr (Murray, 2011). We estimate $M_{mol,tr}$ by assuming that a perfect tracer of H_2 is available, and simply take the actual molecular gas mass M_{mol}. We do this by calculating the molecular fraction f_{H_2} of each gas cell according to the analytic prescription of Krumholz and Gnedin (2011), which was found to agree well with detailed chemistry and radiation transfer calculations. This prescription requires an estimate of the effective dust optical depth τ_c at the position of each gas cell. This is calculated on-the-fly in the simulations using a local Sobolev-like column density estimator (Hopkins et al., 2012a), but we compute τ_c more accurately in post-processing by ray-tracing the dust opacity field to infinity along 64 rays on an equal-area spherical grid. An optical depth τ_i is thus obtained for each ray, and the effective optical depth τ_c is that which gives the spherically-averaged extinction over all angles θ and ϕ:

$$\exp\left(-\tau_c\right) = \frac{1}{4\pi}\int \exp\left(-\tau\left(\theta,\phi\right)\right)\,\mathrm{d}\Omega \approx \langle \exp\left(-\tau_i\right)\rangle_i, \tag{5.8}$$

where $\langle\cdot\rangle_i$ denotes the mean value over all rays.

Modeling $\epsilon_{ff,obs}$ requires a measurement of t_{ff}, which depends upon the mean cloud density and hence its effective volume. For this, we use the 3D equivalent of the technique used in Miville-Deschenes et al. (2017) for deriving effective cloud volumes from CO emission maps. We take the volume of the ellipsoid with axes given by the the eigenvalues of the 3D $f_{\mathrm{H_2}}$-weighted covariance matrix of the gas distribution. Given eigenvalues λ_i, the observed effective volume is taken as $V = 4\pi R_{eff}^3/3$, where $R_{eff} = \left(\lambda_1\lambda_2\lambda_3\right)^{1/6}$.

Lastly, we must account for observational selection effects and reject simulation data that clearly would not be identified as a data point in a catalogue of star-forming GMCs. We measure all relevant SFE statistics only during the fraction of the GMC's lifetime during which it could possibly be counted as an association between emission from young stars and molecular gas emission. We do this by including only simulation snapshots satisfying two criteria:

- Both molecular gas and stars younger than 3.9Myr are present. This effectively determines the beginning of the observable time interval.
- The mean molecular gas surface density $\Sigma_{gas} = M_{mol}/\pi R_{eff}^2$ is $> 10 M_\odot\,\mathrm{pc}^{-2}$, corresponding to the -2σ quantile of measured mean surface density of the star-forming GMCs in Lee et al. (2016). This approximates the latter boundary of the observable cloud lifetime, since $\Sigma_{gas} \rightarrow 0$ as the cloud is disrupted.

Evolution of observables

In the first panel of Figure 5.3 we plot the evolution of the true and observable masses and SFEs in the simulation with $M = 2\times10^5 M_\odot$, $R = 30$pc, and random seed 1. M_{mol} is initially close to the actual total gas mass present, missing only the gas mass in the low surface density tail of the log-normal turbulent column density PDF (e.g. Thompson and Krumholz, 2016), which is not self-shielding. We therefore expect that M_{mol} measured in observations is a reasonably faithful estimate of the total gas mass of molecular clouds that have not yet undergone significant star formation, insofar as the tracer-to-$\mathrm{H_2}$ conversion factor is accurate.

As massive stars form, M_{mol} begins to decrease increasingly rapidly as stellar feedback starts to disrupt the cloud. Two physical effects cause this: gas launched in feedback-driven outflows tends to expand to the point that it is no longer self-shielding to the UV background, and gas near massive stars is ionized, forming HII regions. Once the cloud is fully disrupted and star formation has ceased, M_{mol} decays rapidly toward 0 with a roughly exponential behaviour with an e-folding time of only $\sim 0.5\,\mathrm{Myr}$.

$M_{\star,tr}$ always underestimates $M_\star$, but it is a reasonably good estimate during the initial ramp-up of the SFR because the total stellar mass formed is dominated by the most recently-formed stars. Toward the end of the star formation history, when the SFR starts to drop, $M_{\star,tr}$ begins to underestimate $M_\star$ more significantly, eventually decaying to 0 after star formation has ceased. The observable masses in all other simulations follow these same general patterns as the run shown in Figure 5.3. However, we do find that more massive clouds tend to have a longer span of time during which $M_{\star,tr}$ underestimates $M_\star$ noticeably. This is due to their longer star-forming lifetimes compared to the tracer lifetime ($t_{ff} \propto M^{1/4}$ at constant Σ).

In the second panel of Figure 5.3 we plot the evolution of the true and observable SFEs that result from these evolving stellar and gas masses. ϵ increases monotonically toward ϵ_{int}, but ϵ_{obs} does not necessarily approach a constant because it is a ratio of two rapidly-changing observed masses. During the cloud disruption phase, M_{mol} ϵ_{ff} rises with the initial increase in SFR, peaks, and decays to 0 as the cloud is disrupted, but again $\epsilon_{ff,obs}$ continues to increase without bound even more rapidly than ϵ_{obs}. This is due to a combination of effects: the ratio $M_{\star,tr}/M_{mol}$ increases rapidly, and the observed t_{ff} also increases due to the expanding effective cloud volume. The observed $\epsilon_{ff,obs}$ can be doubly boosted by orders of magnitude beyond the true ϵ_{ff}, which never exceeds a few per cent.

Distributions of ϵ_{obs} and $\epsilon_{ff,obs}$

The manner in which ϵ_{obs} and $\epsilon_{ff,obs}$ vary throughout the cloud lifetime will imprint upon the distributions of values observed for an ensemble of clouds at random points in their lifetimes. In Figure 5.4 we plot the quantiles of these distributions by cloud mass and compare them with the observations of Lee et al. (2016), Evans et al. (2014), and Vutisalchavakul et al. (2016). For each simulation we also overlay ϵ_{int} for each simulation for comparison with ϵ_{obs} and the true per-freefall SFE averaged over the star-forming lifetime, $\langle\epsilon_{ff}\rangle_t$, for comparison with $\epsilon_{ff,obs}$.

The ϵ_{obs} and $\epsilon_{ff,obs}$ distributions from the simulations are able to reproduce all essential features of the observed ones: they are all fairly broad, with significant scatter about a median value on the order of 1%. The spreads in ϵ_{obs} and $\epsilon_{ff,obs}$ dwarf the true variation in ϵ_{int} and the time-averaged $\langle \epsilon_{ff} \rangle_t$ from one cloud to another. Heavy lower tails result from the initial gradual growth of the SFR (Figure 5.2). Excursions of ϵ_{obs} in excess of 10% occur due to the rapid depletion of molecular gas, and even heavier upper tails are found for $\epsilon_{ff,obs}$ because this effect is combined with an increase in the observed t_{ff} as the cloud expands.

Trends in observed SFE with GMC mass

The median observed SFEs are generally fairly close to the true SFEs. However, although there is no systematic trend in the true ϵ_{int} with cloud mass, the median ϵ_{obs} is anticorrelated with cloud mass, scaling as $\epsilon_{obs} \propto M^{-0.25}$. This trend is also found in observations (Murray, 2011; Lee et al., 2016), with Lee et al. (2016) finding $\epsilon_{obs} \propto M^{-0.31}$, and has several possible explanations.

The use of free-free emission as a stellar mass tracer introduces a selection bias for star-forming regions that host massive stars. Assuming a universal and stochastically-sampled IMF, the effect of this would be to bias measurements toward star-forming regions hosting a stellar mass greater than a certain threshold mass $M_{\star,min}$, above which the IMF is well-sampled and massive stars are expected to be present. This translates into an effective threshold for ϵ_{obs}, $\epsilon_{min} = M_{\star,min}/M \propto M^{-1}$, which accounts nicely for the trend found in Murray (2011), but is much steeper than the trend found in in Lee et al. (2016). Murray (2011) also noted that uncertainties in M_{gas} will tend to scatter points along a locus $\epsilon_{obs} \propto M^{-1}$, which again is steeper than the trend that is observed in Lee et al. (2016).

In the simulations, we find that the trend is due to the fact that more massive clouds have longer lifetimes, so $M_{\star,tr}$ will tend to underestimate $M_\star$. If the cloud lifetime scales $\propto t_{ff}$, which we find, then we expect a scaling $\epsilon_{obs} \propto t_{ff}^{-1} \propto M^{-1/4}$, hence the ~ 0.5dex decrease over 2dex in cloud mass. This is much closer to the observed scaling, so we favour this explanation.

Ochsendorf et al. (2017) also identified an anticorrelation of $\epsilon_{ff,obs}$ with total mass in star-forming complexes in the Lee et al. (2016) Milky Way clouds as well as the LMC, of strength ranging from $\propto M^{-0.11}$ to $\propto M^{-0.49}$ respectively. Our simulations do not predict a correlation as strong as is observed in the LMC, and thus are not able to explain this trend. As Ochsendorf et al. (2017) argued, the greater importance of diffuse, CO-dark gas in the overall mass budget in the lower-metallicity environment of the LMC might explain the difference in the strength of the trend between the Milky Way and the LMC. Since we have assumed that all molecular gas is being traced, this type of effect is not captured in our analysis.

Conclusions

We find the spread in SFE in a given sample of clouds to be driven by two effects: 1) the slow initial growth of stellar populations and the late dispersal of clouds; and 2) systematic trends with cloud mass within the sample. Both effects may explain why the datasets of Evans et al. (2014) and Vutisalchavakul et al. (2016) have less spread than Lee et al. (2016): the samples both span a much narrower range in M and Σ_{gas} (for a summary of cloud properties see Table 5.2). A narrower range, and in particular a greater lower bound on Σ_{gas} would capture less of the the late cloud disruption stage. A narrower range in mass scale will capture less of the systematic scalings with mass scale that we have found.

The normalization of the observed SFEs—set by the physics of stellar feedback as shown in the simulations—is recovered within factors of ~2–3. An order unity discrepancy can be easily accounted for by the systematic errors expected from models (e.g., uncertainties in massive star formation, stellar evolution, and stellar feedback; see discussion in Grudić et al. (2018b)) and from observations (e.g., errors in tracer conversion factors and the identification of gravitationally-bound gas). Vutisalchavakul et al. (2016) point out that the SFR estimator they used underestimates the total star formation in the Milky Way by a factor of 2–3, which may explain why their SFEs are noticeably lower than the simulations and other observations.

In summary, we find that most of the observed spread in the SFE of molecular clouds can be explained by the variation that occurs during the evolution a single cloud, subject to the effects of feedback from massive stars. There is also a spread due to a systematic trend between the observable SFE and the bulk properties of the cloud, but this does *not* imply a trend in the true SFE. Indeed, most of the various SFE observations could be attributed to a population of clouds for which ϵ_{int} actually varies very little. This is in line with a picture where molecular clouds in the Milky Way form with only small spread in Σ_{gas} (e.g., due to the properties of supersonic turbulence: Larson 1981; Ballesteros-Paredes et al. 2011; Hopkins 2012), and as a result do not vary greatly in ϵ_{int} because it is a function of surface density due to

$\epsilon_{ff,obs} - \alpha_{vir}$ dataset	Kendall τ	p-value
Lee et al. (2016)	0.142	0.00359
Vutisalchavakul et al. (2016)	0.194	0.0313
Evans et al. (2014)	-0.0533	0.708

Table 5.1: Parameters of the Kendall τ-test for correlation between α_{vir} and $\epsilon_{ff,obs}$ in our GMC data compilation. Both significant correlations ($p < 0.05$) are positive ($\tau > 0$), consistent with a monotonic increase of both α_{vir} and $\epsilon_{ff,obs}$ with cloud age.

the scalings of self-gravity and stellar feedback (e.g. Fall et al., 2010; Grudić et al., 2018b; Kim et al., 2018a).

5.4.3 Evolution of α_{vir}

The results of this section suggest an interpretation of the upper tails of the SFE distributions in terms of molecular cloud dispersal: molecular gas is destroyed or ejected at the end of the cloud lifetime due to stellar feedback, causing the M_{gas} term in the denominator of the SFE to become small and the inferred SFE to rise, although the actual SFR is dropping. If molecular clouds are initially gravitationally bound, with $\alpha_{vir} \leq 2$, as we have simulated, then a key prediction of this picture is an increase of α_{vir} from the initial bound state to greater values as the cloud evolves. We have verified that when the simulations reach the threshold of detectability, the clouds have $\alpha_{vir} \sim 10 - 20$, similar to the maximum value observed. However, Lee et al. (2016) searched for a correlation between the size of the HII bubble associated with a cloud and its virial parameter, and none was found. Since we find ϵ_{ff} to be a monotonic and fairly sensitive function of the cloud evolutionary stage (Figure 5.3), we may also test for correlations between $\epsilon_{ff,obs}$ and α_{vir} in our data compilation. The results of the Kendall τ-test for correlations between $\epsilon_{ff,obs}$ and α_{vir} are given in Table 5.1. We find a positive correlation between α_{vir} and ϵ_{ff} for both the Lee et al. (2016) and Vutisalchavakul et al. (2016) datasets at 2.9σ and 2.1σ significance, respectively.

Nevertheless, these correlations are rather weak, and the lack of correlation with HII region size is still puzzling – clearly the picture is more complicated than a universal evolution from $\alpha_{vir} = 2$ to > 10. However, many factors might explain the scatter and weakness of the trend in α_{vir} with cloud evolution, either by introducing scatter or by increasing the expected mean measured value of α_{vir}. The empirically-measured

α_{vir} is (Bertoldi and McKee, 1992):

$$\alpha_{vir} = \frac{5\sigma_v^2 R}{GM}, \tag{5.9}$$

where σ_v is the measured 1D velocity dispersion. This only equals the virial ratio $\frac{2E_{turb}}{|E_{grav}|}$ in the case of a uniform sphere with a flat internal size-linewidth relation. If GMCs are triaxial, intrinsic scatter is immediately introduced by using only 1D and 2D information for σ_v and R respectively. Correcting the size-linewidth relation to that of supersonic turbulence raises the threshold for marginal boundness from 2 to $10/3 \sim 3.3$ (Miville-Deschenes et al., 2017). It is also possible that the typical virial parameter at which a GMC starts to form stars is even greater than this threshold: a cloud that is not globally bound may still have bound subregions that can collapse and form stars, so theory predicts the SFR to be a continuously decreasing function of α_{vir}, rather than a sharp cutoff (e.g. Padoan et al., 2012). Furthermore, the traditional concept of gravitational boundness of clouds in terms of α_{vir} neglects the fact that GMCs are in a state of supersonic turbulence, and hence are dissipating kinetic energy on a crossing time (Gammie and Ostriker, 1996). This could potentially allow them to reach higher virial parameters than an equivalent dissipationless system without dispersing. If a significant fraction of star formation is in less-bound clouds, then the actual variation of α_{vir} throughout the observable cloud lifetime might actually be quite modest, weakening any observed correlation. Lastly, it is possible that a significant fraction of molecular emission from a cloud does not originate in the dynamically-active region that is causally connected to the star formation event and directly affected by feedback. A molecular cloud consisting of a diffuse molecular envelope and a more tightly-bound, star-forming core might not be observed to have a large variation in α_{vir} throughout its observable lifetime.

5.4.4 Effects of different feedback mechanisms

Stellar radiation, winds from OB stars, and supernova explosions all contribute to the disruption of clouds, but which of these feedback mechanisms is the most dominant? In answering this question, we focus upon the cloud model with mass $2 \times 10^6 M_\odot$ and radius 100 pc, because it provides the most dynamically interesting environment : the cloud lifetime of $\sim$ 10Myr is sufficiently long for Type II SNe from the first massive stars to occur during it, but is not so long that the net fluxes of OB winds and stellar radiation from the stellar population are seriously reduced by the deaths of these massive stars. As such, all mechanisms could potentially be important.

We have re-simulated the $2 \times 10^6 M_\odot$, 100 pc cloud model with random seed 1, with several combinations of feedback physics, performing three runs that neglect stellar radiation, OB winds, and SNe respectively, as well as runs where radiation and SNe are the only feedback, with results summarized in Table 5.3. Radiative feedback is clearly the most important: when it is neglected, both the true and observed SFE values increase by $0.3 - 0.5$ dex. However, if the other feedback mechanisms are neglected, the change in SFE is quite small, < 0.1 dex. Because the star-forming lifetime is > 3.5 Myr, we find that SNe alone are able to moderate star formation and disrupt the this cloud model, giving a $\epsilon_{int} \sim 10\%$ compared to $\sim 4\%$ with all feedback mechansisms. However, this would not be the case for the smaller cloud models, which evolve on a shorter freefall timescale.

It should be noted that although we find that radiative feedback alone to be sufficient to set the cloud SFE, the interplay of different feedback mechanisms in concert may have other effects not considered here. For example, although SNe may be subdominant in setting the cloud SFE, they can conceivably enhance the terminal momentum of the cloud once it is disrupted. Such an effect could easily be important in the greater galactic context, where feedback supports the galactic disk against collapse (Thompson et al., 2005; Ostriker and Shetty, 2011; Faucher-Giguère et al., 2013; Orr et al., 2018b).

5.5 Star Formation in Dense Gas

Because only a small fraction of the initial gas mass of a GMC is converted to stars (e.g. Figure 5.2), one expects that the densest regions of molecular clouds are the most tightly correlated with star formation activity. Thus far we have examined the behaviour of SFE observables derived from integrated quantities for entire GMCs, and found that molecular cloud evolution under the influence of feedback from massive stars is a satisfactory explanation for the observed ranges of cloud SFEs. We now examine the properties of dense subregions of molecular clouds and determine whether our model can also explain observations on this smaller scale. We shall consider both observations pertaining to the total gas mass above a certain density threshold within a cloud, and the properties of individual dense clumps.

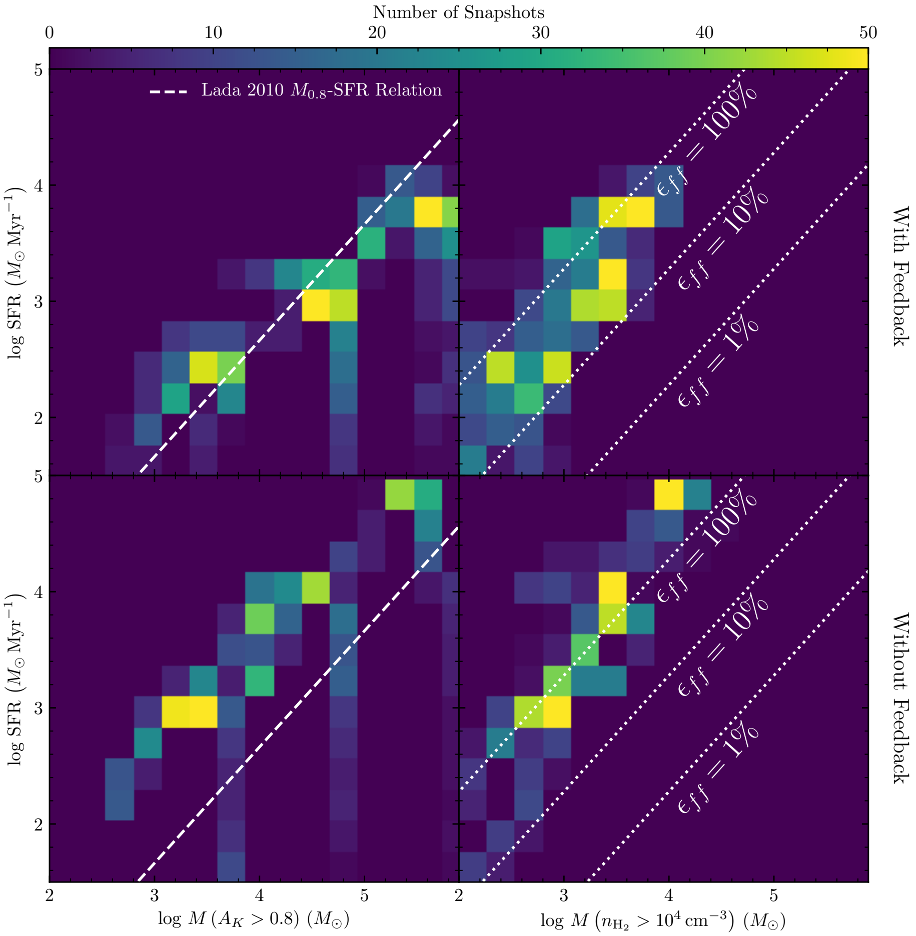

Figure 5.1: SFR as a function of "dense" gas mass in the simulations, for both 2D and 3D density thresholds. We plot 2D histograms of the compilation of all simulation snapshots in $M_{gas} - SFR$ space to give a sense of the relative amount of time spent by the simulations at a given point. *Left:* SFR as a function of gas mass above 0.8 mag extinction, compared to the Lada et al. (2010) relation, for simulations with (top) and without (bottom) stellar feedback. *Right:* SFR as a function of gas mass with molecular gas density n_{H_2} greater than 10^4 cm^{-3}, for simulations with (top) and without (bottom) stellar feedback.

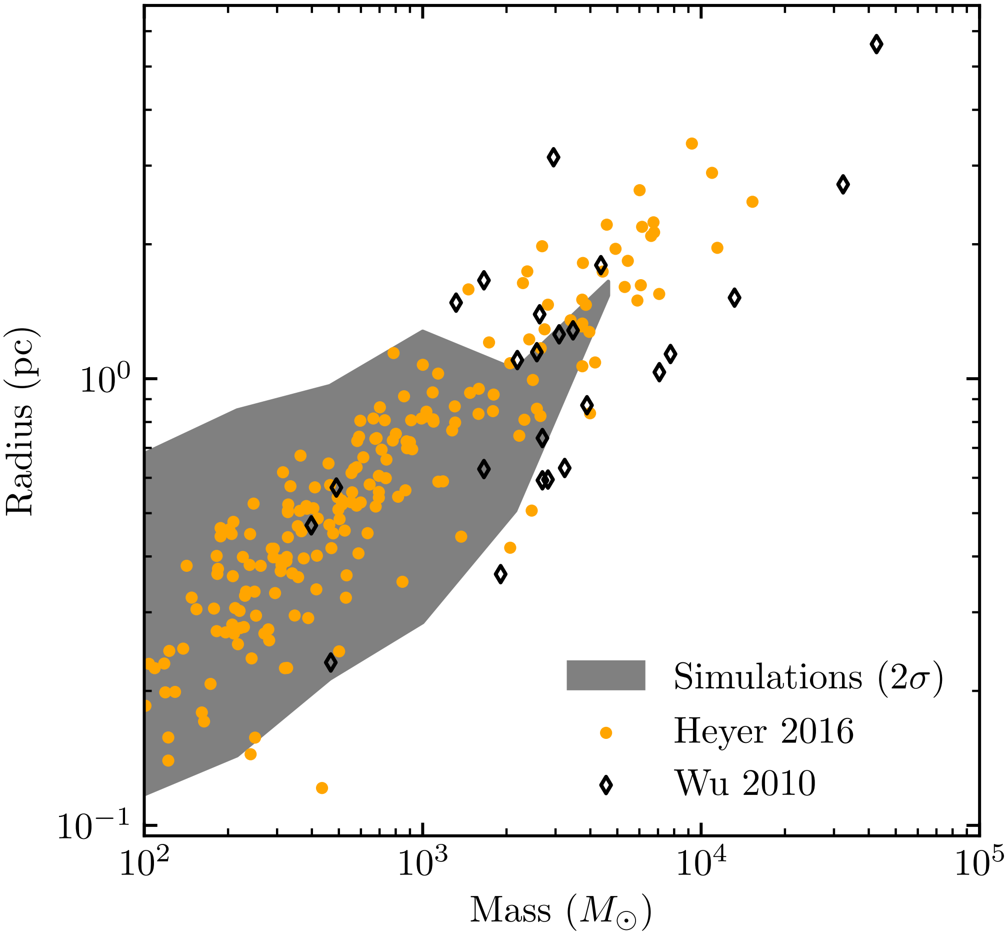

Figure 5.2: Mass versus effective radius for the dense clumps catalogued in the simulations, compared with the star-forming dense clumps in Wu et al. (2010) and Heyer et al. (2016). The grey contour encloses the $\pm 2\sigma$ contours of clump size at a given mass.

5.5.1 SFR versus gas mass above a 2D/3D density threshold

In nearby star-forming regions, a proportional relation was found between the SFR and the gas mass at above a certain K-band extinction threshold by Lada et al. (2010):

$$\mathrm{SFR} = 4.6 \times 10^{-8} \left(\frac{M_{0.8}}{M_\odot}\right) \left(M_\odot\,\mathrm{yr}^{-1}\right), \tag{5.10}$$

where $M_{0.8}$ is the gas mass of the cloud with K-band extinction greater than 0.8mag, corresponding to a gas surface density of $116\,\mathrm{M}_\odot\,\mathrm{pc}^{-2}$. To compare the simulations with this relation, we calculate the K-band extinction of a gas cell by calculating the column density via the ray-tracing method described in §5.4.2, but using the same K-band dust opacity assumed in Lada et al. (2010) (Lombardi, 2009). In the

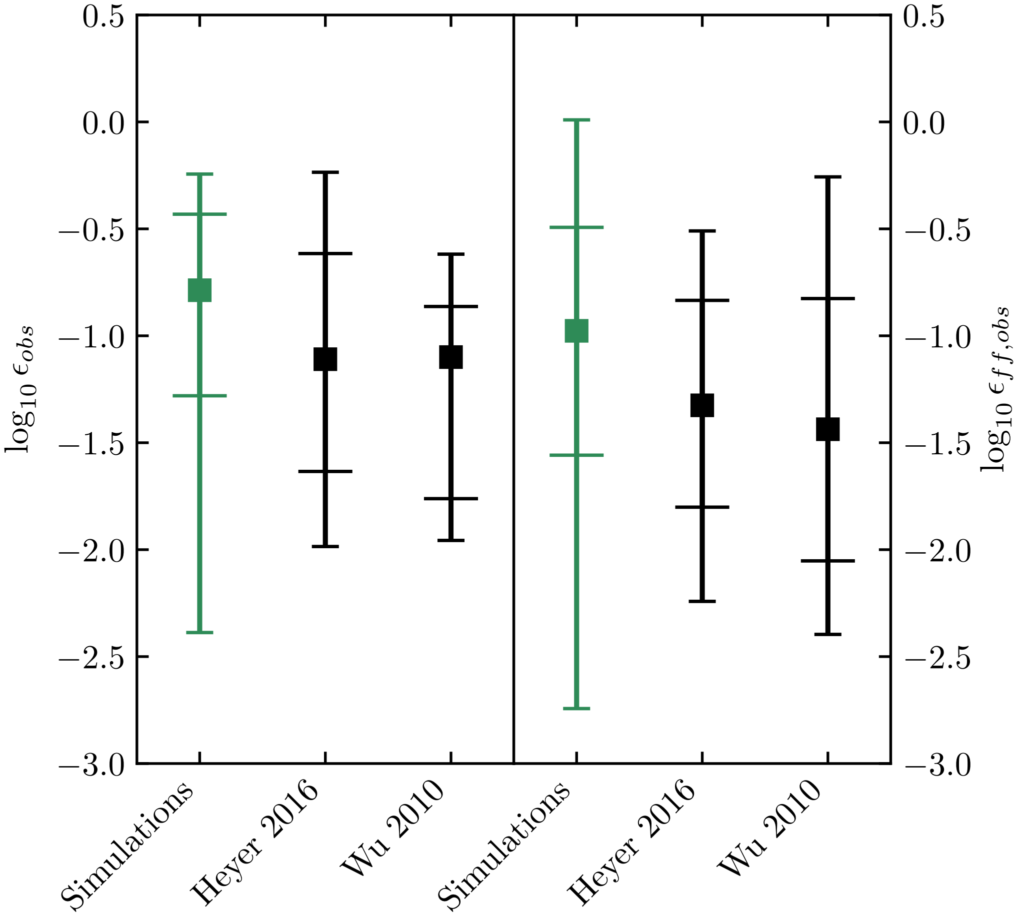

Figure 5.3: Comparison of the distributions (medians, $\pm\sigma$, and $\pm 2\sigma$ quantiles) of ϵ_{obs} and $\epsilon_{ff,obs}$ for dense ($n_{\mathrm{H}_2} > 10^4 \mathrm{cm}^{-3}$) clumps in the simulations with the star-forming dense clump datasets from Wu et al. (2010) and Heyer et al. (2016). We plot $\epsilon_{ff,obs}$ as calculated from the same procedure as Heyer et al. (2016), which assumes a fixed tracer-identified SF timescale $\tau_{tr} = 0.5\mathrm{Myr}$.

left panels of Figure 5.1 we plot the average SFR over $\tau_{SF} = 2\mathrm{Myr}$ (similar to the YSO count-inferred SFR in Lada et al. 2010) as a function of $M_{0.8}$. We find that the clouds simulated with stellar feedback do spend a significant fraction of their lifetime on or near the relation. On the other hand, the simulations without feedback almost always lie ~ 1 dex above the relation. We thus reproduce the finding of Geen et al. (2017) that some form of feedback is necessary to place star-forming clouds on the Lada et al. (2010) relation. While it is tempting to then claim that the relation is explained by feedback from massive stars, we caution that this type of mechanism cannot explain the SFR of the lowest-mass star-forming regions considered in Lada et al. (2010), because the stellar masses present are so low that no massive stars are expected to be present. Rather, we have simulated only what would be considered high-mass star forming-systems. Explaining the Lada et al. (2010) relation for low-mass systems in terms of feedback may require another mechanism that can moderate star formation in the absence of of massive stars.

Lada et al. (2010) further conjectured that $M_{0.8}$ might correspond to the gas mass denser than $n_{\mathrm{H}_2} = 10^4\,\mathrm{cm}^{-3}$, denoted M_{dense}. If so, the Lada et al. (2010) relation would suggest a simple universal star formation relation:

$$\mathrm{SFR} = \epsilon_{ff} M_{dense}/t_{ff}, \tag{5.11}$$

where $t_{ff} = 0.3\,\mathrm{Myr}$ is the freefall time at that density and $\epsilon_{ff} \sim 1\%$. This would roughly agree with the star formation relation suggested by the $L_{IR} - L_{HCN}$ correlation (Wu et al., 2005, 2010; Bigiel et al., 2016) under the assumption that HCN emission does actually trace the gas mass of characteristic density $\sim 10^4\mathrm{cm}^{-3}$ (Krumholz and Tan 2007; Onus et al. 2018, however note recent evidence to the contrary: Kauffmann et al. 2017; Goldsmith and Kauffmann 2017). We plot the relation between M_{dense} and the SFR in the rightmost panels of Figure 5.1, and find that the simulations lie well above a $\epsilon_{ff} \sim 1\%$ relation, and the relation is steeper than linear. As in Clark and Glover (2014) and Geen et al. (2017), we find a correlation but no general proportionality between M_{dense} and $M_{0.8}$ in the simulations, so Equation 5.11 does not follow from Equation 5.10. Both with and without feedback, the simulations lie mostly in the range $\epsilon_{ff} = 10\% - 100\%$, so feedback from massive stars as implemented here does not appear to be sufficient to achieve “slow" star formation in dense gas.

5.5.2 Individual Dense Clumps

To compare to observations of individual dense clumps in Wu et al. (2010) and Heyer et al. (2016), we identify contiguous regions with $n_{\mathrm{H}_2} > 10^4\mathrm{cm}^{-3}$ in the simulations, and associate these with sink particles younger than 0.5Myr found within $2R_{eff}$ of the gas centre of mass, with R_{eff} computed as in §5.4.2. We find that the stellar masses associated with the dense clumps are relatively insensitive to the choice of cutoff radius beyond this value because young sink particles are tightly clustered around dense clumps. Within this population we find stellar-mass objects that would be more readily identified as “cores” rather than “clumps”. To make a reasonable comparison with observed dense clumps, we apply a mass cut of $100M_{\odot}$, which excludes these cores.

The mass-size relation of simulated clumps is compared to observations in Figure 5.2. We find that in the mass-size plane the clump catalogue from the simulations overlaps most of the dense clumps in Heyer et al. (2016) and roughly half of those in Wu et al. (2010). This supports the interpretation of dense clumps as dense subregions that formed dynamically within a larger molecular gas complex. However, although we have simulated cloud models similar to the most massive Milky Way GMCs, we do not find dense clumps with masses as great as the most massive in either catalogue. This might be due to a genuine missing physical mechanism that might slow down gas consumption in dense clumps, allowing them to live longer and accrete to greater masses. However, resolution effects might also account for the discrepancy: observations with finite spatial and/or spectral resolution would be more likely to lump together multiple small clumps into a larger single clump.

In Figure 5.3 we plot the distributions for ϵ_{obs} and ϵ_{ff} of dense clumps in the simulations compared to observations. We compute ϵ_{obs} from the total dense gas and stellar mass. We compute $\epsilon_{ff,obs}$ via Eq. 5.6 using the fiducial star formation timescale $\tau_{tr} = 0.5\mathrm{Myr}$ used in Heyer et al. (2016). We find a similar amount of scatter to what is observed, which is presumably due to similar effects to what we have found on GMC scales. However, as in the previous subsection, we find efficiencies that are generally greater than what is observed: both ϵ_{obs} and $\epsilon_{ff,obs}$ for dense clumps are systematically ~ 0.3 dex greater than the observations, which themselves are really upper bounds (see discussion in 5.2.3). Moreover, the efficiencies and bulk properties of the observed dense clumps agree well despite the use of different methodologies, and the bulk properties of Heyer et al. (2016) in particular were derived independently of any assumptions about the characteristic density traced by HCN. It therefore seems quite possible that there is a genuine discrepancy in the efficiency of star formation in dense gas in the simulations: the physics that we have included may not be sufficient to slow down star formation in dense gas down to the levels observed.

5.5.3 Possible missing physics

Assuming that the discrepancy in the SFE of dense gas shown in this section is genuine, and not due to some unknown systematic, there are several pieces of physics neglected here that might affect the clump SFEs:

- Multiply-scattered IR radiation pressure in the optically-thick limit (e.g Krumholz and Thompson, 2012a; Davis et al., 2014a; Skinner and Ostriker, 2015; Zhang and Davis, 2017; Tsz-Ho Tsang and Milosavljevic, 2017), which can conceivably become comparable or greater in magnitude to the radiation pressure from direct stellar emission at the gas surface density of these clumps, $> 10^3\,\mathrm{M}_\odot\,\mathrm{pc}^{-2}$.

- Radiative heating from protostellar accretion, which has been found to be sufficient, and possibly necessary, to set the characteristic mass scale of stars (Bate, 2009; Krumholz, 2014; Guszejnov et al., 2016; Federrath et al., 2017). The simulations form sink particles of stellar mass, so this may well be dynamically relevant on the scales resolved.
- Protostellar outflows, which have been shown to be able to slow down star formation in high-resolution periodic box simulations on scales similar to dense clumps (Myers et al., 2014b; Federrath, 2015b; Cunningham et al., 2018), but have not been treated in the present context, in which dense clumps form and disperse dynamically within a larger molecular cloud.
- Hard-scattering N-body interactions, which would not necessarily bring down the actual SFE, but would reduce the observed SFE if able to dynamically eject YSOs from their natal clumps, as in the classic competitive accretion picture (Bonnell et al., 2001). Such interactions depend sensitively upon the relative masses of protostars in a clump, so this effect is only expected to have the correct behaviour in simulations that resolve the IMF self-consistently, which we have not attempted to do here – a numerically-converged IMF likely requires some subset of the physics mentioned in the above points (see references). In a previous iteration of these simulations, we encountered a bug that caused spurious ejection of sink particles from clumps, and found that the resulting measured SFE was in good agreement with observations. Therefore, the efficient removal of stellar mass in a clump crossing time might reduce the SFE to observed levels.

5.6 Interpretation of the Properties of Star-Forming GMCs

5.6.1 Does SFE scale with cloud properties?

An objective of star formation theory is to use observations of star-forming clouds to gain insights about the underlying physical mechanisms that determine their evolution and lead to star formation. Constraints can be obtained by comparing observations to the various theories of turbulence-regulated and feedback-regulated

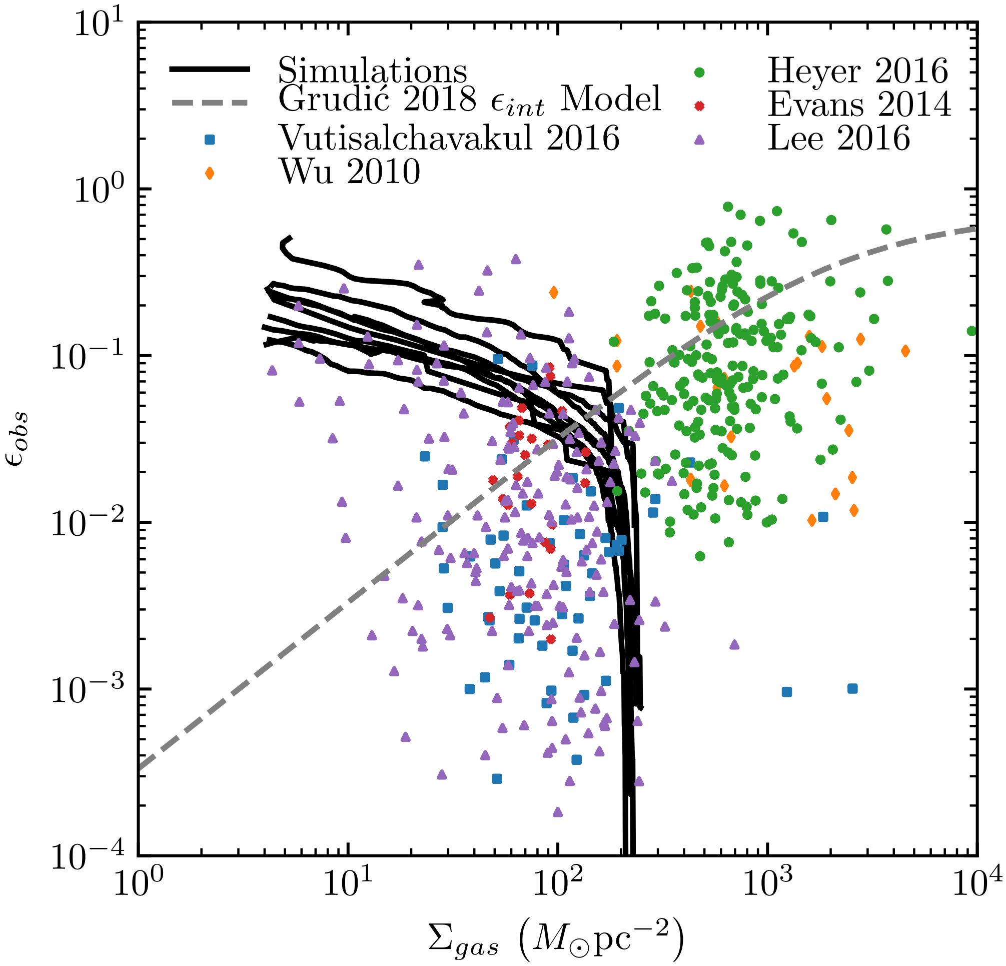

Figure 5.1: Tracks traced out by the simulations in the $\Sigma_{gas} - \epsilon_{obs}$ plane compared with data from star-forming Milky Way clouds and clumps (§5.2.3) and the Grudić et al. (2018b) theory for the dependence of ϵ_{int} upon Σ_{gas}. For consistency, Σ_{gas} is computed using the effective R_{eff} (see 5.4.2), which is less than the nominal bounding radius R and thus gives a somewhat greater surface density than the nominal $M/\pi R^2$. Both the observed SFEs and surface densities evolve throughout the GMC lifetime, which scatters the data. The prediction of GMC evolution subject to stellar feedback is therefore not a functional dependence of ϵ_{int} on Σ_{gas}, but rather a complicated joint probability distribution function that will depend upon the statistics of the underlying cloud population. This complicates the task of discerning true systematic scalings from the observational data.

star formation, which make specific predictions for ϵ_{int} and ϵ_{ff} in terms of the bulk properties of GMCs, such as M, R, and α_{vir}. For example, hydrodynamics simulations with stellar feedback generally predict ϵ_{int} to scale in some manner with escape velocity, density, or surface density. Grudić et al. (2018b) pointed out that the median ϵ_{obs} appears to scale by a factor of ~ 10 over the surface density range separating Milky Way GMCs and dense clumps, which is also roughly a factor of 10 (Figure 5.1). However, so far such SFE scalings have not yet been conclusively demonstrated in observational studies within a single population of homogeneously-catalogued gas structures. Our simulations suggest that this may be due, at least in part, to the fact that the observable quantities predicted by theory vary in a complex manner that complicates the comparison of theoretical models with observations.

The observed M_{mol}, R_{eff} (and hence Σ_{gas}) and ϵ_{obs} of a star-forming GMCs will all vary by orders of magnitude throughout the cloud lifetime (see Figure 5.1), so numerical simulations of star formation with stellar feedback from massive stars predict a large spread in ϵ_{obs} in ϵ_{ff}. Therefore, ϵ_{obs} cannot be treated as a one-to-one function of the bulk cloud properties. To properly investigate possible SFE scalings due to feedback-regulated star formation, it is necessary to model the posterior distribution of predicted *observable* GMC properties, which is very broad in both the space of GMC bulk properties and in observed SFE. Furthermore, because a GMC will begin its star-forming process below the threshold of detectable massive star formation, and end its evolution in catastrophic dispersal only to be found below the detectable threshold of molecular emission brightness, some understanding of the selection function is also important to model the likelihood. Failing this, any true underlying scalings in SFE with cloud properties can easily be obscured or fit incorrectly. Although the simulations equip us with some idea of the likelihood function for a given cloud model, fitting to data from a population of clouds makes it necessary to forward-model the statistics of the cloud parameters within an entire galactic GMC population, which is beyond the scope of this work.

5.6.2 Turbulence regulation vs. feedback regulation

The results of this work do permit certain definite conclusions about the physics governing molecular cloud evolution. We have shown that our simulated GMC models do predict the observed distribution of SFEs of Milky Way GMCs in some detail (Figure 5.4), and are able to reproduce the observed anticorrelation of ϵ_{obs} with total cloud mass (Lee et al., 2016). Lee et al. (2016) showed that turbulence-regulated SFE theories derived from the log-normal density PDF and a gravitational collapse criterion (e.g. Krumholz and McKee, 2005; Hennebelle and Chabrier, 2011b; Padoan and Nordlund, 2011) predict neither of these features, generally predicting a positive correlation of SFE with cloud mass with much less scatter than is observed. We therefore favour the model of dynamic star formation in feedback-disrupted GMCs as an explanation for the observed properties of star-forming GMCs in the Milky Way. The observed scatter is due to the large variation in observable gas and stellar mass throughout the cloud lifetime, both due to a dynamic SFR during the initial collapse phase and the depletion of stellar and molecular gas tracers due to stellar evolution and cloud disruption. Furthermore, the normalization of the SFE is not due to regulation by turbulence, but rather stellar feedback from massive stars setting the stellar mass that can be formed before star formation ceases. This is not to minimize the importance of turbulence in the dynamics of star-forming clouds, which is self-evident. Rather, the specific predictions of analytic theories that assume the properties of statistically-stationary, non-self-gravitating turbulence fail to capture the full dynamics of self-gravitating clouds subject to the effects of feedback.

5.7 Summary

In this work, we have presented MHD simulations intended to directly model star-forming GMCs in the Milky Way, accounting for the stellar feedback mechanisms due to massive stars: stellar winds, supernova explosions, and radiation, including the effects of photon momentum in multiple bands, and heating mechanisms due to UV photons. From these simulations we have arrived at several conclusions about the nature of local star-forming molecular clouds:

- When the effects of magnetic fields and feedback from massive stars are included, the simulations predict an dynamically-rising star formation rate in molecular clouds (Figure 5.2), as predicted analytically (Murray and Chang, 2015) and found in previous works that considered only gravity and isothermal (magneto-) hydrodynamics (Padoan et al., 2012; Federrath and Klessen, 2012; Lee et al., 2015; Murray et al., 2017) or a different subset of relevant feedback mechanisms (Raskutti et al., 2016; Vazquez-Semadeni et al., 2017; Geen et al., 2017). After this initial growth phase, stellar feedback eventually causes the SFR to level off and drop to 0 as the molecular cloud is disrupted.

- The simulations predict a normalization and spread in the observed SFEs that is reasonably consistent with those of observed Milky Way GMC SFEs.

The diversity in the measured SFE of molecular clouds in the Milky Way is similar to the range of SFE values that is measured across the star-forming lifetime of a single molecular cloud subject to stellar feedback. This stands in contrast to quasi-static models of molecular cloud evolution (Zuckerman and Evans, 1974; Krumholz et al., 2006), where molecular cloud properties vary on timescales longer than a cloud free-fall time.

- According to the above interpretation of the SFE spread, very large ($> 10\%$) or very small ($< 0.1\%$) observed SFEs in individual clouds do not imply that GMCs actually exhibit such great variation in the fraction of their mass that they convert to stars, because these correspond only indirectly to the true SFE values. The true SFE variation could actually be quite small, and the observed scatter would still be observed. Because these effects are a consequence of nonlinear molecular cloud evolution subject to the interplay of feedback, gravity, and hydrodynamics, we concur with Lee et al. (2016) that theories invoking gravity and turbulence alone cannot explain the observed range of SFE.

- The observed trend of decreasing ϵ_{obs} with cloud mass (Murray, 2011; Lee et al., 2016) can be understood as an observational effect arising from the use of only recently-formed stars as a tracer of stellar mass, which underestimates the total stellar mass formed in more massive clouds, which have longer lifetimes. The true SFE in the simulations has no strong trend with mass.

- We examined the relations between gas mass above 2D and 3D density thresholds in the simulations and the SFR. Simulations lie on the Lada et al. (2010) $M_{0.8}$ – SFR relation (Equation 5.10) if and only if stellar feedback is included, however this does not explain the relation in low-mass star-forming regions where massive stars are absent. However, with or without feedback, the simulations lie well above the proposed corresponding 3D relation for dense ($> 10^4 \mathrm{cm}^{-3}$) gas (Equation 5.11) that assumes that $M_{0.8} = M_{dense}$. This is in agreement with previous simulation work showing that $M_{0.8} \neq M_{dense}$ in general (Clark and Glover, 2014; Geen et al., 2017).

- We identify contiguous regions of dense ($> 10^4\,\mathrm{cm}^{-3}$) gas within the simulated GMCs with observed dense clumps (Wu et al., 2010; Heyer et al., 2016), and find that their bulk properties are mostly in good agreement with observed clumps, except for a dearth of predicted clumps more massive than $3000\,\mathrm{M}_\odot$.

> We measure the clump SFE in a manner replicating observation techniques and find that ϵ_{obs} and $\epsilon_{ff,obs}$ are both systematically 0.3 dex greater than is observed. It is possible that feedback from main sequence massive stars is insufficient to bring the SFE of dense gas down to the levels observed.

We can identify several avenues for further progress on this problem. Our simulations relied upon ad-hoc initial conditions generated by stirring supersonic MHD turbulence and then "switching on" gravity. This is fairly artificial, because in a real galaxy it is likely that gravity plays a role in the actual formation of the molecular cloud and the generation of its turbulent motions. Furthermore, the extent to which even gravitationally-bound clouds can be treated as isolated objects is not well-established, even if they only survive for roughly a free-fall time as they do in the simulations. To address these questions, future studies should account for the greater galactic context of molecular cloud formation and dispersal.

For purposes of determining the stellar feedback budget, we made the single phenomenological assumption of a Kroupa (2002) IMF, which was sampled within sink particles according to the simple prescription of Su et al. (2018). While the universality of the IMF across most Milky Way environments is reasonably well-established (Offner et al., 2014), in reality the IMF must somehow emerge from the dynamics of star-forming clouds. Therefore, the manner in which we have decoupled the formation of massive stars from the actual local cloud dynamics is not fully self-consistent. If special conditions are actually necessary for massive star formation, the simulations would not capture the effect and might overestimate feedback. A fully self-consistent molecular cloud simulation with sufficient resolution and physics to *predict* the IMF would be necessary to validate our approach. This presents a challenging resolution requirement due to the factor of $\sim 10^6$ disparity in mass scale between the average molecular cloud and the average star. However, recent cloud-collapse simulations without stellar feedback have managed to scale to a relative mass resolution of $< 10^{-8}$ (Guszejnov et al., 2018b), demonstrating that GMC simulations with such a dynamic range are becoming possible.

Lastly, we caution that many conclusions about molecular clouds can be sensitive to the definition of a cloud. For instance, there is no one well-defined way to decompose a CO emission map into clouds, because the ISM exhibits substructure on all scales from the galactic scale height to individual stars, with no obvious preferred intermediate scale. It is likely that GMCs do exist as well-defined dynamical entities in the sense that they may be identified with the largest self-gravitating gas structures within a galaxy (Rosolowsky et al., 2008; Hopkins, 2012), but these do not necessarily correspond to observationally-catalogued GMCs on a one-to-one basis. A more sensitive quantitative comparison of simulated SFEs with observations than we have presented here should account for this by applying the same observational cloud decomposition and cross-correlation algorithms to mock observations.

Acknowledgements

We thank Neal J. Evans II, Mark Krumholz, Diederik Kruijssen, Marta Reina-Campos, and Sharon Meidt for enlightening discussions that informed and motivated this work. We also thank Shea Garrison-Kimmel and Alex Gurvich for helpful suggestions for data presentation and visualization. Support for MYG and PFH was provided by a James A Cullen Memorial Fellowship, an Alfred P. Sloan Research Fellowship, NSF Collaborative Research Grant #1715847 and CAREER grant #1455342, and NASA grants NNX15AT06G, JPL 1589742, 17-ATP17-0214. CAFG was supported by NSF through grants AST-1412836, AST-1517491, AST-1715216, and CAREER award AST-1652522, by NASA through grant NNX15AB22G, and by a Cottrell Scholar Award from the Research Corporation for Science Advancement. NM acknowledges the support of the Natural Sciences and Engineering Research Council of Canada (NSERC). This research was undertaken, in part, thanks to funding from the Canada Research Chairs program. NM's work was performed in part at the Aspen Center for Physics, which is supported by National Science Foundation grant PHY-1607611. Numerical calculations were run on the Caltech compute cluster "Wheeler," allocations from XSEDE TG-AST130039 and PRAC NSF.1713353 (awards OCI-0725070 and ACI-1238993) supported by the NSF, and NASA HEC SMD-16-7592. This research has made use of use of NASA's Astrophysics Data System, `ipython` (Pérez and Granger, 2007), `numpy`, `scipy` (Jones et al., 2001), and `matplotlib` (Hunter, 2007).

C h a p t e r 6

THE ELEPHANT IN THE ROOM: THE IMPORTANCE OF WHERE AND WHEN MASSIVE STARS FORM IN MOLECULAR CLOUDS

M. Y. Grudić and P. F. Hopkins. arXiv e-prints, arXiv:1809.08344, September 2018.

Abstract

Most simulations of galaxies and massive giant molecular clouds (GMCs) cannot explicitly resolve the formation (or predict the main-sequence masses) of *individual* stars. So they must use some prescription for the amount of feedback from an *assumed* population of massive stars (e.g. sampling the initial mass function [IMF]). We perform a methods study of simulations of a star-forming GMC with stellar feedback from UV radiation, varying only the prescription for determining the luminosity of each stellar mass element formed (according to different IMF sampling schemes). We show that different prescriptions can lead to widely varying (factor of ~ 3) star formation efficiencies (on GMC scales) even though the average mass-to-light ratios agree. Discreteness of sources is important: radiative feedback from fewer, more-luminous sources has a greater effect for a given total luminosity. These differences can dominate over other, more widely-recognized differences between similar literature GMC-scale studies (e.g. numerical methods, cloud initial conditions, presence of magnetic fields). Moreover the differences in these methods are not purely numerical: some make different implicit assumptions about where and how massive stars form, and this remains deeply uncertain in star formation theory.

6.1 Introduction

Massive stars are rare, but their radiation, winds, and supernova explosions dominate the energy liberated from a stellar population. It is thought that feedback from massive stars is a crucial element for regulating star formation on scales ranging from entire galaxies to individual star clusters (McKee and Ostriker, 2007; Naab and Ostriker, 2017). In the latter case, significant theoretical efforts have been devoted to understanding how feedback from massive stars sets the star formation efficiency (SFE) of star-forming giant molecular clouds (GMCs), the fraction of the initial gas mass that is converted to stars before feedback disrupts the cloud and halts star formation. An understanding of the SFE of GMCs is important for understanding the origins of the star cluster mass function and its connection to the GMC mass function (Elmegreen and Efremov, 1997; Fall et al., 2010), the origins of gravitationally bound globular clusters (Hills, 1980; Baumgardt and Kroupa, 2007; Kruijssen, 2012), and the distribution and pre-conditioning of supernova explosions, which affects the efficiency of stellar feedback on galactic scales (Keller et al., 2014; Fielding et al., 2018).

Significant progress has been made on this problem as the necessary computational techniques have become available. Many numerical experiments have been performed in which a self-gravitating molecular cloud is evolved in isolation, subject to self-gravity, hydrodynamics, stellar feedback, and possibly detailed cooling and chemistry physics (Murray et al. 2010; Vazquez-Semadeni et al. 2010; Dale et al. 2012, 2013; Colin et al. 2013; Dale et al. 2014; Skinner and Ostriker 2015; Raskutti et al. 2016; Howard et al. 2016, 2017; Vazquez-Semadeni et al. 2017; Dale 2017; Kim et al. 2017a; Gavagnin et al. 2017; Grudić et al. 2018b; Kim et al. 2018a, for review see Krumholz et al. 2014; Dale 2015). For GMC properties consistent with those found in the local Universe ($\Sigma_{gas} \sim 50\,\mathrm{M}_{\odot}\,\mathrm{pc}^{-2}$, $M \sim 10^4 - 10^6\,\mathrm{M}_{\odot}$, Bolatto et al. 2008), the most important feedback mechanism for regulating star formation on GMC scales is generally agreed to be UV photons from massive stars. UV photons heat and ionize the ISM upon absorption by gas or dust, while also imparting momentum upon absorption, creating expanding HII regions that ultimately unbind the remaining gas in the cloud. However, theoretical consensus on the specific SFE at which cloud disruption occurs (or even whether it occurs at all, Howard et al. 2016) has been slower to develop. As an extreme example, Raskutti et al. (2016) simulated a molecular cloud of initial mass $5 \times 10^4 M_{\odot}$ and radius 15pc and obtained a SFE of $\sim 40\%$, while Grudić et al. (2018b) simulated the same cloud model with nominally the same feedback physics and obtained $\sim 4\%$, an order of magnitude smaller.

Discrepancies are not necessarily surprising when one considers the compounded variations that can arise when using different hydrodynamics methods, sink particle prescriptions, and perhaps most importantly, radiative transfer approximations. Variations due to these numerical details warrant some exploration, as studies that compare radiative transfer methods while controlling for other factors are few, and none are exhaustive. Raskutti et al. (2016) performed simulations treating the effects of photon momentum (ie. radiation pressure) from UV photon absorption with an M1 radiation transfer scheme (Skinner and Ostriker, 2013), which Kim et al. (2017a) subsequently compared to adaptive ray tracing results using otherwise the same code, and found a SFE a factor of ~ 2 smaller. Hopkins and Grudić (2018) also performed GMC simulations comparing the ray-based LEBRON radiative transfer approximation (Hopkins et al., 2018a) with an M1 scheme (Rosdahl and Teyssier, 2015), and also found agreement at the factor of ~ 2 level. Therefore, variations in radiative transfer techniques can likely account for some of the variation found in the literature, but probably not all of it. This motivates the consideration of other factors.

Several of the studies cited above compared additional physics (e.g. including or ignoring magnetic fields), or varying the cloud initial conditions (e.g. considering clouds with or without pre-initialized fully-developed turbulence, with or without significant rotational support, and with or without a global density profile): the general conclusion is that these, too, can influence the predicted star formation efficiency by at most a factor ~ 2 (see references above and Klessen et al. 2000; Krumholz et al. 2011; Price and Bate 2008). Others have shown that including or excluding other sources of feedback besides UV radiation alone, e.g. O/B stellar winds (which carry a similar momentum flux to the UV radiation field), can have a similar effect.

In Hopkins and Grudić (2018) we argued that another potential error source can arise when using the most common method for coupling radiation pressure to gas, which underestimates the imparted momentum from a point source if the photon mean free path is smaller than the fluid resolution. Krumholz (2018) subsequently pointed out another previously-overlooked numerical pitfall: photon absorption around an accreting massive star can occur deep in the potential well on scales smaller than the resolution limit of most simulations, preventing it from imparting momentum on larger scales. They argued that the failure to resolve this effect could also explain some of the discrepancy, and proposed a subgrid model to approximate this effect in numerical simulations.

This led us to consider the broader important question that we will address here: how do the details of how the *sources* of stellar feedback are modeled in simulations affect the cloud-scale SFE? Clearly, when simulations attempt to model the formation of massive stars self-consistently, the details of the IMF will become important for feedback, as UV luminosity is a steep function of stellar mass. However, most GMC-scale and all galaxy-scale hydrodynamics simulations either lack the resolution or the physical realism to do this self-consistently, so feedback is often treated with phenomenological prescription, *assuming* an underlying stellar mass distribution that is being sampled in some manner. In this work we will compare several such techniques, and determine the effect of these numerical choices upon the cloud-scale SFE in simulations.

6.2 Simulations

6.2.1 Numerical methods

We simulate an isolated turbulent molecular cloud with GIZMO, a multi-physics N-body and hydrodynamics code (Hopkins, 2015)[1]. We solve the equations of hydrodynamics with the Lagrangian Meshless Finite Mass (MFM) method. We account for a wide range of ISM heating and cooling physics, using the rates and implementations used in the FIRE-2 simulations (Hopkins et al., 2018a)[2]. Star formation is treated with an accreting sink particle method described in Guszejnov et al. (2018b), which uses multiple checks for sink formation and accretion, similar to Federrath et al. (2010). For simplicity, we consider only the effects of feedback due to the absorption of UV photons from stars, accounting for the effects of photo-heating and radiation pressure as in Hopkins et al. (2018a).

6.2.2 Initial conditions

We replicate the initial conditions of the fiducial cloud model in Kim et al. (2018a), a GMC with a top-hat density profile with mass $10^5 M_\odot$ and radius 20 pc. The initial velocity field is a solenoidal Gaussian random field with power spectrum $|\tilde{\mathbf{v}}(\mathbf{k})|^2 \propto k^{-4}$ (Gammie and Ostriker, 1996), normalized so that the initial kinetic energy is equal to the gravitational potential energy. The initial metallicity of the cloud is normalized to solar abundances, accounted for self-consistently in the cooling function and the dust opacity to UV photons as in Hopkins et al. (2018a). In all simulations we resolve the initial gas mass in 128^3 Lagrangian gas cells, for a mass resolution of $0.048\,\mathrm{M}_\odot$. Initial conditions were generated with the MakeCloud code[3].

---

[1] `http://www.tapir.caltech.edu/~phopkins/Site/GIZMO.html`

[2] `https://fire.northwestern.edu/`

[3] `https://github.com/omgspace/MakeCloud`

6.2.3 IMF sampling models

We perform simulations with a range of different prescriptions for the specific bolometric and ionizing luminosities assigned to the stellar mass elements (ie. sink particles) in the simulation. These are all intended to mimic certain aspects of the effect of sampling a finite number of stars from an underlying probability distribution function (ie. the IMF). Each recovers the same net specific luminosities in the limit $M_\star >> 10^3$, but each approaches that limit in a different manner as stars form in the simulation. All of these prescriptions have advantages and disadvantages – in this work we remain agnostic about the relative physical realism of these models, which is difficult to evaluate without a self-consistent treatment of the physics of massive star formation. We consider only models that work under the assumption that the IMF can indeed by interpreted as probability distribution to be sampled from until a given stellar mass reservoir is exhausted. This must break down at some level, due to mass conservation if no other reason. However, the details of how the IMF emerges are poorly understood, and the stochastic sampling hypothesis is consistent with current observations (Bastian et al., 2010a; Fumagalli et al., 2011; Offner et al., 2014).

`IMFMEAN`: Simple IMF-averaging

The simplest approach is to assume that all stellar mass elements in the simulation have the same specific luminosity as a well-sampled IMF, which for a very young stellar population with age ≪ 3.5 Myr and a Kroupa (2002) IMF is approximately

$$\left\langle \frac{L_\star}{M_\star} \right\rangle_{IMF} = 1140 L_\odot M_\odot^{-1} \tag{6.1}$$

This is approximately constant until $t \approx 3.5\,\mathrm{Myr}$, then decreases appropriately as massive stars die according to an adopted stellar evolution model (e.g. Leitherer et al., 1999). The well-sampled assumption is expected to be valid in systems where the total stellar mass is $>> 10^3 M_\odot$, and is a common choice for galaxy simulations that might not even resolve mass scales smaller than this (Hopkins et al., 2011a; Agertz et al., 2013; Hopkins et al., 2018a), although it has also been used in smaller-scale cluster formation simulations (Grudić et al., 2018b,a; Hopkins and Grudić, 2018; Kim et al., 2018b). This is the only prescription that guarantees that the specific luminosity is always equal to the ensemble over all possible IMF samplings. However, this is not necessarily desirable in all problems. The method has a serious drawback in the regime of low-mass star cluster formation: when sampling an IMF from a small reservoir of stellar mass, most realizations sample no massive stars at all. Therefore, the mean specific luminosity is due to those very few possible samplings that do contain massive stars and have specific luminosities much greater than the mean. The effect of this is to give a specific luminosity that is much larger than the vast majority of possible realizations of low-mass clusters, and much less than those few realizations that do, averaging out a major source of physically-real stochasticity.

In addition to the standard `IMFMEAN` scheme, we consider a variant supplemented by the subgrid model introduced by Krumholz (2018), `IMFMEAN-K18`. To mimic the effect of photon absorption in a dust destruction front at unresolved scales, we simply switch off UV feedback from a sink particle when its accretion rate exceeds the threshold value

$$\frac{\dot{M}}{M_\odot\,\mathrm{yr}^{-1}} > 6.5 \times 10^{-4} \left(\frac{L}{10^6 L_\odot}\right)^{3/4}. \tag{6.2}$$

Because our sink particles accrete discrete Lagrangian gas cells, we apply exponential smoothing to the accretion rate for this check, with an e-folding time $\tau_{accr} = 10^5$yr, motivated by the fiducial timescale for massive star formation. We have experimented with setting this parameter to 10^4yr and 10^6yr and found that it has no important effect on the SFE.

`IMFMED`: scaling to a median value

An alternative approach to using the IMF-averaged mean is to use the median or most likely (which are close) value over the ensemble of IMF samplings, assuming that the total stellar mass formed in the simulation can be interpreted as a coeval stellar population. Kim et al. (2016) developed this approach by sampling stellar populations with the SLUG code (da Silva et al., 2012) for a range of cluster masses and deriving a fitting formula to the median value sampled at each mass scale. The median value is very small for star clusters less than a couple $100 M_\odot$, and scales steeply toward the well-sampled value once $M_\star \sim 1000 M_\odot$. This model was used in their subsequent RHD simulations (Kim et al., 2017a, 2018a), and is the one we implement here.

The `IMFMED` model will give a value more representative of a “typical” sampling. The disadvantage of this approach is that it lacks locality: star formation in one region of the cloud influences the amount of feedback everywhere else, which is unphysical and cannot generalize to more complicated systems in which the very definition of a progenitor cloud, and hence which stars belong to which coeval population, is ill-defined. It and `IMFMEAN` share another disadvantage: every sink particle has the same light-to-mass ratio, which is artificially smoother than the true distribution of luminous sources in a star cluster. This motivates our next prescription.

`POISSON`: Poisson-sampling quantized sources

To model the discreteness of luminous sources, we can sample a quantized number of 'O-stars' in each sink particle, such that the expectation value is still the IMF-averaged value. We adopt the presciption of Su et al. (2018), which assigns to each sink particle a number of 'O-stars' sampled from a Poisson distribution, with expectation value

$$\mu = \frac{m_{particle}}{\Delta m}, \tag{6.3}$$

where $m_{particle}$ is the mass of the sink particle and Δm was taken to be $100 M_\odot$ in Su et al. (2018). Then, each 'O-star' is taken to have luminosity

$$L = \Delta m \left\langle \frac{L_\star}{M_\star} \right\rangle_{IMF}. \tag{6.4}$$

This technique has the advantage of giving a more realistic *number* of feedback-injecting sources for a given amount of stellar mass. It also captures the effect of under-sampling the IMF, but stochastically rather than causally as `IMFmed`. Although the version used in Su et al. (2018) sampled only one species of 'O-star', it is in principle extensible to an arbitrary number of species (Sormani et al., 2017). The details of how the luminosity is discretized, ie. few sources versus many, is potentially important. Feedback from a single luminous source might be more efficient than that of many smaller sources because it is more concentrated and less subject to momentum cancellation (e.g. Dale, 2017; Kim et al., 2018a). On the other hand, it could also be effectively weaker because luminous sources are only likely to appear once a certain amount of stellar mass has formed, at which point collapse may be more advanced and the resulting structure more difficult to disrupt. We consider two variants of this prescription, with $\Delta m = 100 M_\odot$ and $\Delta m = 1000 M_\odot$, denoted `POISSON100` and `POISSON1000` respectively.

A notable omission from this section is the prescription of Howard et al. (2016), which interprets each sink particle as an individual cluster, and effectively applies

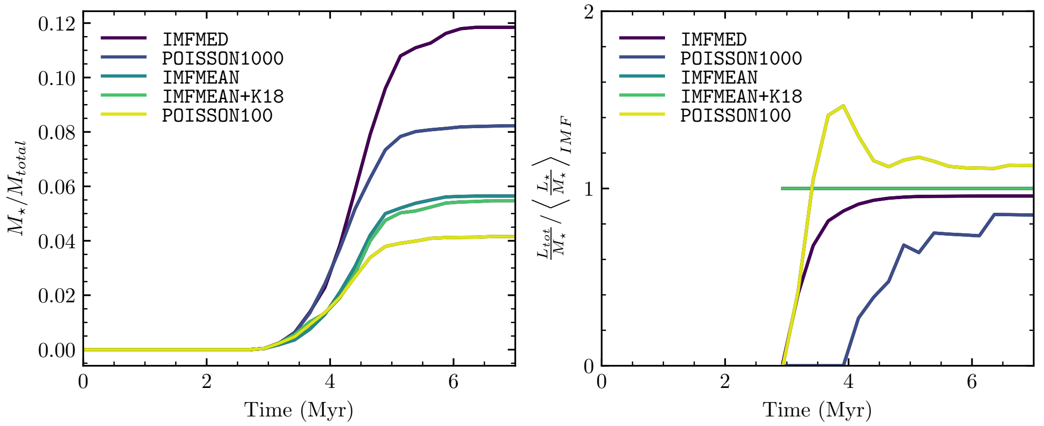

Figure 6.1: *Left*: Integrated star formation efficiency (fraction of cloud mass converted to stars) in the simulations as a function of time, for simulations run with each of the different subgrid feedback models considered (§6.2.3). *Right*: bulk stellar light-to-mass ratio according to the different prescriptions, normalized to the IMF-averaged value. Note that the `IMFMEAN-K18` curve does not include the effect of turning off feedback according to Equation 6.2, but we find that the effect is small (see discussion in §6.3). The different prescriptions all approach the same IMF-averaged value in the limit $M_\star >> 10^3 M_\odot$, but they differ in how they approach this limit.

a variant of the `IMFMED` prescription to each of these clusters individually. We have experimented with this prescription and found it to be numerically problematic because the characteristic mass of sink particles drops as a function of mass resolution, as has generally been found in other simulations (Bate, 2009; Federrath et al., 2017; Guszejnov et al., 2018b). Thus in the limit of high resolution, feedback is made effectively weaker, and numerical convergence in the SFE is not achieved. This type of prescription can only converge for sink particle algorithms that imprint a characteristic size or density scale other than the numerical resolution, which requires certain assumptions about the nature of star cluster formation that we will not consider here.

6.3 Results

The simulated clouds evolve according to the usual sequence of events found in this type of simulation (e.g. Grudić et al., 2018b): turbulence dissipates in shocks on the crossing timescale, and the cloud collapses into dense substructures that eventually form stars. Eventually, the cumulative effect of stellar feedback is sufficient to disrupt the cloud, halting star formation. In Figure 6.1 we plot the integrated star formation efficiency $M_\star/M$ and the light-to-mass ratio as a function of time for each of the five different prescriptions used.

The SFE varies considerably with the feedback prescription used: `IMFMED` ended with a SFE of 12%, while `POISSON100` gave 4%, with the others lying in between. This is despite the fact that the final light-to-mass ratios from each prescription all agreed within 10%, as at least $4000 M_\odot$ forms in each simulation. We therefore find that the details of IMF sampling prescriptions for feedback can have a considerable effect on the SFE of simulated molecular clouds. In particular, we find that the `IMFMEAN` value of 5% is reasonably consistent with Grudić et al. (2018b), which used that prescription, while `IMFMED` gives a SFE of 12%, consistent with Kim et al. (2018a), explaining the discrepancy between those specific works.

The `IMFMEAN+K18` prescription gives results that are nearly indistinguishable from the standard `IMFMEAN` prescription, despite the fact that it always gives less feedback. We have generally found that the fraction of time during which the criteria for turning off feedback (Equation 6.2) are satisfied is very short compared to the lifetime of the GMC. Star particles accrete rapidly out of dense cores, and accretion halts either when the gas is exhausted or when the star particle is dynamically ejected out of its natal clump and into a void. Once Equation 6.2 is no longer satisfied, feedback turns on and generally drives an outflow around the star. Once this outflow has been initiated, it tends not to end. Therefore even a brief lapse in the accretion rate can effectively end the accretion history.

Even assuming an infinite reservoir for accretion, an upper bound on the amount of time that Equation 6.2 can apply can be derived from the observed properties massive stars. To maximize this time, we assume that Equation 6.2 holds as an equality. The luminosity of stars more massive than $\sim 20 M_\odot$ is:

$$\frac{L}{10^6 L_\odot} \approx 0.03 \frac{M}{M_\odot}. \tag{6.5}$$

Substituting this into Equation 6.2 gives

$$\frac{\dot{M}}{M_\odot\,\mathrm{yr}^{-1}} = 4.7 \times 10^{-5} \left(\frac{M}{M_\odot}\right)^{3/4}. \tag{6.6}$$

Over the mass range of massive stars, the solution to this equation is well-approximated by exponential growth with an e-folding time of 40 kyr, so within a few 100 kyr the maximum stellar mass on the order of $100\,\mathrm{M}_\odot$ must be reached. Because this is much shorter than even the shortest GMC lifetimes, the effect upon the cloud-scale SFE is small. However, we emphasize that the prescription could easily have more important effects on smaller scales or shorter timescales, such as influencing the accretion history of individual protostars or the formation of a dense star cluster.

6.4 Discussion

We have shown that when simulating the evolution of an isolated molecular cloud, the specific prescription for massive stellar feedback used can affect the star formation efficiency of the cloud (and by extension, the properties of the star cluster formed) at least at the factor of ~ 3 level. This is despite the fact that all simulations eventually form at least several $10^3 M_\odot$ in stars, so the IMFs in all cases are well-sampled and the final light-to-mass ratios do not differ widely.

The simplest analytic estimate of the feedback-regulated SFE of a molecular cloud can be obtained by simply equating the bulk momentum injection rate due to feedback to the weight of the cloud due to self-gravity. In the limit of small SFE (Fall et al., 2010; Murray et al., 2010; Hopkins et al., 2012a; Grudić et al., 2018b; Kim et al., 2018a):

$$\mathrm{SFE} \propto \Sigma_{\mathrm{gas}} / \frac{\mathrm{L}_\star}{\mathrm{M}_\star}, \tag{6.7}$$

where Σ_{gas} is the mean surface density of the cloud. If this force balance is assumed to hold at the time of cloud disruption, then we would expect that the variation in SFE would not exceed the variation in $\frac{L_\star}{M_\star}$, but the simulations show that this is not the case: all simulations end with the same $\frac{L_\star}{M_\star}$ within 10%, yet the variation in SFE is a factor of 3.

We generally find that prescriptions that take longer to approach the fully-sampled specific luminosity have SFE that can be a factor 2-3 higher than the fiducial `IMFMEAN` prescription. The physical reason for this is of course that the efficiency of feedback does not depend only upon the bulk ionization or momentum deposition rate: it also depends on *where* and *when* the absorption event occurs, a point deftly illustrated in recent work (Jumper and Matzner, 2018; Krumholz, 2018). Specifically, recombination and cooling times are shorter at higher density, suppressing radiative heating effects, while momentum imparted in a deeper potential well provides less terminal momentum, and if the well is sufficiently deep the momentum might not be sufficient to launch a wind at all.

This raises a point that is more broadly important: the effectiveness of feedback from massive stars depends on much more than just the bulk light-to-mass ratio arising from the IMF – it depends on when and under what conditions massive stars form. This should hold quite generally, so although we have only considered schemes for injecting feedback from an assumed IMF, this has implications for calculations that attempt to resolve the IMF self-consistently. The particulars of where massive stars form in the cloud, when they form relative to other stars, and how long they take to form should all influence the behaviour of stellar feedback. The resulting influence on feedback influences the evolution of the entire cloud and the stellar population that will form.

Counter-intuitively, the `POISSON1000` simulation had lower SFE than the `IMFMED` simulation despite the fact that its light-to-mass ratio was lower at all times. This implies that feedback in the `POISSON1000` was more effective for a given specific luminosity. The effect is due to the different discretizations of luminosity among the sink particles: with `IMFMED`, all sink particles have the same specific luminosity, while for `POISSON1000` the luminosity was concentrated in only five sources at the time star formation ended. Therefore, radiative feedback from fewer, more-luminous sources is more efficient, a result analogous to what has been found for the clustering of supernova explosions (Keller et al., 2014; Fielding et al., 2018). We can conjecture that the true IMF-resolved solution is probably closer to the discrete limit, because the bolometric and especially the ionizing luminosity will generally be dominated by the few most-massive stars.

We note that similar experiments to those shown here were considered on a *galactic* scale in (Su et al., 2018), who argued that galaxy-averaged quantities (e.g. stellar masses, sizes, morphologies, abundance patterns, statistics of their star formation histories) were not strongly influenced by the IMF sampling scheme. This is not surprising, as the spatial and time scales of self-regulation via feedback in those simulations are much longer ($\gg 10\,\mathrm{Myr}$), so most of the dynamics occurs in the well-sampled IMF limit (even in dwarf galaxies). Moreover other studies have shown that even artificially raising or lowering the GMC-scale star formation efficiency by much larger factors than those seen here produces relatively weak effects on galactic properties, because of global self-regulation by outflows and pressure balance in the ISM (Hopkins et al., 2011a; Agertz and Kravtsov, 2015; Faucher-Giguère et al., 2013; Orr et al., 2018b). However, our study here suggests that sub-galactic but still large-scale quantities, e.g. properties of star clusters and lifetime/mass of molecular gas at any given time, could be significantly influenced by the physics discussed here.

It is of course possible to develop more sophisticated IMF-sampling schemes (for examples, see Hu et al., 2016; Fujimoto et al., 2018; Emerick et al., 2018), coupled to more detailed stellar evolution models for feedback, and this can provide some improvements for coarse-grained IMF prescriptions (especially for phenomena like SNe occurring on much longer timescales). However, we stress that on the spatial and time scales of GMCs, this is not obviously "more correct": the real issue is not the statistical method by which the IMF is sampled. Rather, it is the fact that these (and all of the methods discussed here) are fundamentally assigning the question of where and when massive stars form to a "sub-grid" model, which does not know about the local (resolved) conditions in the GMC/ISM. Most of the stellar mass will form wherever nature can form a $\sim 0.1\,M_{\odot}$ star – but low-mass cores in low-density environments almost certainly cannot form the $\gtrsim 40\,M_{\odot}$ stars that dominate the UV production in a massive cluster. And allowing massive stars to form "stochastically" in such environments may likely over-estimate their effects. It is also not obvious that neglecting the accretion/formation and protostellar/pre-main sequence evolution of such stars is a valid approximation on the $\sim 1\,$Myr timescales of interest here.

As such, what we have shown is that significant, intrinsic uncertainties clearly still exist about the effects of stellar feedback at the GMC scale, at least at the level demonstrated here. These uncertainties will remain until the emergence of the IMF from GMC dynamics is understood in a self-consistent framework. Sub-grid feedback prescriptions should ultimately be informed by simulations that are able to follow the formation of a stellar population at the level of resolution required to model the formation of individual massive stars in an accurate and robust manner, so that one can model in a physically-motivated manner when and where in a simulation massive stars form.

Acknowledgements

We thank Mark Krumholz, Stella Offner, Claude-André Faucher-Giguère, Norman Murray, Eliot Quataert, James Dale, Ian Bonnell, Hui Li, Jeong-Gyu Kim, Eve Ostriker, Michael S. Fall, Christopher Matzner, Benny Tsang, and Milos Milosavljević for enlightening discussions that informed and motivated this work. Support for MYG and PFH was provided by a James A Cullen Memorial Fellowship, an Alfred P. Sloan Research Fellowship, NSF Collaborative Research Grant #1715847 and CAREER grant #1455342, and NASA grants NNX15AT06G, JPL 1589742, 17-ATP17-0214. Numerical calculations were run on the Caltech compute cluster "Wheeler," allocations from XSEDE TG-AST130039 and PRAC NSF.1713353 supported by the NSF, and NASA HEC SMD-16-7592. This research has made use of the NASA Astrophysics Data System, `ipython` (Pérez and Granger, 2007),

`numpy`, `scipy` (Jones et al., 2001), `numba` (Lam et al., 2015), and `matplotlib` (Hunter, 2007).

Chapter 7

A UNIFIED MODEL FOR THE FORMATION OF STELLAR CLUSTERS AND ASSOCIATIONS I: CLOUDS TO CLUSTERS

M. Y. Grudić, P. F. Hopkins., N. Murray, J.M.D. Kruijssen, L.C. Johnson, D. Guszejnov, C.-A. Faucher-Giguère, and X. Ma. To be submitted to MNRAS.

Abstract

An extensive suite of 160 MHD simulations of turbulent, star-forming giant molecular clouds (GMCs) with stellar feedback is described, extending previous work by simulating 10 different random realizations for each point in the parameter space of cloud mass and size. It is found that once the clouds disperse due to stellar feedback, both self-gravitating star clusters and unbound stars generally remain, which arise from the same underlying continuum of stellar density. The fraction of stars that are born within gravitationally-bound star clusters is related to the overall cloud star formation efficiency set by stellar feedback, but has significant scatter due to stochastic variations in the small-scale details of the star-forming gas flow. A GMC produces a population of clusters described by mass and size distributions set at the cloud level. We use these numerical results to calibrate a general, parametrized model for mapping the bulk properties of self-gravitating GMCs onto the star cluster populations they form, expressed statistically in terms of these distributions. Synthesizing cluster catalogues from GMC catalogues, we find that this model predicts star cluster properties that are difficult to distinguish statistically from observed cluster populations, with no tuned parameters. This marks the first conclusive success of numerical simulations at self-consistently predicting the bulk properties of star clusters in detail, using observed GMC properties as initial conditions. According to our model, star cluster masses are a highly sensitive probe of the strength of stellar feedback: if feedback were even modestly (factor of ~ 2) weaker on GMC scales, the most massive young star clusters in M83 would be > 4 times more massive than is observed.

7.1 Introduction

Star formation is a statistically-correlated process in both space and time. It is clear that star formation is in some sense *clustered*, with most stars forming as part of roughly co-eval stellar structures of elevated stellar density (Lada and Lada, 2003; McKee and Ostriker, 2007; Krumholz et al., 2018). At present, it is dominated by massive complexes formed in the most massive giant molecular clouds (GMCs), of mass scale $10^6 - 10^7 M_\odot$ in local galaxies (Bolatto et al., 2008; Colombo et al., 2014; Miville-Deschenes et al., 2017; Freeman et al., 2017). However, many important questions remain regarding the detailed relationship between giant molecular clouds, young stellar associations, and the subset of stars formed that are in gravitationally-bound star clusters.

The most basic question is what fraction of the gas mass of of a GMC is converted to stars, the *star formation efficiency* (SFE). Observationally, this can be inferred from measurements of the present gas mass and stellar mass in star-forming regions. Although such measurements have ranged over many orders of magnitude $\sim 10^{-4} - 1$ (e.g. Myers et al., 1986), observations appear to be consistent with a picture where GMCs convert a few per cent of their mass into stars, once the scatter due molecular cloud evolution is accounted for (see Feldmann and Gnedin (2011), Lee et al. (2016), Grudić et al. (2018c) and references therein). This efficiency is largely consistent with theoretical models wherein GMCs are disrupted by feedback from main sequence massive stars (Williams and McKee, 1997; Krumholz et al., 2006; Fall et al., 2010; Murray et al., 2010; Kim et al., 2018a). In a previous study (Grudić et al., 2018b), we presented MHD simulations of star formation in gas clouds with a wide range of parameters including all such feedback channels, finding that the cloud surface density sets the relative strengths of feedback and gravity, and hence the SFE achieved before the cloud is disrupted. In Grudić et al. (2018c), we argued that this is the only theory proposed thus far that reproduces the measured star formation efficiencies of GMCs in the Milky Way (see also Geen et al. 2017).

A complete theory of star formation in GMCs must go further, describing not only how many stars form, but how those stars are organized spatially and dynamically. Regarding this, the most important distinction to be made is between *monolithic* and *hierarchical* pictures of star formation. In the monolithic scenario, all stars originate in star clusters of high stellar density, most of which subsequently expand and dissolve into the field due to gas expulsion and N-body evolution (Lada and Lada, 1991; Kroupa et al., 2001). In the hierarchical scenario, stellar structure is inherited from a hierarchy of ISM structure spanning a wide range of scales. As a result, stars form with a wide range of natal stellar densities, and gravitationally-bound, dynamically-relaxed clusters are simply the result of the upper tail-end of a larger continuum that happens to have locally-high star formation efficiency (Elmegreen, 2002, 2008; Bonnell et al., 2011; Kruijssen, 2012). The observational case for the latter scenario has strengthened in recent years, with the general finding that young stellar structure does indeed appear to span a broad range of scales and a continuum of densities (Bressert et al., 2010; Gouliermis et al., 2015; Grasha et al., 2017; Gouliermis, 2018). Recently it was also found that the kinematics of OB assocations are incompatible with the hypothesis that they consist only of formerly-dense clusters that have since expanded (Ward and Kruijssen, 2018).

Whether star cluster formation is hierarchical or monolithic, the next important question after the SFE is the fraction of the stars locked into bound clusters at the end of star formation:

$$f_{bound} = \frac{M_{\star,bound}}{M_\star}. \tag{7.1}$$

It has long been thought that the value of f_{bound} is typically $<<$ 1, at least in the conditions of local galaxies (Elmegreen, 1983). Simple physical arguments can be made that f_{bound} is an increasing function of the local star formation efficiency (Hills, 1980; Mathieu, 1983), which have been refined by N-body experiments (Baumgardt and Kroupa, 2007). In the monolithic picture, f_{bound} corresponds to the fraction of clusters that experience “infant mortality", the expansion that occurs when gas within the cluster is expelled by stellar feedback. According to the hierarchical picture, it typically argued that bound clusters form in regions where feedback is inefficient, *exhausting* gas locally so that they generally avert infant mortality (Kruijssen et al., 2012b). Meanwhile, there would be a population of stars that never get a chance to orbit within a bound, virialized structure in the first place – in this scenario, f_{bound} corresponds to the mass fraction of the bound population.

It has historically been quite difficult to reliably measure f_{bound} through direct observations of any one star-forming cloud complex, as very good astrometric data are needed[1]. On the other hand, under certain assumptions, it is possible to measure an average f_{bound} integrated over an entire galaxy or a patch of a galaxy (Bastian, 2008; Goddard et al., 2010):

$$\Gamma = \frac{\dot{M}_{bound}}{\dot{M}_\star}, \tag{7.2}$$

where $\dot{M}_{clusters}$ and $\dot{M}_\star$ are the mass formation rates of stars in bound clusters and of all stars in the region. Extragalactic studies can only determine $\dot{M}_{dense}$ by measuring

---

[1] However, recently progress has been made in estimating the boundedness of young star clusters in the Milky Way: Ginsburg and Kruijssen (2018); Kuhn et al. (2019).

the mass in dense stellar structures within a certain age bin, and stellar density is not necessarily a sufficient condition for boundedness. However, it is a reasonable approximation if measured over a proper choice of age bin, using only clusters that are too old to have survived as an unbound entity (ie. older than the crossing time of the progenitor cloud, $\sim 10\,\mathrm{Myr}$), but too young to be likely to be disrupted or to have lost much mass due to galactic or internal dynamical processes ($\leq 100\,\mathrm{Myr}$). This measurement has been performed most convincingly over different regions of several local spiral galaxies (Adamo et al., 2015; Johnson et al., 2016; Messa et al., 2018), with the general finding that regions of greater mean ISM pressure, molecular gas fraction, and gas surface density tend to have greater values of Γ, in line with analytic models invoking stellar feedback (Kruijssen, 2012).

Of the material that does remain bound, one must then ask what the distribution of masses and sizes of bound structures is. The maximum cluster mass in particular is expected to be a sensitive probe of star formation physics, because if GMCs constitute the gas supply potentially available for cluster formation, then the maximum cluster mass satisfies

$$M_{cl,max} \leq \epsilon_{int} M_{GMC,max}, \tag{7.3}$$

where $M_{GMC,max}$ is the maximum GMC mass in a given environment, and

$$\epsilon_{int} = \frac{M_\star}{M_{GMC}} \tag{7.4}$$

is the star formation efficiency of the cloud, which is believed to be determined by the strength of stellar feedback. Note that the above does not necessarily hold as an equality for two reasons: only a fraction of stars formed will be in bound clusters, and one GMC can potentially produce multiple bound clusters – GMCs can produce star cluster *complexes*, where the distribution of cluster masses is described by some underlying distribution at the cloud level.

This is the first in a series of three papers intended to address the above questions about the nature of star cluster formation. In this work, Paper I, we extend our previous work that focused on various aspects of the SFE of GMCs (Grudić et al., 2018b,c; Hopkins and Grudić, 2018; Grudić and Hopkins, 2018), using an expanded suite of numerical simulations to map out the behaviour of star-forming GMCs across parameter space, and, crucially, across 10 different random realizations for the initial turbulent flow of each cloud model. From these numerical results we construct a more complete model that describes the following statistical properties of star formation in GMCs:

- Their star formation efficiency.
- The fraction of stars formed that are locked into gravitationally-bound clusters.
- The mass function of bound star clusters, including the maximum cluster mass, determined at the level of individual clouds.
- The size-mass relation of bound clusters.
- The initial density profiles of bound clusters.

In doing so, we will link the physics of MHD turbulence, gravity, radiative processes, star formation, and stellar feedback to the observables that provide the most sensitive probes of star formation physics, for the first time in a self-consistent framework, and show that this framework contains the necessary and sufficient physics to reproduce these key observations.

In Paper II, we will describe an end-to-end model of galactic star cluster formation that couples the model in the present work to the Hopkins (2012) excursion-set theory for the properties of GMCs, predicts the properties of star cluster populations provided only the bulk (ie. kpc-scale) galactic properties, and provides a new sub-grid prescription for star cluster populations in cosmological simulations (e.g. Pfeffer et al., 2018). In Paper III, we couple the model in the present paper to the FIRE cosmological zoom-in simulations, and make the first predictions about star cluster formation across cosmic time within a self-consistent framework motivated by star formation physics at the GMC scale.

This paper is structured as follows. In Section 7.2, we will describe our simulation and analysis methods, and present the raw numerical results of the study. In Section 7.3, we describe an analytic statistical model for mapping clouds onto cluster populations that reproduces the results of the simulations, and can be applied to a general cloud population. In Section 7.4, we compare model predictions with observations in local spiral galaxies, and demonstrate that the model is able to account for key observed scalings in star cluster populations. In 7.5, we discuss various predictions and applications of our model, and compare it with other models. Finally, in 7.6, we summarize our main findings and outline future work.

7.2 Simulations

7.2.1 Numerical Methods

We perform a suite of simulations of isolated GMCs with GIZMO, a mesh-free, Lagrangian finite-volume Godunov code designed to capture the advantages of both grid-based and smoothed-particle hydro-dynamics (SPH) methods, described fully in Hopkins (2015) [2]. We solve the equations of ideal magnetohydrodynamics using the Lagrangian Meshless Finite Mass method (Hopkins and Raives, 2016), augmented with a novel constrained-gradient method to further reduce $\nabla \cdot \mathbf{B}$ errors (Hopkins, 2016).

Gravity

The gravitational field is summed using the fast Barnes and Hut (1986) tree algorithm introduced in GADGET-3 (Springel, 2005). However, we have modified the original node-opening criterion used in the GADGET-3 algorithm for our problem. In the original algorithm, a node was opened if the field contribution of its quadrupole moment was greater than some small fraction of the total field at the point of interest. In our problem, this can allow the external tree-force on a dense star cluster to be degraded in accuracy due to its locally-strong gravitational field, and so we wished for some control on the force accuracy that is unaffected by the cluster's internal structure. To achieve this, we enforced the Barnes and Hut (1986) geometric node-opening criterion with an opening angle $\Theta = 0.5$, in addition to the other criterion. The gravitational softening of both gas and star particles is adaptive, with correction terms to ensure energy and momentum conservation as as described in Hopkins (2015). A minimum Plummer-equivalent softening of 10^{-2} pc is enforced only for star particles, however we found that the stellar densities needed for this to have a a significant effect are almost never achieved in our parameter space.

Star formation

Our simulations do not attempt to resolve the formation, motion, and feedback of *individual* stars. Rather, as in Grudić et al. (2018b), they simulate the stellar mass distribution as an ensemble of collisionless star particles. In Grudić et al. (2018a) we found that this simulation technique succeeds at producing star clusters of a similar density profile shape to observed young, massive star clusters in local galaxies. The

---

[2] A public version of this code is available at `www.tapir.caltech.edu/~phopkins/Site/GIZMO.html`.

star formation criteria are as described in Grudić et al. (2018b): gas cells may only be converted to stars if they are self-gravitating (the virial criterion, Hopkins et al. 2013) at the resolution scale, molecular, and in a converging flow.

We do not impose a threshold density for star formation. In our initial experiments varying the density threshold, we found that it was either irrelevant compared to the virial criterion if set low, or very clearly imprinted a characteristic, numerically-imposed 3D density on the star clusters if set high. We thus decided to rely mainly on the virial criterion, which is has more physical motivation. However, we initially found that this alone was not strict enough, because momentary noise in the velocity gradient could potentially allow premature star formation, and convergence of cloud star formation histories with resolution was slow because the low-resolution runs would form stars systematically sooner. We thus implemented a smoothing procedure for the virial criterion. If $\alpha_{vir} = \frac{E_{kin}}{|E_{grav}|}$ is the local virial parameter, then at each timestep we update dimensionless quantity

$$A\left(t + \Delta t\right) = \frac{\Delta t}{\tau} \frac{1}{1 + \alpha_{vir}\left(t\right)} + \left(1 - \frac{\Delta t}{\tau}\right) A\left(t\right), \tag{7.5}$$

ie. $A\left(t\right)$ is $\frac{1}{1+\alpha_{vir}} \in [0, 1]$, exponentially smoothed with an e-folding time τ. Star formation is allowed when $A\left(t\right) > 1/2$, corresponing to $\alpha_{vir} < 1$. We found that setting $\tau = t_{ff}/8$, ie. smoothing over a window just $1/8$ the local freefall time, was sufficient de-noise the virial criterion, accelerating the convergence of cloud star formation histories with resolution.

Cooling and Stellar Feedback

Our treatment of ISM physics and stellar feedback largely follows the FIRE simulations[3], and all algorithms are presented in detail in Hopkins et al. (2018a). We account for an extensive range of radiative cooling and heating processes, using a standard implicit algorithm, and follow cooling down to a numerically-imposed floor of 10 K.

We include all stellar feedback mechanisms from main-sequence stars: stellar winds, radiation, and supernova explosions, all of which are dominated by the most massive ($\geq 8\,\mathrm{M}_\odot$) stars for young stellar populations. Each star particle is assigned feedback fluxes consistent with a simple stellar population with a well-sampled Kroupa (2002) IMF, with luminosities, mass loadings, and momentum fluxes taken from a

---

[3] `http://fire.northwestern.edu`

STARBURST99 (Leitherer et al., 1999) simulation (see Hopkins et al. (2018a) for details). We caution that the results of GMC simulations with stellar feedback *do* depend somewhat on the specific prescription for assigning feedback fluxes to star particles, even assuming a given IMF (Grudić and Hopkins, 2018). However, here we will only target the parameter space of relatively massive GMCs, where cloud lifetimes are long compared to the formation time of massive stars, and the IMF should indeed be well-sampled. We have verified in tests that the results of this paper are much less sensitive to the small-scale details of how massive star formation is modeled than the less-massive ($10^5 M_\odot$) cloud simulated in Grudić and Hopkins (2018).

Mass, energy, and momentum fluxes from stellar winds and supernova explosions are injected into particles within the hydrodynamic stencil surrounding a star particle according to the fully-conservative scheme described in Hopkins et al. (2018c). The energy-conserving Sedov-Taylor phase of individual supernova blast-waves is resolved explicitly in all simulations, with the most coarsely-resolved runs having a mass resolution of $140\,\mathrm{M}_\odot$, and most others much finer.

We use the LEBRON radiative transfer approximation (for details see Hopkins et al. 2018a), which accounts for absorption of single-scattered photons within the a stencil around a star particle (including ionizing radiation, expanding the search radius until ionizing photons are exhausted). Photons not absorbed within the stencil are propagated through the simulation domain using an the optically-thin approximation that uses the gravity solver, with extinction corrections at the source and absorber. The radiation field is computed in far-UV, near-UV, optical/NIR and FIR bins, subject to extinction according to appropriate flux-mean opacities, including dust extinction. We have shown in previous work that this radiative transfer approximation gives cloud SFEs in reasonable agreement (factor of ~ 2) with results from an M1 closure scheme (e.g. Rosdahl and Teyssier 2015, as demonstrated in Hopkins and Grudić 2018), and even better agreement with the results of a state-of-the-art adaptive ray tracing scheme (e.g. Kim et al. 2018a, as shown in Grudić and Hopkins 2018).

Cluster identification

We identify self-gravitating star clusters at the end of the simulations with our own version of the SUBFIND algorithm (Springel et al., 2001). This algorithm organizes the stellar density field into a hierarchy of structures surrounding density peaks, and then at each level of the hierarchy subjects the structures to an iterative unbinding procedure to determine each group's gravitationally-bound subset. Cluster membership is determined according to the *smallest* structures in this hierarchy that can be constructed. We use fast neighbor-lookup and gravitational potential routines provided by scipy (Jones et al., 2001) and pykdgrav[4], respectively. We have also run our analysis using the simpler cluster-finding algorithm described in Grudić et al. (2018a) based on grouping stars into common potential wells, and have found that none of the results of this study were senstive to the choice of algorithm.

7.2.2 Initial Conditions

Our initial conditions consist of a spherical cloud of uniform density with total mass M_{GMC} and radius R_{GMC}, embedded in a warm, diffuse medium in thermal pressure equilibrium that fills a periodic box of side length $20R_{GMC}$. The initial velocity field of the gas in the cloud consists entire of a Gaussian random field with power spectrum $|\tilde{\mathbf{v}}\left(\mathbf{k}\right)|^2 \propto k^{-4}$ (Gammie and Ostriker, 1996), and a natural mixture of solenoidal and compressive modes (ie. $E_{solenoidal} = 2E_{compressive}$). The velocity field is normalized so that the initial kinetic energy of the cloud is equal in magnitude to its gravitational potential energy. This is a more realistic model of GMCs than the more abstract numerical experiments in Grudić et al. (2018c), which were intended to isolate a certain surface density scale by ensuring rotational support, which GMCs do not generally have (Braine et al., 2018). The warm, diffuse medium is initially at rest. The magnetic field is initially uniform, and normalized so that the magnetic energy in the cloud is 1% of its turbulent energy.

Our parameter space consists of clouds on a $4 \times 2 \times 2$ grid of surface densities ($64\,\mathrm{M}_{\odot}\,\mathrm{pc}^{-2}$, $127\,\mathrm{M}_{\odot}\,\mathrm{pc}^{-2}$, $254\,\mathrm{M}_{\odot}\,\mathrm{pc}^{-2}$, and $509\,\mathrm{M}_{\odot}\,\mathrm{pc}^{-2}$), radii (100 pc and 300 pc), and metallicities ($0.01\,\mathrm{Z}_{\odot}$ and $Z_{\odot}$). We intentionally targeted a parameter space representative of the largest and most massive GMCs in local spiral galaxies (e.g. Colombo et al., 2014; Rice et al., 2016; Miville-Deschenes et al., 2017; Freeman et al., 2017). The reasons for doing so are twofold. We expect that the most massive (and hence most detectable) clusters originate in the most massive GMCs, and that the total mass of stars formed is dominated by the most massive star-forming complexes (Williams and McKee, 1997; Murray, 2011; Lee et al., 2016, e.g.). Hence overall, it is likely that the most massive GMCs produce the dominant contribution to the top end of the observable star cluster mass function, an observation that we will confront in Section 7.4. We also expect that this regime of massive star cluster

---

[4] `https://github.com/omgspace/pykdgrav`

formation is the regime in which our approximations of collisionless stellar dynamics and IMF-averaged feedback are the most accurate. Our choice of metallicities is intended to bracket the the range of metallicities of observed globular clusters and galaxies (Forbes and Bridges, 2010; Kirby et al., 2013).

In all simulations, the cloud component is resolved in 10^6 Lagrangian gas cells. For each point in parameter space, we simulate 10 different random realizations of the initial turbulent velocity field. In doing so, we map out not only the *scalings* across parameter space, but the range of intrinsic cloud-to-cloud variations due to small-scale details of the turbulent gas flow, which can potentially be important for star cluster formation.

7.2.3 Simulation Results

All simulations follow the sequence of events that is typical in GMC simulations that make a reasonably complete accounting of stellar feedback. The initial turbulent motions dissipate on a crossing timescale (Stone et al., 1998), inevitably leading to localized runaway collapse and eventually star formation. The SFR accelerates at first (Murray and Chang, 2015; Lee et al., 2015, 2016), but eventually levels off and begins to drop as feedback begins to evacuate the gas (Grudić et al., 2018c; Li et al., 2019). Eventually, all gas is evacuated by feedback and star formation ceases entirely. All clouds were evolved for two initial cloud free-fall times,

$$t_{ff,0} = \frac{\pi}{2}\sqrt{\frac{R_{GMC}^3}{GM_{GMC}}}, \tag{7.6}$$

and we generally find that star formation has almost ceased entirely by $\sim 1 t_{ff,0}$, and the central region is essentially gas-free by $2t_{ff,0}$.

At the end of star formation, the state of our fiducial cloud model, with mass $M_{GMC} = 4 \times 10^6 M_\odot$ and $R_{GMC} = 100\,\mathrm{pc}$, is plotted in Figure 7.1, and is representative of the result of all simulations in the suite. The result is a highly sub-structured, hierarchically-clustered configuration, similar to observed complexes of young stars (e.g. Kuhn et al., 2014; Gouliermis, 2018). Some stars are in bound clusters, but distinct clustered substructures also exist that are not bound. The unbound component eventually disperses in roughly a cloud crossing time, while the bound component survives and virializes through violent relaxation.

All simulated clouds produce *some* mass in gravitationally-bound stars, although there were a few cases in the lowest-$\Sigma_G GMC$ runs where the only cluster masses fell

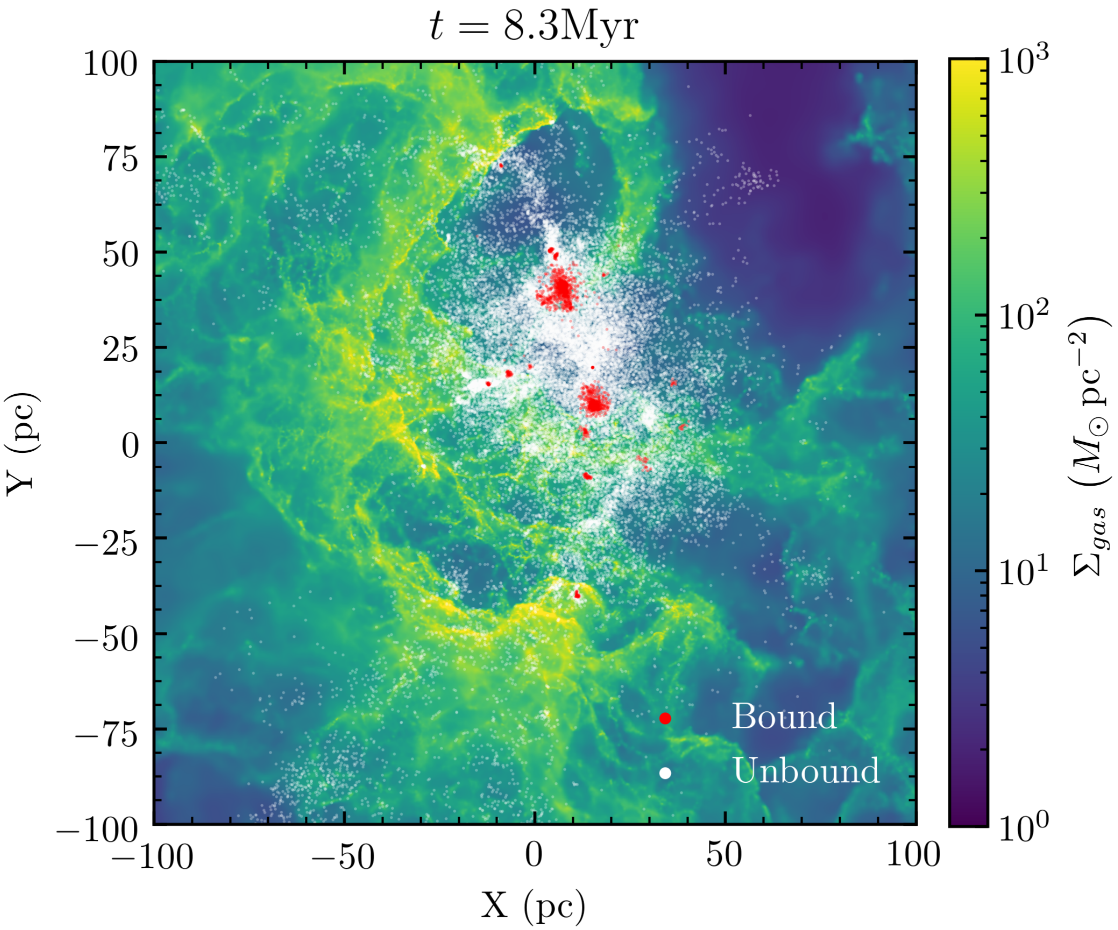

Figure 7.1: State of the fiducial cloud model with $M = 4 \times 10^6 M_\odot$, $R = 100$pc, and random seed 1, after $t_{ff} \sim 8.3$ Myr, when star formation has essentially ceased due to gas evacuation. Positions of star particles are plotted atop the gas surface density distribution. Star particles not assigned to any bound cluster are shown in white, and bound star particles in red. The GMC produced a highly-sub-structured complex of both unbound and bound stellar mass, with most stellar mass in the unbound association in this case ($f_{bound} \sim 10\%$). This is similar to the configuration of observed complexes of newly-formed stars (see e.g. Kuhn et al. (2014), Fig. 2).

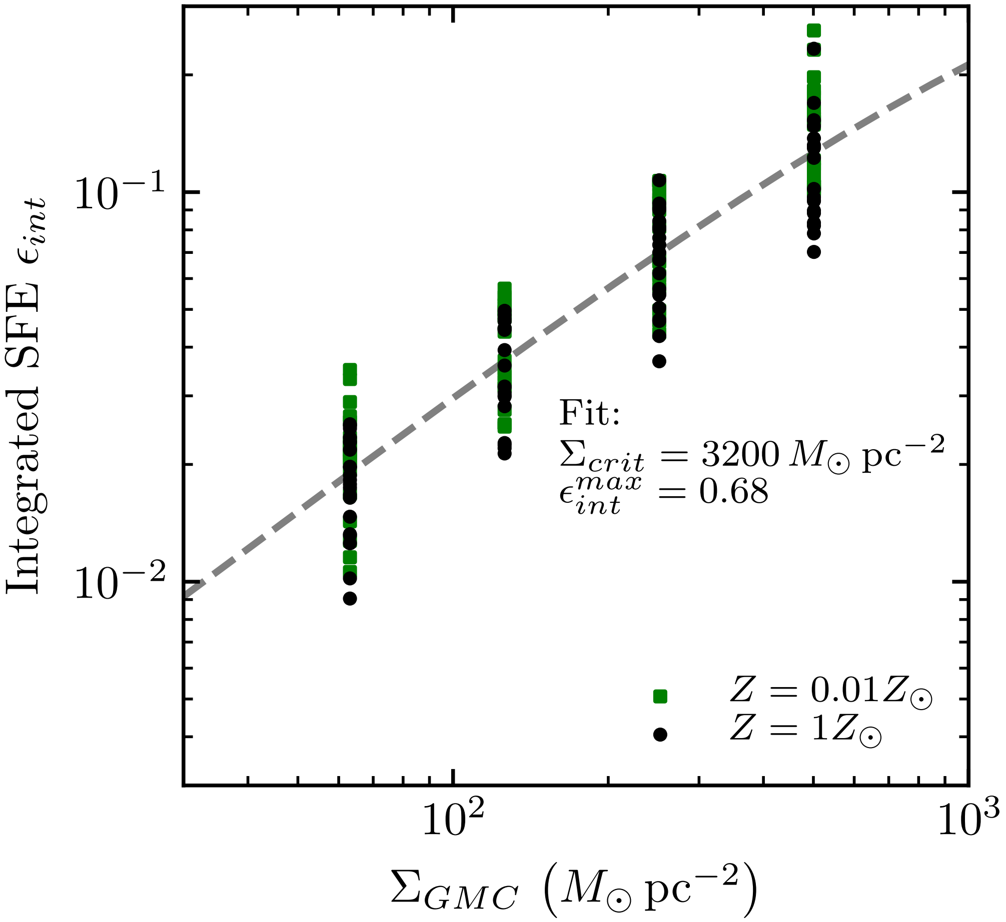

Figure 7.2: Integrated star formation efficiency $\epsilon_{int} = \frac{M_\star}{M_{GMC}}$ as a function of the mean initial cloud surface density, $\Sigma_{GMC} = \frac{M_{GMC}}{\pi R_{GMC}^2}$. ϵ_{int} scales roughly $\propto \Sigma_{GMC}$, and is well-fit by Equation 7.7 with $\Sigma_{crit} = 3200\,\mathrm{M}_\odot\,\mathrm{pc}^{-2}$ and $\epsilon_{int}^{max} = 0.68$, with 0.13 dex of residual scatter. This scatter is driven by cloud-to-cloud variations in the details of the initial turbulent gas flow, but is relatively small compared to the scatter in the bound fraction of star formation (e.g. Figure 7.4).

below our resolution cut of 32 particles. The formation of bound versus unbound stellar systems are not different modes of star formation, but rather, it would seem, different aspects of the same underlying continuum, as is generally argued within the hierarchical picture of star cluster formation.

Star formation efficiency

For this new simulation suite, which has different parameter space and initial cloud kinematics from the Grudić et al. (2018c) suite, we repeated the excercise of determining the strongest predictor of the integrated SFE, ϵ_{int}, in terms of the initial cloud parameters. We again found that the cloud surface density Σ_{GMC} was the tightest predictor of ϵ_{int}, in agreement with the picture where ϵ_{int} is simply determined by the force balance of feedback and gravity within the cloud, which yields an inevitable dimensional scaling (Fall et al., 2010; Murray, 2011).

We plot the relation between Σ_{GMC} and ϵ_{int} in Figure 7.2, and see that as before it scales roughly $\propto \Sigma_{GMC}$, with a modest scatter 0.13 dex between the different metallicities and statistical realizations of the cloud models. We perform an unweighted least-squares fit on $\log \epsilon_{int}$ as a function of Σ_{GMC} as in (Grudić et al., 2018c):

$$\epsilon_{int} = \left(\frac{1}{\epsilon_{int}^{max}} + \left(\frac{\Sigma_{GMC}}{\Sigma_{crit}} \right)^{-1} \right)^{-1}, \tag{7.7}$$

and find best-fit parameters $\Sigma_{crit} = 3200 \pm 100\,\mathrm{M_\odot\,pc^{-2}}$ and $\epsilon_{int}^{max} = 0.8 \pm 0.3$[5]. We therefore confirm that the SFE scaling formula of Fall et al. (2010) and Grudić et al. (2018b) holds for clouds whose internal motions are dominated by turbulence. We also find that our model with $M_{GMC} = 2 \times 10^6\,\mathrm{M_\odot}$ and $R_{GMC} = 100\,\mathrm{pc}$ has a SFE of $1-3\%$, exactly as was found in Grudić et al. (2018c) where we used rather different using “pre-stirred" turbulent initial conditions from a driven turbulent box simulation. The details of how turbulence is initialized in isolated cloud simulations does not appear to materially affect the outcome of star formation when feedback is fully accounted for. It is likely that both the pre-stirring and Gaussian random field methods are equally artificial, as the initial turbulent motions are not self-consistent with effects of gravity and feedback.

The relative robustness of the SFE to the different statistical realizations suggests that the star formation efficiency depends simply on the balance of feedback and gravity on the *cloud* scale. Since the cloud bulk properties are essentially a controlled variable here, we accordingly see little variation from cloud to cloud of a given set of parameters.

The bound fraction of star formation

At the end of each simulation, at time $2t_{ff,0}$, we ran the cluster-finding algorithm described in Section 7.2.1 to group the star particles in to bound star clusters.

---

[5] We are hardly able to constrain the maximum SFE ϵ_{int}^{max} here due to our choice of parameter space, where the SFE does not exceed 25%, unlike (Grudić et al., 2018b) which surveyed much higher Σ_{GMC}.

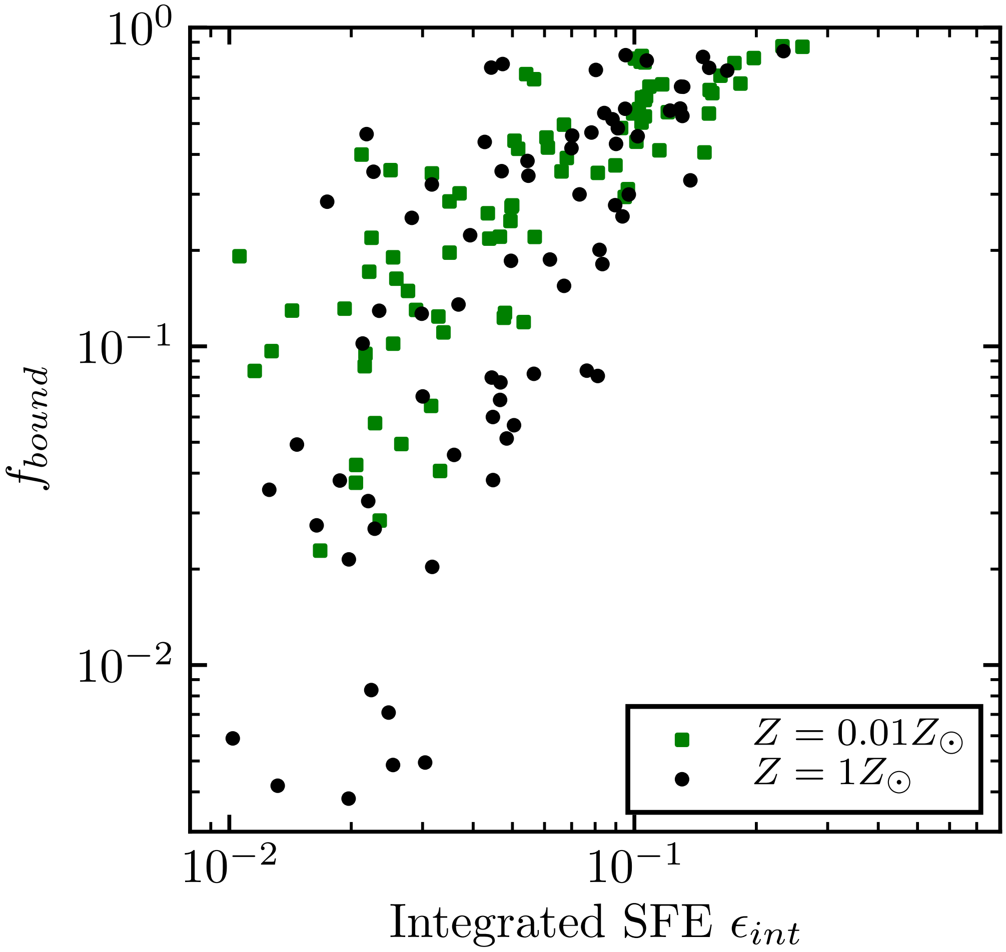

Figure 7.3: Fraction of stars formed in bound clusters f_{bound} as a function of the integrated star formation efficiency ϵ_{int}. The two efficiencies are correlated, but not generally equal, and with significant scatter from one turbulent realization to another at lower ϵ_{int}. f_{bound} saturates to ~ 1 at a SFE of $\sim 20\%$. It is also systematically greater at low metallicity due to the lack of strong OB winds.

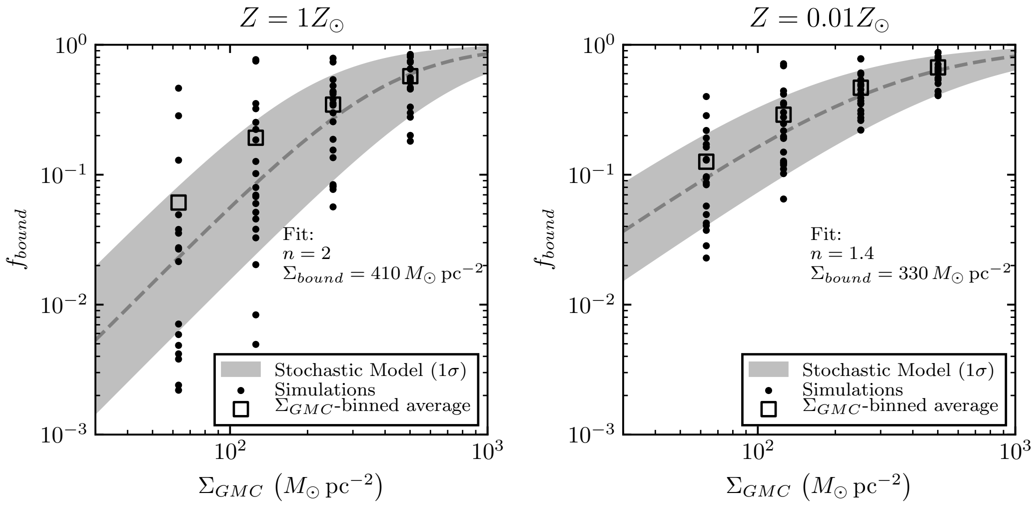

Figure 7.4: f_{bound}, the fraction of stars in bound clusters at the end of star formation in the simulated GMC, as function of GMC surface density Σ_{GMC} for solar metallicity (*left*) and 1% solar metallicity (*right*). We plot the result for each individual simulation (dots) as well as the SFE-weighted average for each bin in Σ_{GMC} (squares). Unlike the SFE, the relation is notably metallicity-dependent. We perform different fits of equation 7.8 for each respective metallicity, with best-fit parameters listed above - the solar-metallicity relation is a steeper function of Σ_{GMC}, and reaches the 50% mark at slightly greater surface density. The shaded regions indicate the $\pm\sigma$ region our model for the scatter in f_{bound} (Equations 7.9 and 7.10)

.

Across the entire suite, we identified 6181 bound clusters resolved in more than 32 star particles (which will serve as our resolution cut in this work, as this is the stencil size over which the gravitational softening is adapted). Every cloud produced at least one bound cluster, and typically many more, with a mean multiplicity of 38. As expected from analytic work (Hills, 1980; Mathieu, 1983), N-body experiments (Tutukov, 1978; Lada et al., 1984; Kroupa et al., 2001; Baumgardt and Kroupa, 2007), and recent star formation simulations with an idealized feedback model (Li et al., 2019), the fraction of stars remaining in bound clusters at the end of star formation is an increasing function of ϵ_{int} (Fig. 7.3). Also in agreement with the aforementioned *numerical* works, the bound fraction saturates to ~ 1 at considerably lower SFE than the 50% required in the limit of fast gas evacuation in the classic Hills (1980) derivation – the typical f_{bound} is 50% when $\epsilon_{int} \sim 10\%$. However, the most striking result of Figure 7.3 is the massive scatter at fixed ϵ_{int}: the relation between the two quantities is not one-to-one, and must be modeled statistically.

This is also readily seen in Figure 7.4, where we plot f_{bound} as a function of Σ_{GMC}.

At fixed Σ_{GMC} (which is effectively fixed ϵ_{int} as well), f_{bound} varies by as much as 2 dex, particularly at lower Σ_{GMC}. Surprisingly, there is at least one cloud at any given surface densities that is able to form $> 50\%$ of its stars in bound clusters. We find systematically higher f_{bound} is achieved in the runs at 1% solar metallicity, which we will show in Section 7.2.3 can be isolated to the lack of strong OB winds, whose mass loading scales $\propto Z$ as described in Hopkins et al. (2018a).

Despite the large scatter, a clear scaling in the *typical* bound fraction can be discerned. For each metallicity, we performed unweighted least-squares fits of $\log f_{bound}$ to a generic saturating power-law in Σ_{GMC}:

$$f_{bound} = \left(1 + \left(\frac{\Sigma_{bound}\left(Z\right)}{\Sigma_{GMC}}\right)^{n(Z)}\right)^{-1}, \tag{7.8}$$

where $\Sigma_{bound}\left(Z\right)$ denotes the metallicity-dependent surface density at which $f_{bound} = 50\%$ and $n\left(Z\right)$ is metallicity-dependent power-law slope in the limit $\Sigma_{GMC} << \Sigma_{bound}$. We found $\Sigma_{bound}\left(Z_{\odot}\right) = 410\,\mathrm{M_{\odot}\,pc^{-2}}$, $\Sigma_{bound}\left(0.01 Z_{\odot}\right) = 330\,\mathrm{M_{\odot}\,pc^{-2}}$, $n\left(Z_{\odot}\right) = 2$, and $n\left(0.01 Z_{\odot}\right) = 1.4$.

We can model the stochastic variation in f_{bound} shown in Figure 7.4 by introducing a logarithmic variance in the "effective" value of Σ_{GMC} that is plugged into Equation 7.8. The effective surface density Σ' is distributed according to a log-normal distribution centered on the actual Σ_{GMC}:

$$P\left(\log \Sigma' | \sigma_b\right) = \frac{1}{\sqrt{2\pi\sigma_b^2}} \exp\left(\frac{-\left(\log \Sigma' - \log \Sigma_{GMC}\right)^2}{2\sigma_b^2}\right). \tag{7.9}$$

Once sampled from this distribution, the effective surface density is then plugged into Equation 7.8:

$$f_{bound} = \left(1 + \left(\frac{\Sigma_{bound}\left(Z\right)}{\Sigma'}\right)^{n(Z)}\right)^{-1}. \tag{7.10}$$

The results of this model are plotted as the shaded regions in Figure 7.4. We have found that the scatter Σ_{GMC}-depdendent scatter in f_{bound} is well-reproduced by the parameter $\sigma_b = 0.6$, ie. the "effective" surface density that matters for star cluster formation varies intrinsically by 0.26 dex from one cloud to another, due to the varying small-scale details of the cluster-forming gas flows.

This procedure can also be repeated to account for the variations in ϵ_{int} (Figure 7.2, but we find that this is not as nearly important for obtaining a faithful description of the similation results as it is for f_{bound}. First, ϵ_{int} is not as steep a function of Σ_{GMC}, so

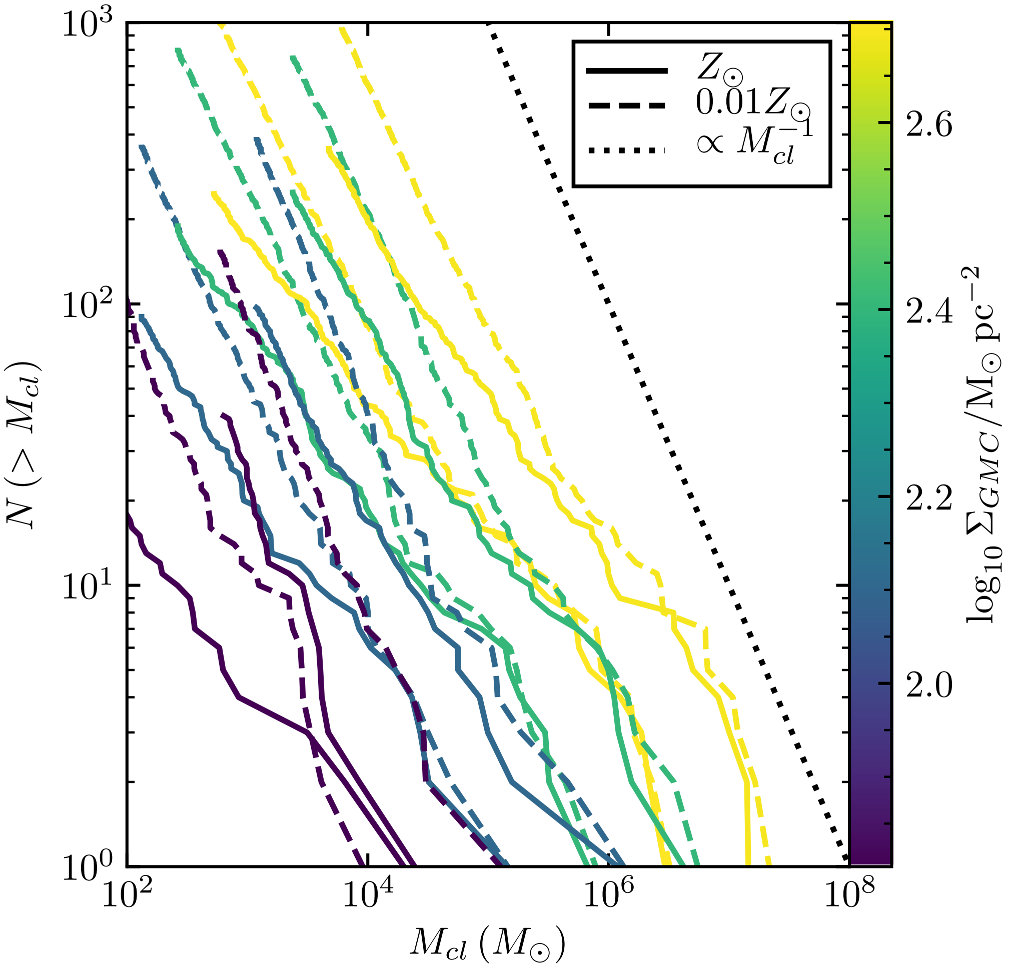

Figure 7.5: Cumulative mass functions of bound clusters produced by each cloud in parameter space, stacked over the ten random initial turbulent seedings. Curves are colour-coded according to the initial cloud surface density Σ_{GMC}, and we differentiate between solar-metallicity (solid) and 1% solar metallicity (dashed) cloud models. The dotted line shows the cumulative mass function expected from a typical star cluster mass function of the form $\frac{\mathrm{d}N}{\mathrm{d}M_{cl}} \propto M_{cl}^{-2}$. See Figure 7.2 for model predictions of the mass function in a real galaxy.

variations in the “effective" surface density do not compound as drastically. Second, and the maximum-likelihood value of σ for modeling variations in ϵ_{int} is less than half of the value required for f_{bound}.

Mass distribution of bound star clusters

As shown in Figure 7.1, the simulated GMCs typically produce multiple bound star clusters of varying masses and sizes – the mapping from clouds to clusters is not

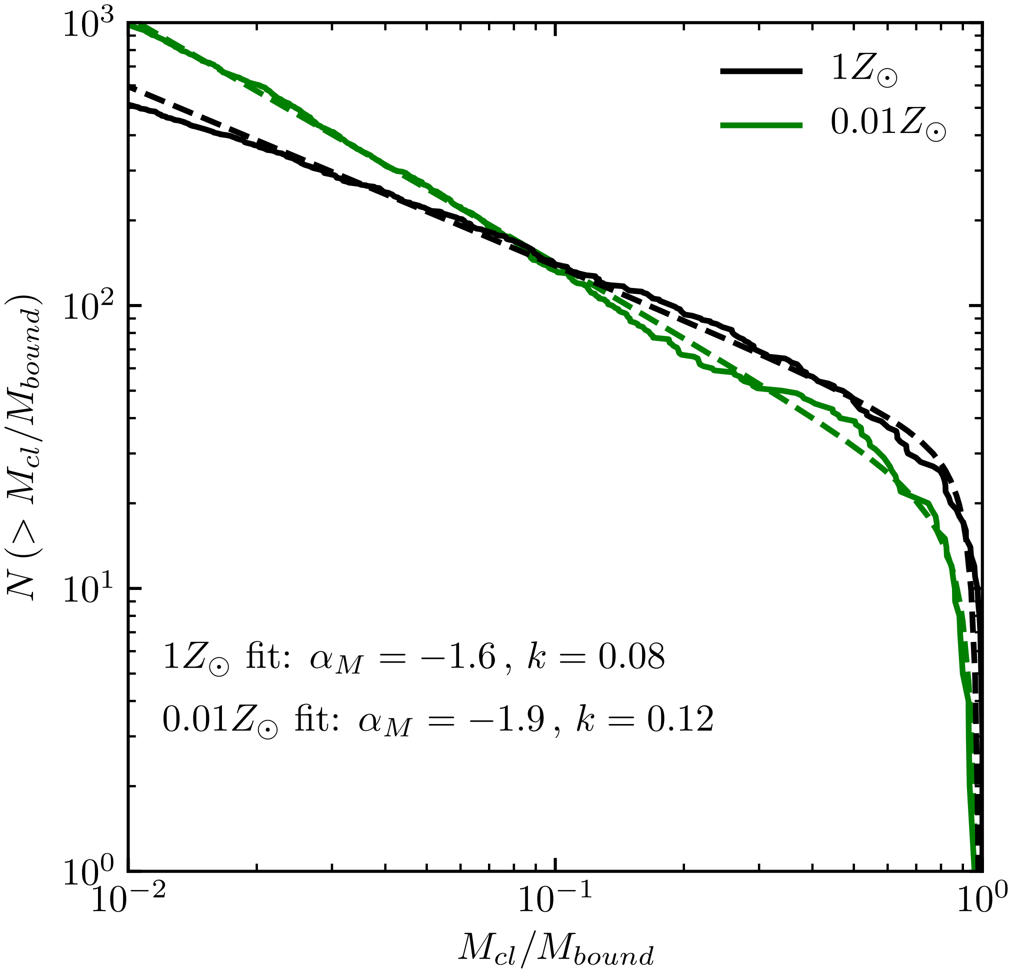

Figure 7.6: Cumulative distribution of bound star clusters in all simulations, relative to the total bound mass in the respective run. The total mass tends to be dominated by the massive primary cluster. We separate the distributions by metallicity, as the low-metallicity runs tend to have steeper mass functions. Fits to Equation 7.11 are shown as dashed lines.

one-to-one. Rather, it must be understood in terms of a *distibution* of cluster masses that emerges at the level of individual clouds. In general, we find that the mass distribution can be described in terms of a primary cluster that dominates the total mass in bound clusters, and a population of less-massive clusters whose masses are distributed according to a power-law.

In Figure 7.5 we show the stacked cumulative mass functions from all realizations of a give set of cloud parameters – ie., the mass distribution that would be observed if a galaxy formed clusters from many GMCs, but with uniform bulk properties. The distributions are all fairly top-heavy, due to the few particularly massive clusters in the population that constitute the primary cluster in each respective cloud. However, the asymptotic slopes of the mass functions toward lower masses tend to have power-law behaviour, often scaling roughly $\propto M_{cl}^{-1}$, consistent with the mass distribution ~ -2 that is typically measured in young star cluster populations (e.g. Chandar et al., 2017). However, the mass distributions from the solar metallicity clouds have preferentially shallower slopes, more consistent with a mass function of slope ~ -1.6. It should be emphasized that the mass distributions in Figure 7.5 do not in themselves constitute predictions of a galactic star cluster mass distribution, as GMC bulk properties are not uniform in real galaxies.

The cloud-level mass functions can be better summarized when collapsed down in terms of the mass relative to the total bound mass, M_{cl}/M_{bound}. In Figure 7.6 we plot the stacked mass relative functions for the two different metallicities, over all simulations. The cumulative distributions are strongly concave down (such that the PDF $\frac{\mathrm{d}N}{\mathrm{d}M_{cl}}$ is in fact *peaked*) in the vicinity of M_{cl}/M_{bound} because the primary tends to be so dominant, but they then level off to a power-law form. We fit these cumulative distributions to the model

$$N\left(> M_{cl}\right) = N_0 \left(\frac{M_{cl}}{M_{bound}}\right)^{1-\alpha_M(Z)} \exp\left(\frac{-k\left(Z\right)}{1 - \frac{M_{cl}}{M_{bound}}}\right), \tag{7.11}$$

where N_0 is a normalization factor, $\alpha_M\left(Z\right)$ is the slope of the asymptotic power-law mass function for small masses, and $k\left(Z\right)$ is a dimensionless shape parameter that models the heavy top end of the distribution. Again we form metallicity-dependent fits, finding $\alpha_M\left(Z_\odot\right) = -1.6$, $k\left(Z_\odot\right) = 0.08$, $\alpha_M\left(0.01 Z_\odot\right) = -1.9$, and $k\left(0.01 Z_\odot\right) = 0.12$. We therefore see that even controlling for GMC properties, a power-law star cluster mass distribution of of between -1.6 and -1.9 emerges, due to the cluster multiplicity inherent in hierarchical star formation.

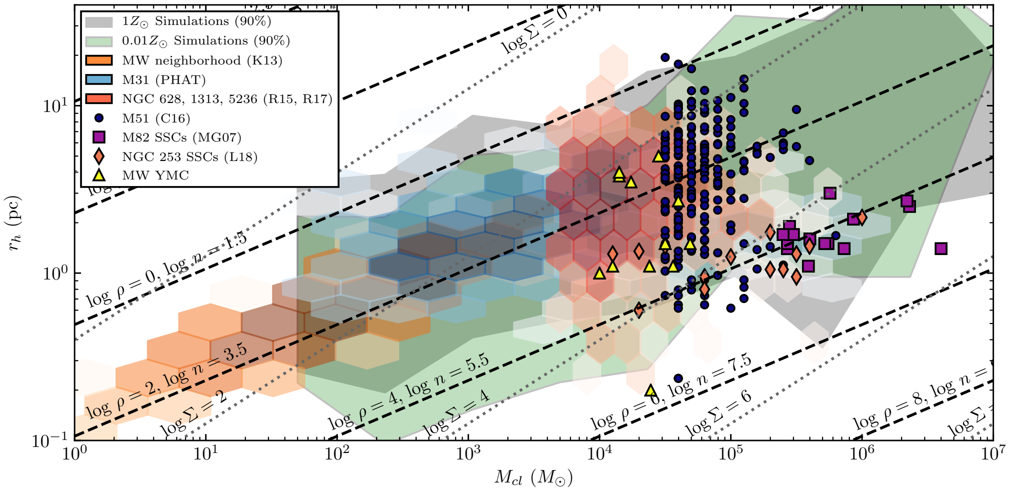

Figure 7.7: Size-mass relation of the star cluster catalogue extracted from the simulation suite, compared with observed catalogues. We plot the mass-binned contours containing 90% of simulated clusters, with $Z_\odot$ runs and $0.01Z_\odot$ runs shown in grey and green respectively. Observational data include nearby (< 2 kpc) clusters in the Milky Way (Kharchenko et al. 2013, K13), Milky Way young massive clusters from the compilation of Krumholz et al. (2018) (MW YMC), and young clusters in NGCs 628, 1313, and 5236 (Ryon et al. 2015, 2017, R15, R17), M31 (Johnson et al. 2012; Fouesneau et al. 2014, PHAT), M82 (McCrady and Graham 2007, MG07), and NGC 254 (Leroy et al. 2018, L18). For reference, we plot lines of constant effective surface density $\Sigma_{eff} = \frac{M_{cl}}{2\pi r_h^2}$ in units of $M_\odot\,\mathrm{pc}^{-2}$, and constant effective 3D density $\rho_{eff} = \frac{3M_{cl}}{8\pi r_h^3}$ in units of $M_\odot\,\mathrm{pc}^{-3}$, and equivalent number density of hydrogen in units of cm^{-3}. This figure is largely reproduced from Krumholz et al. (2018) with permission, code and data courtesy of Mark Krumholz.

Size-mass relation

We measured the clusters' projected half-light radii r_h integrated along the z axis in the simulation coordinates, centred on the point of maximum intensity. The results are summarized in Figure 7.7, where we compare the range of sizes of simulated star clusters with various populations of clusters in the local Universe.

We find that the simulated clusters generally do lie in the space of mass and size of observed young star clusters, with less-massive clusters tending to be smaller and vice versa, but with such a weak dependence that no trend at all would likely be seen in a cluster catalogue spanning < 2 dex in mass. As with real star cluster populations, the most salient feature of the simulated mass-size relation is the considerable *dispersion* at fixed mass. Across the entire simulated catalogue, we find a dispersion in cluster size of 0.48 dex, which remains roughly constant with mass.

We have tried fitting r_h to a general power-law of the form $\propto M_{GMC}^{\alpha_1} \Sigma_{GMC}^{\alpha_2} Z^{\alpha_3} M_{cl}^{\alpha_4}$, and the logarithmic least-squares best fit is well-approximated by

$$r_h = 3\,\mathrm{pc} \left(\frac{M_{GMC}}{10^6\,\mathrm{M}_\odot}\right)^{\frac{1}{5}} \left(\frac{\Sigma_{GMC}}{100\,\mathrm{M}_\odot\,\mathrm{pc}^{-2}}\right)^{-1} \left(\frac{Z}{Z_\odot}\right)^{\frac{1}{10}} \left(\frac{M_{cl}}{10^4\,\mathrm{M}_\odot}\right)^{\frac{1}{3}} \pm 0.37\,\mathrm{dex}, \quad (7.12)$$

where ± 0.37 dex denotes the remaining scatter that is not driven by variations in the quantities considered above, which is well-approximated by a log-normal distribution. Thus, although the intrinsic scatter is considerable, we do find a mass-size relation that is set by the cloud properties. Neglecting the very weak dependencies upon cloud mass and metallicity, the size-mass relation lies along lines of constant 3D stellar density, with the 3D density of clusters set by Σ_{GMC}:

$$\rho_{eff} \equiv \frac{3M_{cl}}{8\pi r_h^3} \approx 44\,\mathrm{M}_\odot\,\mathrm{pc}^{-3} \left(\frac{\Sigma_{GMC}}{100\,\mathrm{M}_\odot\,\mathrm{pc}^{-2}}\right)^3 \pm 1.1\,\mathrm{dex} \quad (7.13)$$

This naturally explains the observed characteristic 3D density of young star clusters in local spiral galaxies (the line $\log \rho = 2$ in Figure 7.7), where most stars form in clouds with $\sim 50 - 100\,\mathrm{M}_\odot\,\mathrm{pc}^{-2}$. It also explains the relative compactness of star clusters formed in starburst galaxies like M82 for their mass (McCrady and Graham, 2007) compared to young clusters in typical spiral galaxies: the central region of M82 has a mean gas surface density of $\sim 500\,\mathrm{M}_\odot\,\mathrm{pc}^{-2}$ (Weiß et al., 2001), ie. ~ 5 times greater than the typical GMC surface density in galaxies where clusters lie along the typical size-mass relation, and hence the typical star cluster density is $5^3 \sim 2$ dex greater.

Note that this relation may hit a wall at extremely high $>> 10^3\,\mathrm{M}_\odot\,\mathrm{pc}^{-2}$ surface density, where we expect that star formation should become highly efficient, and exhaust all gas before the system can contract far beyond that surface density (Grudić et al., 2019).

The roles of different feedback mechanisms

To determine which specific feedback mechanisms are responsible for the setting the various quantities presented in this section, we ran a series of simulations on our

Run	ϵ_{int}	f_{bound}	$M_{cl,max}$ ($M_\odot$)
Standard, $Z_\odot$	4.6%	6.7%	5×10^3
Standard, $0.01Z_\odot$	4.3%	22%	10^4
No winds	4.6%	18%	1.3×10^4
No radiation	10.4%	70.4%	2.7×10^5
No SNe	4.6%	5.3%	6×10^3
No feedback	30% +	90%+	3.2×10^5+

Table 7.1: ϵ_{int}, f_{bound}, and the maximum bound cluster mass in test runs that turn off various subsets of the feedback physics included in the standard suite, run for the fiducial cloud with $M_{GMC} = 4 \times 10^6\,\mathrm{M}_\odot$ and $R_{GMC} = 100\,\mathrm{pc}$. Results of the 'No feedback' model are given with a '+' because this model was only run for half as long as the others, and at this time these quantities were still rising.

fiducial cloud model ($M_{GMC} = 4 \times 10^6\,\mathrm{M}_\odot$, $R_{GMC} = 100\,\mathrm{pc}$, and $Z = Z_\odot$) in which we varied the feedback physics included. Specifically, we tried switching off stellar winds, radiation, supernovae, and all feedback mechanisms in turn. We summarize the results of this experiment in Table 7.1.

Neglecting feedback altogether results in runaway collapse and very high ϵ_{int}, f_{bound}, and star cluster mass. We did not run the no-feedback run past $t_{ff,0}$ due to the computational expense of integrating the extremely dense star clusters that formed, and at this time 30% of the cloud mass had been converted into stars, with no sign of stopping.

Neglecting radiation increased ϵ_{int} from 4.6% to 10.4%, and f_{bound} from 6.7% to 70%. Radiative feedback is therefore apparently crucial in moderating star cluster formation, and also plays the dominant role in setting the cloud-scale SFE, although stellar winds and SNe are still able to moderate star formation somewhat.

The results of the run neglecting SNe are nearly identical to the standard run, so we find that SNe are practically irrelevant to both the cloud-scale SFE and the formation of bound clusters in this region of parameter space. They are unable to moderate star formation on the scale of cluster-forming clumps because the clusters generally form over much shorter timescales than the $\sim 3\,\mathrm{Myr}$ that it takes for the first SNe to go off.

Neglecting stellar winds did not change ϵ_{int} at all. However, the bound fraction and maximum cluster mass of the model with no stellar winds at *solar* metallicity were very close to those of the standard $0.01Z_\odot$ run. We are therefore able to isolate the metallicity dependence of cluster formation efficiency shown in Section 7.2.3

to the effective absence of stellar winds at low metallicity. It is interesting that stellar winds should affect cluster formation so drastically while leaving the cloud-scale SFE untouched. In the dense ($\Sigma_{gas} > 10^3\,\mathrm{M_\odot\,pc^{-2}}$) clumps where individual clusters form, it is expected that both radiative feedback and the momentum-injecting component of stellar wind feedback are inefficient due to their intrinsic scaling with respect to gravity. On the other hand, a hot stellar wind bubble that has not had a chance to vent may behave more in the regime of energy-conserving feedback, which is more efficient than momentum-conserving feedback on small scales: $\epsilon_{int} \propto \Sigma^{\frac{3}{2}} R^{\frac{1}{2}}$, versus being $\propto \Sigma$ for momentum-conserving feedback (Fall et al., 2010).

To summarize, having some type of stellar feedback is crucial for setting both the cloud-scale SFE and the bound fraction of star formation. Radiative feedback is the most important, but stellar winds can be a uniquely efficient feedback mechanism on small scales, potentially affecting the outcome of star cluster formation. A major caveat to this is that observational evidence of stellar winds doing actual work is lacking (Harper-Clark and Murray, 2009; Rosen et al., 2014).

7.3 Statistical Model: Mapping Clouds to Clusters

7.3.1 Translating cloud parameters

Equipped with general results for ϵ_{int}, f_{bound}, and the star cluster size and mass distributions from the previous section, we are nearly ready to construct a statistical model that is able to reproduce our simulation results for any set of GMC parameters. But first, if the model is to be used on observational data, or clouds in a simulated galaxy, we must address some ambiguities in the model inputs: the cloud bulk parameters.

Note that for real clouds, there is some ambiguity about what the proper cloud size R_{GMC}, and more crucially surface density Σ_{GMC} to use is, as real clouds are not uniform spheres. For a general mass distribution $\rho\left(\mathbf{x}\right)$, we will define R_{GMC} as the radius of a sphere of equal moment of inertia:

$$R_{GMC} \equiv \sqrt{\frac{5}{3M_{GMC}} \int \rho\left(x\right) r^2 \,\mathrm{d}^3\mathbf{x}}, \tag{7.14}$$

where r is the distance from the cloud centre of mass. This trivially reduces to our definition for a spherical top-hat distribution.

A common definition of the effective radius used in GMC catalogues is the root mean square of the intensity-weighted second moments of the 2D CO intensity (e.g.

Parameter	Used in	Affects	$Z_\odot$ value	$0.01Z_\odot$ value
Σ_{crit}	Eq. 7.7	SFE	$3200\,\mathrm{M_\odot\,pc^{-2}}$	$3200\,\mathrm{M_\odot\,pc^{-2}}$
ϵ_{int}^{max}	Eq. 7.7	SFE	0.8	0.8
Σ_{bound}	Eq. 7.10	f_{bound}	$410\,\mathrm{M_\odot\,pc^{-2}}$	$330\,\mathrm{M_\odot\,pc^{-2}}$
n	Eq. 7.10	f_{bound}	2	1.4
σ_b	Eq 7.9	f_{bound}	0.6	0.6
α_M	Eq 7.11	Mass function	-1.6	-1.9
k	Eq 7.11	Mass function	0.08	0.12

Table 7.1: Summary of model parameters. None of these are free parameters: the are calibrated to reproduce the star cluster statistics of the simulation results in Section 7.2.3.

Freeman et al., 2017). For a Gaussian cloud model, this definition is a factor of $\sqrt{3}$ less than the definition in Equation 7.14, and is a factor of $\sqrt{\frac{15}{2\pi}}$ less for a uniform sphere model. The two conversion factors are nearly equal – we will adopt the latter.

Another common definition of the effective radius of a cloud is the radius of a circle with area equal to the pixels that the cloud occupies. This is more problematic for us, because it ultimately depends on the specific intensity cut that is used to define the cloud boundary. For this reason, we advise caution if applying this model to data that uses this definition – it is not at all clear that the effective radius provided is actually representative of the mass distribution of the cloud. A decently representative value of Σ_{GMC} is crucial for the model, so modest errors in R_{GMC} will compound into major errors in star cluster properties.

7.3.2 Algorithm

Having resolved the above ambiguity, we are now equipped with the cloud bulk parameters that are the inputs to the model: its mass M_{GMC}, radius R_{GMC}, mean surface density $\Sigma_{GMC} = \frac{M_{GMC}}{\pi R_{GMC}^2}$, and metallicity Z. The mapping from clouds to clusters then proceeds as follows:

1. Compute the metallicity-dependent model parameters provided by the simulations: $\Sigma_{bound}(Z)$, $n(Z)$ (Equation 7.10), $\alpha_M(Z)$, and $k(Z)$ (Equation 7.11). For an arbitrary metallicity, we use a linear interpolant in $\log Z$, using the values provided at $0.01Z_\odot$ and $Z_\odot$ in Table 7.1. For any parameter $p(Z)$:

$$p(Z) = \frac{\log_{10} Z + 2}{2} p(Z_\odot) - \frac{\log_{10} Z}{2} p(0.01Z_\odot) \qquad (7.15)$$

2. Compute the SFE (Equation 7.7) and the total stellar mass formed:

$$M_\star = \epsilon_{int} M_{GMC} \tag{7.16}$$

3. Of this total stellar mass that forms, compute the fraction f_{bound} of this stellar mass in bound clusters with Equations 7.9 and 7.10. The total mass in bound clusters is then:

$$M_{bound} = M_{GMC} \epsilon_{int} f_{bound}. \tag{7.17}$$

   The mass that is not in bound clusters constitutes the unbound association component of the stellar population formed in the cloud.

4. Sample the relative cluster masses M_{cl}/M_{bound} from the cloud-level mass distribution (Equation 7.11), until the sum of the masses exceeds M_{bound}. Reject the final cluster if it commits a lesser mass conservation error than keeping it.

5. Sample the cluster half-mass radii according to the size distribution (Equation 7.12), which depends on the individual cluster masses and the cloud bulk properties.

Finally, using the results of Grudić et al. (2018a), we can also model the specific shapes of the star cluster density profiles. Young star clusters are generally well-fit by the Elson et al. (1987) density profile:

$$\rho(r) = \rho_0 \left(1 + \frac{r^2}{a^2}\right)^{-\frac{\gamma+1}{2}}, \tag{7.18}$$

where a is a scale radius, related to the effective radius by

$$a = \frac{r_h}{\sqrt{2^{\frac{2}{\gamma-2}} - 1}} \tag{7.19}$$

and γ is the power-law slope of the outer surface density profile of the cluster. We found in Grudić et al. (2018a) that γ has a universal distribution in observed and simulation star cluster populations, that is seemingly uncorrelated with any other cluster property, but is apparently set during the star formation process. For our synthetic cluster population, we sample γ randomly using the following fit to the universal CDF on the interval $\gamma \in [2, 10]$:

$$N(<\gamma) = 1.064 \left(\frac{\gamma - 2}{\gamma - 0.8}\right)^{0.54}. \tag{7.20}$$

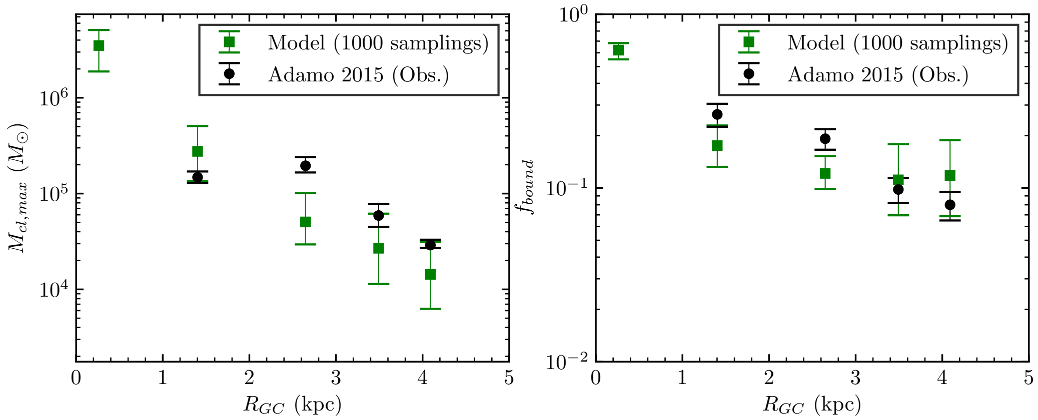

Figure 7.1: Comparison of model predictions in M83 from the Freeman et al. (2017) GMC catalogue with the Adamo et al. (2015) star cluster catalogue. This comparison assumes that the present-day statistics of the GMC population represent those of the population that formed the clusters that are presently observed. Data are binned by galactocentric radius, with bin edges 0, 0.45, 2.3, 3.2, 3.9, 4.5, and 10 kpc. with *Left*: Maximum star cluster mass as a function of galactocentric radius. *Right*: The fraction of star formation in bound clusters f_{bound}, as a function of galactocentric radius. Model predictions are within 1σ of observations in all except the third bin, which hosts the most massive ($2 \times 10^5 M_\odot$) cluster in the catalogue.

7.4 Comparison with Observations

We will now test the model described in the previous section by predicting properties of the star cluster population in M83 from the properties of its GMCs. We use the Freeman et al. (2017) catalogue, taking M_{GMC} to be the mass inferred from the clouds' CO luminosity, and correcting the effective radii by a factor of $\sqrt{\frac{15}{2\pi}}$ to obtain R_{GMC}, as defined in Equation 7.14. We also assume solar abundances for all clouds. To evaluate the confidence intervals of the model predictions, we ran 1000 random realizations of the model on the cloud catalogue, and all confidence intervals shown in this section correspond to the $\pm\sigma$ quantiles over that ensemble. We compare our cluster predictions with data from Adamo et al. (2015). We bin the data by galactocentric radius as in Adamo et al. (2015), with bin edges 0, 0.45, 2.3, 3.2, 3.9, 4.5, and 10 kpc.

First, we predict the maximum cluster mass expected to form in each region of the galaxy, assuming that the currently-observed maximum GMC mass in each region is representative of the typical maximum GMC mass over the past 300 Myr, the age bin of the Adamo et al. (2015) catalogue. We plot these predictions in Figure 7.1, panel 1, and find 1σ agreement with the observed maximum cluster mass in all

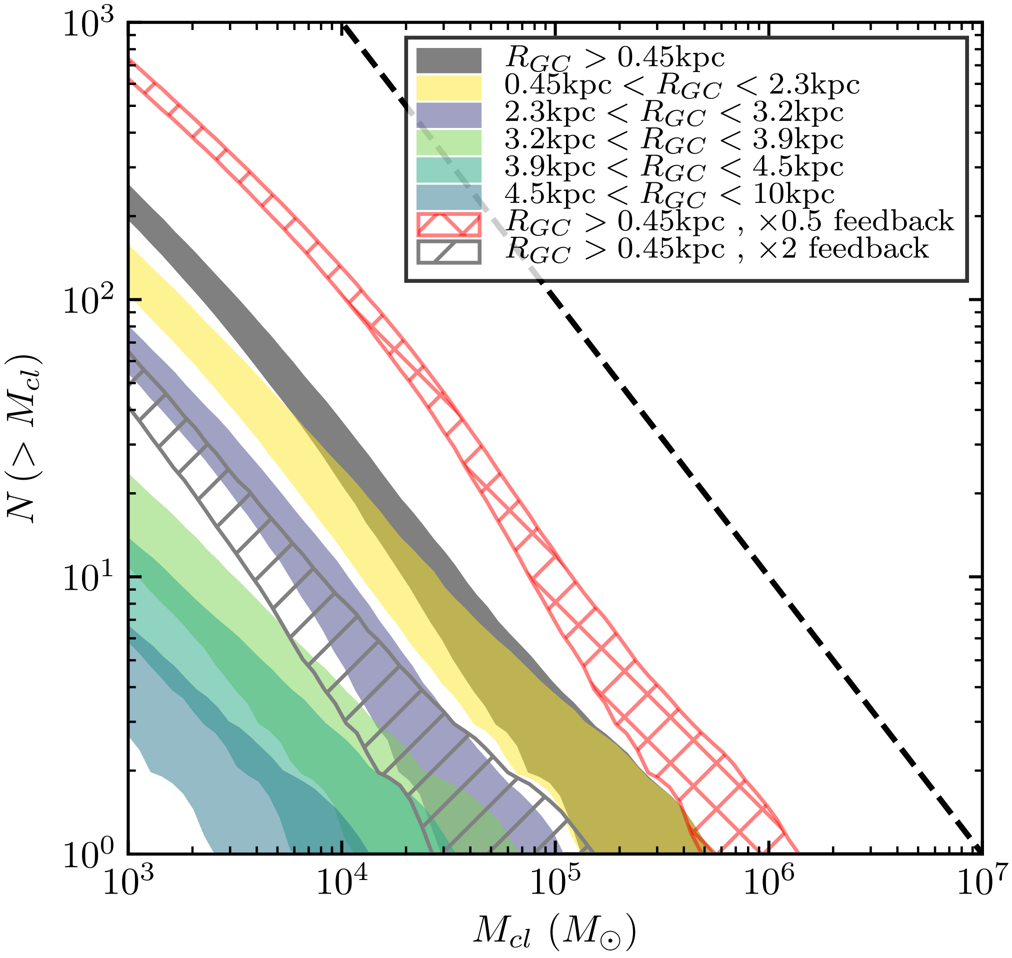

Figure 7.2: Cumulative distribution of cluster masses obtained by mapping a catalogue of GMCs in M83 GMC (Freeman et al., 2017) onto their predicted star clusters, in the different equal-area radial bins defined in Adamo et al. (2015). Coloured contours indicate the 1σ confidence intervals 1000 statistical realizations of the model. Hatched contours indicate model runs in which the strength of feedback was doubled (grey) and halved (red), which causes the distribution to shift down and up respectively. The dashed line plots the CDF of the standard young star cluster mass function, $\frac{\mathrm{d}N}{\mathrm{d}M_{cl}} \propto M^{-2}$. Note that the data presented here is *not* a prediction of the *observed* mass function, which is expected to arise from the integrated formation rates of GMCs over the age bin of the catalogue.

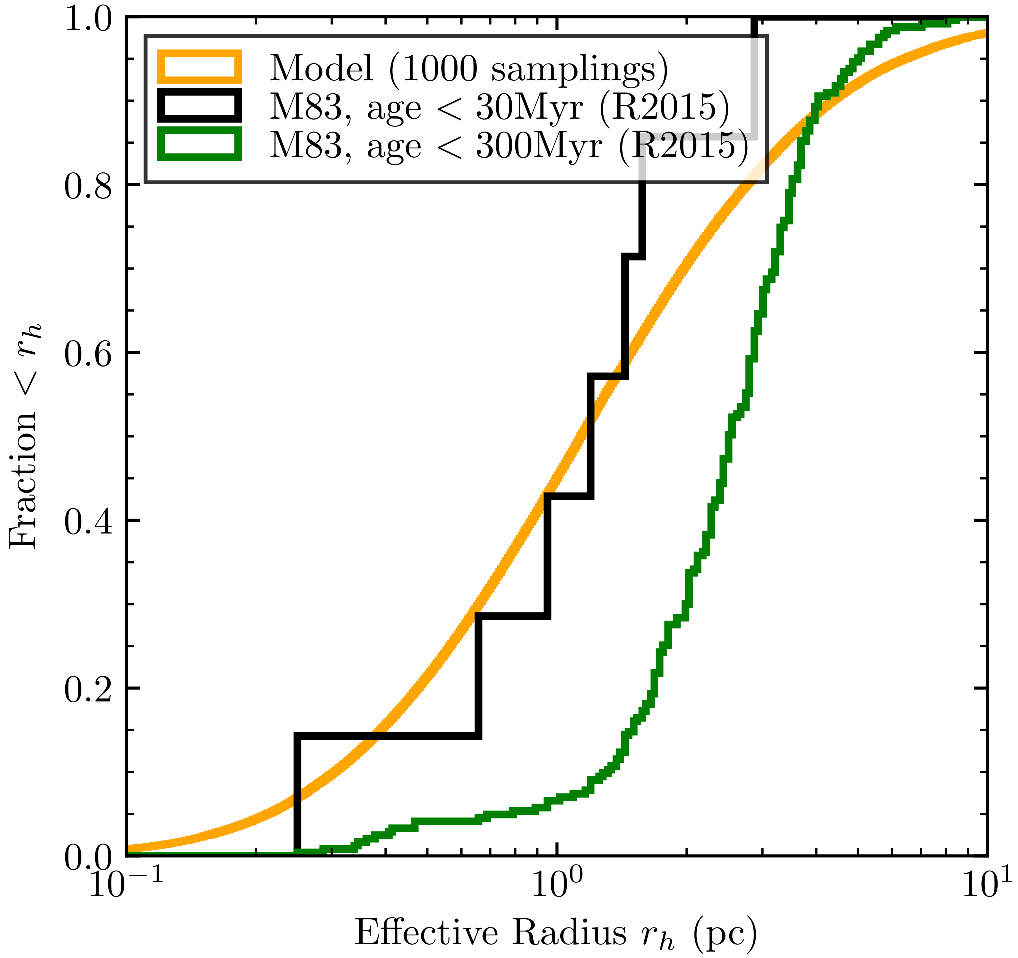

Figure 7.3: Size distribution of clusters more massive than $10^4\,M_\odot$ in M83, comparing model predictions with Ryon et al. (2015) for the entire dataset (age < 300 Myr), and a subset of young (age < 30 Myr) clusters. The model distribution is well-described be a log-normal with dispersion 0.44 dex and median 1 pc. The model predictions and observed distribution for young clusters are statistically indistinguishable. However, this is not so for the entire population, as the observed clusters are systematically larger, and have less size dispersion, possibly indicating evolutionary effects.

cases except for the $2.3 - 3.2$ kpc bin, due to the single most massive cluster in the catalogue, which agrees only within 2σ. We also predict the formation of a cluster of mass $3.5 \pm 1.5 \times 10^6 M_\odot$ from a cloud in the galactic centre, where no cluster data are available. However, we caution that cloud identification is highly uncertain in the galactic centre, and this result is only as reliable as the provided cloud properties.

Next, we predict the fraction of bound star formation by summing the total cluster mass in each bin and dividing it by the total stellar mass formed according to Equation 7.7. This prediction is relatively robust to assumptions about the cloud population, provided that the surface densities of the presently-observed clouds are representative of those that formed over the past 300 Myr. We compare this with the closest possible observational proxy for f_{bound}, the value of Γ measured in Adamo et al. (2015) over an age bin from $10 - 50$ Myr. Again we find 1σ agreement in all cases except for bin 3, which only agrees within 2σ. We predict $f_{bound} \approx 60\%$ in the galactic centre bin, where GMC surface densities are much greater than in the rest of the disk.

We now analyze the mass distributions generated from the model. It is important to note that the presently-observed mass function of GMCs in a galaxy is not expected to map directly onto the observed star cluster population: the star cluster population results from the mapping of the mass-dependent distribution of GMC formation rates $\frac{\mathrm{d}N_{GMC}}{\mathrm{d}t\mathrm{d}M_{GMC}}$, integrated over the age bin of the population, in this case the past 300 Myr. The presently-observed mass function is only proportional to this formation rate distribution under the assumption that the cloud lifetime does not depend on mass. Most evidence seems to point to the lifetimes of less-massive clouds being shorter (Heyer and Dame, 2015), and possibly proportional to the cloud freefall time, $t_{ff} \propto M^{\frac{1}{4}}$ at fixed Σ_{GMC}. Therefore, it is not expected that the direct mapping of the present GMC population should fully resemble the star cluster mass distribution, and we do not attempt to compare them in any rigorous statistical manner.

The cumulative distributions of the model cluster masses are shown in Figure 7.2. We find that the mass functions in the innermost 2 bins, and the galaxy as a whole, are well-described be a power-law of slope -2 over the range $\sim 5000 - 10^6 M_\odot$. At larger radii, the slope is closer to the ~ -1.6, which is likely imprinted by the cloud-level mass distribution in the model (Equation 7.11). There is a radial gradient in the maximum mass, driven mainly by the gradient in the maximum GMC mass, rather than any strong gradient in the typical cloud surface density.

It is also illustrative to re-run the model while varying the parameters. We ran ensembles where we doubled and halved the parameters Σ_{crit} and Σ_{bound}. Because these parameters are determined by the strength of feedback, this is tantamount to varying the strength of feedback in the model by a factor of 2 and 1/2 respectively. The effect of varying the strength of feedback is to shift the mass distribution upward or downward by a factor of $4 - 8$. In other words, the star cluster mass function is highly sensitive to the strength of stellar feedback. This provides a relatively tight constraint on the strength of stellar feedback on cloud scales. According to our model, we can say with reasonable certainty that a young star cluster of mass in excess of $10^6 M_\odot$ would be found in the disk of M83 if feedback were a factor of 2 weaker.

Lastly, we compare the size distribution of simulated star clusters more massive than $> 10^4 M_\odot$ with data from Ryon et al. (2015) in Figure 7.3. The predicted size distribution is well-described by a log-normal distribution with scatter 0.44 dex and median 1 pc. To determine the compatibility of the size distributions with observational data, we ran a 2-sample Anderson-Darling test comparing our model data with both the young (< 30 Myr) cluster population and the full (< 300 Myr) one. We found that the hypothesis that the effective radii of the full population and our model population are drawn from the same underlying distribution can be rejected at $> 3\sigma$ significance, which is unsurprising because we are only modeling the properties of star clusters *at formation*, and neglect their subsequent evolution in the galactic environment. On the other hand, the hypothesis that the *young* population and our model population are sampled from the same distribution can be rejected at only $< 0.3\sigma$ significance, ie. the distributions are statistically indistinguishable.

We therefore find that observations are compatible with a picture where star clusters in M83 form with a typical effective radius of ~ 1 pc, but with significant intrinsic scatter of ~ 0.44 dex *due to the star formation process*. The subsequent evolutionary processes have the effect of increasing the median cluster size, as well as reducing the scatter to the observed 0.25 dex. This is qualitatively in line with theoretical expectations: star clusters that form “too" small will be relatively dense, and experience dynamical relaxation and mass loss on shorter timescales, puffing them up. Star clusters that form “too" large will be much more subject to disruption, and those that survive will be truncated by the galactic tidal field (Krumholz et al., 2018).

7.5 Discussion

7.5.1 The initial mass function of star clusters

Slope

The mass distribution of star clusters is the most fundamental statistic of a star cluster population. It has been measured in various local galaxies, with the typical finding that it is well-fit by a power-law of the form

$$\frac{\mathrm{d}N}{\mathrm{d}M_{cl}} \propto M_{cl}^{\alpha_M}, \tag{7.21}$$

with α_M being typically ~ -2, with some, but relatively little variation when measured across entire galaxies (Chandar et al., 2015, 2017; Krumholz et al., 2018). The simplest explanation for this mass function is that GMCs also have a mass function of this form. Although GMC mass functions are typically measured to be top-heavy (ie. slope shallower than -2), it can be argued that the GMC lifetime is likely mass-dependent ($t_{ff} \propto M^{\frac{1}{4}}$ at fixed Σ_{GMC}), and thus the distribution of *cloud formation rates*, which longer-lived clusters should trace, is steeper (Fall et al., 2010). and hence the cluster mass function is inherited from the GMC mass function, assuming a constant SFE.

Our model would indeed map a $\propto M^{-2}$ GMC population onto a $\propto M^{-2}$ cluster mass function, but the slope of the mass function is actually more robust within our model: in Section 7.4, we map the GMC mass function in M83 onto the star cluster mass function (Figure 7.2), and obtain a $\propto M^{-2}$ mass function in regions where the GMC mass function is not at all well-described by any power-law (see Freeman et al. (2017), Fig. 5). In essence, the mapping from clouds to clusters in our model tends to spread the bound cluster mass evenly over different orders of magnitude in M_{cl}, which gives the observed mass function slope. This robustness may be necessary to explain the relative lack of diversity in young cluster mass functions compared to GMC mass functions.

High-mass cut-off

In certain instances where it has been possible to get good statistics on star clusters within a certain localized region of a galaxy (Adamo et al., 2015; Johnson et al., 2017), some evidence has been found for a "Schechter-like" truncation in the mass function, ie.

$$\frac{\mathrm{d}N}{\mathrm{d}M_{cl}} \propto M^{\alpha_M} \exp\left(\frac{-M_{cl}}{M_\star}\right). \tag{7.22}$$

This is generally believed to reflect some important characteristic physical scale encoded in the structure of the ISM, in star formation physics, or in galactic dynamics. According to our model, a bound fraction of ~ 1 is theoretically possible for any cloud, and so the absolute maximum bound cluster mass that can form is simply

$$M_{cl,max} = \epsilon_{int}\left(\Sigma_{GMC}\right) M_{GMC,max}, \tag{7.23}$$

where $\epsilon_{int}\left(\Sigma_{GMC}\right)$ is given by Equation 7.7. Thus, interpreted in this manner, a truncation in the cluster mass function is the result of a truncation in the GMC mass function. It has been proposed that this truncation is set by the Toomre mass, the maximum mass that can collapse against galactic shear (e.g. Hopkins, 2012; Reina-Campos and Kruijssen, 2017), and this picture agrees well with observations in M83 (Freeman et al., 2017).

Low-mass cut-off

There is no evidence of a lower cut-off in the star cluster mass function in any of our models that is not simply consistent with simulation resolution – the mass function exhibits power-law behaviour as far down as can be resolved (Figures 7.5, 7.6). We therefore rule out a lower cutoff in the cluster mass function that arises solely from star formation and feedback physics as we have simulated them. On the other hand, sufficiently low-mass clusters have relaxation times that are comparable to their crossing times, and their energetics tend to be dominated by a small number of binaries rather than virial motion. In this regime, our approximation of collisionless star particles in inapplicable. It is reasonable to assume that if there is a lower truncation in the initial cluster mass function, collisional N-body dynamics will have an important role to play in it.

7.5.2 Comparison with Kruijssen 2012

Our model is not the first to succeed in reproducing the star cluster population statistics plotted in Figure 7.1[6] – in Adamo et al. (2015), it was found that the Kruijssen et al. (2012b) model was able to predict f_{bound} equally well. It was then combined with the Kruijssen (2014) to predict the maximum star cluster mass (here using our notation):

$$M_{cl,max} = \epsilon_{int} f_{bound} M_{Toomre}, \tag{7.24}$$

where M_{Toomre} is the maximum gas mass that can collapse according to the Toomre instability, and ϵ_{int} was given an assumed fiducial value of 10%. Again, $M_{cl,max}$ was

---

[6] Although it is the first to do so in terms of explicit GMC properties.

predicted equally well. It is illustrative to compare and contrast this framework with the one in the present work. Kruijssen (2012) and this work present the same overall physical picture: hierarchical star formation produces stars over a wide range of densities, and in denser conditions feedback is less able to moderate star formation, leading to bound star cluster formation. However, the models do have important conceptual differences regarding the specific manner in which feedback moderates star formation.

To summarize, Kruijssen (2012) modeled the galactic ISM using the density statistics of isothermal, supersonic turbulence (Krumholz and McKee, 2005), which are fixed by three galactic bulk parameters: the Toomre stability parameter Q, the mean disk gas surface density Σ_{gas}, and the orbital frequency Ω. These determine a log-normal gas density PDF which, according to the hierarchical star formation paradigm, maps onto the distribution of densities ρ at which stars form. A feedback timescale t_{fb} is introduced, identified with the time required for feedback to disrupt a molecular cloud and halt star formation, on the order of several Myr, with only weak residual dependence on the three parameters. Locally-high ϵ_{int} occurs in the upper tail of the initial stellar density distribution where $t_{ff} << t_{fb}$, as star formation can proceed with a per-freefall efficiency of $\sim 1\%$ for many freefall times until $\epsilon_{int} \sim 1$ locally, and the bound fraction can be correspondingly high.

This picture conflicts with the findings of the present work, and other recent, similar numerical works (Geen et al., 2017; Kim et al., 2018a; Li et al., 2019), on multiple counts. We do not find a universal per-freefall SFE $\epsilon_{ff} \sim 1\%$, nor any scaling that agrees with any turbulence-regulated star formation theory along the lines of Krumholz and McKee (2005). Simulations of feedback-moderated star formation on GMC scales invariably find that ϵ_{ff} and ϵ_{int} are intimately linked to one another, and scale with cloud parameters in a manner similar to Equation 7.7. The dimensional scalings of Kruijssen et al. (2012b) and the present work are also quite different. t_{fb} imposes a characteristic *timescale* that determines SFE and f_{bound}, while our Σ_{crit} and Σ_{bound} predict scalings with gas surface density. In the full parameter space of galactic conditions, these theories must therefore inevitably diverge in their predictions. Why, then, do they agree so well in M83?

The answer actually lies in Kruijssen (2012), who fits an empirical relation between orbital frequency and gas surface density in galaxies:

$$\frac{\Omega}{\mathrm{Myr}^{-1}} = 0.058 \left(\frac{\Sigma_{gas}}{100\,\mathrm{M}_{\odot}\,\mathrm{pc}^{-2}}\right)^{0.49}. \tag{7.25}$$

Converting $t_{fb} \sim 3\,\mathrm{Myr}$ to a surface density scale using this relation yields $\Sigma \sim \left(\frac{1}{3\,\mathrm{Myr}\times 0.058\mathrm{Myr}^{-1}}\right)^2 100\,\mathrm{M}_{\odot}\,\mathrm{pc}^{-2} = 3300\,\mathrm{M}_{\odot}\,\mathrm{pc}^{-2}$, ie. Σ_{crit}! This essentially means that the predictions of the two models will be in reasonable agreement in any galaxy that lies along Equation 7.25 (which M83 does).

This is not to say that the success enjoyed by the Kruijssen (2012) model so far is merely the consequence of some coincidental empirical relation. There may in fact be some deep connection between t_{fb} and Σ_{crit} that ultimately *sets* the $\Sigma_{gas} - \Omega$ relation. t_{fb} is clearly relevant to the moderation of star formation on galactic scales via supernova explosions, and can potentially explain variations in kpc-scale galactic ISM conditions (Orr et al., 2018c). Meanwhile, Σ_{crit} determines the efficiency of star formation on GMC scales, where early feedback dominates. But these scales are not actually decoupled and independent, and must achieve some level of agreement in a star-forming disk in statistical equilibrium. We conjecture that the combined physics of stellar feedback acting on both GMC and galactic scales could cause a galactic gas disk to approach equilibrium via either gas exhaustion or wind launching until Equation 7.25 is roughly achieved. This possible connection between the characteristic scales in different feedback physics warrants further theoretical consideration.

7.5.3 On “boost factors" for stellar feedback

Some cosmological zoom-in simulations have invoked a “boost factor" f_{boost} in the energy or momentum flux due to stellar feedback from a stellar population (Li et al., 2018). In those works a boost factor on the order of 10 was necessary for cosmological zoom-in simulations to obtain galactic stellar masses in agreement with observations. More recently, a suite of GMC-scale simulations similar to ours was run with a simplified, locally-coupled momentum-based feedback model (Li et al., 2019), and it was found in that case that $f_{boost} \sim 10$ was necessary for GMCs of surface density comparable to those in local galaxies ($\Sigma_{GMC} \sim 100\,\mathrm{M}_{\odot}\,\mathrm{pc}^{-2}$) to achieve realistic SFE (ie. a few per cent).

We caution that these results should not be interpreted as justification for a *physical* interpretation of f_{boost}, or an interpretation that the feedback presently accounted for is insufficient to moderate star formation to observed levels. In this work our simulations, which include all feedback mechanisms from main sequence stars, with both local and nonlocal coupling, achieve correct star formation efficiencies, cluster formation efficiencies, and star cluster masses, without any boost factor. As such, in analogy to the results of the FIRE simulations on galactic scales (Hopkins et al., 2018a), we conclude that the main-sequence stellar feedback expected from a stellar population is sufficient to moderate star formation on GMC scales to observed levels.

The discrepancy in the GMC-scale SFE between this work and Li et al. (2019) is very likely explained by the difference in the feedback implementations used, and we expect that a more comprehensive treatment of feedback would lead to lower SFE, similarly to what was found between Raskutti et al. (2016) and Kim et al. (2017a). On the other hand, the source of the discrepancy between Li et al. (2018) and Hopkins et al. (2018a) on galaxy scales remains less clear.

7.6 Summary and future work

In this work we have used numerical simulations of star-forming GMCs to explore the mapping between GMCs and the star clusters that they form. We have found that mapping is complex, and not one-to-one, due to of the variety of outcomes made possible by stochastic variations in the internal turbulent flows of the clouds. In essence, the overall SFE of GMCs is reasonably predictable because the efficiency of feedback depends upon the *macrostate* of the cloud, whereas cluster formation occurs on much smaller scales within the cloud, and is thus determined by the specific *microstate* of turbulence.

Despite this complexity, we have been able to explore the range of variations from one microstate to another and have found that the mapping from clouds to clusters does admit a statistical model (Section 7.3) that encodes fairly simple scalings in cluster formation efficiency, star cluster sizes, and star cluster masses. When we apply this model to a real population of GMCs, we successfully predict the fraction of star formation in bound clusters, the maximum cluster mass, and the size distribution of massive clusters. This marks the first conclusive success of numerical simulations at reproducing the properties of star clusters in detail, using the observed GMC properties as initial conditions. Our key findings are as follows:

- All GMCs will form some fraction of their stars in bound clusters – the formation of bound clusters and unbound associations are part of the same continuum, and not distinct processes. The star formation efficiency ϵ_{int} and the bound fraction of star formation f_{bound} are correlated, but distinct quantities (Figure 7.3). Both scale as an increasing function of the cloud surface density Σ_{GMC}, eventually saturating to an order-unity value (eg. Fall et al., 2010; Murray et al., 2010; Grudić et al., 2018b). However, f_{bound} scales more steeply, from a typical value of a few per cent in GMCs with surface density $\sim 50\,\mathrm{M}_\odot\,\mathrm{pc}^{-2}$ in our galaxy (Goddard et al., 2010), to $10-30\%$ in nearby spiral galaxies in which GMC surface densities are systematically a factor of ~ 2 higher (Faesi et al., 2018). The cloud-scale f_{bound} saturates to ~ 1 when the cloud scale SFE is $10-20\%$, in good agreement with Li et al. (2019).

- For a given set of cloud parameters, f_{bound} exhibits large variations, especially at low Σ_{GMC}. We construct a model that reproduces the scatter shown in Figure 7.4 (Equations 7.9 and 7.10).
- GMCs generally form multiple bound clusters, with masses distributed according to a cloud-scale mass distribution (Equation 7.11). The primary cluster tends to dominate the total bound mass.
- Stellar feedback is crucial in setting star cluster properties. Radiation is the most important, stellar winds are somewhat important, and SNe are essentially irrelevant because they come too late (see Table 7.1). Because cluster masses are so sensitive to the strength of feedback (Figure 7.2), they provide a tight observational constraint on it.
- The formation of bound clusters from 1% solar metallicity gas is more efficient than at solar metallicity (Figure 7.4). We have isolated this effect to the weaker stellar wind feedback expected from low-metallicity OB stars (Section 7.2.3), whose winds are effectively irrelevant compared to other feedback mechanisms.
- The weak size-mass relation of star clusters is set during the star formation process, which produces large intrinsic scatter in cluster radii. There is a relation, however: star clusters from a given cloud form with a 3D density that scales cubically with the surface density of the parent cloud (Equation 7.13), explaining the difference in density between Milky Way clusters and super star clusters in starburst galaxies (Section 7.2.3).

We will expand and apply the model in this work in the two subsequent papers in this series. In Paper II, we will describe an end-to-end model of galactic cluster formation that couples the model in this work to a model for the statistics of GMCs, with only the galactic bulk properties as inputs, similar to Kruijssen (2012). This model can be used as a sub-grid prescription for star cluster formation in cosmological simulations that do not resolve the bulk properties of GMCs self-consistently. In Paper III, we will use this model to post-process the FIRE cosmological zoom-in simulations, which *do* resolve GMC bulk properties, and apply the model to the problem of cosmological globular cluster formation.

Though our success in predicting cluster bulk properties is encouraging, the problem of star cluster formation is hardly solved. Because our method of simulating star formation is approximate, we anticipate that comparisons with observed cluster properties that go beyond simple bulk properties will reveal interesting discrepancies. The extragalactic observations that we have compared with are likely the *easiest* constraints to satisfy. Meanwhile, the detailed cluster kinematics, and temporal and spatial age distributions that can be observed in the Milky Way and its satellites may well provide more powerful constraints on the star formation process.

At this point, we strongly suspect that the most worthwhile gains in simulation realism can only be made by attacking the harder version of the problem: resolving the formation and motion of individual stars self-consistently, rather than assuming the IMF and using a simple stellar population formalism. Simulations are reaching the scales where the granularity of stars can easily become important, and the details of how and when individual stars form can have major implications for stellar feedback, and hence the subsequent cloud evolution (Grudić and Hopkins, 2018). Due to computational cost, this has never been done on the scale of massive GMCs that can actually sample the IMF, and hence the effects of feedback from massive stars have yet to be demonstrated in a fully self-consistent calculation that *predicts* massive star formation. However, the advent of massively-scalable, Lagrangian hydro codes with fast, accurate radiation MHD methods and well-developed feedback coupling techniques (ie. AREPO and GIZMO) should make this possible in the coming years.

Questions of particular importance for future simulations are the behaviour of protostellar and main-sequence feedback acting in concert (ie. does regulating star formation on small scales ultimately affect cloud-scale behaviour?), what are the necessary and sufficient physics to satisfy constraints on the IMF turnover mass (e.g. Bate, 2009; Krumholz, 2011; Federrath et al., 2017; Guszejnov et al., 2016, 2019), and what deviations from universality might be expected in different environments. These questions can only be addressed properly with a full accounting of stellar feedback.

Acknowledgements

We thank Erik Rosolowsky and Mark Krumholz for useful discussions and for providing data and analysis code from Freeman et al. (2017) and Krumholz et al. (2018) respectively. We thank Charles Lada, Anna Rosen, Hui Li, Mark Vogelsberger, Bruce Elmegreen, Angela Adamo, Eve Ostriker, Jeong-Gyu Kim, Marta Reina-Campos, and Sebastian Trujillo-Gomez for enlightening discussions that informed and motivated this work. Support for MYG and PFH was provided by an Alfred P. Sloan Research Fellowship, NSF Collaborative Research Grant #1715847 and CAREER grant #1455342, and NASA grants NNX15AT06G, JPL 1589742, 17-ATP17-0214. CAFG was supported by NSF through grants AST-1412836, AST-1517491, AST-1715216, and CAREER award AST-1652522, by NASA through grant NNX15AB22G, and by a Cottrell Scholar Award from the Research Corporation for Science Advancement. NM acknowledges the support of the Natural Sciences and Engineering Research Council of Canada (NSERC). This research was undertaken, in part, thanks to funding from the Canada Research Chairs program. Numerical calculations were run on the Caltech compute cluster "Wheeler," allocations from XSEDE TG-AST130039 and PRAC NSF.1713353 (awards OCI-0725070 and ACI-1238993) supported by the NSF, and NASA HEC SMD-16-7592.

This research has made use of use of NASA's Astrophysics Data System, `ipython` (Pérez and Granger, 2007), `numpy`, `scipy` (Jones et al., 2001), and `matplotlib` (Hunter, 2007).

BIBLIOGRAPHY

B. P. Abbott, R. Abbott, T. D. Abbott, M. R. Abernathy, F. Acernese, K. Ackley, C. Adams, T. Adams, P. Addesso, R. X. Adhikari, and et al. Observation of Gravitational Waves from a Binary Black Hole Merger. *Physical Review Letters*, 116(6):061102, February 2016. doi: 10.1103/PhysRevLett.116.061102. 2.5.4, 3.5.3

M. Abramowitz and I. A. Stegun. *Handbook of mathematical functions with formulas, graphs, and mathematical tables*. 1965. 3.B.1

A. Adamo, J. M. D. Kruijssen, N. Bastian, E. Silva-Villa, and J. Ryon. Probing the role of the galactic environment in the formation of stellar clusters, using M83 as a test bench. MNRAS, 452:246–260, September 2015. doi: 10.1093/mnras/stv1203. 2.5.4, 7.1, 7.1, 7.4, 7.2, 7.5.1, 7.5.2

A. Adamo, J. E. Ryon, M. Messa, H. Kim, K. Grasha, D. O. Cook, D. Calzetti, J. C. Lee, B. C. Whitmore, B. G. Elmegreen, L. Ubeda, L. J. Smith, S. N. Bright, A. Runnholm, J. E. Andrews, M. Fumagalli, D. A. Gouliermis, L. Kahre, P. Nair, D. Thilker, R. Walterbos, A. Wofford, A. Aloisi, G. Ashworth, T. M. Brown, R. Chandar, C. Christian, M. Cignoni, G. C. Clayton, D. A. Dale, S. E. de Mink, C. Dobbs, D. M. Elmegreen, A. S. Evans, J. S. Gallagher, III, E. K. Grebel, A. Herrero, D. A. Hunter, K. E. Johnson, R. C. Kennicutt, M. R. Krumholz, D. Lennon, K. Levay, C. Martin, A. Nota, G. Östlin, A. Pellerin, J. Prieto, M. W. Regan, E. Sabbi, E. Sacchi, D. Schaerer, D. Schiminovich, F. Shabani, M. Tosi, S. D. Van Dyk, and E. Zackrisson. Legacy ExtraGalactic UV Survey with The Hubble Space Telescope: Stellar Cluster Catalogs and First Insights Into Cluster Formation and Evolution in NGC 628. ApJ, 841:131, June 2017. doi: 10.3847/1538-4357/aa7132. 2.5.4

O. Agertz and A. V. Kravtsov. On the Interplay between Star Formation and Feedback in Galaxy Formation Simulations. ApJ, 804:18, May 2015. doi: 10.1088/0004-637X/804/1/18. 6.4

O. Agertz, A. V. Kravtsov, S. N. Leitner, and N. Y. Gnedin. Toward a Complete Accounting of Energy and Momentum from Stellar Feedback in Galaxy Formation Simulations. ApJ, 770:25, June 2013. doi: 10.1088/0004-637X/770/1/25. 1.2, 2.3.1, 6.2.3

L. A. Aguilar and S. D. M. White. The density profiles of tidally stripped galaxies. ApJ, 307:97–109, August 1986. doi: 10.1086/164396. 3.2

K. R. Anantharamaiah, F. Viallefond, N. R. Mohan, W. M. Goss, and J. H. Zhao. Starburst in the Ultraluminous Galaxy Arp 220: Constraints from Observations of Radio Recombination Lines and Continuum. ApJ, 537:613–630, July 2000. doi: 10.1086/309063. 2.5.2

I. Arad, A. Dekel, and A. Klypin. Phase-space structure of dark matter haloes: scale-invariant probability density function driven by substructure. MNRAS, 353:15–29, September 2004. doi: 10.1111/j.1365-2966.2004.08045.x. 6

Y. Ascasibar and J. Binney. Numerical estimation of densities. MNRAS, 356: 872–882, January 2005. doi: 10.1111/j.1365-2966.2004.08480.x. 6

J. Ballesteros-Paredes, L. W. Hartmann, E. Vázquez-Semadeni, F. Heitsch, and M. A. Zamora-Avilés. Gravity or turbulence? Velocity dispersion-size relation. MNRAS, 411:65–70, February 2011. doi: 10.1111/j.1365-2966.2010.17657.x. 5.4.2

J. Bally. Protostellar Outflows. ARA&A, 54:491–528, September 2016. doi: 10.1146/annurev-astro-081915-023341. 1.2

J. Barnes and P. Hut. A hierarchical O(N log N) force-calculation algorithm. Nature, 324:446–449, December 1986. doi: 10.1038/324446a0. 7.2.1

J. E. Barnes. Gravitational softening as a smoothing operation. MNRAS, 425: 1104–1120, September 2012. doi: 10.1111/j.1365-2966.2012.21462.x. 3.4.2

H. Bartko et al. An Extremely Top-Heavy Initial Mass Function in the Galactic Center Stellar Disks. ApJ, 708:834–840, January 2010. doi: 10.1088/0004-637X/708/1/834. 2.5.7

N. Bastian. On the star formation rate – brightest cluster relation: estimating the peak star formation rate in post-merger galaxies. *Monthly Notices of the Royal Astronomical Society*, 390(2):759–768, 10 2008. ISSN 0035-8711. doi: 10.1111/j.1365-2966.2008.13775.x. URL `https://doi.org/10.1111/j.1365-2966.2008.13775.x`. 7.1

N. Bastian, R. P. Saglia, P. Goudfrooij, M. Kissler-Patig, C. Maraston, F. Schweizer, and M. Zoccali. Dynamical mass estimates for two luminous star clusters in galactic merger remnants. A&A, 448:881–891, March 2006. doi: 10.1051/0004-6361:20054177. 4.1

N. Bastian, K. R. Covey, and M. R. Meyer. A Universal Stellar Initial Mass Function? A Critical Look at Variations. ARA&A, 48:339–389, September 2010a. doi: 10.1146/annurev-astro-082708-101642. 1.2, 6.2.3

N. Bastian, K. R. Covey, and M. R. Meyer. A Universal Stellar Initial Mass Function? A Critical Look at Variations. ARA&A, 48:339–389, September 2010b. doi: 10.1146/annurev-astro-082708-101642. 2.5.7

N. Bastian, A. Adamo, M. Gieles, E. Silva-Villa, H. J. G. L. M. Lamers, S. S. Larsen, L. J. Smith, I. S. Konstantopoulos, and E. Zackrisson. Stellar clusters in M83: formation, evolution, disruption and the influence of the environment. MNRAS, 419:2606–2622, January 2012. doi: 10.1111/j.1365-2966.2011.19909.x. 2.5.4

N. Bastian, F. Schweizer, P. Goudfrooij, S. S. Larsen, and M. Kissler-Patig. Luminosity profiles and sizes of massive star clusters in NGC 7252. MNRAS, 431: 1252–1263, May 2013. doi: 10.1093/mnras/stt253. 3.1, 4.1

M. R. Bate. The importance of radiative feedback for the stellar initial mass function. MNRAS, 392:1363–1380, February 2009. doi: 10.1111/j.1365-2966.2008.14165.x. 1.4, 5.5.3, 6.2.3, 7.6

A. Bauer and V. Springel. Subsonic turbulence in smoothed particle hydrodynamics and moving-mesh simulations. MNRAS, 423:2558–2578, July 2012. doi: 10.1111/j.1365-2966.2012.21058.x. 5.3.1

H. Baumgardt and P. Kroupa. A comprehensive set of simulations studying the influence of gas expulsion on star cluster evolution. MNRAS, 380:1589–1598, October 2007. doi: 10.1111/j.1365-2966.2007.12209.x. 3.1, 5.2, 6.1, 7.1, 7.2.3

P. S. Behroozi, R. H. Wechsler, and C. Conroy. The Average Star Formation Histories of Galaxies in Dark Matter Halos from z = 0-8. ApJ, 770:57, June 2013. doi: 10.1088/0004-637X/770/1/57. 1.2

F. Bertoldi and C. F. McKee. Pressure-confined clumps in magnetized molecular clouds. ApJ, 395:140–157, August 1992. doi: 10.1086/171638. 1.1, 5.4.3

F. Bigiel, A. K. Leroy, M. J. Jiménez-Donaire, J. Pety, A. Usero, D. Cormier, A. Bolatto, S. Garcia-Burillo, D. Colombo, M. González-García, A. Hughes, A. A. Kepley, C. Kramer, K. Sandstrom, E. Schinnerer, A. Schruba, K. Schuster, N. Tomicic, and L. Zschaechner. The EMPIRE Survey: Systematic Variations in the Dense Gas Fraction and Star Formation Efficiency from Full-disk Mapping of M51. ApJ, 822:L26, May 2016. doi: 10.3847/2041-8205/822/2/L26. 5.5.1

J. Binney and S. Tremaine. *Galactic dynamics*. Princeton, NJ, Princeton University Press, 1987, 1987. 3.B.5

T. Böker, M. Sarzi, D. E. McLaughlin, R. P. van der Marel, H.-W. Rix, L. C. Ho, and J. C. Shields. A Hubble Space Telescope Census of Nuclear Star Clusters in Late-Type Spiral Galaxies. II. Cluster Sizes and Structural Parameter Correlations. AJ, 127:105–118, January 2004. doi: 10.1086/380231. 4.2

A. D. Bolatto, A. K. Leroy, E. Rosolowsky, F. Walter, and L. Blitz. The Resolved Properties of Extragalactic Giant Molecular Clouds. ApJ, 686:948–965, October 2008. doi: 10.1086/591513. 2.2.2, 2.5.1, 3.4.2, 3.2, 4.2.3, 5.1, 5.2, 6.1, 7.1

A. D. Bolatto, M. Wolfire, and A. K. Leroy. The CO-to-H_2 Conversion Factor. ARA&A, 51:207–268, August 2013. doi: 10.1146/annurev-astro-082812-140944. 5.2.2

I. A. Bonnell, M. R. Bate, C. J. Clarke, and J. E. Pringle. Competitive accretion in embedded stellar clusters. MNRAS, 323:785–794, May 2001. doi: 10.1046/j.1365-8711.2001.04270.x. 5.5.3

I. A. Bonnell, M. R. Bate, and S. G. Vine. The hierarchical formation of a stellar cluster. MNRAS, 343:413–418, August 2003. doi: 10.1046/j.1365-8711.2003.06687.x. 3.2.1, 3.3, 3.5.2, 4.2.3

I. A. Bonnell, R. J. Smith, P. C. Clark, and M. R. Bate. The efficiency of star formation in clustered and distributed regions. MNRAS, 410:2339–2346, February 2011. doi: 10.1111/j.1365-2966.2010.17603.x. 7.1

M. Boylan-Kolchin, C.-P. Ma, and E. Quataert. Dissipationless mergers of elliptical galaxies and the evolution of the fundamental plane. MNRAS, 362:184–196, September 2005. doi: 10.1111/j.1365-2966.2005.09278.x. 3.3, 3.3.2

J. Braine, E. Rosolowsky, P. Gratier, E. Corbelli, and K. Schuster. Properties and rotation of molecular clouds in M 33. *ArXiv e-prints*, January 2018. 5.3.1, 7.2.2

E. Bressert, N. Bastian, R. Gutermuth, S. T. Megeath, L. Allen, N. J. Evans, II, L. M. Rebull, J. Hatchell, D. Johnstone, T. L. Bourke, L. A. Cieza, P. M. Harvey, B. Merin, T. P. Ray, and N. F. H. Tothill. The spatial distribution of star formation in the solar neighbourhood: do all stars form in dense clusters? MNRAS, 409: L54–L58, November 2010. doi: 10.1111/j.1745-3933.2010.00946.x. 3.1, 7.1

P. M. Bryant and N. Z. Scoville. High-Resolution CO Observations of Luminous Infrared Galaxies. AJ, 117:2632–2655, June 1999. doi: 10.1086/300879. 2.1

B. Burkhart. The Star Formation Rate in the Gravoturbulent Interstellar Medium. *ArXiv e-prints*, January 2018. 5.2

J. I. Castor, D. C. Abbott, and R. I. Klein. Radiation-driven winds in Of stars. ApJ, 195:157–174, Jan 1975. doi: 10.1086/153315. 1.2

R. Chandar, S. M. Fall, and B. C. Whitmore. The Link between the Formation Rates of Clusters and Stars in Galaxies. ApJ, 810:1, September 2015. doi: 10.1088/0004-637X/810/1/1. 2.5.4, 7.5.1

R. Chandar, S. M. Fall, B. C. Whitmore, and A. J. Mulia. The fraction of stars that form in clusters in different galaxies. *The Astrophysical Journal*, 849(2):128, nov 2017. 7.2.3, 7.5.1

P. C. Clark and S. C. O. Glover. On column density thresholds and the star formation rate. MNRAS, 444:2396–2414, November 2014. doi: 10.1093/mnras/stu1589. 5.2.2, 5.5.1, 5.7

H. Cohn. Late core collapse in star clusters and the gravothermal instability. ApJ, 242:765–771, December 1980. doi: 10.1086/158511. 3.2

S. Cole, C. G. Lacey, C. M. Baugh, and C. S. Frenk. Hierarchical galaxy formation. MNRAS, 319:168–204, November 2000. doi: 10.1046/j.1365-8711.2000.03879.x. 3.3.2

P. Colin, E. Vázquez-Semadeni, and G. C. Gómez. Molecular cloud evolution - V. Cloud destruction by stellar feedback. MNRAS, 435:1701–1714, October 2013. doi: 10.1093/mnras/stt1409. 1.2, 5.1, 6.1

D. C. Collins, A. G. Kritsuk, P. Padoan, H. Li, H. Xu, S. D. Ustyugov, and M. L. Norman. The Two States of Star-forming Clouds. ApJ, 750:13, May 2012. doi: 10.1088/0004-637X/750/1/13. 2.4.1, 2.5.3

Dario Colombo, Annie Hughes, Eva Schinnerer, Sharon E. Meidt, Adam K. Leroy, Jérôme Pety, Clare L. Dobbs, Santiago García-Burillo, Gaëlle Dumas, Todd A. Thompson, Karl F. Schuster, and Carsten Kramer. The PdBI Arcsecond Whirlpool Survey (PAWS): Environmental Dependence of Giant Molecular Cloud Properties in M51. ApJ, 784(1):3, Mar 2014. doi: 10.1088/0004-637X/784/1/3. 7.1, 7.2.2

A. J. Cunningham, M. R. Krumholz, C. F. McKee, and R. I. Klein. The effects of magnetic fields and protostellar feedback on low-mass cluster formation. MNRAS, 476:771–792, May 2018. doi: 10.1093/mnras/sty154. 1.2, 5.5.3

Robert L. da Silva, Michele Fumagalli, and Mark Krumholz. SLUG—Stochastically Lighting Up Galaxies. I. Methods and Validating Tests. ApJ, 745:145, February 2012. doi: 10.1088/0004-637X/745/2/145. 6.2.3

J. E. Dale. The modelling of feedback in star formation simulations. New A Rev., 68:1–33, October 2015. doi: 10.1016/j.newar.2015.06.001. 5.1, 6.1

J. E. Dale. The effect of the virial state of molecular clouds on the influence of feedback from massive stars. MNRAS, 467:1067–1082, May 2017. doi: 10.1093/mnras/stx028. 5.1, 6.1, 6.2.3

J. E. Dale, I. A. Bonnell, C. J. Clarke, and M. R. Bate. Photoionizing feedback in star cluster formation. MNRAS, 358:291–304, March 2005. doi: 10.1111/j.1365-2966.2005.08806.x. 1.2

J. E. Dale, B. Ercolano, and I. A. Bonnell. Ionizing feedback from massive stars in massive clusters - II. Disruption of bound clusters by photoionization. MNRAS, 424:377–392, July 2012. doi: 10.1111/j.1365-2966.2012.21205.x. 1.2, 2.4.1, 2.5.3, 5.1, 6.1

J. E. Dale, J. Ngoumou, B. Ercolano, and I. A. Bonnell. Massive stars in massive clusters - IV. Disruption of clouds by momentum-driven winds. MNRAS, 436: 3430–3445, December 2013. doi: 10.1093/mnras/stt1822. 1.2, 5.1, 6.1

J. E. Dale, J. Ngoumou, B. Ercolano, and I. A. Bonnell. Before the first supernova: combined effects of H II regions and winds on molecular clouds. MNRAS, 442: 694–712, July 2014. doi: 10.1093/mnras/stu816. 1.2, 5.1, 6.1

S. W. Davis, Y.-F. Jiang, J. M. Stone, and N. Murray. Radiation Feedback in ULIRGS: Are Photons Movers and Shakers? ApJ*, in press, arXiv:1403.1874*, March 2014a. 1, 5.5.3

S. W. Davis, Y.-F. Jiang, J. M. Stone, and N. Murray. Radiation Feedback in ULIRGs: Are Photons Movers and Shakers? ApJ, 796:107, December 2014b. doi: 10.1088/0004-637X/796/2/107. 2.5.7

W. Dehnen. Phase-space mixing and the merging of cusps. MNRAS, 360:892–900, July 2005. doi: 10.1111/j.1365-2966.2005.09099.x. 3.3, 3.3, 3.5.4

A. Dekel and M. R. Krumholz. Steady outflows in giant clumps of high-z disc galaxies during migration and growth by accretion. MNRAS, 432:455–467, June 2013. doi: 10.1093/mnras/stt480. 2.2.2, 2.6, 4.1

B. Devecchi and M. Volonteri. Formation of the First Nuclear Clusters and Massive Black Holes at High Redshift. ApJ, 694:302–313, March 2009. doi: 10.1088/0004-637X/694/1/302. 2.5.4

C. L. Dobbs and J. E. Pringle. The exciting lives of giant molecular clouds. MNRAS, 432:653–667, June 2013. doi: 10.1093/mnras/stt508. 5.2

D. Downes and P. M. Solomon. Rotating Nuclear Rings and Extreme Starbursts in Ultraluminous Galaxies. ApJ, 507:615–654, November 1998. doi: 10.1086/306339. 2.1, 2.5.2

M. J. Duncan, R. T. Farouki, and S. L. Shapiro. Simulations of galaxy mergers - Cannibalism and dynamical friction. ApJ, 271:22–31, August 1983. doi: 10.1086/161172. 3.5.4

B. G. Elmegreen. Quiescent formation of bound galactic clusters. MNRAS, 203: 1011–1020, June 1983. doi: 10.1093/mnras/203.4.1011. 2.1, 7.1

B. G. Elmegreen. Star Formation in a Crossing Time. ApJ, 530:277–281, February 2000. doi: 10.1086/308361. 2.2.1, 2.4.3

B. G. Elmegreen. Star Formation from Galaxies to Globules. ApJ, 577:206–220, September 2002. doi: 10.1086/342177. 7.1

B. G. Elmegreen. On the Rapid Collapse and Evolution of Molecular Clouds. ApJ, 668:1064–1082, October 2007. doi: 10.1086/521327. 2.2.1

B. G. Elmegreen. Variations in stellar clustering with environment: Dispersed star formation and the origin of faint fuzzies. *The Astrophysical Journal*, 672(2): 1006–1012, jan 2008. doi: 10.1086/523791. 7.1

B. G. Elmegreen and C. Clemens. On the formation rate of galactic clusters in clouds of various masses. ApJ, 294:523–532, July 1985. doi: 10.1086/163320. 2.5.4, 3.1, 5.2

B. G. Elmegreen and Y. N. Efremov. A Universal Formation Mechanism for Open and Globular Clusters in Turbulent Gas. ApJ, 480:235, May 1997. doi: 10.1086/303966. 2.1, 2.5.4, 3.3, 6.1

R. A. W. Elson, S. M. Fall, and K. C. Freeman. The structure of young star clusters in the Large Magellanic Cloud. ApJ, 323:54–78, December 1987. doi: 10.1086/165807. 3.1, 3.2, 3.2, 3.2, 3.2.1, 3.2.1, 3.3.2, 3.1, 3.4, 3.4.1, 3.1, 3.4.1, 3.4.1, 3.4.2, 3.2, 3.4.2, 3.5.3, 3.6, 3.B, 3.B.6, 7.3.2

A. Emerick, G. L. Bryan, and M.-M. Mac Low. Simulating an Isolated Dwarf Galaxy with Multi-Channel Feedback and Chemical Yields from Individual Stars. *ArXiv e-prints*, July 2018. 6.4

N. J. Evans, II, M. M. Dunham, J. K. Jørgensen, M. L. Enoch, B. Merín, E. F. van Dishoeck, J. M. Alcalá, P. C. Myers, K. R. Stapelfeldt, T. L. Huard, L. E. Allen, P. M. Harvey, T. van Kempen, G. A. Blake, D. W. Koerner, L. G. Mundy, D. L. Padgett, and A. I. Sargent. The Spitzer c2d Legacy Results: Star-Formation Rates and Efficiencies; Evolution and Lifetimes. ApJS, 181:321-350, April 2009. doi: 10.1088/0067-0049/181/2/321. 2.1, 2.5.1, 3.1, 5.1, 5.2.1

N. J. Evans, II, A. Heiderman, and N. Vutisalchavakul. Star Formation Relations in Nearby Molecular Clouds. ApJ, 782:114, February 2014. doi: 10.1088/0004-637X/782/2/114. 2.5.2, 5.2, 5.2.1, 5.2.3, 5.4.2, 5.4.2, 5.4.3

E. A. Evstigneeva, M. D. Gregg, M. J. Drinkwater, and M. Hilker. Internal Properties of Ultracompact Dwarf Galaxies in the Virgo Cluster. AJ, 133:1722–1740, April 2007. doi: 10.1086/511958. 4.2

Christopher M. Faesi, Charles J. Lada, and Jan Forbrich. The ALMA View of GMCs in NGC 300: Physical Properties and Scaling Relations at 10 pc Resolution. ApJ, 857(1):19, Apr 2018. doi: 10.3847/1538-4357/aaad60. 7.6

S. M. Fall, M. R. Krumholz, and C. D. Matzner. Stellar Feedback in Molecular Clouds and its Influence on the Mass Function of Young Star Clusters. ApJ, 710: L142–L146, February 2010. doi: 10.1088/2041-8205/710/2/L142. 2.2.2, 2.4.2, 2.6, 3.4.2, 4.1, 4.1, 5.1, 5.4.1, 5.4.2, 6.1, 6.4, 7.1, 7.2.3, 7.2.3, 7.2.3, 7.5.1, 7.6

C.-A. Faucher-Giguère, E. Quataert, and P. F. Hopkins. Feedback-regulated star formation in molecular clouds and galactic discs. MNRAS, 433:1970–1990, August 2013. doi: 10.1093/mnras/stt866. 2.1, 2.3.1, 4.1, 5.2, 5.4.4, 6.4

C. Federrath. Inefficient star formation through turbulence, magnetic fields and feedback. MNRAS, 450:4035–4042, July 2015a. doi: 10.1093/mnras/stv941. 1.2, 4.2.2, 4.3

C. Federrath. Inefficient star formation through turbulence, magnetic fields and feedback. MNRAS, 450:4035–4042, July 2015b. doi: 10.1093/mnras/stv941. 5.2, 5.5.3

C. Federrath and R. S. Klessen. The Star Formation Rate of Turbulent Magnetized Clouds: Comparing Theory, Simulations, and Observations. ApJ, 761:156, December 2012. doi: 10.1088/0004-637X/761/2/156. 1.1, 2.4.1, 2.5.1, 2.5.3, 4.2.2, 4.3, 5.1, 5.2, 5.2, 5.7

C. Federrath, R. Banerjee, P. C. Clark, and R. S. Klessen. Modeling Collapse and Accretion in Turbulent Gas Clouds: Implementation and Comparison of Sink Particles in AMR and SPH. ApJ, 713:269–290, April 2010. doi: 10.1088/0004-637X/713/1/269. 5.3.2, 6.2.1

C. Federrath, J. Schober, S. Bovino, and D. R. G. Schleicher. The Turbulent Dynamo in Highly Compressible Supersonic Plasmas. ApJ, 797:L19, December 2014. doi: 10.1088/2041-8205/797/2/L19. 2.3.2, 5.3.1

C. Federrath, M. Krumholz, and P. F. Hopkins. Converging on the Initial Mass Function of Stars. In *Journal of Physics Conference Series*, volume 837 of *Journal of Physics Conference Series*, page 012007, May 2017. doi: 10.1088/1742-6596/837/1/012007. 1.4, 5.5.3, 6.2.3, 7.6

R. Feldmann and N. Y. Gnedin. On the Time Variability of the Star Formation Efficiency. ApJ, 727:L12, January 2011. doi: 10.1088/2041-8205/727/1/L12. 1.1, 5.1, 7.1

M. Fellhauer and P. Kroupa. Star Cluster Survival in Star Cluster Complexes under Extreme Residual Gas Expulsion. ApJ, 630:879–886, September 2005. doi: 10.1086/432110. 3.2.1

A. Ferrara, F. Haardt, and R. Salvaterra. Can supermassive black hole seeds form in galaxy mergers? MNRAS, 434:2600–2605, September 2013. doi: 10.1093/mnras/stt1350. 2.5.6

D. Fielding, E. Quataert, and D. Martizzi. Clustered Supernovae Drive Powerful Galactic Winds After Super-Bubble Breakout. *ArXiv e-prints*, July 2018. 6.1, 6.4

Duncan A. Forbes and Terry Bridges. Accreted versus in situ Milky Way globular clusters. MNRAS, 404(3):1203–1214, May 2010. doi: 10.1111/j.1365-2966.2010.16373.x. 1.4, 7.2.2

M. Fouesneau, L. C. Johnson, D. R. Weisz, J. J. Dalcanton, E. F. Bell, L. Bianchi, N. Caldwell, D. A. Gouliermis, P. Guhathakurta, J. Kalirai, S. S. Larsen, H.-W. Rix, A. C. Seth, E. D. Skillman, and B. F. Williams. The Panchromatic Hubble Andromeda Treasury. V. Ages and Masses of the Year 1 Stellar Clusters. ApJ, 786:117, May 2014. doi: 10.1088/0004-637X/786/2/117. 7.7

P. Freeman, E. Rosolowsky, J. M. D. Kruijssen, N. Bastian, and A. Adamo. The varying mass distribution of molecular clouds across M83. MNRAS, 468:1769–1781, June 2017. doi: 10.1093/mnras/stx499. 2.1, 7.1, 7.2.2, 7.3.1, 7.1, 7.4, 7.2, 7.5.1, 7.5.1, 7.6

M. Freitag, M. A. Gürkan, and F. A. Rasio. Runaway collisions in young star clusters - II. Numerical results. MNRAS, 368:141–161, May 2006. doi: 10.1111/j.1365-2966.2006.10096.x. 3.5.3

C. S. Frenk and S. M. Fall. An ellipticity - age relation for globular clusters in the Large Magellanic Cloud. I - Measurements. MNRAS, 199:565–580, May 1982. doi: 10.1093/mnras/199.3.565. 3.4.2

Y. Fujimoto, M. R. Krumholz, and S. Tachibana. Short-lived radioisotopes in meteorites from Galactic-scale correlated star formation. MNRAS, 480:4025–4039, November 2018. doi: 10.1093/mnras/sty2132. 6.4

Y. Fukui and A. Kawamura. Molecular Clouds in Nearby Galaxies. ARA&A, 48: 547–580, September 2010. doi: 10.1146/annurev-astro-081309-130854. 2.5.1, 5.2.1

Michele Fumagalli, Robert L. da Silva, and Mark R. Krumholz. Stochastic Star Formation and a (Nearly) Uniform Stellar Initial Mass Function. ApJ, 741:L26, November 2011. doi: 10.1088/2041-8205/741/2/L26. 6.2.3

C. F. Gammie and E. C. Ostriker. Can Nonlinear Hydromagnetic Waves Support a Self-gravitating Cloud? ApJ, 466:814, August 1996. doi: 10.1086/177556. 5.4.3, 6.2.2, 7.2.2

Y. Gao and P. M. Solomon. HCN Survey of Normal Spiral, Infrared-luminous, and Ultraluminous Galaxies. ApJS, 152:63–80, May 2004. doi: 10.1086/383003. 5.2.2

E. Gavagnin, A. Bleuler, J. Rosdahl, and R. Teyssier. Star cluster formation in a turbulent molecular cloud self-regulated by photoionization feedback. MNRAS, 472:4155–4172, December 2017. doi: 10.1093/mnras/stx2222. 5.1, 6.1

S. Geen, J. D. Soler, and P. Hennebelle. Interpreting the star formation efficiency of nearby molecular clouds with ionizing radiation. MNRAS, 471:4844–4855, November 2017. doi: 10.1093/mnras/stx1765. 5.1, 5.4.1, 5.5.1, 5.5.1, 5.7, 7.1, 7.5.2

M. Geha, P. Guhathakurta, and R. P. van der Marel. Internal Dynamics, Structure, and Formation of Dwarf Elliptical Galaxies. I. A Keck/Hubble Space Telescope Study of Six Virgo Cluster Dwarf Galaxies. AJ, 124:3073–3087, December 2002. doi: 10.1086/344764. 4.2

A. Ginsburg and J. M. D. Kruijssen. A High Cluster Formation Efficiency in the Sagittarius B2 Complex. ApJ, 864:L17, September 2018. doi: 10.3847/2041-8213/aada89. 1

Q. E. Goddard, N. Bastian, and R. C. Kennicutt. On the fraction of star clusters surviving the embedded phase. MNRAS, 405:857–869, June 2010. doi: 10.1111/j.1365-2966.2010.16511.x. 7.1, 7.6

P. Goldreich and J. Kwan. Molecular Clouds. ApJ, 189:441–454, May 1974. doi: 10.1086/152821. 1.1, 1.1

P. F. Goldsmith and J. Kauffmann. Electron Excitation of High Dipole Moment Molecules Re-examined. ApJ, 841:25, May 2017. doi: 10.3847/1538-4357/aa6f12. 2.5.1, 5.2.2, 5.5.1

S. P. Goodwin. Constraints on the initial conditions of globular clusters. MNRAS, 294:47, February 1998. doi: 10.1046/j.1365-8711.1998.01192.x. 3.1, 3.5.1

S. P. Goodwin. The effect of the dynamical state of clusters on gas expulsion and infant mortality. Ap&SS, 324:259–263, December 2009. doi: 10.1007/s10509-009-0116-5. 9

D. A. Gouliermis. Unbound Young Stellar Systems: Star Formation on the Loose. PASP, 130(7):072001, July 2018. doi: 10.1088/1538-3873/aac1fd. 3.1, 7.1, 7.2.3

D. A. Gouliermis, D. Thilker, B. G. Elmegreen, D. M. Elmegreen, D. Calzetti, J. C. Lee, A. Adamo, A. Aloisi, M. Cignoni, D. O. Cook, D. A. Dale, J. S. Gallagher, K. Grasha, E. K. Grebel, A. H. Davó, D. A. Hunter, K. E. Johnson, H. Kim, P. Nair, A. Nota, A. Pellerin, J. Ryon, E. Sabbi, E. Sacchi, L. J. Smith, M. Tosi, L. Ubeda, and B. Whitmore. Hierarchical star formation across the ring galaxy NGC 6503. MNRAS, 452:3508–3528, October 2015. doi: 10.1093/mnras/stv1325. 3.1, 3.3, 7.1

K. Grasha, D. Calzetti, A. Adamo, H. Kim, B. G. Elmegreen, D. A. Gouliermis, D. A. Dale, M. Fumagalli, E. K. Grebel, K. E. Johnson, L. Kahre, R. C. Kennicutt, M. Messa, A. Pellerin, J. E. Ryon, L. J. Smith, F. Shabani, D. Thilker, and L. Ubeda. The Hierarchical Distribution of the Young Stellar Clusters in Six Local Star-forming Galaxies. ApJ, 840:113, May 2017. doi: 10.3847/1538-4357/aa6f15. 3.1, 3.3, 7.1

M. Y. Grudić and P. F. Hopkins. The Elephant in the Room: The Importance of Where and When Massive Stars Form in Molecular Clouds. *arXiv e-prints*, September 2018. 7.1, 7.2.1, 7.6

M. Y. Grudić, D. Guszejnov, P. F. Hopkins, A. Lamberts, M. Boylan-Kolchin, N. Murray, and D. Schmitz. From the top down and back up again: star cluster structure from hierarchical star formation. MNRAS, 481:688–702, November 2018a. doi: 10.1093/mnras/sty2303. 2.6, 4.2.3, 6.2.3, 7.2.1, 7.2.1, 7.3.2, 7.3.2

M. Y. Grudić, P. F. Hopkins, C.-A. Faucher-Giguère, E. Quataert, N. Murray, and D. Kereš. When feedback fails: the scaling and saturation of star formation efficiency. MNRAS, 475:3511–3528, April 2018b. doi: 10.1093/mnras/sty035. 1, 3.1, 3.1, 3.1, 3.2, 3.2.1, 3.3, 3.5.2, 3.6, 3.A, 4.1, 4.1, 4.1, 4.2.2, 4.2.2, 4.3, 4.3, 5.1, 5.2, 5.3, 5.3.1, 5.3.2, 5.3.3, 5.4.1, 5.4.2, 5.1, 5.6.1, 6.1, 6.2.3, 6.3, 6.4, 7.1, 7.1, 7.2.1, 7.2.3, 5, 7.6

M. Y. Grudić, P. F. Hopkins, E. Quataert, and N. Murray. The maximum stellar surface density due to the failure of stellar feedback. MNRAS, 483:5548–5553, March 2019. doi: 10.1093/mnras/sty3386. 7.2.3

Michael Y. Grudić, Philip F. Hopkins, Eve J. Lee, Norman Murray, Claude-André Faucher-Giguère, and L. Clifton Johnson. On The Nature of Variations in the Measured Star Formation Efficiency of Molecular Clouds. *arXiv e-prints*, art. arXiv:1809.08348, Sep 2018c. 7.1, 7.1, 7.2.2, 7.2.3, 7.2.3, 7.2.3

M. A. Gürkan, M. Freitag, and F. A. Rasio. Formation of Massive Black Holes in Dense Star Clusters. I. Mass Segregation and Core Collapse. ApJ, 604:632–652, April 2004. doi: 10.1086/381968. 2.5.4, 3.5.3

D. Guszejnov, M. R. Krumholz, and P. F. Hopkins. The necessity of feedback physics in setting the peak of the initial mass function. MNRAS, 458:673–680, May 2016. doi: 10.1093/mnras/stw315. 1.4, 5.5.3, 7.6

D. Guszejnov, P. F. Hopkins, and M. R. Krumholz. Protostellar feedback in turbulent fragmentation: consequences for stellar clustering and multiplicity. MNRAS, 468:4093–4106, July 2017. doi: 10.1093/mnras/stx725. 2.5.3, 3.3, 3.4.2

D. Guszejnov, P. F. Hopkins, and M. Y. Grudić. Universal scaling relations in scale-free structure formation. MNRAS, 477:5139–5149, July 2018a. doi: 10.1093/mnras/sty920. 1.1, 3.3.1, 3.4.2, 3.4.2, 3.6

D. Guszejnov, P. F. Hopkins, M. Y. Grudić, M. R. Krumholz, and C. Federrath. Isothermal Fragmentation: Is there a low-mass cut-off? MNRAS, 480:182–191, October 2018b. doi: 10.1093/mnras/sty1847. 1.4, 5.3.2, 5.7, 6.2.1, 6.2.3

Dávid Guszejnov, Philip F. Hopkins, and Michael Y. Grudić. Universal scaling relations in scale-free structure formation. MNRAS, 477(4):5139–5149, Jul 2018c. doi: 10.1093/mnras/sty920. 2.5.3

Dávid Guszejnov, Philip F. Hopkins, and Andrew S. Graus. Is it possible to reconcile extragalactic IMF variations with a universal Milky Way IMF? MNRAS, 485(4): 4852–4862, Jun 2019. doi: 10.1093/mnras/stz736. 7.6

R. A. Gutermuth, S. T. Megeath, P. C. Myers, L. E. Allen, J. L. Pipher, and G. G. Fazio. A Spitzer Survey of Young Stellar Clusters Within One Kiloparsec of the Sun: Cluster Core Extraction and Basic Structural Analysis. ApJS, 184:18–83, September 2009. doi: 10.1088/0067-0049/184/1/18. 2.5.1

E. Harper-Clark and N. Murray. One-Dimensional Dynamical Models of the Carina Nebula Bubble. ApJ, 693:1696–1712, March 2009. doi: 10.1088/0004-637X/693/2/1696. 7.2.3

A. Heiderman, N. J. Evans, II, L. E. Allen, T. Huard, and M. Heyer. The Star Formation Rate and Gas Surface Density Relation in the Milky Way: Implications for Extragalactic Studies. ApJ, 723:1019-1037, November 2010. doi: 10.1088/0004-637X/723/2/1019. 7, 2.5.2, 3.1, 5.1, 5.2.1, 5.2.3

P. Hennebelle and G. Chabrier. Analytical Star Formation Rate from Gravoturbulent Fragmentation. ApJ, 743:L29, December 2011a. doi: 10.1088/2041-8205/743/2/L29. 1.1, 5.1, 5.2

P. Hennebelle and G. Chabrier. Analytical Star Formation Rate from Gravoturbulent Fragmentation. ApJ, 743:L29, December 2011b. doi: 10.1088/2041-8205/743/2/L29. 2.5.2, 5.6.2

M. Hénon. L'évolution initiale d'un amas sphérique. *Annales d'Astrophysique*, 27: 83, February 1964. 3.2

M. Heyer, R. Gutermuth, J. S. Urquhart, T. Csengeri, M. Wienen, S. Leurini, K. Menten, and F. Wyrowski. The rate and latency of star formation in dense, massive clumps in the Milky Way. A&A, 588:A29, April 2016. doi: 10.1051/0004-6361/201527681. 2.5.1, 2.5.1, 2.5.1, 2.3, 2.5.2, 5.2, 5.2.1, 5.2.3, 5.2.3, 5.2, 5.3, 5.5.2, 5.7

Mark Heyer and T.M. Dame. Molecular clouds in the milky way. *Annual Review of Astronomy and Astrophysics*, 53(1):583–629, 2015. doi: 10.1146/annurev-astro-082214-122324. URL `https://doi.org/10.1146/annurev-astro-082214-122324`. 1.1, 7.4

J. G. Hills. The effect of mass loss on the dynamical evolution of a stellar system - Analytic approximations. ApJ, 235:986–991, February 1980. doi: 10.1086/157703. 2.1, 2.5.4, 3.1, 3.3, 5.2, 6.1, 7.1, 7.2.3

K. Hollyhead, N. Bastian, A. Adamo, E. Silva-Villa, J. Dale, J. E. Ryon, and Z. Gazak. Studying the YMC population of M83: how long clusters remain embedded, their interaction with the ISM and implications for GC formation theories. MNRAS, 449:1106–1117, May 2015. doi: 10.1093/mnras/stv331. 2.1, 3.3

P. F. Hopkins. An excursion-set model for the structure of giant molecular clouds and the interstellar medium. MNRAS, 423:2016–2036, July 2012. doi: 10.1111/j.1365-2966.2012.20730.x. 4.2.2, 4.3, 5.4.2, 5.7, 7.1, 7.5.1

P. F. Hopkins. Why do stars form in clusters? An analytic model for stellar correlation functions. MNRAS, 428:1950–1957, January 2013. doi: 10.1093/mnras/sts147. 3.3

P. F. Hopkins. A new class of accurate, mesh-free hydrodynamic simulation methods. MNRAS, 450:53–110, June 2015. doi: 10.1093/mnras/stv195. 2.3, 3.4, 3.4.1, 5.3, 6.2.1, 7.2.1, 7.2.1

P. F. Hopkins. A constrained-gradient method to control divergence errors in numerical MHD. MNRAS, 462:576–587, October 2016. doi: 10.1093/mnras/stw1578. 7.2.1

P. F. Hopkins and C. Conroy. Are the Formation and Abundances of Metal-Poor Stars the Result of Dust Dynamics? *ArXiv e-prints*, December 2015. 2.4.1

P. F. Hopkins and M. Y. Grudić. Numerical Problems in Coupling Photon Momentum (Radiation Pressure) to Gas. *ArXiv e-prints*, March 2018. 1, 6.1, 6.2.3, 7.1, 7.2.1

P. F. Hopkins and E. Quataert. How do massive black holes get their gas? MNRAS, 407:1529–1564, September 2010. doi: 10.1111/j.1365-2966.2010.17064.x. 2.5.5

P. F. Hopkins and M. J. Raives. Accurate, meshless methods for magnetohydrodynamics. MNRAS, 455:51–88, January 2016. doi: 10.1093/mnras/stv2180. 1.4, 2.3, 5.3, 7.2.1

P. F. Hopkins, Tod R. Lauer, Thomas J. Cox, Lars Hernquist, and John Kormendy. Dissipation and extra light in galactic nuclei. iii. "core" ellipticals and "missing" light. *The Astrophysical Journal Supplement Series*, 181(2):486, 2009. URL `http://stacks.iop.org/0067-0049/181/i=2/a=486`. 3.3.2

P. F. Hopkins, N. Murray, E. Quataert, and T. A. Thompson. A maximum stellar surface density in dense stellar systems. MNRAS, 401:L19–L23, January 2010. doi: 10.1111/j.1745-3933.2009.00777.x. 2.5.5, 4.1, 4.1, 4.2, 4.3

P. F. Hopkins, E. Quataert, and N. Murray. Self-regulated star formation in galaxies via momentum input from massive stars. MNRAS, 417:950–973, October 2011a. doi: 10.1111/j.1365-2966.2011.19306.x. 1.2, 1.2, 6.2.3, 6.4

P. F. Hopkins, E. Quataert, and N. Murray. Self-Regulated Star Formation in Galaxies via Momentum Input from Massive Stars. MNRAS, 417:950–973, October 2011b. doi: 10.1111/j.1365-2966.2011.19306.x. 1.2, 2.3.1, 2.4

P. F. Hopkins, E. Quataert, and N. Murray. The structure of the interstellar medium of star forming galaxies. MNRAS, 421:3488–3521, April 2012a. doi: 10.1111/j.1365-2966.2012.20578.x. 1.2, 2.2.1, 2.3.1, 2.4.2, 3.1, 4.1, 5.1, 5.4.2, 6.4

P. F. Hopkins, E. Quataert, and N. Murray. Stellar feedback in galaxies and the origin of galaxy-scale winds. MNRAS, 421:3522–3537, April 2012b. doi: 10.1111/j.1365-2966.2012.20593.x. 2.3.1

P. F. Hopkins, D. Narayanan, and N. Murray. The meaning and consequences of star formation criteria in galaxy models with resolved stellar feedback. MNRAS, 432:2647–2653, July 2013. doi: 10.1093/mnras/stt723. 2.3.1, 7.2.1

P. F. Hopkins, D. Keres, J. Onorbe, C.-A. Faucher-Giguere, E. Quataert, N. Murray, and J. S. Bullock. Galaxies on FIRE (Feedback In Realistic Environments): Stellar Feedback Explains Cosmologically Inefficient Star Formation. MNRAS, 445:581–603, November 2014. doi: 10.1093/mnras/stu1738. 1.2, 2.1, 2.3.1, 2.5.2, 2.6, 3.1, 3.2.1, 4.1, 5.3

P. F. Hopkins, P. Torrey, C.-A. Faucher-Giguère, E. Quataert, and N. Murray. Stellar and quasar feedback in concert: effects on AGN accretion, obscuration, and outflows. MNRAS, 458:816–831, May 2016. doi: 10.1093/mnras/stw289. 2.3.1

P. F. Hopkins, A. Wetzel, D. Kereš, C.-A. Faucher-Giguère, E. Quataert, M. Boylan-Kolchin, N. Murray, C. C. Hayward, S. Garrison-Kimmel, C. Hummels, R. Feldmann, P. Torrey, X. Ma, D. Anglés-Alcázar, K.-Y. Su, M. Orr, D. Schmitz, I. Escala, R. Sanderson, M. Y. Grudić, Z. Hafen, J.-H. Kim, A. Fitts, J. S. Bullock, C. Wheeler, T. K. Chan, O. D. Elbert, and D. Narayanan. FIRE-2 simulations: physics versus numerics in galaxy formation. MNRAS, 480:800–863, October 2018a. doi: 10.1093/mnras/sty1690. 1.2, 1.2, 1.4, 2.1, 2.1, 2.3.1, 2.4.1, 2.6, 2.A.2, 3.2.1, 5.3, 6.1, 6.2.1, 6.2.2, 6.2.3, 7.2.1, 7.2.3, 7.5.3

Philip F. Hopkins, Michael Y. Grudic, Andrew R. Wetzel, Dusan Keres, Claude-Andre Gaucher-Giguere, Xiangcheng Ma, Norman Murray, and Nathan Butcher. Radiative Stellar Feedback in Galaxy Formation: Methods and Physics. *arXiv e-prints*, art. arXiv:1811.12462, Nov 2018b. 1.4

Philip F. Hopkins, Andrew Wetzel, Dušan Kereš, Claude-André Faucher-Giguère, Eliot Quataert, Michael Boylan-Kolchin, Norman Murray, Christopher C. Hayward, and Kareem El-Badry. How to model supernovae in simulations of star and galaxy formation. MNRAS, 477(2):1578–1603, Jun 2018c. doi: 10.1093/mnras/sty674. 7.2.1

C. S. Howard, R. E. Pudritz, and W. E. Harris. Simulating radiative feedback and star cluster formation in GMCs - I. Dependence on gravitational boundedness. MNRAS, 461:2953–2974, September 2016. doi: 10.1093/mnras/stw1476. 5.1, 6.1, 6.2.3

C. S. Howard, R. E. Pudritz, and W. E. Harris. Simulating radiative feedback and star cluster formation in GMCs - II. Mass dependence of cloud destruction and cluster properties. MNRAS, 470:3346–3358, September 2017. doi: 10.1093/mnras/stx1363. 5.1, 6.1

C.-Y. Hu, T. Naab, S. Walch, S. C. O. Glover, and P. C. Clark. Star formation and molecular hydrogen in dwarf galaxies: a non-equilibrium view. MNRAS, 458: 3528–3553, June 2016. doi: 10.1093/mnras/stw544. 6.4

J. D. Hunter. Matplotlib: A 2d graphics environment. *Computing In Science & Engineering*, 9(3):90–95, 2007. doi: 10.1109/MCSE.2007.55. 5.7, 6.4, 7.6

W. Jaffe. The Envelopes of Spherical Galaxies. In P. T. de Zeeuw, editor, *Structure and Dynamics of Elliptical Galaxies*, volume 127 of *IAU Symposium*, page 511, 1987. 3.2

L. C. Johnson, A. C. Seth, J. J. Dalcanton, L. C. Beerman, M. Fouesneau, A. R. Lewis, D. R. Weisz, B. F. Williams, E. F. Bell, A. E. Dolphin, S. S. Larsen, K. Sandstrom, and E. D. Skillman. Panchromatic Hubble Andromeda Treasury.

XVI. Star Cluster Formation Efficiency and the Clustered Fraction of Young Stars. ApJ, 827:33, August 2016. doi: 10.3847/0004-637X/827/1/33. 2.5.4, 7.1

L. Clifton Johnson, Anil C. Seth, Julianne J. Dalcanton, Nelson Caldwell, Morgan Fouesneau, Dimitrios A. Gouliermis, Paul W. Hodge, Søren S. Larsen, Knut A. G. Olsen, Izaskun San Roman, Ata Sarajedini, Daniel R. Weisz, Benjamin F. Williams, Lori C. Beerman, Luciana Bianchi, Andrew E. Dolphin, Léo Girardi, Puragra Guhathakurta, Jason Kalirai, Dustin Lang, Antonela Monachesi, Sanjay Nanda, Hans-Walter Rix, and Evan D. Skillman. PHAT Stellar Cluster Survey. I. Year 1 Catalog and Integrated Photometry. ApJ, 752(2):95, Jun 2012. doi: 10.1088/0004-637X/752/2/95. 7.7

L. Clifton Johnson, Anil C. Seth, Julianne J. Dalcanton, Lori C. Beerman, Morgan Fouesneau, Daniel R. Weisz, Timothy A. Bell, Andrew E. Dolphin, Karin Sandstrom, and Benjamin F. Williams. Panchromatic Hubble Andromeda Treasury. XVIII. The High-mass Truncation of the Star Cluster Mass Function. ApJ, 839 (2):78, Apr 2017. doi: 10.3847/1538-4357/aa6a1f. 7.5.1

Eric Jones, Travis Oliphant, Pearu Peterson, et al. SciPy: Open source scientific tools for Python, 2001. URL `http://www.scipy.org/`. [Online; accessed <today>]. 5.7, 6.4, 7.2.1, 7.6

P. H. Jumper and C. D. Matzner. Radiation forces on dust envelopes. MNRAS, 480: 905–913, October 2018. doi: 10.1093/mnras/sty1784. 6.4

J. Kainulainen, H. Beuther, T. Henning, and R. Plume. Probing the evolution of molecular cloud structure. From quiescence to birth. A&A, 508:L35–L38, December 2009. doi: 10.1051/0004-6361/200913605. 5.2

Rahul Kannan, Mark Vogelsberger, Federico Marinacci, Ryan McKinnon, Rüdiger Pakmor, and Volker Springel. AREPO-RT: radiation hydrodynamics on a moving mesh. MNRAS, 485(1):117–149, May 2019. doi: 10.1093/mnras/stz287. 1.4

J. Kauffmann, P. F. Goldsmith, G. Melnick, V. Tolls, A. Guzman, and K. M. Menten. Molecular Line Emission as a Tool for Galaxy Observations (LEGO). I. HCN as a tracer of moderate gas densities in molecular clouds and galaxies. A&A, 605: L5, September 2017. doi: 10.1051/0004-6361/201731123. 5.2.2, 5.5.1

A. Kawamura, Y. Mizuno, T. Minamidani, M. D. Filipović, L. Staveley-Smith, S. Kim, N. Mizuno, T. Onishi, A. Mizuno, and Y. Fukui. The Second Survey of the Molecular Clouds in the Large Magellanic Cloud by NANTEN. II. Star Formation. ApJS, 184:1–17, September 2009. doi: 10.1088/0067-0049/184/1/1. 5.2.1

S. Kazantzidis, A. R. Zentner, and A. V. Kravtsov. The Robustness of Dark Matter Density Profiles in Dissipationless Mergers. ApJ, 641:647–664, April 2006. doi: 10.1086/500579. 3.3

B. W. Keller, J. Wadsley, S. M. Benincasa, and H. M. P. Couchman. A superbubble feedback model for galaxy simulations. MNRAS, 442:3013–3025, August 2014. doi: 10.1093/mnras/stu1058. 6.1, 6.4

R. C. Kennicutt and N. J. Evans. Star Formation in the Milky Way and Nearby Galaxies. ARA&A, 50:531–608, September 2012. doi: 10.1146/annurev-astro-081811-125610. 1.1, 3.1, 4.1

R. C. Kennicutt, Jr. The Global Schmidt Law in Star-forming Galaxies. ApJ, 498: 541–+, May 1998a. doi: 10.1086/305588. 1.1, 2.1, 2.4.1, 2.5.2, 10, 4.2.3, 5.2

R. C. Kennicutt, Jr. Star Formation in Galaxies Along the Hubble Sequence. ARA&A, 36:189–232, 1998b. doi: 10.1146/annurev.astro.36.1.189. 2.5.2

E. Keto, L. C. Ho, and K.-Y. Lo. M82, Starbursts, Star Clusters, and the Formation of Globular Clusters. ApJ, 635:1062–1076, December 2005. doi: 10.1086/497575. 2.1, 4.1

N. V. Kharchenko, Piskunov, A. E., Schilbach, E., Röser, S., and Scholz, R.-D. Global survey of star clusters in the milky way - ii. the catalogue of basic parameters. *A&A*, 558:A53, 2013. doi: 10.1051/0004-6361/201322302. URL `https://doi.org/10.1051/0004-6361/201322302`. 7.7

C.-G. Kim and E. C. Ostriker. Momentum Injection by Supernovae in the Interstellar Medium. ApJ, 802:99, April 2015. doi: 10.1088/0004-637X/802/2/99. 2.3.1

J.-G. Kim, W.-T. Kim, E. C. Ostriker, and M. A. Skinner. Modeling UV Radiation Feedback from Massive Stars. I. Implementation of Adaptive Ray-tracing Method and Tests. ApJ, 851:93, December 2017a. doi: 10.3847/1538-4357/aa9b80. 1, 5.1, 6.1, 6.2.3, 7.5.3

J.-G. Kim, W.-T. Kim, and E. C. Ostriker. Modeling UV Radiation Feedback from Massive Stars. II. Dispersal of Star-forming Giant Molecular Clouds by Photoionization and Radiation Pressure. ApJ, 859:68, May 2018a. doi: 10.3847/1538-4357/aabe27. 5.1, 5.4.2, 6.1, 6.2.2, 6.2.3, 6.2.3, 6.3, 6.4, 7.1, 7.2.1, 7.5.2

J.-h. Kim, X. Ma, M. Y. Grudić, P. F. Hopkins, C. C. Hayward, A. Wetzel, C.-A. Faucher-Giguère, D. Kereš, S. Garrison-Kimmel, and N. Murray. Formation of Globular Cluster Candidates in Merging Proto-galaxies at High Redshift: A View from the FIRE Cosmological Simulations. *ArXiv e-prints*, April 2017b. 4.2.1

J.-h. Kim, X. Ma, M. Y. Grudić, P. F. Hopkins, C. C. Hayward, A. Wetzel, C.-A. Faucher-Giguère, D. Kereš, S. Garrison-Kimmel, and N. Murray. Formation of globular cluster candidates in merging proto-galaxies at high redshift: a view from the FIRE cosmological simulations. MNRAS, 474:4232–4244, March 2018b. doi: 10.1093/mnras/stx2994. 6.2.3

Jeong-Gyu Kim, Woong-Tae Kim, and Eve C. Ostriker. Disruption of Molecular Clouds by Expansion of Dusty H II Regions. ApJ, 819:137, March 2016. doi: 10.3847/0004-637X/819/2/137. 6.2.3

I. R. King. The structure of star clusters. III. Some simple dynamical models. AJ, 71:64–+, February 1966. 3.1, 3.5.3, 3.6

Evan N. Kirby, Judith G. Cohen, Puragra Guhathakurta, Lucy Cheng, James S. Bullock, and Anna Gallazzi. The Universal Stellar Mass-Stellar Metallicity Relation for Dwarf Galaxies. ApJ, 779(2):102, Dec 2013. doi: 10.1088/0004-637X/779/2/102. 7.2.2

R. S. Klessen and A. Burkert. The Formation of Stellar Clusters: Gaussian Cloud Conditions. I. ApJS, 128:287–319, May 2000. doi: 10.1086/313371. 3.2.1

R. S. Klessen and A. Burkert. The Formation of Stellar Clusters: Gaussian Cloud Conditions. II. ApJ, 549:386–401, March 2001. doi: 10.1086/319053. 4.2.3

R. S. Klessen, F. Heitsch, and M.-M. Mac Low. Gravitational Collapse in Turbulent Molecular Clouds. I. Gasdynamical Turbulence. ApJ, 535:887–906, June 2000. doi: 10.1086/308891. 6.1

E. Kontizas, M. Kontizas, G. Sedmak, and R. Smareglia. Ellipticities at R(h) of LMC star clusters. AJ, 98:590–595, August 1989. doi: 10.1086/115159. 3.4.2, 3.5.1

J. Kormendy, D. B. Fisher, M. E. Cornell, and R. Bender. Structure and Formation of Elliptical and Spheroidal Galaxies. ApJS, 182:216–309, May 2009. doi: 10.1088/0067-0049/182/1/216. 4.2

A. G. Kritsuk, M. L. Norman, and R. Wagner. On the Density Distribution in Star-forming Interstellar Clouds. ApJ, 727:L20, January 2011. doi: 10.1088/2041-8205/727/1/L20. 2.2.1, 2.5.3, 5.2

A. G. Kritsuk, C. T. Lee, and M. L. Norman. A supersonic turbulence origin of Larson's laws. MNRAS, 436:3247–3261, December 2013. doi: 10.1093/mnras/stt1805. 3.4.2

P. Kroupa. The Initial Mass Function of Stars: Evidence for Uniformity in Variable Systems. *Science*, 295:82–91, January 2002. doi: 10.1126/science.1067524. 2.2.2, 2.3.1, 2.5.1, 5.2.3, 5.3.3, 5.7, 6.2.3, 7.2.1

Pavel Kroupa, Jarrod Hurley, and Sverre Aarseth. The formation of a bound star cluster: from the Orion nebula cluster to the Pleiades. *Monthly Notices of the Royal Astronomical Society*, 321(4):699–712, 03 2001. ISSN 0035-8711. doi: 10.1046/j.1365-8711.2001.04050.x. URL `https://doi.org/10.1046/j.1365-8711.2001.04050.x`. 7.1, 7.2.3

J. M. D. Kruijssen. On the fraction of star formation occurring in bound stellar clusters. MNRAS, 426:3008–3040, November 2012. doi: 10.1111/j.1365-2966.2012.21923.x. (document), 2.5.4, 6.1, 7.1, 7.1, 7.5.2, 7.5.2, 7.5.2, 7.6

J. M. D. Kruijssen. The Current State of Cluster Formation Simulations. *ArXiv e-prints*, April 2013. 3.1

J. M. D. Kruijssen, T. Maschberger, N. Moeckel, C. J. Clarke, N. Bastian, and I. A. Bonnell. The dynamical state of stellar structure in star-forming regions. MNRAS, 419:841–853, January 2012a. doi: 10.1111/j.1365-2966.2011.19748.x. 2.5.4

J. M. Diederik Kruijssen. Globular cluster formation in the context of galaxy formation and evolution. *Classical and Quantum Gravity*, 31(24):244006, Dec 2014. doi: 10.1088/0264-9381/31/24/244006. 7.5.2

J. M. Diederik Kruijssen, Thomas Maschberger, Nickolas Moeckel, Cathie J. Clarke, Nate Bastian, and Ian A. Bonnell. The dynamical state of stellar structure in star-forming regions. MNRAS, 419(1):841–853, Jan 2012b. doi: 10.1111/j.1365-2966.2011.19748.x. 7.1, 7.5.2, 7.5.2

M. R. Krumholz. The big problems in star formation: The star formation rate, stellar clustering, and the initial mass function. Phys. Rep., 539:49–134, June 2014. doi: 10.1016/j.physrep.2014.02.001. 3, 7, 5.5.3

M. R. Krumholz. Resolution requirements and resolution problems in simulations of radiative feedback in dusty gas. MNRAS, 480:3468–3482, November 2018. doi: 10.1093/mnras/sty2105. 1, 6.1, 6.2.3, 6.4

M. R. Krumholz and N. Y. Gnedin. A Comparison of Methods for Determining the Molecular Content of Model Galaxies. ApJ, 729:36–+, March 2011. doi: 10.1088/0004-637X/729/1/36. 2.3.1, 5.2.2, 5.4.2

M. R. Krumholz and C. F. McKee. A General Theory of Turbulence-regulated Star Formation, from Spirals to Ultraluminous Infrared Galaxies. ApJ, 630:250–268, September 2005. doi: 10.1086/431734. 1.1, 2.5.2, 5.1, 5.2, 5.6.2, 7.5.2

M. R. Krumholz and J. C. Tan. Slow Star Formation in Dense Gas: Evidence and Implications. ApJ, 654:304–315, January 2007. doi: 10.1086/509101. 2.2.1, 2.5.2, 5.5.1

M. R. Krumholz and T. A. Thompson. Direct Numerical Simulation of Radiation Pressure-driven Turbulence and Winds in Star Clusters and Galactic Disks. ApJ, 760:155, December 2012a. doi: 10.1088/0004-637X/760/2/155. 1, 5.5.3

M. R. Krumholz and T. A. Thompson. Direct Numerical Simulation of Radiation Pressure-driven Turbulence and Winds in Star Clusters and Galactic Disks. ApJ, 760:155, December 2012b. doi: 10.1088/0004-637X/760/2/155. 2.5.7

M. R. Krumholz and T. A. Thompson. Numerical simulations of radiatively driven dusty winds. MNRAS, 434:2329–2346, September 2013. doi: 10.1093/mnras/stt1174. 2.5.7

M. R. Krumholz, C. D. Matzner, and C. F. McKee. The Global Evolution of Giant Molecular Clouds. I. Model Formulation and Quasi-Equilibrium Behavior. ApJ, 653:361–382, December 2006. doi: 10.1086/508679. 5.1, 5.7, 7.1

M. R. Krumholz, R. I. Klein, C. F. McKee, S. S. R. Offner, and A. J. Cunningham. The Formation of Massive Star Systems by Accretion. *Science*, 323:754, February 2009. doi: 10.1126/science.1165857. 5.3.3

M. R. Krumholz, R. I. Klein, and C. F. McKee. Radiation-hydrodynamic Simulations of the Formation of Orion-like Star Clusters. I. Implications for the Origin of the Initial Mass Function. ApJ, 740:74, October 2011. doi: 10.1088/0004-637X/740/2/74. 1.2, 2, 6.1

M. R. Krumholz, A. Dekel, and C. F. McKee. A Universal, Local Star Formation Law in Galactic Clouds, nearby Galaxies, High-redshift Disks, and Starbursts. ApJ, 745:69, January 2012a. doi: 10.1088/0004-637X/745/1/69. 1.1, 2.4.1, 2.5.2, 4.2.3, 5.2

M. R. Krumholz, R. I. Klein, and C. F. McKee. Radiation-hydrodynamic Simulations of the Formation of Orion-like Star Clusters. II. The Initial Mass Function from Winds, Turbulence, and Radiation. ApJ, 754:71, July 2012b. doi: 10.1088/0004-637X/754/1/71. 5.3.1

M. R. Krumholz, M. R. Bate, H. G. Arce, J. E. Dale, R. Gutermuth, R. I. Klein, Z.-Y. Li, F. Nakamura, and Q. Zhang. Star Cluster Formation and Feedback. *Protostars and Planets VI*, pages 243–266, 2014. doi: 10.2458/azu_uapress_9780816531240-ch011. 3.1, 4.1, 5.1, 6.1

Mark R. Krumholz. ON THE ORIGIN OF STELLAR MASSES. *The Astrophysical Journal*, 743(2):110, nov 2011. doi: 10.1088/0004-637x/743/2/110. 1.4, 7.6

Mark R. Krumholz, Christopher F. McKee, and Joss Bland -Hawthorn. Star Clusters Across Cosmic Time. *arXiv e-prints*, art. arXiv:1812.01615, Dec 2018. 1.2, 7.1, 7.7, 7.4, 7.5.1, 7.6

R.-P. Kudritzki and J. Puls. Winds from Hot Stars. ARA&A, 38:613–666, 2000. doi: 10.1146/annurev.astro.38.1.613. 1.2

M. A. Kuhn, L. A. Hillenbrand, A. Sills, E. D. Feigelson, and K. V. Getman. Kinematics in Young Star Clusters and Associations with Gaia DR2. ApJ, 870: 32, January 2019. doi: 10.3847/1538-4357/aaef8c. 1.4, 1

Michael A. Kuhn, Eric D. Feigelson, Konstantin V. Getman, Adrian J. Baddeley, Patrick S. Broos, Alison Sills, Matthew R. Bate, Matthew S. Povich, Kevin L. Luhman, Heather A. Busk, Tim Naylor, and Robert R. King. The Spatial Structure of Young Stellar Clusters. I. Subclusters. ApJ, 787(2):107, Jun 2014. doi: 10.1088/0004-637X/787/2/107. 7.2.3, 7.1

C. J. Lada and E. A. Lada. Embedded Clusters in Molecular Clouds. ARA&A, 41: 57–115, 2003. doi: 10.1146/annurev.astro.41.011802.094844. 2.5.1, 3.1, 7.1

C. J. Lada, M. Margulis, and D. Dearborn. The formation and early dynamical evolution of bound stellar systems. ApJ, 285:141–152, October 1984. doi: 10.1086/162485. 2.5.4, 3.1, 5.2, 7.2.3

C. J. Lada, M. Lombardi, and J. F. Alves. On the Star Formation Rates in Molecular Clouds. ApJ, 724:687–693, November 2010. doi: 10.1088/0004-637X/724/1/687. (document), 3.1, 5.1, 5.2.2, 5.1, 5.5.1, 5.5.1, 5.7

Charles J. Lada and Elizabeth A. Lada. The nature, origin and evolution of embedded star clusters. In Kenneth Janes, editor, *The Formation and Evolution of Star Clusters*, volume 13 of *Astronomical Society of the Pacific Conference Series*, pages 3–22, Jan 1991. 7.1

Siu Kwan Lam, Antoine Pitrou, and Stanley Seibert. Numba: A llvm-based python jit compiler. In *Proceedings of the Second Workshop on the LLVM Compiler Infrastructure in HPC*, LLVM '15, pages 7:1–7:6, New York, NY, USA, 2015. ACM. ISBN 978-1-4503-4005-2. doi: 10.1145/2833157.2833162. URL `http://doi.acm.org/10.1145/2833157.2833162`. 6.4

R. B. Larson. Numerical calculations of the dynamics of collapsing proto-star. MNRAS, 145:271, 1969. doi: 10.1093/mnras/145.3.271. 2.5.1

R. B. Larson. Turbulence and star formation in molecular clouds. MNRAS, 194: 809–826, March 1981. 1.1, 2.2.2, 2.5.1, 2.5.1, 2.5.4, 3.4.2, 4.1, 5.1, 5.4.2

T. R. Lauer et al. The Centers of Early-Type Galaxies with Hubble Space Telescope. VI. Bimodal Central Surface Brightness Profiles. ApJ, 664:226–256, July 2007. doi: 10.1086/519229. 4.2

E. J. Lee, N. Murray, and M. Rahman. Milky Way Star-forming Complexes and the Turbulent Motion of the Galaxy's Molecular Gas. ApJ, 752:146, June 2012. doi: 10.1088/0004-637X/752/2/146. 5.2.1

E. J. Lee, P. Chang, and N. Murray. Time-varying Dynamical Star Formation Rate. ApJ, 800:49, February 2015. doi: 10.1088/0004-637X/800/1/49. 2.5.3, 5.1, 5.2, 5.4.1, 5.7, 7.2.3

E. J. Lee, M.-A. Miville-Deschenes, and N. W. Murray. Observational Evidence of Dynamic Star Formation Rate in Milky Way Giant Molecular Clouds. ApJ, 833: 229, December 2016. doi: 10.3847/1538-4357/833/2/229. 1.1, 2.1, 2.2.1, 2.2.2, 2.4.3, 2.5.1, 2.5.1, 2.5.2, 3.1, 5.1, 5.2, 5.2.1, 5.2.3, 5.4, 5.4.2, 5.4.2, 5.4.2, 5.4.2, 5.4.3, 5.4.3, 5.6.2, 5.7, 7.1, 7.2.2, 7.2.3

C. Leitherer et al. Starburst99: Synthesis Models for Galaxies with Active Star Formation. ApJS, 123:3–40, July 1999. doi: 10.1086/313233. 1.2, 6.2.3, 7.2.1

A. K. Leroy, A. D. Bolatto, E. C. Ostriker, F. Walter, M. Gorski, A. Ginsburg, N. Krieger, R. C. Levy, D. S. Meier, E. Mills, J. Ott, E. Rosolowsky, T. A. Thompson, S. Veilleux, and L. K. Zschaechner. Forming Super Star Clusters in the Central Starburst of NGC 253. ApJ, 869:126, December 2018. doi: 10.3847/1538-4357/aaecd1. 7.7

H. Li, O. Y. Gnedin, and N. Y. Gnedin. Star Cluster Formation in Cosmological Simulations. II. Effects of Star Formation Efficiency and Stellar Feedback. ApJ, 861:107, July 2018. doi: 10.3847/1538-4357/aac9b8. 7.5.3

Hui Li, Mark Vogelsberger, Federico Marinacci, and Oleg Y. Gnedin. Disruption of giant molecular clouds and formation of bound star clusters under the influence of momentum stellar feedback. *arXiv e-prints*, art. arXiv:1904.11987, Apr 2019. 7.2.3, 7.2.3, 7.5.2, 7.5.3, 7.6

M. Lombardi. NICEST, a near-infrared color excess method tailored to small-scale structures. A&A, 493:735–745, January 2009. doi: 10.1051/0004-6361:200810519. 5.5.1

M. Lombardi, H. Bouy, J. Alves, and C. J. Lada. Herschel-Planck dust optical-depth and column-density maps. I. Method description and results for Orion. A&A, 566:A45, June 2014. doi: 10.1051/0004-6361/201323293. 5.2

J. R. Lu, A. M. Ghez, S. D. Hornstein, M. R. Morris, E. E. Becklin, and K. Matthews. A Disk of Young Stars at the Galactic Center as Determined by Individual Stellar Orbits. ApJ, 690:1463–1487, January 2009. doi: 10.1088/0004-637X/690/2/1463. 4.2

R. H. Lupton, S. M. Fall, K. C. Freeman, and R. A. W. Elson. The internal velocity dispersions of three young star clusters in the Large Magellanic Cloud. ApJ, 347:201–213, December 1989. doi: 10.1086/168110. 3.B

D. Lynden-Bell. Statistical mechanics of violent relaxation in stellar systems. MNRAS, 136:101–+, 1967. URL `http://adsabs.harvard.edu/cgi-bin/nph-bib_query?bibcode=1967MNRAS.136..101L&db_key=AST`. 3.3, 3.5.2

D. Lynden-Bell and P. P. Eggleton. On the consequences of the gravothermal catastrophe. MNRAS, 191:483–498, May 1980. doi: 10.1093/mnras/191.3.483. 3.2

M.-M. Mac Low and R. S. Klessen. Control of star formation by supersonic turbulence. *Reviews of Modern Physics*, 76:125–194, January 2004. doi: 10.1103/RevModPhys.76.125. 1.1, 3.1

A. D. Mackey and G. F. Gilmore. Surface brightness profiles and structural parameters for 53 rich stellar clusters in the Large Magellanic Cloud. MNRAS, 338: 85–119, January 2003a. doi: 10.1046/j.1365-8711.2003.06021.x. 3.1, 3.2, 3.1, 3.6

A. D. Mackey and G. F. Gilmore. Surface brightness profiles and structural parameters for 10 rich stellar clusters in the Small Magellanic Cloud. MNRAS, 338: 120–130, January 2003b. doi: 10.1046/j.1365-8711.2003.06022.x. 3.1, 3.2, 3.1, 3.6

D. Martizzi, C.-A. Faucher-Giguère, and E. Quataert. Supernova feedback in an inhomogeneous interstellar medium. MNRAS, 450:504–522, June 2015. doi: 10.1093/mnras/stv562. 2.3.1

R. D. Mathieu. Dynamical constraints on star formation efficiency. ApJ, 267: L97–L101, April 1983. doi: 10.1086/184011. 2.1, 2.5.4, 3.1, 5.2, 7.1, 7.2.3

C. D. Matzner and C. F. McKee. Efficiencies of Low-Mass Star and Star Cluster Formation. ApJ, 545:364–378, December 2000. doi: 10.1086/317785. 1.2

Christopher D. Matzner and Peter H. Jumper. Star Cluster Formation with Stellar Feedback and Large-scale Inflow. ApJ, 815(1):68, Dec 2015. doi: 10.1088/0004-637X/815/1/68. 1.2

L. Mayer, S. Kazantzidis, A. Escala, and S. Callegari. Direct formation of supermassive black holes via multi-scale gas inflows in galaxy mergers. Nature, 466: 1082–1084, August 2010. doi: 10.1038/nature09294. 2.5.6

L. Mayer, D. Fiacconi, S. Bonoli, T. Quinn, R. Roškar, S. Shen, and J. Wadsley. Direct Formation of Supermassive Black Holes in Metal-enriched Gas at the Heart of High-redshift Galaxy Mergers. ApJ, 810:51, September 2015. doi: 10.1088/0004-637X/810/1/51. 2.5.6

N. McCrady and J. R. Graham. Super Star Cluster Velocity Dispersions and Virial Masses in the M82 Nuclear Starburst. ApJ, 663:844–856, July 2007. doi: 10.1086/518357. 2.1, 2.5.4, 4.1, 4.1, 4.2, 7.7, 7.2.3

T. A. McGlynn. Dissipationless collapse of galaxies and initial conditions. ApJ, 281:13–30, June 1984a. doi: 10.1086/162072. 3.2

T. A. McGlynn. Dissipationless collapse of galaxies and initial conditions. ApJ, 281:13–30, June 1984b. doi: 10.1086/162072. 3.5.4

C. F. McKee and E. C. Ostriker. Theory of Star Formation. ARA&A, 45:565–687, September 2007. doi: 10.1146/annurev.astro.45.051806.110602. 3.1, 3.1, 5.1, 6.1, 7.1

C. F. McKee and J. C. Tan. The Formation of Massive Stars from Turbulent Cores. ApJ, 585:850–871, March 2003. doi: 10.1086/346149. 5.1

C. F. McKee and J. P. Williams. The Luminosity Function of OB Associations in the Galaxy. ApJ, 476:144–165, February 1997. doi: 10.1086/303587. 5.2.1

D. Merritt, S. Tremaine, and D. Johnstone. Models of violently relaxed galaxies. MNRAS, 236:829–841, February 1989. doi: 10.1093/mnras/236.4.829. 3.2

M. Messa, A. Adamo, D. Calzetti, M. Reina-Campos, D. Colombo, E. Schinnerer, R. Chandar, D. A. Dale, D. A. Gouliermis, K. Grasha, E. K. Grebel, B. G. Elmegreen, M. Fumagalli, K. E. Johnson, J. M. D. Kruijssen, G. Östlin, F. Shabani, L. J. Smith, and B. C. Whitmore. The young star cluster population of M51 with LEGUS - II. Testing environmental dependences. MNRAS, 477:1683–1707, June 2018. doi: 10.1093/mnras/sty577. 7.1

L. Mestel and L. Spitzer, Jr. Star formation in magnetic dust clouds. MNRAS, 116: 503, 1956. doi: 10.1093/mnras/116.5.503. 1.1

M.-A. Miville-Deschenes, N. Murray, and E. J. Lee. Physical Properties of Molecular Clouds for the Entire Milky Way Disk. ApJ, 834:57, January 2017. doi: 10.3847/1538-4357/834/1/57. 5.3.1, 5.4.2, 5.4.3, 7.1, 7.2.2

T. J. Mooney and P. M. Solomon. Star formation rates and the far-infrared luminosity of Galactic molecular clouds. ApJ, 334:L51–L54, November 1988. doi: 10.1086/185310. 3.1, 5.1

H. Mouri and Y. Taniguchi. Runaway Merging of Black Holes: Analytical Constraint on the Timescale. ApJ, 566:L17–L20, February 2002. doi: 10.1086/339472. 2.5.4

D. W. Murray, P. Chang, N. W. Murray, and J. Pittman. Collapse in self-gravitating turbulent fluids. MNRAS, 465:1316–1335, February 2017. doi: 10.1093/mnras/stw2796. 5.1, 5.2, 5.4.1, 5.7

N. Murray. Star Formation Efficiencies and Lifetimes of Giant Molecular Clouds in the Milky Way. ApJ, 729:133–+, March 2011. doi: 10.1088/0004-637X/729/2/133. 1.1, 2.1, 2.2.1, 2.2.2, 2.4.3, 2.5.1, 3.1, 5.1, 5.2.1, 5.4, 5.4.2, 5.4.2, 5.7, 7.2.2, 7.2.3

N. Murray and P. Chang. Star Formation in Self-gravitating Turbulent Fluids. ApJ, 804:44, May 2015. doi: 10.1088/0004-637X/804/1/44. 5.1, 5.4.1, 5.7, 7.2.3

N. Murray and M. Rahman. Star Formation in Massive Clusters Via the Wilkinson Microwave Anisotropy Probe and the Spitzer Glimpse Survey. ApJ, 709:424–435, January 2010. doi: 10.1088/0004-637X/709/1/424. 5.2.1

N. Murray, E. Quataert, and T. A. Thompson. The Disruption of Giant Molecular Clouds by Radiation Pressure and the Efficiency of Star Formation in Galaxies. ApJ, 709:191–209, January 2010. doi: 10.1088/0004-637X/709/1/191. 1.2, 2.1, 2.2.2, 2.5.7, 2.6, 3.1, 3.3, 4.1, 4.1, 5.1, 6.1, 6.4, 7.1, 7.6

A. T. Myers, R. I. Klein, M. R. Krumholz, and C. F. McKee. Star cluster formation in turbulent, magnetized dense clumps with radiative and outflow feedback. MNRAS, 439:3420–3438, April 2014a. doi: 10.1093/mnras/stu190. 2, 5.1

A. T. Myers, R. I. Klein, M. R. Krumholz, and C. F. McKee. Star cluster formation in turbulent, magnetized dense clumps with radiative and outflow feedback. MNRAS, 439:3420–3438, April 2014b. doi: 10.1093/mnras/stu190. 5.5.3

P. C. Myers, T. M. Dame, P. Thaddeus, R. S. Cohen, R. F. Silverberg, E. Dwek, and M. G. Hauser. Molecular clouds and star formation in the inner galaxy - A comparison of CO, H II, and far-infrared surveys. ApJ, 301:398–422, February 1986. doi: 10.1086/163909. 1.1, 3.1, 5.1, 5.2, 5.2.1, 7.1

T. Naab and J. P. Ostriker. Theoretical Challenges in Galaxy Formation. ARA&A, 55:59–109, August 2017. doi: 10.1146/annurev-astro-081913-040019. 1.2, 6.1

J. F. Navarro, C. S. Frenk, and S. D. M. White. The Structure of Cold Dark Matter Halos. ApJ, 462:563–+, May 1996. doi: 10.1086/177173. 3.5.4

Å. K. Nordlund and P. Padoan. The Density PDFs of Supersonic Random Flows. In J. Franco and A. Carraminana, editors, *Interstellar Turbulence*, page 218, 1999. 1.1, 2.2.1

M. A. Norris, S. J. Kannappan, D. A. Forbes, A. J. Romanowsky, J. P. Brodie, F. R. Faifer, A. Huxor, C. Maraston, A. J. Moffett, S. J. Penny, V. Pota, A. Smith-Castelli, J. Strader, D. Bradley, K. D. Eckert, D. Fohring, J. McBride, D. V. Stark, and O. Vaduvescu. The AIMSS Project - I. Bridging the star cluster-galaxy divide. MNRAS, 443:1151–1172, September 2014. doi: 10.1093/mnras/stu1186. 4.1, 4.1

B. B. Ochsendorf, M. Meixner, J. Roman-Duval, M. Rahman, and N. J. Evans, II. What Sets the Massive Star Formation Rates and Efficiencies of Giant Molecular Clouds? ApJ, 841:109, June 2017. doi: 10.3847/1538-4357/aa704a. 5.1, 5.4.2

S. S. R. Offner and J. Chaban. Impact of Protostellar Outflows on Turbulence and Star Formation Efficiency in Magnetized Dense Cores. ApJ, 847:104, October 2017. doi: 10.3847/1538-4357/aa8996. 1.2

S. S. R. Offner, P. C. Clark, P. Hennebelle, N. Bastian, M. R. Bate, P. F. Hopkins, E. Moraux, and A. P. Whitworth. The Origin and Universality of the Stellar Initial Mass Function. *Protostars and Planets VI*, pages 53–75, 2014. doi: 10.2458/azu_uapress_9780816531240-ch003. 1.2, 5.7, 6.2.3

A. Onus, M. R. Krumholz, and C. Federrath. Numerical calibration of the HCN-star formation correlation. MNRAS, 479:1702–1710, September 2018. doi: 10.1093/mnras/sty1662. 5.5.1

M. E. Orr, C. C. Hayward, P. F. Hopkins, T. K. Chan, C.-A. Faucher-Giguère, R. Feldmann, D. Kereš, N. Murray, and E. Quataert. What FIREs up star formation: the emergence of the Kennicutt-Schmidt law from feedback. MNRAS, 478: 3653–3673, August 2018a. doi: 10.1093/mnras/sty1241. 2.1, 2.5.2, 4.1

M. E. Orr, C. C. Hayward, P. F. Hopkins, T. K. Chan, C.-A. Faucher-Giguère, R. Feldmann, D. Kereš, N. Murray, and E. Quataert. What FIREs up star formation: the emergence of the Kennicutt-Schmidt law from feedback. MNRAS, 478: 3653–3673, August 2018b. doi: 10.1093/mnras/sty1241. 5.2, 5.4.4, 6.4

Matthew E. Orr, Christopher C. Hayward, and Philip F. Hopkins. A Simple Non-equilibrium Feedback Model for Galaxy-Scale Star Formation: Delayed Feedback and SFR Scatter. *arXiv e-prints*, art. arXiv:1810.09460, Oct 2018c. 7.5.2

E. C. Ostriker and R. Shetty. Maximally Star-forming Galactic Disks. I. Starburst Regulation Via Feedback-driven Turbulence. ApJ, 731:41, April 2011. doi: 10.1088/0004-637X/731/1/41. 2.1, 2.3.1, 4.1, 5.2, 5.4.4

P. Padoan and Å. Nordlund. The Star Formation Rate of Supersonic Magnetohydrodynamic Turbulence. ApJ, 730:40, March 2011. doi: 10.1088/0004-637X/730/1/40. 1.1, 5.1, 5.2, 5.6.2

P. Padoan, A. Nordlund, and B. J. T. Jones. The universality of the stellar initial mass function. MNRAS, 288:145–152, June 1997. 1.1, 2.2.1

P. Padoan, T. Haugbølle, and Å. Nordlund. A Simple Law of Star Formation. ApJ, 759:L27, November 2012. doi: 10.1088/2041-8205/759/2/L27. 1.1, 2.5.3, 5.2, 5.4.3, 5.7

Ruediger Pakmor, Andreas Bauer, and Volker Springel. Magnetohydrodynamics on an unstructured moving grid. MNRAS, 418(2):1392–1401, Dec 2011. doi: 10.1111/j.1365-2966.2011.19591.x. 1.4

F. Palla and S. W. Stahler. Accelerating Star Formation in Clusters and Associations. ApJ, 540:255–270, September 2000. doi: 10.1086/309312. 1.1, 5.1

G. Parmentier, S. P. Goodwin, P. Kroupa, and H. Baumgardt. The Shape of the Initial Cluster Mass Function: What It Tells Us about the Local Star Formation Efficiency. ApJ, 678:347–352, May 2008. doi: 10.1086/587137. 3.1

R. Parra, J. E. Conway, P. J. Diamond, H. Thrall, C. J. Lonsdale, C. J. Lonsdale, and H. E. Smith. The Radio Spectra of the Compact Sources in Arp 220: A Mixed Population of Supernovae and Supernova Remnants. ApJ, 659:314–330, April 2007. doi: 10.1086/511813. 2.5.2

F. R. Pearce, P. A. Thomas, and H. M. P. Couchman. Mergers of Collisionless Systems. MNRAS, 264:497, September 1993. doi: 10.1093/mnras/264.2.497. 3.5.4

M. V. Penston. Dynamics of self-gravitating gaseous spheres-III. Analytical results in the free-fall of isothermal cases. MNRAS, 144:425, 1969. doi: 10.1093/mnras/144.4.425. 2.5.1

Fernando Pérez and Brian E. Granger. IPython: a system for interactive scientific computing. *Computing in Science and Engineering*, 9(3):21–29, May 2007. ISSN 1521-9615. doi: 10.1109/MCSE.2007.53. URL `https://ipython.org`. 5.7, 6.4, 7.6

J. Pfeffer, J. M. D. Kruijssen, R. A. Crain, and N. Bastian. The E-MOSAICS project: simulating the formation and co-evolution of galaxies and their star cluster populations. MNRAS, 475:4309–4346, April 2018. doi: 10.1093/mnras/stx3124. 7.1

H. C. Plummer. On the problem of distribution in globular star clusters. MNRAS, 71:460–470, March 1911. doi: 10.1093/mnras/71.5.460. 3.2, 3.3.2, 3.5.3, 3.6, 3.B

S. F. Portegies Zwart and S. L. W. McMillan. The Runaway Growth of Intermediate-Mass Black Holes in Dense Star Clusters. ApJ, 576:899–907, September 2002. doi: 10.1086/341798. 2.5.4, 3.5.3

S. F. Portegies Zwart, S. L. W. McMillan, and M. Gieles. Young Massive Star Clusters. ARA&A, 48:431–493, September 2010a. doi: 10.1146/annurev-astro-081309-130834. 2.5.4, 3.1, 3.1, 1, 3.2, 3.5.3

S. F. Portegies Zwart, S. L. W. McMillan, and M. Gieles. Young Massive Star Clusters. ARA&A, 48:431–493, September 2010b. doi: 10.1146/annurev-astro-081309-130834. 4.1

D. J. Price and M. R. Bate. The effect of magnetic fields on star cluster formation. MNRAS, 385:1820–1834, April 2008. doi: 10.1111/j.1365-2966.2008.12976.x. 6.1

R. R. Rafikov. Convective Cooling and Fragmentation of Gravitationally Unstable Disks. ApJ, 662:642–650, June 2007. doi: 10.1086/517599. 2.3.1, 2.4.1, 2.5.6

S. Raskutti, E. C. Ostriker, and M. A. Skinner. Numerical Simulations of Turbulent Molecular Clouds Regulated by Radiation Feedback Forces. I. Star Formation Rate and Efficiency. ApJ, 829:130, October 2016. doi: 10.3847/0004-637X/829/2/130. 1, 2.5.3, 8, 2.A.2, 4.1, 5.1, 5.4.1, 5.7, 6.1, 7.5.3

M. J. Rees. Opacity-limited hierarchical fragmentation and the masses of protostars. MNRAS, 176:483–486, September 1976. doi: 10.1093/mnras/176.3.483. 2.4.1

Marta Reina-Campos and J. M. Diederik Kruijssen. A unified model for the maximum mass scales of molecular clouds, stellar clusters and high-redshift clumps. MNRAS, 469(2):1282–1298, Aug 2017. doi: 10.1093/mnras/stx790. 7.5.1

M. Rejkuba, P. Dubath, D. Minniti, and G. Meylan. Bright globular clusters in NGC 5128: the missing link between young massive clusters and evolved massive objects. A&A, 469:147–162, July 2007. doi: 10.1051/0004-6361:20066493. 4.2

Thomas S. Rice, Alyssa A. Goodman, Edwin A. Bergin, Christopher Beaumont, and T. M. Dame. A Uniform Catalog of Molecular Clouds in the Milky Way. ApJ, 822(1):52, May 2016. doi: 10.3847/0004-637X/822/1/52. 7.2.2

A. J. Richings, J. Schaye, and B. D. Oppenheimer. Non-equilibrium chemistry and cooling in the diffuse interstellar medium - I. Optically thin regime. MNRAS, 440:3349–3369, June 2014a. doi: 10.1093/mnras/stu525. 2.3.1

A. J. Richings, J. Schaye, and B. D. Oppenheimer. Non-equilibrium chemistry and cooling in the diffuse interstellar medium - II. Shielded gas. MNRAS, 442: 2780–2796, August 2014b. doi: 10.1093/mnras/stu1046. 2.3.1

C. L. Rodriguez, M. Morscher, B. Pattabiraman, S. Chatterjee, C.-J. Haster, and F. A. Rasio. Binary Black Hole Mergers from Globular Clusters: Implications for Advanced LIGO. *Physical Review Letters*, 115(5):051101, July 2015. doi: 10.1103/PhysRevLett.115.051101. 2.5.4, 3.5.3

C. L. Rodriguez, S. Chatterjee, and F. A. Rasio. Binary black hole mergers from globular clusters: Masses, merger rates, and the impact of stellar evolution. Phys. Rev. D, 93(8):084029, April 2016. doi: 10.1103/PhysRevD.93.084029. 2.5.4, 3.5.3

H. Rogers and J. M. Pittard. Feedback from winds and supernovae in massive stellar clusters - I. Hydrodynamics. MNRAS, 431:1337–1351, May 2013. doi: 10.1093/mnras/stt255. 1.2

J. Rosdahl and R. Teyssier. A scheme for radiation pressure and photon diffusion with the M1 closure in RAMSES-RT. MNRAS, 449:4380–4403, June 2015. doi: 10.1093/mnras/stv567. 2.5.7, 6.1, 7.2.1

A. L. Rosen, L. A. Lopez, M. R. Krumholz, and E. Ramirez-Ruiz. Gone with the wind: Where is the missing stellar wind energy from massive star clusters? MNRAS, 442:2701–2716, August 2014. doi: 10.1093/mnras/stu1037. 7.2.3

A. L. Rosen, M. R. Krumholz, C. F. McKee, and R. I. Klein. An unstable truth: how massive stars get their mass. MNRAS, 463:2553–2573, December 2016. doi: 10.1093/mnras/stw2153. 5.3.3

E. W. Rosolowsky, J. E. Pineda, J. Kauffmann, and A. A. Goodman. Structural Analysis of Molecular Clouds: Dendrograms. ApJ, 679:1338–1351, June 2008. doi: 10.1086/587685. 5.7

J. E. Ryon, N. Bastian, A. Adamo, I. S. Konstantopoulos, J. S. Gallagher, S. Larsen, K. Hollyhead, E. Silva-Villa, and L. J. Smith. Sizes and shapes of young star cluster light profiles in M83. MNRAS, 452:525–539, September 2015. doi: 10.1093/mnras/stv1282. 2.5.4, 3.1, 3.2, 3.1, 3.2, 3.2.1, 3.6, 4.1, 4, 7.7, 7.3, 7.4

J. E. Ryon, J. S. Gallagher, L. J. Smith, A. Adamo, D. Calzetti, S. N. Bright, M. Cignoni, D. O. Cook, D. A. Dale, B. E. Elmegreen, M. Fumagalli, D. A. Gouliermis, K. Grasha, E. K. Grebel, H. Kim, M. Messa, D. Thilker, and L. Ubeda. Effective Radii of Young, Massive Star Clusters in Two LEGUS Galaxies. ApJ, 841:92, June 2017. doi: 10.3847/1538-4357/aa719e. 3.2, 3.1, 3.6, 7.7

T. R. Saitoh, H. Daisaka, E. Kokubo, J. Makino, T. Okamoto, K. Tomisaka, K. Wada, and N. Yoshida. Toward First-Principle Simulations of Galaxy Formation: I. How Should We Choose Star-Formation Criteria in High-Resolution Simulations of Disk Galaxies? PASJ, 60:667–, August 2008. 2.3.1

A. Scally and C. Clarke. Primordial substructure in the Orion Nebula Cluster. MNRAS, 334:156–166, July 2002. doi: 10.1046/j.1365-8711.2002.05503.x. 3.2.1

M. Schmidt. The Rate of Star Formation. ApJ, 129:243, March 1959. doi: 10.1086/146614. 1.1

N. Schneider, S. Bontemps, P. Girichidis, T. Rayner, F. Motte, P. André, D. Russeil, A. Abergel, L. Anderson, D. Arzoumanian, M. Benedettini, T. Csengeri, P. Didelon, J. Di Francesco, M. Griffin, T. Hill, R. S. Klessen, V. Ossenkopf, S. Pezzuto, A. Rivera-Ingraham, L. Spinoglio, P. Tremblin, and A. Zavagno. Detection of two power-law tails in the probability distribution functions of massive GMCs. MNRAS, 453:L41–L45, November 2015a. doi: 10.1093/mnrasl/slv101. 5.2

N. Schneider, T. Csengeri, R. S. Klessen, P. Tremblin, V. Ossenkopf, N. Peretto, R. Simon, S. Bontemps, and C. Federrath. Understanding star formation in molecular clouds. II. Signatures of gravitational collapse of IRDCs. A&A, 578: A29, June 2015b. doi: 10.1051/0004-6361/201424375. 5.2

F. Schweizer and P. Seitzer. Remnant of a “Wet” Merger: NGC 34 and Its Young Massive Clusters, Young Stellar Disk, and Strong Gaseous Outflow. AJ, 133: 2132–2155, May 2007. doi: 10.1086/513317. 4.1

N. Scoville, L. Murchikova, F. Walter, C. Vlahakis, J. Koda, P. Vanden Bout, J. Barnes, L. Hernquist, K. Sheth, M. Yun, D. Sanders, L. Armus, P. Cox, T. Thompson, B. Robertson, L. Zschaechner, L. Tacconi, P. Torrey, C. C. Hayward, R. Genzel, P. F. Hopkins, P. van der Werf, and R. Decarli. ALMA Resolves the Nuclear Disks of Arp 220. ApJ, 836:66, February 2017. doi: 10.3847/1538-4357/836/1/66. 2.5.2

N. Z. Scoville and J. C. Good. The far-infrared luminosity of molecular clouds in the Galaxy. ApJ, 339:149–162, April 1989. doi: 10.1086/167283. 5.1

S. Shen, H. J. Mo, S. D. M. White, M. R. Blanton, G. Kauffmann, W. Voges, J. Brinkmann, and I. Csabai. The size distribution of galaxies in the Sloan Digital Sky Survey. MNRAS, 343:978–994, August 2003. doi: 10.1046/j.1365-8711.2003.06740.x. 3.3.2

F. H. Shu. Self-similar collapse of isothermal spheres and star formation. ApJ, 214: 488–497, June 1977. doi: 10.1086/155274. 1.1

F. H. Shu, F. C. Adams, and S. Lizano. Star formation in molecular clouds - Observation and theory. ARA&A, 25:23–81, 1987. doi: 10.1146/annurev.aa.25.090187.000323. 5.1

M. A. Skinner and E. C. Ostriker. A Two-moment Radiation Hydrodynamics Module in Athena Using a Time-explicit Godunov Method. ApJS, 206:21, June 2013. doi: 10.1088/0067-0049/206/2/21. 2.5.3, 6.1

M. A. Skinner and E. C. Ostriker. Numerical Simulations of Turbulent Molecular Clouds Regulated by Reprocessed Radiation Feedback from Nascent Super Star Clusters. ApJ, 809:187, August 2015. doi: 10.1088/0004-637X/809/2/187. 2.5.7, 4.3, 5.1, 5.5.3, 6.1

L. J. Smith and J. S. Gallagher. M82-F: a doomed super star cluster? MNRAS, 326: 1027–1040, September 2001. doi: 10.1046/j.1365-8711.2001.04627.x. 2.5.7

R. Smith, R. Slater, M. Fellhauer, S. Goodwin, and P. Assmann. Formation rates of star clusters in the hierarchical merging scenario. MNRAS, 416:383–390, September 2011. doi: 10.1111/j.1365-2966.2011.19039.x. 9

R. Smith, S. Goodwin, M. Fellhauer, and P. Assmann. Infant mortality in the hierarchical merging scenario: dependence on gas expulsion time-scales. MNRAS, 428:1303–1311, January 2013. doi: 10.1093/mnras/sts106. 9

P. M. Solomon, A. R. Rivolo, J. Barrett, and A. Yahil. Mass, luminosity, and line width relations of Galactic molecular clouds. ApJ, 319:730–741, August 1987. doi: 10.1086/165493. 2.2.2, 2.5.1, 2.5.4, 3.4.2, 5.1

M. C. Sormani, R. G. Treß, R. S. Klessen, and S. C. O. Glover. A simple method to convert sink particles into stars. MNRAS, 466:407–412, April 2017. doi: 10.1093/mnras/stw3205. 5.3.3, 6.2.3

L. Spitzer. *Physical processes in the interstellar medium*. 1978. doi: 10.1002/9783527617722. 1.2

L. Spitzer. *Dynamical evolution of globular clusters*. 1987. 3.2

L. Spitzer, Jr. and S. L. Shapiro. Random Gravitational Encounters and the Evolution of Spherical Systems. III. Halo. ApJ, 173:529, May 1972. doi: 10.1086/151442. 3.2

V. Springel. The cosmological simulation code GADGET-2. MNRAS, 364:1105–1134, December 2005. doi: 10.1111/j.1365-2966.2005.09655.x. 2.3, 3.4, 7.2.1

V. Springel and L. Hernquist. Cosmological smoothed particle hydrodynamics simulations: a hybrid multiphase model for star formation. MNRAS, 339:289–311, February 2003. doi: 10.1046/j.1365-8711.2003.06206.x. 2.3.1, 2.5.5

V. Springel, S. D. M. White, G. Tormen, and G. Kauffmann. Populating a cluster of galaxies - I. Results at [formmu2]z=0. MNRAS, 328:726–750, December 2001. doi: 10.1046/j.1365-8711.2001.04912.x. 7.2.1

Volker Springel. E pur si muove: Galilean-invariant cosmological hydrodynamical simulations on a moving mesh. MNRAS, 401:791–851, January 2010. doi: 10.1111/j.1365-2966.2009.15715.x. URL `http://adsabs.harvard.edu/cgi-bin/nph-data_query?bibcode=2009arXiv0901.4107S&link_type=ABSTRACT`. 2.3

J. M. Stone, T. A. Gardiner, P. Teuben, J. F. Hawley, and J. B. Simon. Athena: A New Code for Astrophysical MHD. ApJS, 178:137–177, September 2008. doi: 10.1086/588755. 2.3

James M. Stone, Eve C. Ostriker, and Charles F. Gammie. Dissipation in Compressible Magnetohydrodynamic Turbulence. ApJ, 508(1):L99–L102, Nov 1998. doi: 10.1086/311718. 1.1, 7.2.3

K.-Y. Su, P. F. Hopkins, C. C. Hayward, C.-A. Faucher-Giguere, D. Keres, X. Ma, and V. H. Robles. Feedback first: the surprisingly weak effects of magnetic fields, viscosity, conduction, and metal diffusion on galaxy formation. *ArXiv e-prints*, July 2016. 2.4.1

K.-Y. Su, P. F. Hopkins, C. C. Hayward, X. Ma, M. Boylan-Kolchin, D. Kasen, D. Kereš, C.-A. Faucher-Giguère, M. E. Orr, and C. Wheeler. Discrete effects in stellar feedback: Individual Supernovae, Hypernovae, and IMF Sampling in Dwarf Galaxies. MNRAS, 480:1666–1675, October 2018. doi: 10.1093/mnras/sty1928. 5.3.3, 5.7, 6.2.3, 6.2.3, 6.2.3, 6.4

J. C. Tan, M. R. Krumholz, and C. F. McKee. Equilibrium Star Cluster Formation. ApJ, 641:L121–L124, April 2006. doi: 10.1086/504150. 2.2.1

J. C. Tan, M. T. Beltrán, P. Caselli, F. Fontani, A. Fuente, M. R. Krumholz, C. F. McKee, and A. Stolte. Massive Star Formation. *Protostars and Planets VI*, pages 149–172, 2014. doi: 10.2458/azu_uapress_9780816531240-ch007. 5.3.3

J. E. Taylor and J. F. Navarro. The Phase-Space Density Profiles of Cold Dark Matter Halos. ApJ, 563:483–488, December 2001. doi: 10.1086/324031. 3.4.1

T. A. Thompson and M. R. Krumholz. Sub-Eddington star-forming regions are super-Eddington: momentum-driven outflows from supersonic turbulence. MNRAS, 455:334–342, January 2016. doi: 10.1093/mnras/stv2331. 2.2.2, 2.6, 4.1, 5.4.2

T. A. Thompson, E. Quataert, and N. Murray. Radiation Pressure-supported Starburst Disks and Active Galactic Nucleus Fueling. ApJ, 630:167–185, September 2005. doi: 10.1086/431923. 2.1, 2.3.1, 4.1, 5.2, 5.4.4

Paul Torrey, P. F. Hopkins, Claude-André Faucher-Giguère, Mark Vogelsberger, Eliot Quataert, Dušan Kereš, and Norman Murray. An instability of feedback-regulated star formation in galactic nuclei. MNRAS, 467(2):2301–2314, May 2017. doi: 10.1093/mnras/stx254. 2.1, 2.5.5

T. H. Troland and R. M. Crutcher. Magnetic Fields in Dark Cloud Cores: Arecibo OH Zeeman Observations. ApJ, 680:457-465, June 2008. doi: 10.1086/587546. 2.3.2

B. T.-H. Tsang and M. Milosavljević. Radiation pressure driving of a dusty atmosphere. MNRAS, 453:1108–1120, October 2015. doi: 10.1093/mnras/stv1707. 1, 2.5.7

B. Tsz-Ho Tsang and M. Milosavljevic. Radiation pressure in super star cluster formation. *ArXiv e-prints*, September 2017. 1, 2.5.3, 4.3, 5.5.3

A. V. Tutukov. Early Stages of Dynamical Evolution of Star Cluster Models. A&A, 70:57, November 1978. 2.1, 2.5.4, 3.1, 5.2, 7.2.3

J. Utreras, F. Becerra, and A. Escala. Unveiling the Role of Galactic Rotation on Star Formation. ApJ, 833:13, December 2016. doi: 10.3847/0004-637X/833/1/13. 2.5.2

T. S. van Albada. Dissipationless galaxy formation and the R to the 1/4-power law. MNRAS, 201:939–955, December 1982. doi: 10.1093/mnras/201.4.939. 3.2

A. van der Wel, M. Franx, P. G. van Dokkum, R. E. Skelton, I. G. Momcheva, K. E. Whitaker, G. B. Brammer, E. F. Bell, H.-W. Rix, S. Wuyts, H. C. Ferguson, B. P. Holden, G. Barro, A. M. Koekemoer, Y.-Y. Chang, E. J. McGrath, B. Häussler, A. Dekel, P. Behroozi, M. Fumagalli, J. Leja, B. F. Lundgren, M. V. Maseda, E. J. Nelson, D. A. Wake, S. G. Patel, I. Labbé, S. M. Faber, N. A. Grogin, and D. D. Kocevski. 3D-HST+CANDELS: The Evolution of the Galaxy Size-Mass Distribution since z = 3. ApJ, 788:28, June 2014. doi: 10.1088/0004-637X/788/1/28. 4.1, 4.3

E. Vazquez-Semadeni. Hierarchical Structure in Nearly Pressureless Flows as a Consequence of Self-similar Statistics. ApJ, 423:681–+, March 1994. doi: 10.1086/173847. 1.1, 2.2.1

E. Vazquez-Semadeni. Collapsing molecular clouds and their evolving star formation rate. *IAU General Assembly*, 22:2250878, August 2015. 5.1, 5.4.1

E. Vazquez-Semadeni, A. Gonzalez-Samaniego, and P. Colin. Hierarchical star cluster assembly in globally collapsing molecular clouds. MNRAS, 467:1313–1328, May 2017. doi: 10.1093/mnras/stw3229. 5.1, 5.7, 6.1

Enrique Vazquez-Semadeni, Pedro Colin, Gilberto C. Gomez, Javier Ballesteros-Paredes, and Alan W. Watson. Molecular cloud evolution. iii. accretion versus stellar feedback. *The Astrophysical Journal*, 715(2):1302, 2010. URL `http://stacks.iop.org/0004-637X/715/i=2/a=1302`. 5.1, 6.1

J. V. Villumsen. Simulations of galaxy mergers. MNRAS, 199:493–516, May 1982. doi: 10.1093/mnras/199.3.493. 3.5.4

J. S. Vink, A. de Koter, and H. J. G. L. M. Lamers. Mass-loss predictions for O and B stars as a function of metallicity. A&A, 369:574–588, April 2001. doi: 10.1051/0004-6361:20010127. 2.4.1

S. von Hoerner. Internal structure of globular clusters. ApJ, 125, March 1957. doi: 10.1086/146321. 3.2

N. Vutisalchavakul, N. J. Evans, II, and M. Heyer. Star Formation Relations in the Milky Way. ApJ, 831:73, November 2016. doi: 10.3847/0004-637X/831/1/73. 1.1, 2.1, 2.5.1, 2.5.1, 2.5.2, 5.1, 5.2, 5.2.1, 5.2.3, 5.4.2, 5.4.2, 5.4.3, 5.4.3

L. Wang, R. Spurzem, S. Aarseth, M. Giersz, A. Askar, P. Berczik, T. Naab, R. Schadow, and M. B. N. Kouwenhoven. The DRAGON simulations: globular cluster evolution with a million stars. MNRAS, 458:1450–1465, May 2016. doi: 10.1093/mnras/stw274. 3.5.3

Peng Wang, Zhi-Yun Li, Tom Abel, and Fumitaka Nakamura. Outflow Feedback Regulated Massive Star Formation in Parsec-Scale Cluster-Forming Clumps. ApJ, 709(1):27–41, Jan 2010. doi: 10.1088/0004-637X/709/1/27. 1.2

Jacob L. Ward and J. M. Diederik Kruijssen. Not all stars form in clusters - measuring the kinematics of OB associations with Gaia. MNRAS, 475(4):5659–5676, Apr 2018. doi: 10.1093/mnras/sty117. 7.1

A. Weiß, N. Neininger, S. Hüttemeister, and U. Klein. The effect of violent star formation on the state of the molecular gas in M 82. A&A, 365:571–587, January 2001. doi: 10.1051/0004-6361:20000145. 7.2.3

S. D. M. White. Further simulations of merging galaxies. MNRAS, 189:831–852, December 1979. doi: 10.1093/mnras/189.4.831. 3.3.2, 3.5.4

J. P. Williams and C. F. McKee. The Galactic Distribution of OB Associations in Molecular Clouds. ApJ, 476:166–183, February 1997. doi: 10.1086/303588. 2, 3.1, 5.1, 7.1, 7.2.2

C. D. Wilson, W. E. Harris, R. Longden, and N. Z. Scoville. Two Populations of Young Massive Star Clusters in Arp 220. ApJ, 641:763–772, April 2006. doi: 10.1086/500577. 2.5.4

J. Wu, N. J. Evans, II, Y. Gao, P. M. Solomon, Y. L. Shirley, and P. A. Vanden Bout. Connecting Dense Gas Tracers of Star Formation in our Galaxy to High-z Star Formation. ApJ, 635:L173–L176, December 2005. doi: 10.1086/499623. 2.5.1, 5.2.2, 5.5.1

J. Wu, N. J. Evans, II, Y. L. Shirley, and C. Knez. The Properties of Massive, Dense Clumps: Mapping Surveys of HCN and CS. ApJS, 188:313-357, June 2010. doi: 10.1088/0067-0049/188/2/313. 2.5.1, 2.5.1, 2.5.1, 7, 5.2, 5.2.2, 5.2.3, 5.2.3, 5.2, 5.3, 5.5.1, 5.5.2, 5.7

T. M. Yoast-Hull, J. S. Gallagher, and E. G. Zweibel. Equipartition and cosmic ray energy densities in central molecular zones of starbursts. MNRAS, 457:L29–L33, March 2016. doi: 10.1093/mnrasl/slv195. 2.4.1

D. Zhang and S. W. Davis. Radiation Hydrodynamic Simulations of Dust-driven Winds. ApJ, 839:54, April 2017. doi: 10.3847/1538-4357/aa6935. 1, 2.5.7, 5.5.3

H. Zinnecker and H. W. Yorke. Toward Understanding Massive Star Formation. ARA&A, 45:481–563, September 2007. doi: 10.1146/annurev.astro.44.051905.092549. 5.3.3

B. Zuckerman and N. J. Evans, II. Models of massive molecular clouds. ApJ, 192: L149–L152, September 1974. doi: 10.1086/181613. 1.1, 5.1, 5.7